Machine Protection and High Energy Density States in Matter for High Energy Hadron Accelerators

THÈSE N^{O} 6051 (2014)

PRÉSENTÉE LE 7 FÉVRIER 2014

À LA FACULTÉ DES SCIENCES DE BASE
LABORATOIRE DE PHYSIQUE DES ACCÉLÉRATEURS DE PARTICULES
PROGRAMME DOCTORAL EN PHYSIQUE

ÉCOLE POLYTECHNIQUE FÉDÉRALE DE LAUSANNE

POUR L'OBTENTION DU GRADE DE DOCTEUR ÈS SCIENCES

PAR

Juan BLANCO SANCHO

acceptée sur proposition du jury:

Prof. O. Schneider, président du jury
Prof. L. Rivkin, Prof. R. Schmidt, directeurs de thèse
Dr A. Fabich, rapporteur
Dr J. Wenninger, rapporteur
Dr M. Wohlmuther, rapporteur

ÉCOLE POLYTECHNIQUE
FÉDÉRALE DE LAUSANNE

Suisse
2014

It doesn't matter how beautiful your theory is,
it doesn't matter how smart you are.
If it doesn't agree with experiment, it's wrong.
— Richard P. Feynman

Acknowledgments

This thesis is the result of four years of work with the help of many colleagues and friends. I would like to thank my supervisor Dr. Leonid Rivkin and the EPFL for giving me this opportunity.

I would especially like to thank my supervisor at CERN, Rüdiger Schmidt, for his infinite patience, support and great ideas. I had not been able to finish this thesis without his faith in me.

A big thank to all my colleagues at CERN for their support and affection: B. Todd, M. Zerlauth, I. Romera, A. Castañeda, A. Gomez, J. L. Vo Duy, P. Dahlen ,B. Puccio, P. Nouvel, J. Salvador, C. Martin, S. Gabourin, J. P. Boudonnat, B. Collignon and A. Cauphy.

The HiRadMat experiment would have not been possible without the contributions and work from R. Schmidt, N. A. Tahir, F. Burkart, D. Wollmann, D. Grenier, E. Griesmayer, K. Cornelis, K. Weiss, J. Zak, N. Charitonidis, I. Efthymiopoulos, A. Fabich, C. Maglioni, and C. Theis.

I also have to thank all my friends in Geneva and specially Antonio, Raul, Ivan, Pepe, Luna, Jacobo, Sandra, Sophie, Oriol, Isaac, Raquel, Lucia, Montse, Kurmi, Chiara, Paca, ...

Also many thanks to Pablo Mayoral for his help.

To my family because they are always beside me.

Geneva, 15 October 2013 J. Blanco Sancho

Abstract

The Large Hadron Collider (LHC) is the largest accelerator in the world. It is designed to collide two proton beams with unprecedented particle energy of 7 TeV. The energy stored in each beam is 362 MJ, sufficient to melt 500 kg of copper. An accidental release of even a small fraction of the beam energy can result in severe damage to the equipment. Machine protection systems are essential to safely operate the accelerator and handle all possible accidents. This thesis deals with the study of different failure scenarios and its possible consequences. It addresses failure scenarios ranging from low intensity losses on high-Z materials and superconductors to high intensity losses on carbon and copper collimators. Low beam losses are sufficient to quench the superconducting magnets and the stabilized superconducting cables (bus-bars) that connects the main magnets. If this occurs and the energy from the bus-bar is not extracted fast enough it can lead to a situation similar to the accident in 2008 at LHC during powering tests. Inadequate beam aborts combined with failures in the collimation system setup can lead to severe damage on the tertiary collimators.

One of the critical failures scenarios is when the entire beam is lost at a single point. Several failures at the LHC could lead to the full beam deflected with non-nominal angle, into a 10 m long graphite absorber, into a septum magnet, or into superconducting magnets. This thesis presents detailed numerical simulations of the full LHC beam impact on carbon and SPS beam on copper. Simulations have been carried out employing a particle interaction and transport package, FLUKA, and a two-dimensional hydrodynamic code, BIG2. Results suggest the existence of a hydrodynamic process that boosts the beam penetration range. Results for LHC suggest that the beam can penetrate up to 25 m in carbon whereas the range of the shower from a single proton in carbon is just about 3 m. This hydrodynamic effect is called 'hydrodynamic tunneling'. Hydrodynamic tunneling is the result of the extreme conditions (temperature and pressure) that occurs in the beam heated region of the target. A large part of the beam heated region enters into the Warm Dense Matter (WDM) state.

An experiment to reproduce the hydrodynamic tunneling was performed at the High Radiation to Materials (HiRadMat) facility at the CERN on July 2012. High intensity beam was directed on a copper target. The experiment uses a new diamond detector designed for the high radiation environments. The experiment was also a good opportunity to investigate new types of instrumentation for high radiation environments: SEM detectors, strain gauges and temperature probes. Experiment results are consistent with hydrodynamic tunneling of protons.

Keywords: LHC Machine Protection, High Energy Hadron Accelerators, LHC, Hydrodynamic Tunneling simulations, BIG2-FLUKA Simulations, High-Fluence Diamond detectors, Hydrodynamic Tunneling Experiment, HiRadMat Experiment, High Energy Density Matter produced by LHC and SPS accelerators, Bus-bars quench studies and HiRadMat beam window design.

Résumé

Le LHC est le plus grand accélérateur au monde. Il a été conçu pour proportionner une collision entre deux rayons protons avec une énergie de particules jamais vue de 7 TeV. L'énergie stockée dans chaque rayon est de 362 MJ, assez pour fondre 500 kg de cuivre. Une fuite accidentée d'une partie même minuscule du rayon peut mener à des dégâts importants au matériel. Les systèmes de protection pour machines sont essentiels pour assurer l'opération en toute sécurité de l'accélérateur et pour gérer tout accident éventuel. Cette thèse étudie différents scénarios de faillite et leurs conséquences. Elle étudie des scénarios de petites pertes d'intensité sur des matériaux high-Z et super-conducteurs, et de pertes importantes sur des collimateurs de carbone et cuivre. Des petites pertes de rayons son suffisants pour étancher les aimants super-conducteurs et les câbles super-conducteurs stabilisés (bus-bars) qui connectent les aimants principaux. Si cela se produit et l'énergie du bus-bar n'est pas extrait rapidement, il pourrait se produire une situation similaire à l'accident de 2008 à l'accélérateur pendant les tests d'électricité. Un arrêt inadéquat de rayon en plus d'un échec de l'installation du système de collimation peut engendrer des dégâts importants aux collimateurs tertiaires.

Un des scénarios de faillite grave est quand le rayon est complètement perdu à un point donné. Plusieurs faillites au LHC pourrait engendrer la déviation du rayon à un long absorbeur de graphite de 10 m, à un (septum magnet) ou à des aimants super-conducteurs. Cette thèse offre des simulations numériques détaillées de l'impact du rayon LHC sur le carbone et du rayon SPS sur le cuivre. Des simulations ont été réalisé en utilisant l'interaction de particules, le paquet transport, FLUKA, et un code hydrodynamique de deux dimensions, BIG2. Les résultats pour le LHC suggèrent que le rayon peut pénétrer jusqu'à 25 m dans le carbone tandis que la portée d'un seul proton douche dans le carbone et de seulement 3 m. Cet effet hydrodynamique s'appelle 'creusement hydrodynamique'. Le creusement hydrodynamique est le résultat de conditions extrêmes (température et pression) qui ont lieu dans la partie de la cible chauffée par le rayon. Une grande partie de la région chauffée par le rayon entre dans un état de Warm Dense Matter (WDM).

Une expérience pour reproduire le creusement hydrodynamique a été réalisée dans l'établissement High Radiation to Materials (HiRadMat) au CERN en juillet 2012. Un rayon haute intensité a été dirigé sur une cible de cuivre. L'expérience utilise un nouveau détecteur de diamant conçu pour environnements de radiation élevée. L'expérience fût aussi une bonne occasion pour examiner de nouveaux types d'instruments pour des environnements de radiation élevée : détecteurs SEM, jauges de pression et sondes de température. Les résultats obtenus de l'expérience sont en accord avec le creusement hydrodynamique des protons.

Mots-clés : LHC Protection Machine, Haute Energie Hadron Accélérateurs, LHC, Les Simulations Hydrodynamiques de Tunneling, BIG2-FLUKA Simulations, Haut-Fluence Détecteurs de Diamant, Expérience Tunneling Hydrodynamique, Expérience HiRadMat, Haut Matière d'Énergie de Densité produites par le LHC et SPS accélérateurs, Bus-bars 'quench' études et Conception de fenêtre de faisceau HiRadMat.

Contents

List of Figures

List of Tables

Introduction

The Large Hadron Collider (LHC) is the largest accelerator in the world. Two counter rotating proton beams are accelerated from injection energy of 450 GeV to 7 TeV at top energy. The energy stored in each beam is 362 MJ, sufficient to melt 500 kg of copper. An accidental release of even a small fraction of the beam energy can result in severe damage to the accelerator and equipment. Machine protection systems are essential to safely operate the accelerator and handle all possible accidents. However, beam loss scenarios need to be studied to understand the risk for accidental beam losses and their consequences. This information is essential in order to design the protection systems of the machine correctly, to set admissible risk levels, and to determine the inventory of the spare parts needed to possibly replace damaged equipment.

The first part of the thesis is devoted low intensity beam loss scenarios. Low beam losses on tungsten collimators can provoke damage of the material and possibly a leak of refrigerating water into the beam pipes. Low intensity losses due to aperture limitations can quench superconducting magnet coils and the stabilized superconducting cables. An undetected quench of a superconducting cable at top energy can lead to an accident at least as severe as the accident that happened during powering test in 2008.

The second part of the thesis presents results of the studies performed until summer 2012 for the calculations of high intensity high dense beam impacting high-Z materials. A particle transport and Monte-Carlo interaction code and a 2-D hydrodynamic code are combined to accurately simulate the process. The thesis describes the methodology used to combine the two computer codes in order to estimate the consequences if such beam impacts on material. Hydrodynamic motion plays an important role in this process. A hydrodynamic effect called 'hydrodynamic tunneling' increases the penetration range protons, possibly by an order of magnitude.

The last part of the thesis presents an experiment dedicated to reproducing the 'hydrodynamic tunneling'. The experiment setup, detectors and experiment phases are described. Experiment results are compared with two hypothesis: 'hydrodynamic tunneling' and no 'hydrodynamic tunneling'.

The work from this thesis has triggered other work studies that continue the line of research shown in this thesis.

- Chapter 1 introduces CERN and describes the LHC accelerator and its main injection chain.

- Chapter 2 explains the fundamentals of accelerator physics and in particular transverse dynamics. The matrix formulation is explained for particle dynamics through main accelerator magnets.
- Chapter 3 gives a brief description of the different mechanisms of particle-matter interaction. The particle transport and Monte-Carlo interaction code (FLUKA) is introduced.
- Chapter 4 describes High Energy Density Matter regime, the main thermodynamical equations and the most relevant characteristics of the 2-D hydrodynamic code (BIG2) that has been used for the calculations presented here.
- Chapter 5 presents LHC machine protection systems and lists LHC failure modes by beam loss duration and intensity.
- Chapter 6 studies the failure scenario of an asynchronous beam dump combined with a failure in the collimation system setup. This scenario can lead to severe damage of the tertiary collimators protecting the main focusing superconducting magnets.
- Chapter 7 analyzes three failure scenarios in the LHC in which low intensity beam losses can quench superconducting magnets and the stabilized superconducting cables (bus-bars). A case is considered in which the bus-bar is warmed up to 80 K in a very short time by the energy deposition from beam losses. For such failure, the energy extraction system cannot extract fast enough the energy stored in the magnet circuit.
- Chapter 8 presents calculations of the impact of the full LHC beam on a carbon target. The calculations are done by combining FLUKA and BIG2 codes. Results suggest the existence of a hydrodynamic effect that boosts the beam penetration range. The same hydrodynamic effect is seen for the calculations of the full SPS beam impact on a copper target. This effect is called 'hydrodynamic tunneling'.
- An experiment to reproduce the 'hydrodynamic tunneling' seen in simulations is described in Chapter 9. It also presents the novel design of a diamond detector prepared for high radiation environments that has been used in the experiment. The first part of the chapter is devoted to the beam commissioning of the HiRadMat facility where the experiment took place.
- Chapter 10 presents the phases of the experiment. Results from the experiment are analysed such as the experience with the diamond detectors and the post irradiation studies.
- Chapter 11 summarizes all results presented in the thesis, together with the conclusions.

1 CERN, LHC and injection chain

1.1 CERN

CERN (Conseil Européen pour la Recherche Nucléaire) is the European Laboratory for Particle Physics. It is the largest particle accelerator facility in the world, hosting more than 13.000 visiting engineers and physicist and ~ 2250 staff employees. It is located in Geneva on the border between Switzerland and France.

Figure 1.1: CERN aerial view. In yellow, the LHC with its four main experiments. In blue, SPS accelerator. In red, PS accelerator.

Founded in 1954, it currently has twenty member states, from Europe, two international organizations (UNESCO, European Commission) and five countries with observer status (Turkey, Japan, India, Russia and United States). It also has co-operation agreements with many countries in the world.

1.2 LHC

The Large Hadron Collider (LHC) [9] is the largest accelerator in the world and the most complex machine ever built. Accelerators with higher energy and higher intensity are needed to discover massive elementary particles. According to Einstein relation $E = mc^2$ mass is proportional to energy so, in order to produce massive particles a large amount of energy is needed. One of the main LHC goals is the discovery and study the Higgs boson [10]. Other LHC goals are to try to find insights of physics beyond the standard model (physics that does not comply with the S. M.), to study the quark-gluon plasma (high energy state of matter that dominated the universe after the inflationary epoch), CP symmetry violation, extra dimensions, etc.

It consists of a ~ 27 km ring at 150 m underground. Two counter rotating proton beams are accelerated from 450 GeV to 7 TeV. Then the beams are collided at four points of the accelerator where experiments are located. Each beam is comprised of up to 2808 bunches of $1.15 \cdot 10^{11}$ protons. The nominal energy stored per beam is two orders of magnitude higher than any other proton machine and corresponds to 362 MJ per beam, sufficient to melt 500 kg of copper. LHC can also operate with heavy ions (mainly lead). Fully stripped lead with an energy of 2.76 TeV/u can be collided with other lead ions or with protons.

The discovery potential of the LHC is associated with the nominal energy at the collision center of mass and with the number of collisions per unit time per area (luminosity). The LHC design nominal luminosity is $10^{34}\,\mathrm{cm^{-2}s^{-1}}$, that it is two orders of magnitude higher than the peak TeVatron luminosity [11].

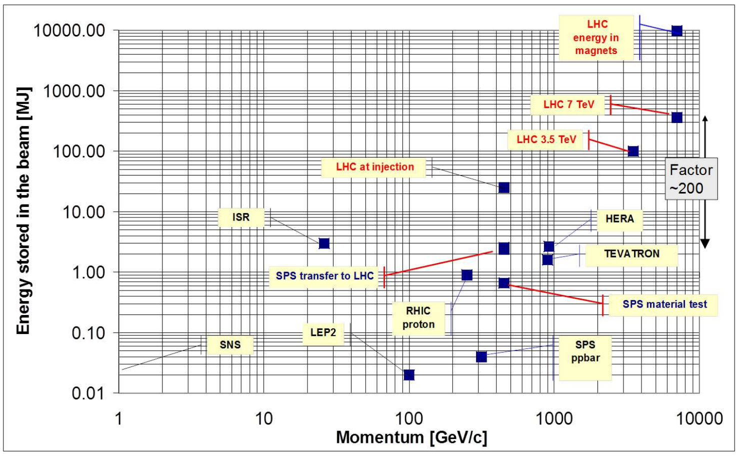

Credit: *R. Assmann*

Figure 1.2: Total energy stored in the beam versus momentum for different accelerators.

LHC ring is divided into eight arc sectors with a straight sections in between them, that make up the whole circumference. Each straight section or interaction point (IP) is dedicated to a specific function for the accelerator. The four main experiments: ATLAS (A Toroidal LHC Aparatus), ALICE (A Large Ion Collider Experiment), CMS (Compact Muon Solenoid) and LHCb

(LHC beauty) are located on the first, second, fifth and eighth straight sections. The third and seventh are dedicated to collimation systems. The LHC radiofrequency, for acceleration, is installed on the fourth straight section. Eight superconducting cavities of 400 Mhz per ring are used to accelerate the beams. The beam dump system is located on IP6. The beam injection sections for beam 1 & 2 are located at IP2 and IP8 respectively.

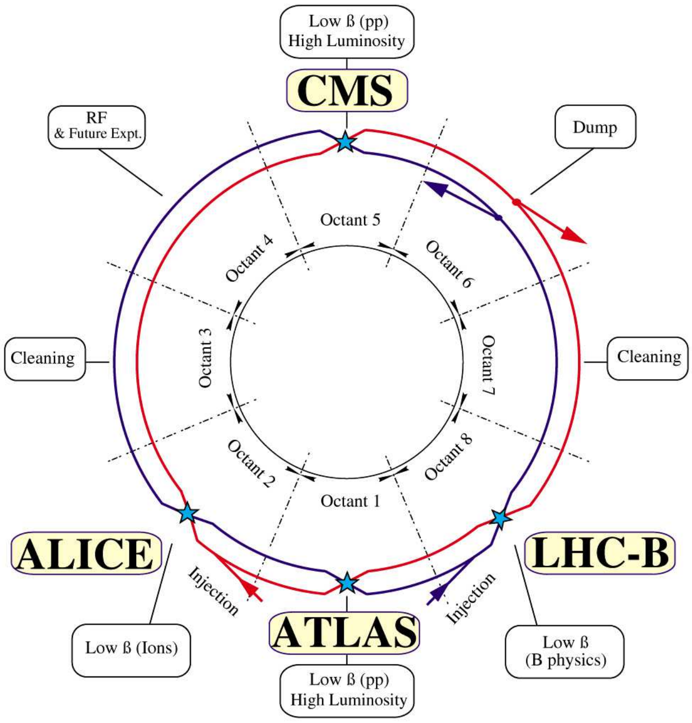

Figure 1.3: LHC Layout.

LHC has more than 10000 magnets of which 90% are superconducting. Superconducting magnet coils are made of NdTi filaments in a copper matrix. Niobium-titanium alloy becomes superconducting below 9.2 K; at LHC the coils are cooled to 1.9 K to carry a current of more than 12000 A. The main superconducting magnets are the main dipoles (MB) and the main quadrupoles (MQ) of the accelerator. The function of the MB is to deflect the beam so that the beam makes a complete revolution. The field strength of the MB magnets defines the maximum energy at which the LHC can operate. Using the formula for the magnetic rigidity, the maximum proton energy for the LHC is given by the maximum magnetic field of the bending magnets (8.33 T) and accelerator radius that is given by the Large Electron-Positron collider radius (the LHC machine is installed in the tunnel previously used by LEP). Equation 1.1 shows the relation between the magnetic rigidity ($B\rho$) and the particle momentum (p) and charge (q). The function of the main quadrupoles is to focus the beam in both vertical and horizontal planes so the particles are continuously confined and the beam size remains small. The total energy stored in LHC magnets is 11 GJ, that is equivalent to the kinetic energy an aircraft carrier at 50 km/h.

$$B\rho = \frac{p}{q} \tag{1.1}$$

1.3 LHC injector chain

Particles injected into the LHC have previously gone through several accelerators. Initially, protons are obtained by heating up H_2 until it becomes a plasma and then separating the protons with an electric field. Then, a series of linear accelerator components (RFQ and Alvarez linac) accelerate, focalize and bunch the proton beam. At this point protons have an energy of 50 MeV and the beam is bunched. The PS booster is the first circular machine in the path of protons to the LHC. It consist of four superimposed rings, one on top of the other, with a radius of 25 m that accelerates protons up to 1.4 GeV. After the booster, the Proton Synchrotron (PS) accelerates protons to 26 GeV. Initially, six proton bunches are injected into the PS and by using radio frequency cavities each bunch is splitted into three. At top energy (26 GeV) each of the eighteen bunches is splitted into two bunches twice (72 bunches). Four consecutive extractions from the PS (288 bunches) are injected into the Super Proton Synchrotron (SPS) [12] and further accelerated up to 450 GeV that is the injection energy of the LHC.

It has been proposed to upgrade the LHC injector chain in view of the high luminosity LHC program, and later for the high energy LHC project (HELHC).

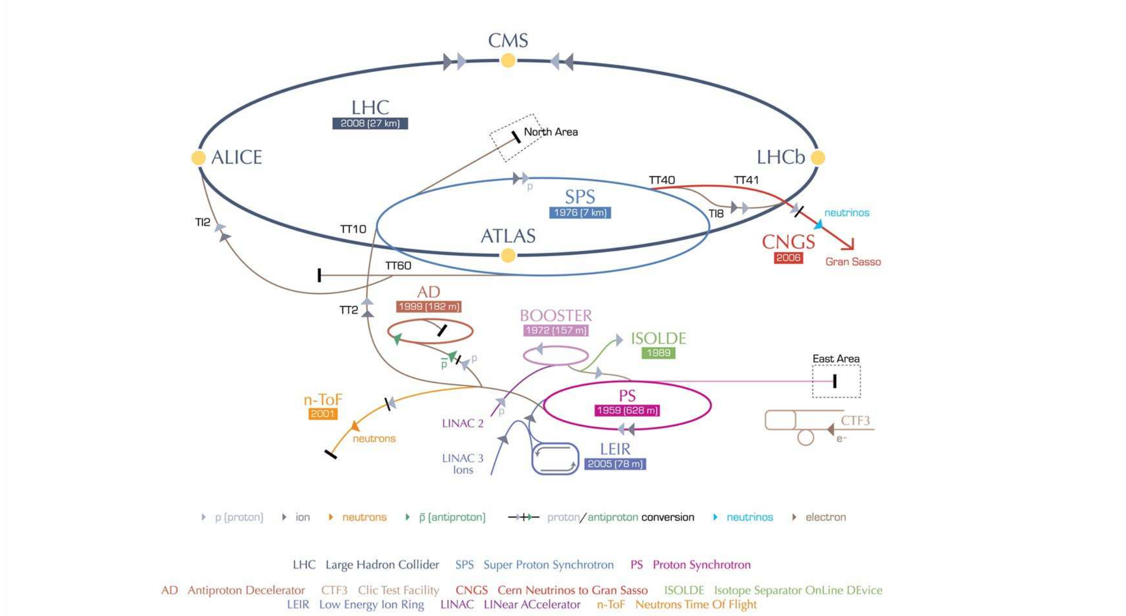

Figure 1.4: CERN accelerator complex.

2 Accelerator Physics

This chapter introduces the basic equations governing the motion of the particles in the transverse plane and the different concepts used to define the optics of a particle accelerator. A more in detail description and further concepts can be found in [13, 14].

2.1 Lorentz Force

A moving charge particle under the influence of an electric or magnetic field experiments a force given by the Lorentz equation.

$$\bar{F} = q\left[\bar{E} + \left(\bar{v} \times \bar{B}\right)\right] \tag{2.1}$$

The electric field exerts a force in the same direction of the field and proportional to the particle charge. The magnetic field exerts a force, to a moving particle, perpendicular to the direction of the particle trajectory and the magnetic field and proportional the the particle velocity. A closer look to the formula, shows that for a relativistic particle ($|\bar{v}| \approx c$) with charge q the force exerted by a magnetic field is c times stronger than the one by an electric field. Therefore, for a relativistic charge q, the force of 1 T is equivalent to $E \equiv cB = 3 \cdot 10^8\,\mathrm{m/s} \cdot 1\,\mathrm{Vs/m^2} = 3\,\mathrm{MV/cm}$.

Electric fields as opposed to magnetic fields are mainly used to accelerate particles. A charged particle in an electric field is accelerated in the direction of the field while a particle moving in a magnetic field will steer around the magnetic field lines. The work done by a magnetic field is zero because the force is perpendicular to the direction of motion. Magnetic fields are mainly used to guide the particles, especially at relativistic speeds.

For a particle moving at a relativistic speed $\beta = \frac{v}{c} \approx 1$ the Lorentz force equation is modified by a factor $\gamma = \frac{1}{\sqrt{1-\beta^2}}$ (Lorentz factor).

$$\bar{F} = \gamma q \left[\bar{E} + \left(\bar{v} \times \bar{B}\right)\right] \tag{2.2}$$

2.2 Hill's equation

In order to define the movement of a charge particle it is needed to define a coordinate system. This coordinate system is attached to the particle and it moves with it. Locally, the reference orbit has a curvature (ρ). The coordinate system is defined by the three vectors $\left(\bar{x}, \bar{y}, \bar{s}\right)$ at any point along the reference orbit. $\bar{x}$ is given by the vector form by the center of curvature to the particle position at any given moment. The vector $\bar{s}$ is always tangential to the reference orbit and perpendicular to $\bar{x}$. $\bar{y}$ is given by the cross product of $\bar{s} \times \bar{x}$ The longitudinal coordinate is defined by $\bar{s}$ and transverse plane by $\left(\bar{x}, \bar{y}\right)$.

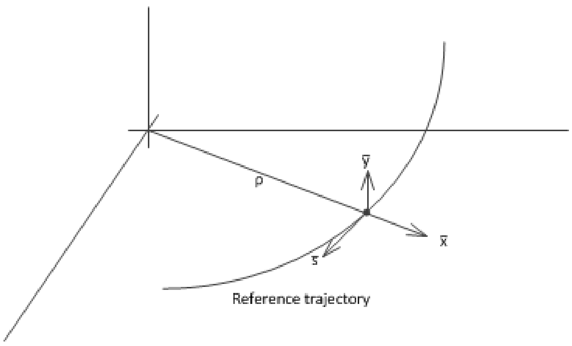

Figure 2.1: Coordinate system.

Where the position of a particle is given by

$$\bar{R} = r\bar{x} + y\bar{y} = (\rho + x)\bar{x} + y\bar{y} \tag{2.3}$$

In order to deduce the equation governing the movement of a particle under the influence of a magnetic field some assumptions are made:

- The magnetic field will not have a longitudinal component ($B_s = 0$) (only transverse fields).
- $\gamma = constant$ The particle will not radiate energy.
- The longitudinal movement is decoupled from the transverse. Oscillations in the longitudinal direction have a lower frequency than the ones in the transversal plane.

- In the transverse plane, there is no coupling between x and y (no skew magnets).

The magnetic field in the vicinity of the origin can be expressed as

$$B_y(x) = B_{y0} + \frac{dB_y}{dx}x + \frac{1}{2!}\frac{d^2B_y}{dx^2}x^2 + \frac{1}{3!}\frac{d^3B_y}{dx^3}x^3 + \dots \quad (2.4)$$

Multiplying by e/p we get

$$\frac{e}{p}B_y(x) = \frac{1}{\rho} + kx + \frac{1}{2!}mx^2 + \frac{1}{3!}ox^3 + \dots \quad (2.5)$$

The magnetic field is expressed as an infinite sum of multipolar elements: dipole, quadrupole,... Table 2.1 shows the definition and its effect on the beam of the first terms of the expansion.

Table 2.1: Main multipolar terms, their associated parameter and its effect on the beam.

Multipole	Parameter	Effect on the beam
Dipole	$1/\rho$	Bending
Quadrupole	k	Focusing
Sextupole	m	Chromaticity correction
Octupole	o	Field error compensation

We consider a charge particle crossing a magnetic field with a local curvature radius (ρ). For the particle, the Lorentz force has to be equal to the centripetal force.

$$\bar{F} = \frac{d\bar{p}}{dt} = \frac{d}{dt}\left(m_0\gamma\bar{v}\right) = q\left(\bar{E} + \bar{v}\times\bar{B}\right) \quad (2.6)$$

where

$$\bar{F} = \frac{d\bar{p}}{dt} = \frac{d}{dt}\left(m_0\gamma\dot{\bar{R}}\right) = \left(m_0\gamma\ddot{\bar{R}}\right) \quad (2.7)$$

evaluating $\ddot{\bar{R}}$

$$\ddot{\bar{R}} = \left(\ddot{r} - r\dot{\theta}^2\right)\bar{x} + \left(2\dot{r}\dot{\theta} + r\ddot{\theta}\right)\bar{s} + \ddot{y}\bar{y} \quad (2.8)$$

in the $\bar{x}$ direction

$$\ddot{r} - r\dot{\theta}^2 = -\frac{ev_s B_y}{\gamma m_0} = -\frac{e{v_s}^2 B_y}{\gamma m_0 v_s} = -\frac{e{v_s}^2 B_y}{p} \tag{2.9}$$

changing the independent variable to s

$$\frac{d}{dt} = \frac{ds}{dt}\frac{d}{ds} \tag{2.10}$$

$$x = -\frac{e{v_s}^2 B_y}{\gamma m_0 v_s} = -\frac{e{v_s}^2 B_y}{p} \tag{2.11}$$

using the multipolar expression for B_y

$$\frac{d^2 x}{ds^2} + \left[\frac{1}{\rho^2} + \frac{e}{p}\frac{\partial B_y}{\partial x}\right] x = 0, \tag{2.12}$$

$$\frac{d^2 y}{ds^2} - \frac{1}{\rho^2} - \frac{e}{p}\frac{\partial B_y}{\partial x} y = 0. \tag{2.13}$$

The equation of motion [15] for for both x and y axis is in the form

$$x" + K(s)x = 0 \tag{2.14}$$

The derived equation of motion is the formula of a simple harmonic oscillator in which the spring constant (K) depends on the position (s). There is not a general solution for this pair of equations as the K parameter depends on the actual distribution of magnets in the accelerator. However, if we consider the magnets as discrete elements with a finite length inside which the magnet strength is constant. Then, we can derive an individual solution for each type.

2.3 Matrix Formulation

The solutions of Hill's equation are presented in a matrix format 2×2. For each element, the matrix represents how the motion of a particle changes when passing through that kind of element. Therefore, the motion of a particle through a series of elements in an accelerator can be expressed as a 2×2 matrix that is the result of multiplying the different individual matrix for each element. Three different solutions for the Hill's equation are presented: K=0 (drift space), K>0 (defocusing quadrupole) and K<0 (focusing quadrupole).

$$M = M_n \cdots M_3 M_2 M_1 \tag{2.15}$$

2.3.1 Drift Space

For a drift space with a finite length l where $K = 0$ the solution for Equation 2.14 in matrix notation is the following

$$\begin{pmatrix} x \\ x' \end{pmatrix}_{out} = \begin{pmatrix} 1 & l \\ 0 & 1 \end{pmatrix} \begin{pmatrix} x \\ x' \end{pmatrix}_{in} \tag{2.16}$$

2.3.2 Quadrupole magnet

For a quadrupole magnet with a finite length l with a gradient strength $K > 0$ the matrix representation is the following

$$\begin{pmatrix} x \\ x' \end{pmatrix}_{out} = \begin{pmatrix} cos(\sqrt{K}l) & \frac{1}{\sqrt{K}} sin(\sqrt{K}l) \\ -\sqrt{K} sin(\sqrt{K}l) & cos(\sqrt{K}l) \end{pmatrix} \begin{pmatrix} x \\ x' \end{pmatrix}_{in} \tag{2.17}$$

for a gradient strength $K < 0$

$$\begin{pmatrix} x \\ x' \end{pmatrix}_{out} = \begin{pmatrix} cosh(\sqrt{|K|}l) & \frac{1}{\sqrt{|K|}} sinh(\sqrt{|K|}l) \\ \sqrt{|K|} sinh(\sqrt{|K|}l) & cosh(\sqrt{|K|}l) \end{pmatrix} \begin{pmatrix} x \\ x' \end{pmatrix}_{in} \tag{2.18}$$

These matrix can be simplified if we can consider the length of the quadrupoles small compared to the focal length (l « f) where the focal length can be expressed as $f = 1/Kl$.

$$\begin{pmatrix} x \\ x' \end{pmatrix}_{out} = \begin{pmatrix} 1 & l \\ -\frac{1}{f} & 1 \end{pmatrix} \begin{pmatrix} x \\ x' \end{pmatrix}_{in} \tag{2.19}$$

2.4 Closed form solution

If we consider a circular accelerator, then the K(s) parameter from the Hill's equation becomes periodic. For this case it is possible to obtain a general solution.

$$K(s) = K(s+C) \tag{2.20}$$

where C is the circumference of the accelerator.

Then we can express a general solution for the equation like a simple harmonic oscillator with an amplitude and a phase advance that are dependent on *s*.

$$x = Aw(s)cos(\psi(s)+\delta) \tag{2.21}$$

Substituting the solution into the equation one can obtain the parameters w(s) and $\psi(s)$. Finally the solution can be rewritten as

$$x = \sqrt{\epsilon\beta(s)}cos(\psi(s)+\delta) \tag{2.22}$$

The amplitude of the oscillations are given by $\sqrt{\epsilon\beta(s)}$

The phase of the betatron oscillation $\psi(s)$ also called phase advance or betatron phase

$$\psi(s) = \int \frac{ds}{\beta(s)} \rightarrow \Delta\psi = \int_{s0}^{s0+\Delta s} \frac{ds}{\beta(s)} \tag{2.23}$$

The phase advance of a complete turn around the accelerator is 2π times the betatron oscillations and it is called tune.

$$\nu = \frac{1}{2\pi}\oint \frac{ds}{\beta(s)} \tag{2.24}$$

2.5 Courant-Snyder Parameters

The general solution for the equation of movement was written as a function of $w(s)$ and $\psi(s)$ and later re-written as as a function of ϵ (emittance), β (beta function) and ψ (betatron phase). The matrix that transforms x and x' from one point to another in the accelerator as a function of $w(s)$, $w'(s)$ and ψ. As we did with the general solution, one can define a new set of variables to rewrite it as a function of ϵ, β, α and γ. These fundamental variables are called Courant-Snyder parameters or twiss parameters.

$$\alpha(s) = -\frac{1}{2}\frac{d\beta}{ds} \tag{2.25}$$

$$\gamma(s) = \frac{1-\alpha^2}{\beta} \tag{2.26}$$

The transport matrix from $s_1 \to s_2$ can be expressed as a function of the Courant-Snyder parameters and the phase advance at the origin and destination.

$$M(s_1 \to s_2) = \begin{pmatrix} \left(\frac{\beta_2}{\beta_1}\right)^{1/2} (cos(\Delta\psi)) + \alpha_1 sin(\Delta\phi) & (\beta_1\beta_2)^(1/2) sin(\Delta\phi) \\ -\frac{1+\alpha_1\alpha_2}{(\beta_1\beta_2)^(1/2)} sin(\Delta\psi) + \frac{\alpha_1-\alpha_2}{(\beta_1\beta_2)^(1/2)} cos(\Delta\psi) & \left(\frac{\beta_1}{\beta_2}\right)^{1/2} (cos(\Delta\psi)) - \alpha_2 sin(\Delta\phi) \end{pmatrix} \tag{2.27}$$

Using the general solution 2.22 of the Hill's equation for a periodic system and deriving it with respect to s. One can isolate the emittance ϵ and write it is as a function of the Courant-Snyder parameters

$$\epsilon = \gamma x^2 + 2\alpha x x' + \beta x'^2 \tag{2.28}$$

With the assumption of $\gamma = cte$ (no deceleration or acceleration) and according to the Liouville's theorem the emittance is an invariant (Courant-Snyder Invariant). This is also the equation of an ellipse with an area of $\pi\epsilon$.

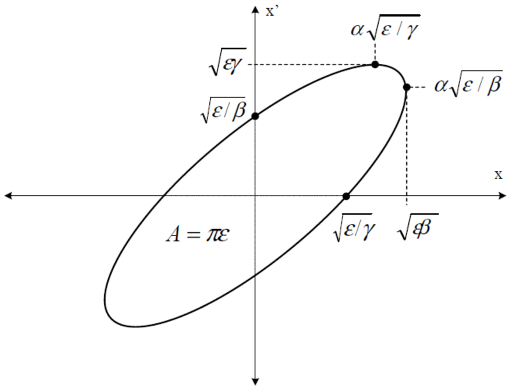

Figure 2.2: Phase space ellipse.

The normalized emittance remains constant even if γ does not and it is defined as follows

$$\epsilon_N = \epsilon\gamma\frac{v}{c} \tag{2.29}$$

2.6 Dispersion

Not all particles follow the ideal trajectory, in deed hardly anyone does. Particles with a slightly different momentum than the ideal particle will follow a different trajectory when going through a bending magnet. In a circular machine, these particles will follow a different closed orbit than the reference one. If the particle has slightly more momentum, its trajectory will be further out while if its momentum is smaller it will be more inside. The curvature radius is given by the magnetic rigidity of the particle. The dispersion is a function that relates the displacement of an off-momentum particle with respect to the idea particle as a function of the fractional momentum difference $\frac{\Delta p}{p}$.

$$x = D(p,s)\frac{\Delta p}{p} \tag{2.30}$$

2.7 Beam size

The particle distribution in the transverse plane will be considered gaussian (Gaussian distribution). This assumption is a fairly good a approximation for a particle beam. The following differential equation gives the particle distribution in the transversal plane for a given beam emittance and momentum the accelerator functions beta and dispersion.

$$n(x)dx = \frac{1}{\sqrt{2\pi}\sigma} e^{(} - x^2/(2\sigma^2))dx \tag{2.31}$$

Knowing the emittance of the beam and the lattice functions of the accelerator, it is possible to calculate the beam size at any point. The following formula gives the the rms beam size.

$$\sigma = \sqrt{\epsilon\beta + D\frac{\Delta p}{p}} \tag{2.32}$$

e

3 Particle-Matter Interaction

This chapter introduces the basic concepts and the processes associated with particles-matter interactions. Electromagnetic processes are described more in detail while ones governed by the strong force are briefly mentioned. A more detailed description can be found in the literature [1, 16, 17].

3.1 Cross Section and Mean Free Path

The cross-section σ is defined for N_b incident particles attenuated by a thin target with thickness l and density ρ_t

$$N_e = N_b \cdot \rho_t \cdot l \cdot \sigma \tag{3.1}$$

N_e is the number of events observed. The cross-section has dimension of area (cm^2 or $barn = 10^{-24}\,\mathrm{cm}^2$).

The total cross-section of a particle-target is given by the addition of all the partial cross-sections.

$$\sigma_{total} = \sum_i \sigma_i \tag{3.2}$$

The total nuclear cross-section of particle in a given medium is sum of all nuclear cross-section:

$$\sigma_{total} = \sigma_{inelastic} + \sigma_{diff} + \sigma_{elastic}. \tag{3.3}$$

The total proton-proton cross section at 7 TeV is approximately 110 mbarns. The total cross section can be decomposed into three components: inelastic, elastic and single diffractive. Each component is associated with a different type of interaction. In an elastic interaction the particles kinetic energy is preserved in the center-of-mass frame. On the contrary, during an inelastic interaction, the kinetic energy is not preserved.

- inelastic $\sigma_{inelastic} = 60$ mbarn
- single diffractive $\sigma_{diff} = 12$ mbarn
- elastic $\sigma_{elastic} = 40$ mbarn

The mean free path λ of a particle is the average length between two interactions; it measures the probability of undergoing an interaction between a particle and the medium. For a particle traversing a medium with density ρ and atomic number A, the mean free path in the medium expressed in cm is given by

$$\lambda = \frac{A}{sigma_{total} \cdot N_A \cdot \rho}, \tag{3.4}$$

where N_A is the Avogadro's number.

The inelastic interaction length is very insensitive to the particle energy over a wide energy range. For protons in carbon the inelastic interaction length at 450 GeV is 46.1 cm while at 7 TeV is 42.1 cm.

3.2 Electro-Magnetic Processes

3.2.1 Stopping Power

Charged particles going through matter and lose energy mainly by the interaction of its own electro-magnetic field with the one generated by atomic electrons. The Bethe formula [18, 19, 20, 21, 22] describes the average mean rate energy loss (stopping power) in the region $0.1 \leq \beta\gamma \leq 1000$ by a charged particle going through matter (intermediate-Z material) within a few % error. The energy loss rate is given in $MeV g^{-1} cm^2$. In passing through matter, particles can ionize or excite the atoms of the medium. If the energy transferred is sufficient, it can tear off an electron from its atom or otherwise, if the energy transferred is low it can excite an electron to a higher energy state.

$$-\frac{dE}{dx} = K \cdot z^2 \frac{Z}{A} \frac{1}{\beta^2} \left[\frac{1}{2} ln \frac{2 \cdot m_e c^2 \cdot \beta^2 \cdot \gamma^2 \cdot T_{max}}{I^2} - \beta^2 - \frac{\delta(\beta \cdot \gamma)}{2} \right] \tag{3.5}$$

$K = 4\pi N_A r_e^2 m_e c^2 = 0.307075\,\text{MeVg}^{-1}\text{cm}^2$ is a constant. N_A is the Avogadro's number $6.0221415 \cdot 10^{23}\,\text{mol}^{-1}$. r_e is the classical electron radius 2.817940325 fm. $m_e c^2 = 0.511\,\text{MeV}$ is the electron mass in MeV. z is the projectile atomic number. Z/A is the medium atomic number over the mass number. $\beta = v/c$. T_{max} is the maximum kinetic energy that can be transferred to a free electron in a single collision. For a particle with mass M and momentum $p = M\beta\gamma c$, T_{max} is given by

$$T_{max} = \frac{2m_e \cdot c^2 \cdot \beta^2 \cdot \gamma^2}{1 + 2 \cdot \gamma \cdot m_e/M + (m_e/M)^2}. \tag{3.6}$$

I is the mean excitation energy. The following formula gives an approximation for I (by Felix Bloch [23])

$$I = 10\,\text{eV}Z. \tag{3.7}$$

Where Z is the atomic number of the absorber material. Nowadays, it is more accurate to get the value of I as a function of Z from the Particle Data Group (PDG) tables [1].

$\delta(\beta\gamma)$ is the density-effect correction to ionization energy loss. As the particle energy increases, its electric field flattens and extends, the range for distant collisions extends and the maximum transferred energy increases. However, a screening effect prevents interactions with a large impact parameter thus limiting the energy loss. The density effect correction is usually computed using the Sternheimer's parametrization.

At low energies, a new term $U = \frac{C}{Z}$ should be included inside the logarithmic term of Equation 3.5. This term is referred as the shell correction and accounts for the non-participation of inner electrons in the collision process.

At relativistic energies when the particle's speed is close to the speed of light ($\beta \approx 1$) the dE/dx curve reaches a minimum. A particle with at the dE/dx minimum is called Minimum Ionizing Particle (MIP). This minimum occurs for $\beta_{min}\gamma_{min} \approx 3$.

Knock-on electrons or δ-rays are electrons that have acquired sufficient energy from the interaction with an incoming particle, to cause secondary ionizations.

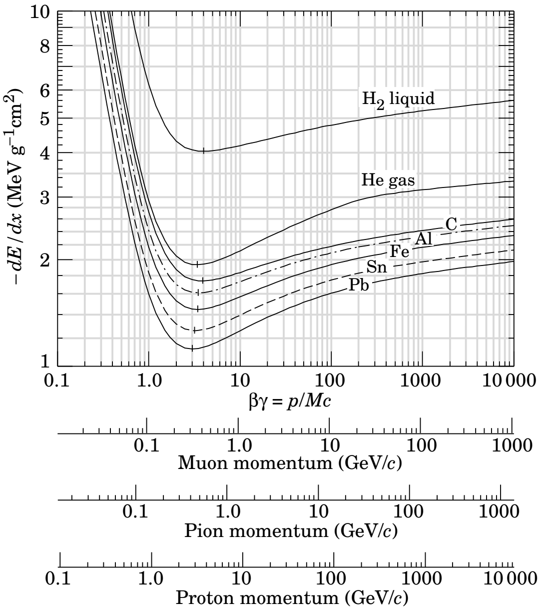

Figure 3.1: Mean energy loss rate in liquid (bubble chamber) hydrogen, gaseous helium, carbon, aluminum, iron, tin, and lead.

3.3 Multiple Coulomb Scattering

A charged particle traversing a material is deflected many times by small angle, mostly, due to Coulomb scattering from nuclei. This effect is modeled by Multiple Coulomb Scattering theory (MCS) [24, 25]. For hadrons, the strong interaction also contribute to the MCS. Molière's Theory derives mathematically the multiple scattering of electrons and other charged particles. The probability distribution of the it is roughly Gaussian for small deflection angles, but at larger angles it behaves like Rutherford scattering, with larger tails than a Gaussian distribution.

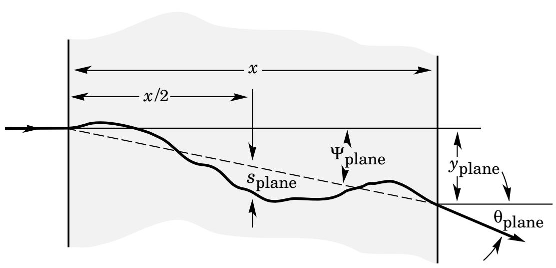

Figure 3.2: Quantities used to describe multiple Coulomb scattering. The particle is incident in the plane of the figure. [1]

A charged particle traversing a material with x thickness will exit the material with an offset

y_{plane} and an angular deflection θ_{plane}.

$$\theta_{plane}^{rms} = \frac{1}{\sqrt{2}}\theta_{space}^{rms} = \theta_0 = \frac{13.6\,\text{MeV}}{\beta \cdot c \cdot p} z \sqrt{x/X_0\,[1 + 0.038 \cdot ln\,(x/X_0)]} \tag{3.8}$$

Where p,βc and z are refer to the projectile momentum, velocity and atomic number. x/X_0 is the thickness of the material being traversed expressed in radiation lengths. $\theta_{space}^2 \approx (\theta_{plane,x}^2 + \theta_{plane,y}^2)$. The parameters shown in Figure 3.2 are given by

$$\psi_{plane}^{rms} = \frac{1}{\sqrt{3}} \cdot \theta_{plane}^{rms} = \frac{1}{\sqrt{3}} \cdot \theta_0, \tag{3.9}$$

$$y_{plane}^{rms} = \frac{1}{\sqrt{3}} \cdot x \cdot \theta_{plane}^{rms} = \frac{1}{\sqrt{3}} \cdot x \cdot \theta_0, \tag{3.10}$$

$$s_{plane}^{rms} = \frac{1}{4\sqrt{3}} \cdot x \cdot \theta_{plane}^{rms} = \frac{1}{4\sqrt{3}} \cdot x \cdot \theta_0, \tag{3.11}$$

3.3.1 Radiation length

High energy electrons traveling through matter mainly lose energy by bremsstrahlung while high energy photons by e^+e^- pair production. Radiation length (X_0) is both the distance over which an electron has lost $1/e$ of its energy or 7/9 of the mean free path for pair production by a high energy photon. Usually measured in g/cm^2. X_0 has been calculated and tabulated by Y.S. Tsai [26]. X_0 is also the appropriate scale length for describing high energy electro-magnetic cascades.

$$\frac{1}{X_0} = 4\alpha r_e^2 \frac{N_A}{A} \left[Z^2 \left(L_{rad} - f(Z)\right) + Z L'_{rad}\right] \tag{3.12}$$

Where α is the fine structure constant $\frac{e^2}{(4\cdot\pi\cdot\epsilon_0)\cdot\hbar\cdot c}$. L_{rad} and L'_{rad} coefficients are taken from Table 3.1.

Table 3.1: Tsai's L_{rad} and L'_{rad} coefficients for X_0 calculation.

Element	Z	L_{rad}	L'_{rad}
H	1	5.31	6.144
He	2	4.79	5.621
Li	3	4.74	5.805
Be	4	4.71	5.924
Others	>4	$ln(184.15Z^{1/3})$	$ln(1194Z^{2/3})$

$f(Z)$ is an infinite sum. The following formula can be used, with good accuracy, for elements up to uranium.

$$f(Z) = (\alpha \cdot Z)^2 \left[\left(1 + (\alpha \cdot Z)^2\right)^{-1} + 0.20206 - 0.0369 \cdot (\alpha Z)^2 + 0.0083 \cdot (\alpha Z)^4 - 0.002 \cdot (\alpha Z)^6 \right] \tag{3.13}$$

3.3.2 Energy loss by electrons

At low energy, electrons and positrons lose energy by ionization. Møller(e^-) and Bhabha(e^+) scattering and positron annihilation also contribute but to a lesser extend. At high energies (≥ 10 MeV) the energy loss is dominated by Bremsstrahlung ($e^\pm \to e^\pm + \gamma$).

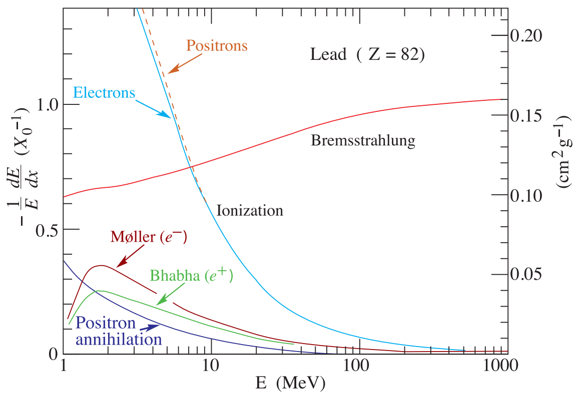

Figure 3.3: Fractional energy loss per radiation length in lead as a function of electron or positron energy. Electron (positron) scattering is considered as ionization when the energy loss per collision is below 0.255 MeV, and as Møller (Bhabha) scattering when it is above. [1]

The critical energy (Ec) is the energy at which loss rate by Bremsstrahlung and Ionization are equal. The critical energy can be approximated by $E_c \approx 610\,\text{MeV}/(Z+1.24)$ for solids and by $E_c \approx 710\,\text{MeV}/(Z+0.92)$ for gases.

$$\left|\frac{dE}{dX}\right|_{brems} \approx \frac{E}{X_0} \tag{3.14}$$

3.3.3 Energy loss by photons

Figure 3.5 shows the different contributions to the total energy loss by photons. At low energies, the photoelectric effect dominates, although Compton scattering, Rayleigh scattering, and photonuclear absorption also contribute. The discontinuities in the photoelectric cross section

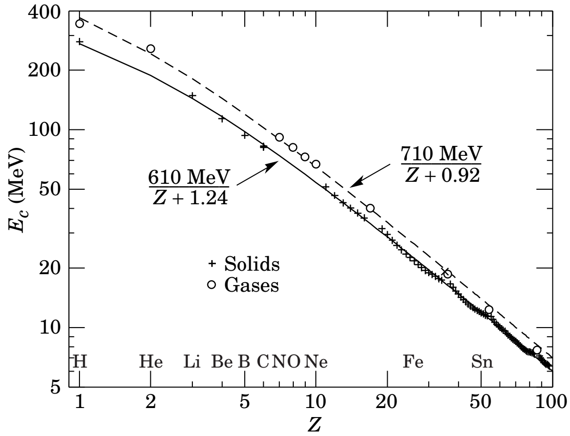

Figure 3.4: Electron critical energy for the chemical elements. [2]

are given by the absorption lines. At higher energies pair production dominates.

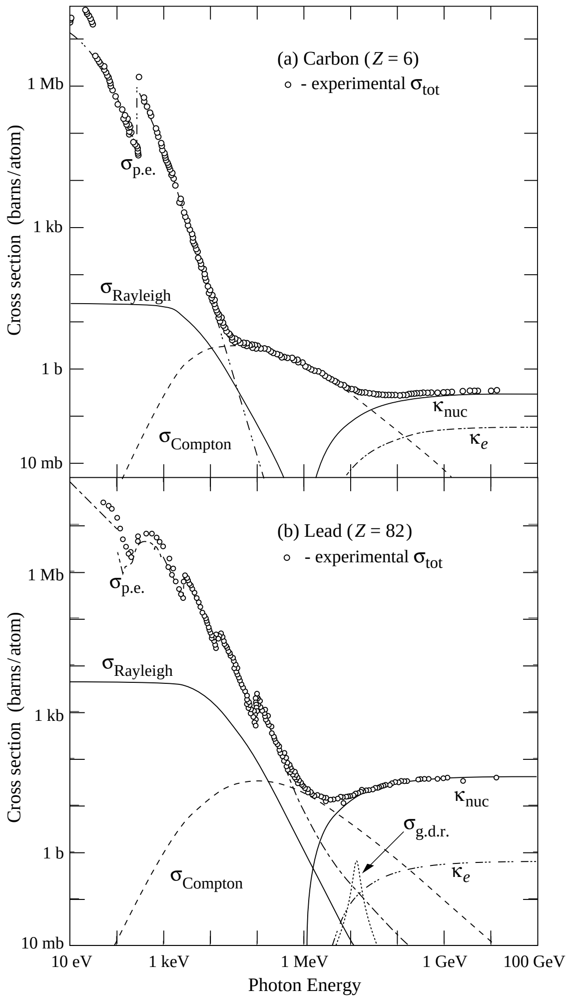

Figure 3.5: Photon total cross sections as a function of energy in carbon and lead, showing the contributions of different processes. [3, 4]

3.4 Electromagnetic Showers

As shown in Figure 3.3, the energy loss by high energy $e^{\pm}$ it is mainly via Bremsstrahlung; high energy photons lose energy, mainly by pair production. X_0 is the appropriate scale length for describing high energy electromagnetic cascades. A high energy electrons or positrons will lose energy by radiating a photon that eventually will create a pair e^+e^- which in turn will radiate more photons. This process grows exponentially until $e^{\pm}$ energy will fall below the critical energy and then they will lose energy via ionization and excitation rather than Bremsstrahlung. Therefore the maximum length of the electromagnetic cascade is reached when the average energy of all cascade components falls below the critical energy.

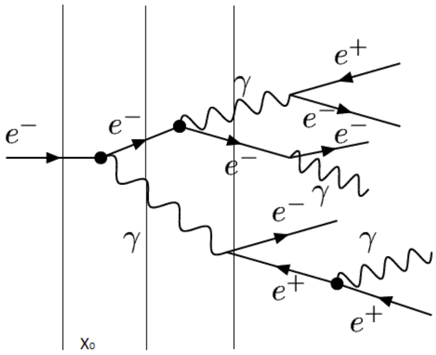

Figure 3.6: Schematic drawing of an electromagnetic cascade.

The maximum length of the cascade can be approximated by

$$x_{max} \approx \left(ln\left(\frac{E}{E_c}\right) + C_j \right) X_0, j = e, \gamma, \tag{3.15}$$

where $C_e = -0.5$ for electron-induced cascades and $C_\gamma = +0.5$ for photon-induced cascades from EGS4 [27]. A similar form for the electron number maximum was obtained by Rossi [2], but with $C_e = -1.0$ and $C_\gamma = -0.5$.

In the transverse plane, the electromagnetic shower can be characterized by the Moliere radius ($R_M =$), that it is an intrinsic property of the absorber material. 90% of the electromagnetic shower is contained within one Moliere radius.

$$R_M = 0.0265 \cdot X_0(Z + 1.2). \tag{3.16}$$

3.5 Nucleon-Nucleon Interactions

Figure 3.7 shows the total and elastic scattering cross section for proton-proton and proton-neutron interactions. Below pion production the total cross section is given entirely by the elastic cross section, meaning that elastic scattering is the only possible interaction. At lower energies (<300 MeV), the cross section drastically increases and the difference between p-p and p-n is about a factor of three. The factor three is explained by symmetry and isospin: $\sigma_T^1 = \sigma_{pp}$ and $\sigma_T^0 = 2\sigma_T^{pn} - \sigma_T^{pp}$. For higher energies the p-p and p-n total and elastic cross sections are equal.

For p-p elastic interaction the angular distribution is quite isotropic at low energies (<300 MeV) while for energies exceeding few 100 MeV the distribution start to develop a strong forward peak. For p-n elastic interaction the angular distribution loses the isotropic characteristic for lower energies than for the p-p reaction. At high energy the angular distribution also develops a strong forward peak, while the backward peak (charge exchange p-n) becomes smaller than the forward one.

The first non-elastic channel for nucleon-nucleon interaction is the pion production $N_1 + N_2 \rightarrow N_1' + N_2' + \pi$. The energy threshold for pion production opens at 290 MeV and becomes important at 700 MeV. For energies exceeding $3-4$ GeV the number of channels grow quickly and the decomposition of the total cross section into channels becomes difficult. Fortunately, above few GeV, different models can be used. Those model have a stronger theoretical base and also less experimental dependency.

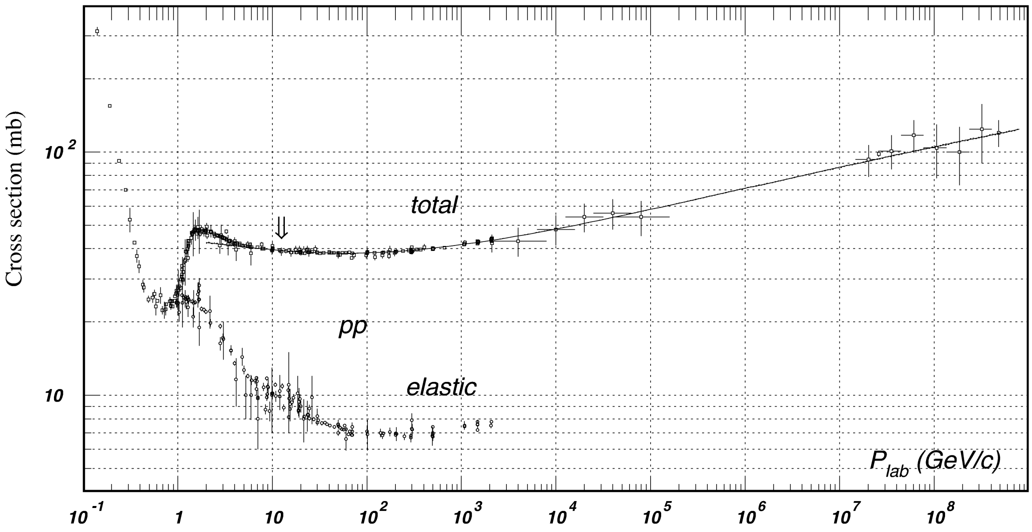

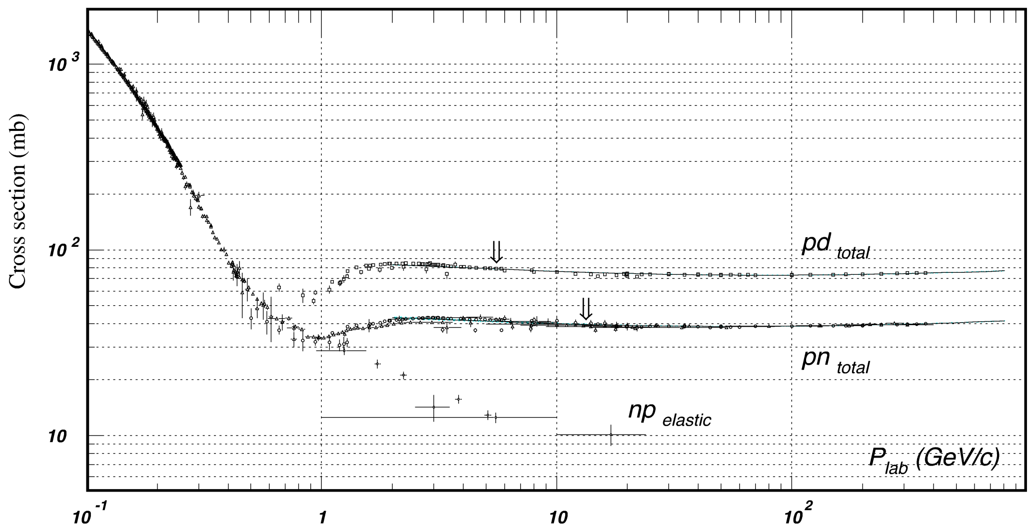

Figure 3.7: Total and elastic cross-section for proton-proton (pp) and proton-neutron (pn) scattering. [1]

3.6 Hadronic Showers

As soon as the energy from the primary hadron beam exceeds a few then of MeV inelastic interactions start to play a major role and secondaries have enough energies to trigger further interactions, giving rise to a hadronic shower. Secondary particles will further interact and create new secondaries. If the particles energy is higher than the pion production threshold then the production of π_0 and η mesons will start to transfer energy from the hadronic shower to the electromagnetic shower. π_0 and η mesons decay into $e^{\pm}$ and γ particles and those will start a electromagnetic shower as explained before. The development of hadron initiated showers is determined both by the relatively rare nuclear interactions (both elastic and nonelastic) and by atomic processes (dE/dx, MCS, etc..) which take place very frequently.

The hadronic shower maximum depends on the beam energy and the inelastic interaction length. It can be approximated by

$$x_{max} \approx (0.6 \cdot ln(E) - 0.2) \cdot \lambda_{inelastic}, \text{ with E expressed in GeV.} \tag{3.17}$$

Shower depth for 95% longitudinal containment is given by

$$x_{95\%} \approx x_{max} + 4 \cdot 10^{0.15} \lambda_{inelastic} \tag{3.18}$$

Transversally, 95% of the hadronic shower is contained within one $\lambda_{inelastic}$.

3.7 General Features Of High-Energy Showers

The following five points describe some general features of high energy showers extracted from a lecture of "Physics of High Energy Reaction" given by Alfredo Ferrari and Paola R. Sala [17].

- The most energetic particles of the shower concentrate around the beam axis (regardless of their identity). The energy deposition profile around the beam axis is dominated by the stopping power of those particles and the electromagnetic showers associated with $\pi_0's$.
- Neutral particles, in practice neutrons as they are the only neutral hadrons with long enough life time, dominate at low energies where the range of charged particles becomes shorter than the interaction length. The interaction of low energy neutrons (ex. recoils and photons) defines the energy deposition profiles at the tails.
- It is important to have a good description of the interactions (mostly neutrons) at

moderate to low energies because most of the interactions fall in that range.

- In addition, it is also important to have a good description of high energy interactions. High energy particles define the longitudinal shower development as they carry a good fraction of the energy and also have a long interaction length.
- The high energy cascade can be identified with the aid of pions as they can only be produced by shower particles. In the final stages of the nuclear interactions (evaporation, fragmentation, etc.) a lot of neutrons and, in lower quantity, protons are produced.

3.8 FLUKA

FLUKA [28, 29] is a general purpose tool for calculations of particle transport and interactions with matter. It covers a wide range of applications: from accelerator shielding, energy deposition (calorimetry), activation, etc.

FLUKA can handle about 60 different particles including photons and electrons from 1 keV to thousands of TeV, neutrinos, muons of any energy, hadrons of energies up to 20 TeV (up to 10 PeV by linking FLUKA with the DPMJET code) and all the corresponding antiparticles, neutrons down to thermal energies (0.025 eV < energy < 20 MeV) and heavy ions. FLUKA includes 25 pre-defined single-element materials and several pre-defined compounds. Any new compound can be defined via atoms, mass or volume fractions. The stopping power of charged particles is calculated from the Sternheimer parameters and the ionization potential.

FLUKA can also transport polarized photons (e.g., synchrotron radiation) and optical photons. Time evolution and tracking of emitted radiation from unstable residual nuclei can be performed online.

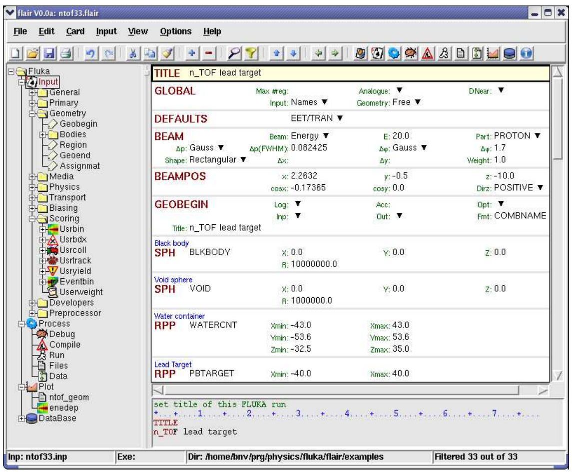

Figure 3.8: FLUKA input file edited with FLAIR

In FLUKA, the geometries are described using Combinational Geometry (CG). Geometries are constructed by intersecting, adding and subtracting objects that can be either infinite (planes, cylinders, etc.) or finite (boxes, cylinders, spheres, etc.).

FLUKA can track charged particles inside magnetic or electric fields.

4 High Energy Density Matter

Most of the matter that we see around us, including us, is made of baryonic matter (protons, neutrons, atoms,...). However, in the universe the situation is very different. Most of the energy in the universe is in the form of dark matter (26.8%). Dark energy adds a 68.3% more. The remaining ~ 5% is what we commonly refer as matter. The matter that surround us in earth is mainly in liquid, solid or gas state. But in our galaxy most of that ~ 5% of matter is in the form of plasma. Hot dense plasmas are in the core of starts, low density plasmas form the intergalactic medium.

Warm dense matter (WDM) is a extreme regime of HEDM, not clearly defined, of high density similar to solids, and high temperature like in plasmas. It is expected to appear in solids heated up to plasma temperature. Temperatures are ranging from $0.2 - 10\,\mathrm{eV}$ and densities between $0.01 - 100\,\mathrm{g/cm^3}$. The core of large planets (Ex. Jupiter) are thought to be in the form of WDM.

It is of great interest to perform experiments with WDM in the laboratory. Conventionally, it is created by high power lasers [30, 31] (National Ignition Facility), high current Z-Pinch [32] (Sandia NL) or with explosives. Particle accelerator methods provide a very fast way to heat up samples homogeneously. Large samples of WDM can also be created in a controlled and reproducible way with proton accelerators [33, 34, 35].

No relations between T,P,V and ρ have been derived from first principles for this regime so the Equation Of State (EOS) are based on empirical data. Using accelerators allows to explore the different points of the EOS. Knowing the equation of state of materials for these regimes is important in fields such as astrophysics, plasma physics, inertial confinement physics, basic science, ...

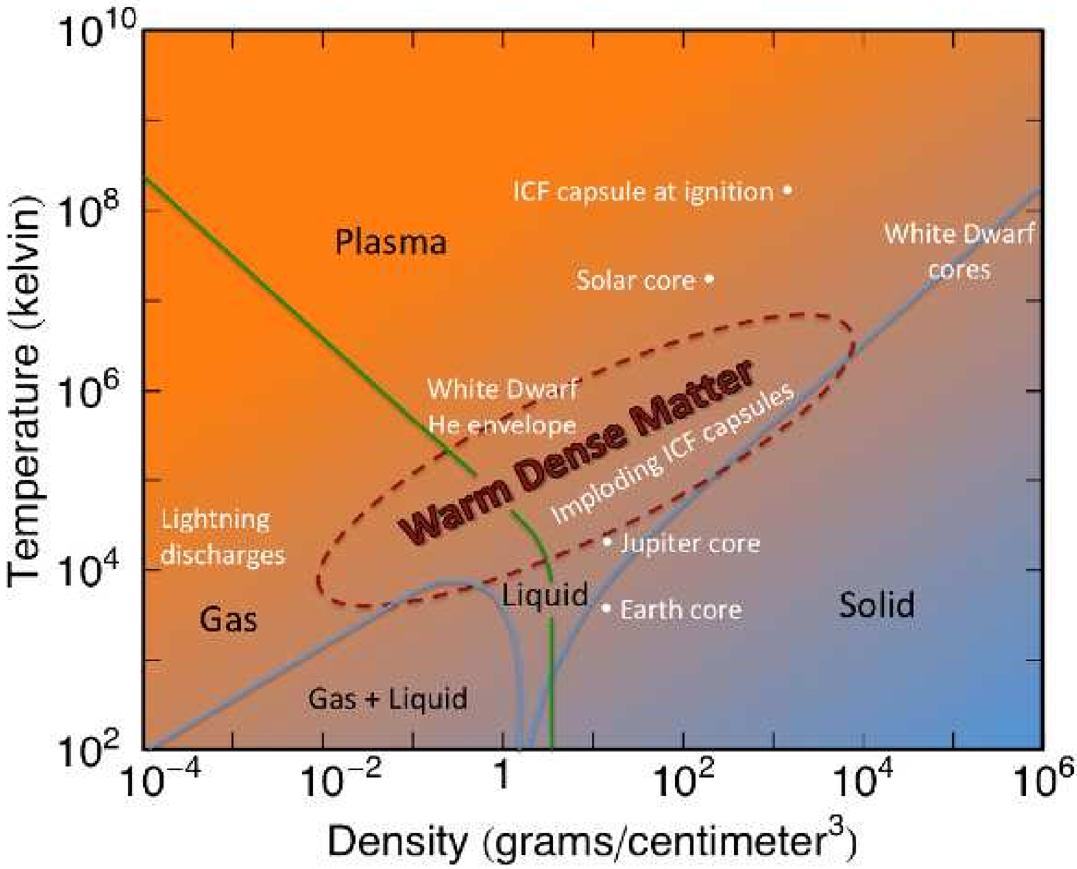

Credit: *M. Desjarlais*

Figure 4.1: Warm Dense Matter region.

4.1 BIG2

The hydrodynamic motion of a fluid heated by a particle beam can be calculated with BIG2 [36] code. BIG2 code is a hydrodynamic numerical code developed by Alexander Shutov, Oleg Vorobiev, and Alexander Ni at Chernogolovka (Russia). It uses a unique rezoning in which there are no separate Lagrangian and Eulerian steps like in a traditional ALE (Arbitrary Lagrangian Eulerian). It uses a quadrilateral mesh in which adjacent blocks can have different resolutions. Collisions of cells are supported by the code. The empirical Chernogolovka Equations Of State for several materials (Ex. copper, carbon,...) are one of the strengths of the code. It covers extreme regimes like: plasma or Warm Dense Matter (WDM).

BIG2 uses a Godunov scheme [37, 38] where non-stationary fronts and interfaces are tracked as boundaries of subregions that move in time. A Godunov scheme is numerical scheme for solving partial differential equations in which the conservative variables are considered constant over the cells during each time step. In each subregion and at each time step, a new grid is created by the use of boundary-fitted coordinates. The solution of the fundamental fluid equations are calculated by evaluating them on the calculated grid (Riemann problem).

The foundational axioms of fluid dynamics used are the three conservations laws together with the equation of state of the fluid. The first conservation law is the conservation of mass; it states that in any close system the mass of the system is preserved.

$$\frac{\partial \rho}{\partial t} = -\nabla \left(\rho \cdot \bar{u} \right) \tag{4.1}$$

The second conservation law is the conservation of momentum.

$$\frac{\partial}{\partial t} \left(\rho \cdot \bar{u} \right) = -\nabla \left(\rho \cdot \bar{u} \cdot \bar{u} \right) - \nabla p \tag{4.2}$$

The third conservation law is the conservation of energy.

$$\frac{\partial}{\partial t} \left(\rho \cdot e \right) = -\nabla \left(\rho \cdot e \cdot \bar{u} \right) - \nabla \left(p \cdot \bar{u} \right) + \rho \cdot w_{beam} \tag{4.3}$$

In order to solve system of equations composed of the three conservation laws it is necessary a introduce a fourth equation. The equation of state is a thermodynamical relation between the pressure, temperature and density of the fluid. The ideal gas equation is an example of an EOS that is a valid approximation for certain gases under specific conditions. Other equations of state are a combination of equations and empirical for different states of the fluid. The data comes directly from experiments: ex: Chernogolovka EOS. It is difficult have access to the EOS of materials for some regimes because the data is intimately linked to ballistic and nuclear experiments.

BIG2 code has application in various scientific fields like impact and detonation problems and high-intensity high-dense beam problems.

5 Failure Modes and Machine Protection

5.1 LHC Operating Cycle

LHC beams are produced in the CERN accelerator complex. They are accelerated in the SPS from 26 GeV to 450 GeV. Then they are transferred through the SPS-LHC transfer lines to LHC IP2 for beam 1 and to LHC IP8 for beam 2. During the injection phase, 12 batches of either 216 or 288 bunches are injected. The injection phase takes about 30 min to complete.

Once the beams are circulating around the LHC at 450 GeV, the field on the main bending magnets is ramped up from ≈ 0.54 T to ≈ 8.33 T that corresponds to a beam energy of 7 TeV. After the accident in 2008, the LHC top energy has been limited to 3.5 TeV and later in 2012 increased to 4 TeV. The ramp up phase takes about 13 min to complete. During injection and ramp phases, the beams are kept separated in the collision points.

After the beams are ramped up and they are stably circulating around the LHC, the beams are prepared for collision. First, the beam size is reduced (squeezed) in the interaction points from $\beta^* = 11$ m to 0.55 m. Secondly, the beams are led to collide in the interaction points. The squeeze and crossing phase takes about ≤ 18 min.

The beams collide for several hours ($\approx 0-30$ h) during which the experiments acquire data from collisions. At the end of the fill or after a failure is detected, the beams are dumped and the magnets are slowly ramped down to prepare for the next injection. When the beams need to be dump, the beam is extracted from the LHC ring through a dedicated transferline (one for each beam) to the beam dump blocks. The LHC extraction is managed by the LHC Beam Dump System. The average turn around time is 3 h. Figure 5.1 shows the LHC operational cycle.

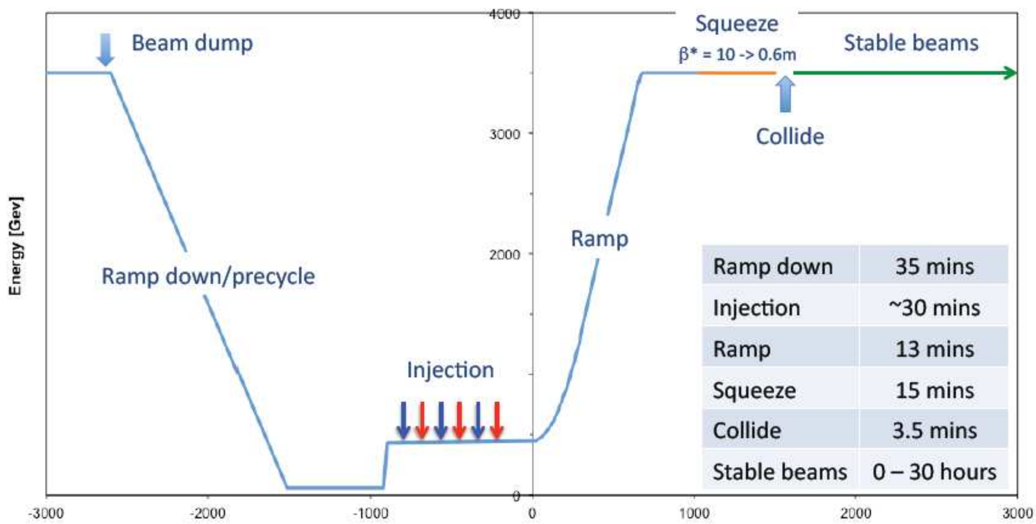

Credit: *M. Lamont*

Figure 5.1: The LHC operational cycle.

5.1.1 LHC Beam Dump System

LHC beams have an unprecedented stored energy of 362 MJ, with a beam size in the order of hundreds of micrometers. The damage potential of such beams requires a dedicated system for the beam extraction. The task of this extraction system is to safely extract the beam from the LHC when requested, reduce the beam energy density and dispose it on a dedicated absorber. The LHC Beam Dump System (LBDS) is located at IP6 of the LHC. Figure 5.2 shows the IP6 schema. The system is composed of 15 fast kicker magnets (MKD) that deflects the beam by 0.27 mrad and 15 vertical deflecting Lamberston septum magnets (MSD) that deflects the beam by 2.4 mrad.

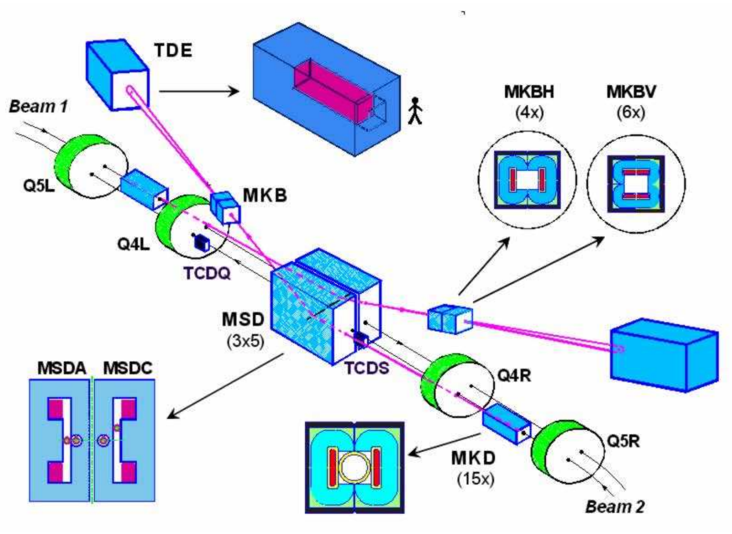

Figure 5.2: LHC Interaction Point 6 schema.

The beam energy density is diluted by two sets of orthogonally deflecting kickers (MKB), 4 horizontal and 6 vertical per beam. The beam is rasterized or painted on the transversal plane in spiral figure. The beam spiral figure grows during the 600 m tunnel that separates the extraction system from the dedicated absorber until it reaches a circumference of about 120 cm and a beam size of $\sigma_{x,y} = 1.6$ mm.

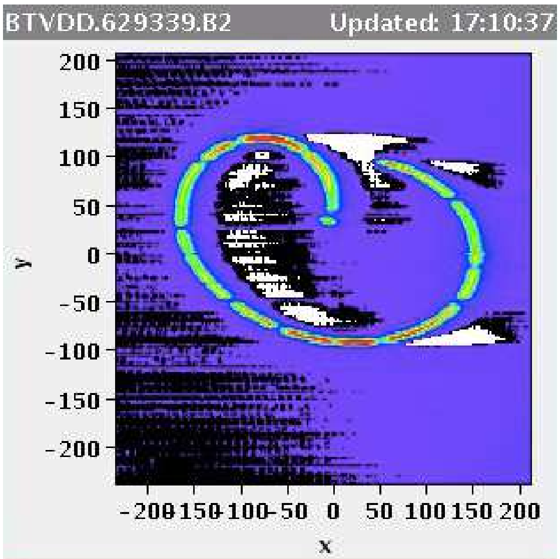

Figure 5.3: Beam 2 transversal profile at the entrance of the beam dump block at IP6. (3.5 GeV)

LHC beams are always extracted by the LBDS system either by a normal end of fill dump or because of a user request after a failure. The beam extraction trigger comes from the BIS when any user system request it. After a beam extraction request from the BIS, the LBDS system waits until the abort gap of the beam is synchronized with the powering up of the extraction kickers. The abort gap is a 3 μs long region with no particles. In order to have a clear extraction of the beam, with minimal beam losses, the powering up of the extraction kickers must occur during the abort gap region. Otherwise, if the extraction kickers are powered up with the beam passing by several bunches will be deflected with a wrong angle (asynchronous beam dump). There are several collimators and absorbers (Ex: TCDQ, TCDS) protecting magnets and equipment for the case of an asynchronous beam dump.

There are two beam dump absorbers, one for each beam. Each absorber consists of a 8 m long carbon cylinder of 70 cm diameter, contained in a steel cylinder. The beam dump block is cooled with water and shielded by concrete and iron blocks. Figure 5.3 shows the beam 2 transversal profile at the entrance of the beam dump block.

5.2 Failure Modes

LHC operates in a new regime in terms of beam energy and intensity. The beam energy is a factor of 7 above any other accelerators built. The energy stored in the LHC magnets is 11 GJ at top energy, this is equivalent to the kinetic energy of an aircraft carrier at 50 km/h. The energy stored in each of the LHC beams is $\approx$ 362 MJ, sufficient to melt 500 kg of copper and equivalent to $\approx$ 86 kg of TNT. The beam power for one revolution is 3.9 TW. An uncontrolled released of even a small fraction of the beam energy is sufficient to damage accelerator equipment and provoke long down-times [39]. As an example, an instantaneous loss of 10^{-9} times the nominal LHC beam intensity can quench a superconducting magnet [40] (lose superconductivity). Beam losses can be classified according to the beam loss time. Figure 5.4 shows the classification of beam losses and the protection systems that prevent them.

The origin of failures [41] leading to beam losses is equipment in wrong state or hardware problems. Losses can be categorized into five groups depending on the loss duration: Ultra-fast losses occur in less than four LHC revolution turns, fast losses occur in between 356 μs and 10 ms, intermediate losses occur in between 10 ms and 10 s, slow occur 10 s to 100 s and steady state losses have times over 100 s.

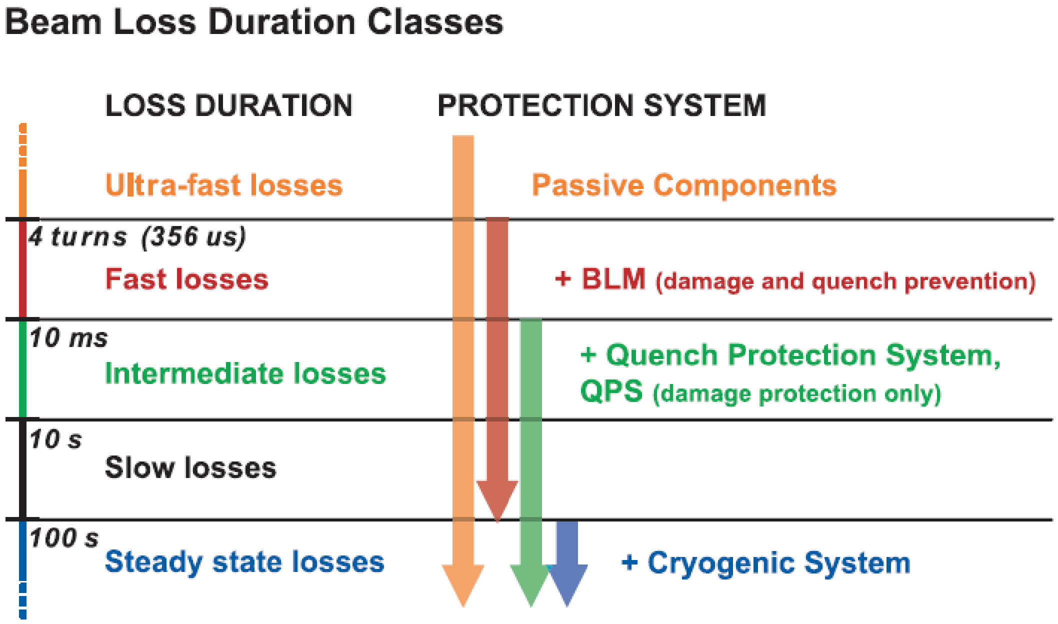

Credit: *E. B. Holzer*

Figure 5.4: Beam Loss Duration Categories.

Ultra-fast losses can only be mitigated by passive protection systems. Active protection systems have reaction times higher than the time scale of the loss. Ultra-fast losses are extremely dangerous because of the tremendous damage potential of the LHC beam. Typical scenarios for ultra-fast losses are injection and extraction losses [42, 43] and asynchronous beam dumps [44]. At injection, if the injection kickers do not fire at the proper time or do not fire at all, the injected beam will be deflected with a wrong angle. The circulating beam can also be deflected by a misfire of the injection kickers. A two jaw absorber (TDI) protects the magnets and accelerator components from any damage from the miskicked beam.

For an asynchronous extraction of the beam, when the extraction kicker magnets fire not synchronously with the beam abort gap, some bunches deflected by the kickers can escape the dump protection system. For the case of beam 2, bunches with an amplitude above $10.28 \times \sigma$ will be intercepted at the local protection devices of the extraction dump. Particles between $5.08 \times \sigma$ and $10.28 \times \sigma$ can impact on collimators around the machine. Bunches between $8.3 \times \sigma$ and $10.28 \times \sigma$, that is between 2-2.5 bunches in terms of equivalent beam intensity, can impact on the tertiary collimator (TCT) jaw at IP5 if the hierarchy between TCT and dump protection is violated. For that case, particles will have a maximum amplitude of $10\ \sigma$ generated with a phase advance of $\pi/2$ respect to the pre-fired kicker (worst case scenario) [45]. This type of failure is assumed to happen once per 300 years [46].

Fast losses occur in the range of hundreds of μs to 10 ms. The collimation system [47], Beam Loss Monitor system [48] (BLM) and Quench Protection System [49] (QPS) protects against these losses. The QPS system monitors the voltage across the superconducting magnets and dumps the beam when it detects a significant rise of the voltage across a s.c. magnet. After the incident of 2008 a new QPS system (nQPS) was installed in the LHC to prevent against quenches in the magnet splices. The BLM system monitors the particle loss rate around the machine and dumps the beam in case the integrated loss rate exceeds a certain threshold. BLM system reacts faster than the QPS system covering the whole timescale range (μs to ms). Fast losses can occur due to failures in normal conducting magnets, aperture limitation problems or magnet quenches.

Slow losses have a time scale in the order of tens of seconds. The longer integration times of the BLM system monitors these losses. Slow losses can be produced due to many different type of failures, as an example by orbit changes generated by abnormal operation of the orbit corrector magnets.

For nominal operation of LHC at 7 TeV if the beam life time (time after which the beam intensity is reduced by a factor $1/e$) of about 18 h the corresponding steady-state losses are 3×10^9 p/s. Steady-state losses are continuously depositing energy on accelerator components and have to be kept low, because a small temperature increase on the magnet coils can cause them to lose superconductivity. LHC magnet coils have to be kept cooled at 1.9 K to remain in superconducting condition. Steady-state losses have to be compensated by LHC Cryogenics.

5.3 Machine Protection Systems

The LHC machine protection systems [50] (MPS) 'backbone' consists of magnet and beam interlock system, LBDS, active detection systems (BLM, BCM, QPS, Software Interlock System (SIS),...), injection protection, collimation,.. There are more than 10000 interlock conditions to abort the beam. Apart from the accident of the accident of 2008, thanks to the MPS no equipment damage has been observed. However, this level of safety comes at expense of many false triggers (41 false beam dumps in 2010 and 71 in 2011) [51]. A false trigger occurs when a user system request a beam dump not because of a real interlock condition in the accelerator but because of an internal failure of the system itself.

5.3.1 BIS

The Beam Interlock System [52] (BIS) is the system that ensures that LHC operates safely with beam. The system is designed to fulfill two principles: reliability and availability. The BIS permits the injection of beam into the LHC only when all the necessary systems are ready for beam. When the beam is circulating in the LHC if any system connected request a beam dump, the BIS delivers the dump request to the LHC Beam Dump System (LBDS).

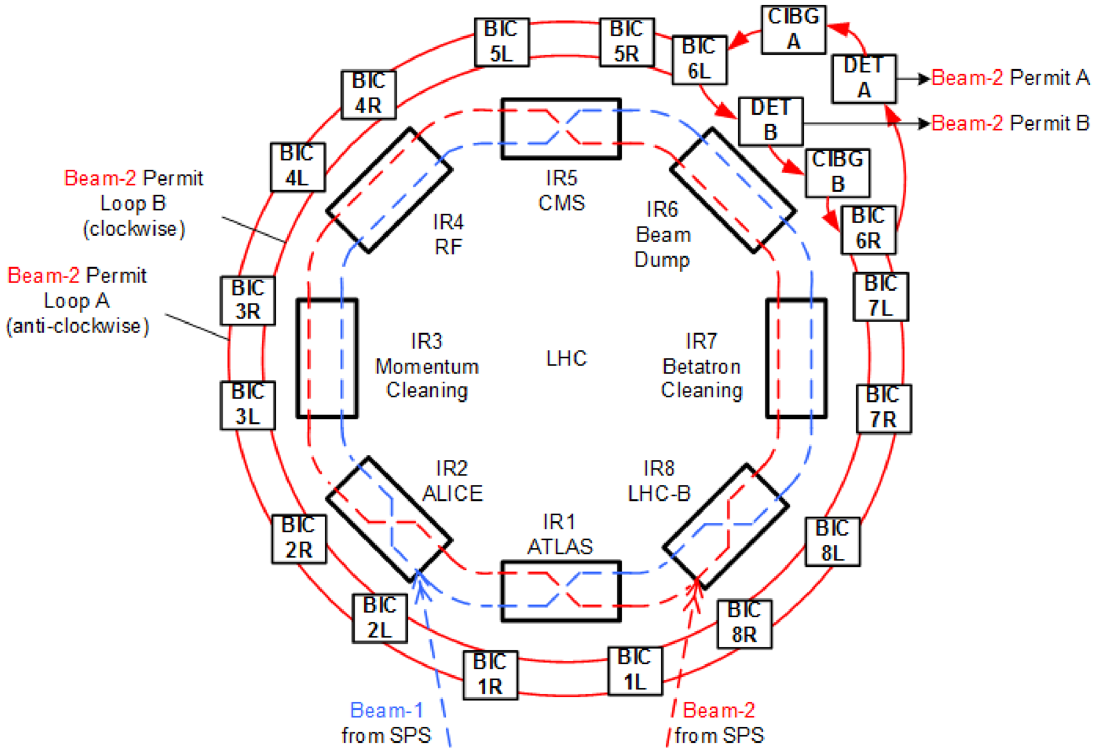

Credit: *B. Todd*

Figure 5.5: Beam Interlock System in the LHC.

More than 120 systems distributed around the ~ 27 km circumference of LHC are connected to the BIS (see Figure 5.5). From now on, they are called users. The users are connected to the BIS via a special box (CIBU). The BIS consists of 17 controllers (BIC's) distributed around the LHC. The users are connected to the nearest controller (BIC). Each controller gathers all the "*beam permit*" signals from the users and calculates a "*local beam permit*" signal. In a rough approach, each controller calculates an 'AND' function over all the beam permit inputs. The controllers act as an optical switch retransmitting (local beam permit = TRUE) or stop transmitting (local beam permit = FALSE) the generated frequency around the machine. Figure 5.6 shows a simplified version of the BIC logic.

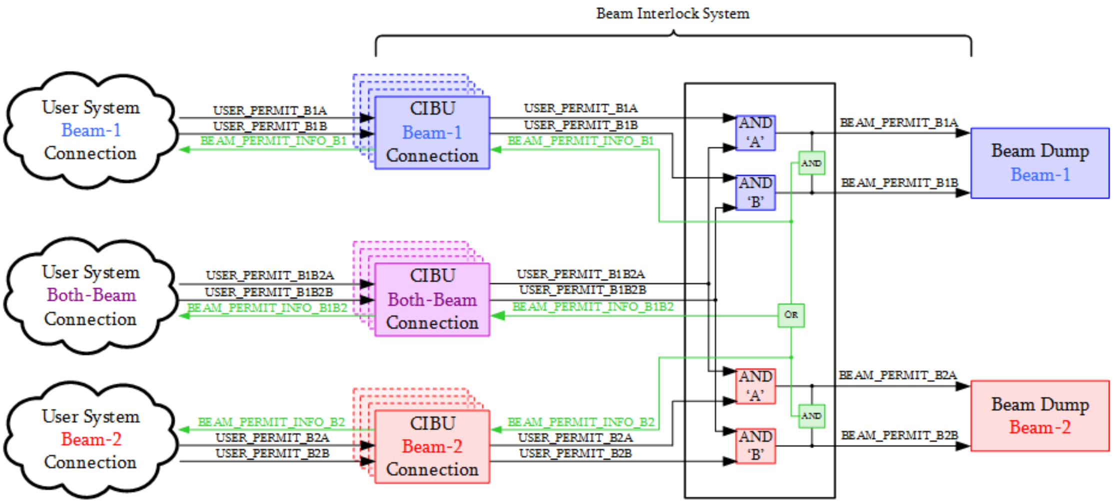

Credit: *B. Todd*

Figure 5.6: Beam Interlock Controller function.

The LBDS is continuously monitoring the frequency that goes around the machine and if at any point the frequency disappears (beam dump request), the beam is extracted from the machine. The whole process, from the user removing the beam permit signal to the moment when the beam is extracted takes around 2-4 LHC revolutions ($\approx 380\,\mu$s).

5.3.2 Beam Loss Monitors

The LHC the beam loss system continuously monitors the rate and location of particle losses. The system is designed to detect beam losses in the LHC and dump the beams before a magnet quench or any accelerator component is damaged. The beam loss system is the last line of defense to prevent any damage to the accelerator. This system actively protects against losses in the range of hundreds of microseconds to tens of seconds.

The system is composed of more than 3000 ionization chambers (IC) placed next to the superconducting magnets. Each ionization chamber has a set of thresholds for different time scales. If the particle loss rate exceeds the threshold, the beam will be extracted. The system reaction time is in the order of 3-4 turns.

Apart from the IC, the system also uses secondary electron emission monitors (SEM) and little ionization chambers (LIC) for the regions of the LHC where the particle losses are very high. The system has recently added pCVD diamond detectors that monitors 'UFO' beam losses (possibly dust particles falling into the beam) and injection losses. Diamond detectors have a ns reaction time and are radiation hard.

5.3.3 Collimation System

There are 108 collimators around the LHC and transfer lines, almost all of them are moveable with up to 5 degrees of freedom. In the LHC they are located mainly at IP3 and IP7 but also at IP6 and before the strong focusing superconducting magnets near the interaction points. Figure 5.7 shows the location of all collimators around the LHC.

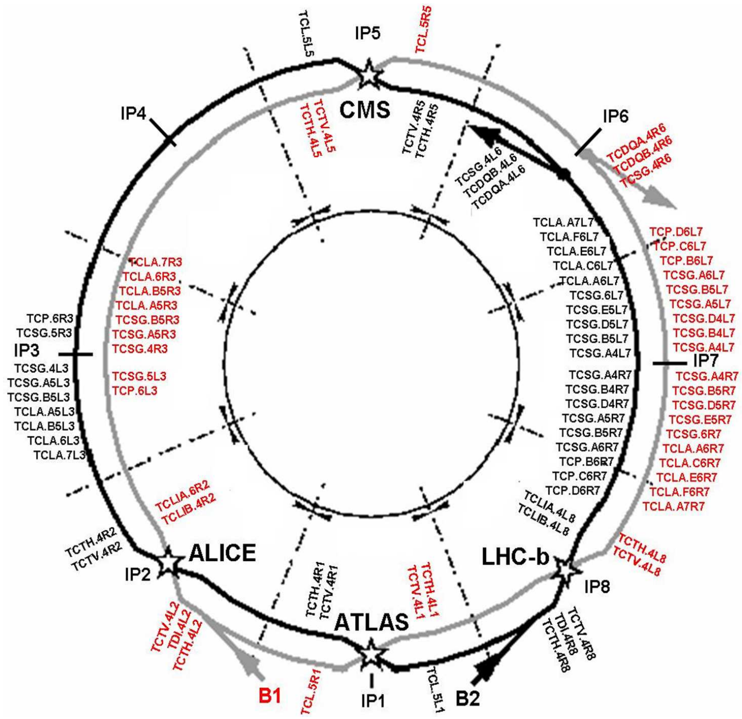

Figure 5.7: Collimators location in the LHC.

The primary task of the LHC collimator system is to clean the beam by intercepting the particles that are away from the beam core (halo particles). Otherwise, these particles will eventually be lost around the machine and may lead to quenches on the superconducting magnets. The idea is to deflect the halo particles with the primary and secondary collimators and intercept them with absorbers on locations far away from the superconducting magnets (IP3 & IP7). The collimation scheme is based on the multi-stage scattering and absorbing scheme (see Figure 5.8).

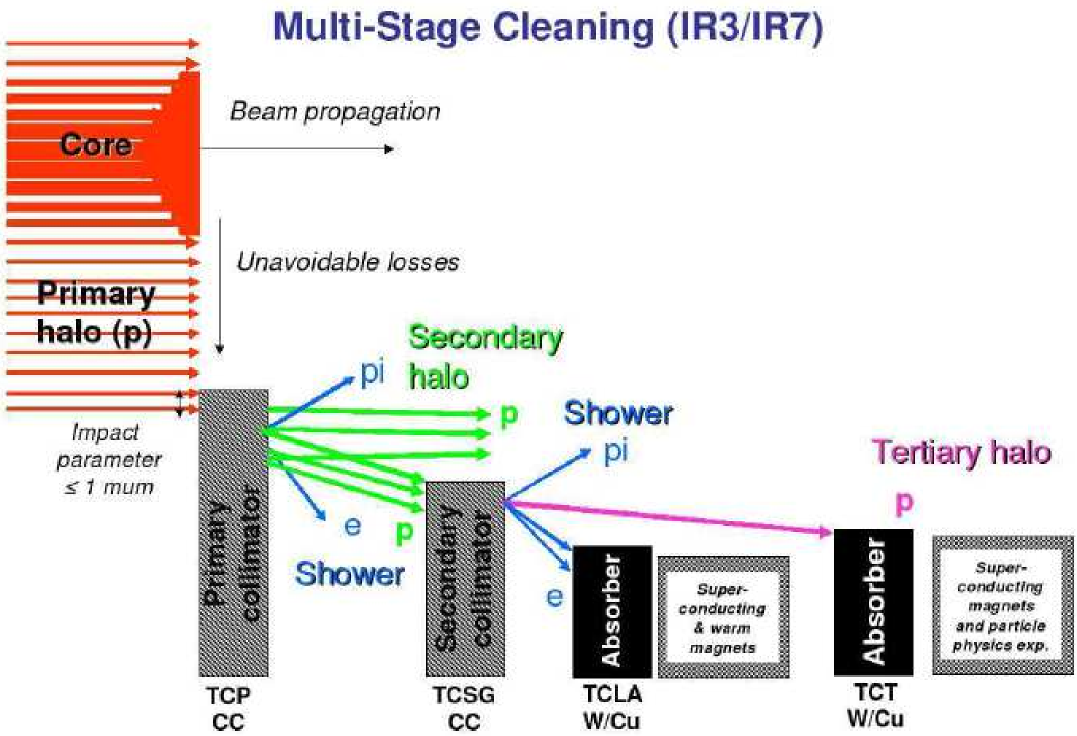

Figure 5.8: LHC Multi-stage collimator schema.

A series of absorbers protect the injection and extraction regions for the case of miskicked beams (misfired kickers, wrong defection angle, asynchronous beam dumps...). The collimators located in the transfer lines protect the LHC from inadequate beam from the SPS (Ex: wrong beam momentum). The collimators located in the transfer lines protect the LHC from inadequate beam from the SPS (Ex: wrong beam momentum, position or angle). Transfer line collimators are spaced by $\approx 60^\circ$ in phase advance both in horizontal and vertical planes.

Primary and secondary collimators are made of carbon fiber reinforced graphite. Tertiary collimators are made of tungsten and copper. The jaw support for all of them is made of copper and host the water cooling system.

6 Low Intensity Beam Losses on High-Z Materials

A key concept of the LHC machine protection strategy is the LHC Safe Beam Intensity [53]. This is an intensity limit below which equipment can be setup with relaxed machine protection constraints. The knowledge of damage levels is important in order to define the thresholds of different protection elements, retraction collimators, etc. From the machine protection point of view it is important to study the robustness [54] of a tertiary collimator (TCT) and understand what can be considered as a safe beam.

Tertiary collimators are part of the collimation scheme, and normally absorb the tertiary beam halo created by the secondary collimators; they protect the cold aperture of the strong focusing quadrupoles at the interaction points (IP). TCT collimator have two jaws made of tungsten which is a material with a high atomic number (Z) and a high density (ρ) and therefore, it has small nuclear interaction length and radiation length. Tungsten has the highest melting point of any metal. All these properties make tungsten a very suitable material for an absorber. However, in case of accidental beam impact, the risk of damage to the collimator's jaw is much larger than for carbon collimators due to the larger energy deposited (higher Z and ρ).

6.1 Asynchronous beam dump

For an asynchronous extraction of the beam, when the extraction kicker magnets fire not synchronously with the beam abort gap, some bunches deflected by the kickers can escape the dump protection system (Figure 6.1). For the case of beam 2, bunches with an amplitude above $10.28 \times \sigma$ will be intercepted at the local protection devices of the extraction dump. Particles between $5.08 \times \sigma$ and $10.28 \times \sigma$ can impact on collimators around the machine. Bunches between $8.3 \times \sigma$ and $10.28 \times \sigma$, that is between 2-2.5 bunches in terms of equivalent beam intensity, can impact on the TCT jaw at IP5 if the hierarchy between TCT and dump protection is violated. During normal LHC operation all the collimators must keep a hierarchy in which the primary collimators are the closest to the beam. Secondary collimators sit further away from the beam than primary collimators. Tertiary collimators are more retracted from the beam than secondary. For an asynchronous beam dump with the wrong collimator hierarchy, particles will have a maximum amplitude of 10 σ generated with a phase advance of $\pi/2$ respect to the pre-fired kicker (worst case scenario) [45]. This type of failure is assumed to happen once per 300 years [46].

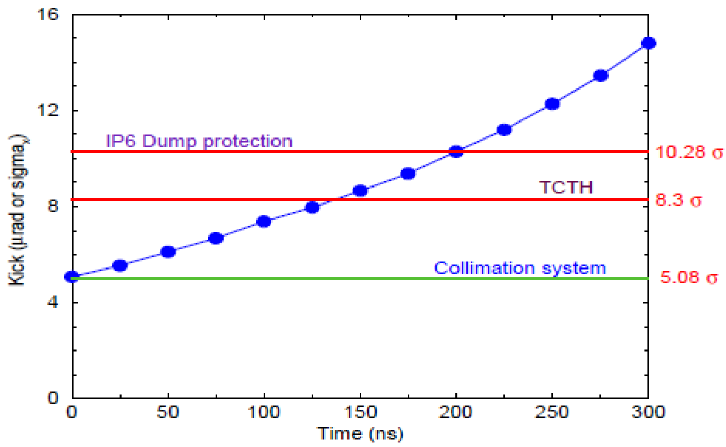

Figure 6.1: Angular kick for 13 bunches at prefire of the beam dump kicker module.

6.2 Scenarios

Different impact scenarios have been considered to study the sensitivity of the damage with respect to the beam energy, beam emittance and accelerator optics. The melting point of Tungsten is 3695 K and it will be used as a reference temperature to consider damage in the material. However, transient heat deposition induced pressure waves (elastic, plastic) can damage materials well below the melting point. For a realistic damage threshold, thermo-mechanical stress levels have to be taken into account. Different scenarios that cover the different accelerator phases and beam parameters have been analyzed.

	ϵ_n	3.5 μm	2 μm	1 μm	0.3 μm
0.55 mβ^* fully squeezed optics	7 TeV	x	x	x	x
	5 TeV	x	x	x	x
fully unsqueezed optics	7 TeV			x	
	5 TeV				
3.5 mβ^* squeezed optics	7 TeV	x	x	x	
	5 TeV	x	x	x	

Table 6.1: Simulations parameter summary

Fully squeezed optics refers to the optics used in LHC during luminosity operation. The beam size at the interaction point is reduced by the action of strong focusing quadrupole magnets.

Fully unsqueezed optics ($\beta^* = 18$ m) are the LHC optics used during injection at 450 GeV. $\beta^* = 3.5$ m squeezed optics refers to an intermediate optics in which the beam size at the interaction points is not as small as for the 'Fully squeezed optics'.

6.3 TCT Fluka model

Tertiary collimators are very complex devices. They equip two tungsten jaws that, depending on the collimator type, can be either horizontal or vertical. Each jaw has two stepper motors to adjust the horizontal position and the tilt. Each jaw is composed of five tiles of tungsten (INERMET 180) in the center surrounded by a support structure of copper (on the lateral, at the front and rear). The jaws are fixed into a copper support that gives rigidity to the system and houses the refrigeration system. The whole system is enclosed into a vacuum tank.

A detailed model of the TCT jaw and jaw support was implemented in FLUKA. It includes the tungsten and copper jaws, jaw support, and the steel screws. The refrigeration system of the jaws and the vacuum tank, RF fingers, etc are not included in the model because the analysis will not treat thermo-mechanical induced stress. Figure 6.2 shows the bottom view of the TCT FLUKA model.

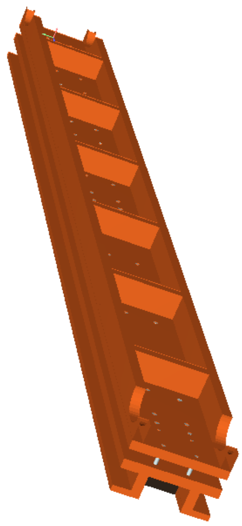

Figure 6.2: Tertiary collimator model (bottom view).

6.4 Beam optics parameters

For each of the three different beam optics considered, the Courant-Snyder parameters have been calculated at the position of the TCT collimator at point 5. The beam size and beam angle for one sigma is deduced from the optic parameters α, β and ϵ_n. The impact angle is calculated for an amplitude of 10σ. The impact parameter is assumed to be 5 mm from the edge of the jaw for all simulations.

	beta	alpha	sigma	sigma'	impact angle	FWHM
	[m]		[m]	[rad]	[rad]	[m]
H	1567.68	-1.8512	8.57E-4	1.01E-6	1.01E-5	2.01E-3
V	601.25	-9.8573	5.31E-4	8.70E-6	0.0	1.25E-3

Table 6.2: Beam optic parameters at TCT location for the squeezed optics ($\beta^* = 0.55$ m) at 7 TeV.

	beta	alpha	sigma	sigma'
	[m]		[m]	[rad]
H	160.0728	7.457E+1	2.74E-4	-1.3E-6
V	79.4563	-4.16E-2	1.93E-4	1.01E-7

Table 6.3: Beam optic parameters at TCT location for the unsqueezed case at 7 TeV.

	beta	alpha	sigma	sigma'	impact angle	FWHM
	[m]		[m]	[rad]	[rad]	[m]
H	275.49		3.59E-4	0.0	0.0	8.46E-4
V	110.78		2.27E-4	0.0	0.0	5.36E-4

Table 6.4: Beam optic parameters at TCT location for the squeezed case $\beta^* = 3.5$ m at 7 TeV.

6.5 Results

The calculated peak energy deposition on the jaw is shown in Figure 6.3. For fixed particle energy and machine optics, the peak energy deposition increases with decreasing emittance (ϵ_n). For the same emittance (ϵ_n) and machine optics, the energy deposition increases with the particle energy. The worst case scenario is the unsqueezed optics in which the beam size at location of the tertiary collimator is the smallest of all three optics. On the contrary, for a squeezed beam, the beam in the interaction point is very small while the beam at the low-β triple region is large.

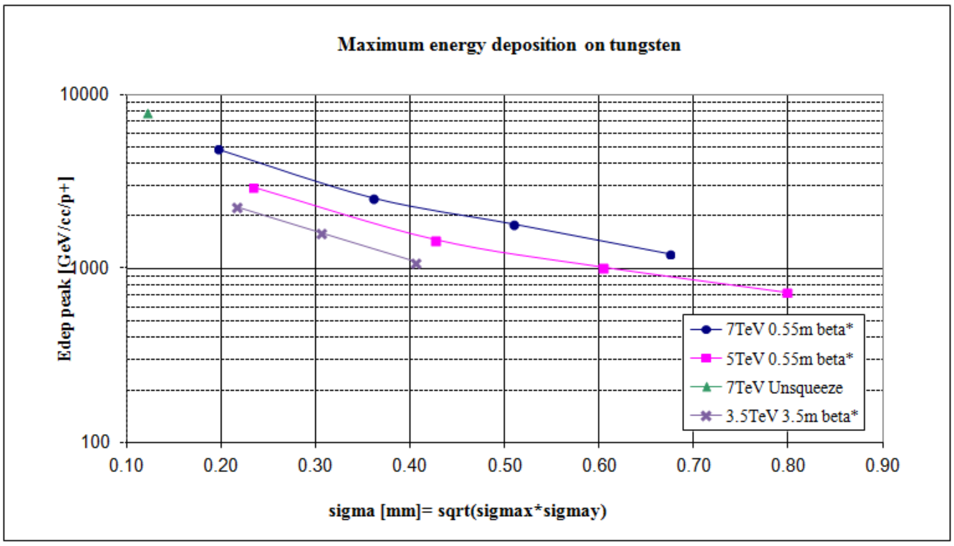

Figure 6.3: Maximum Energy deposition in tungsten per primary proton.

The peak temperature is below the melting point for every scenario. Although the peak temperature is below the melting point of tungsten the jaw can be damaged (for a pilot beam) due to thermo-mechanical stress: elastic and plastic pressure waves. Pressure waves travel further inside the jaw reaching the copper support and the water cooling pipes. An excesive pressure on the water cooling pipes can lead to a severe leakage accident. The safe beam intensity calculated as the minimum number of protons needed to achieve melting in the jaw for each case is shown on Figure 6.4.

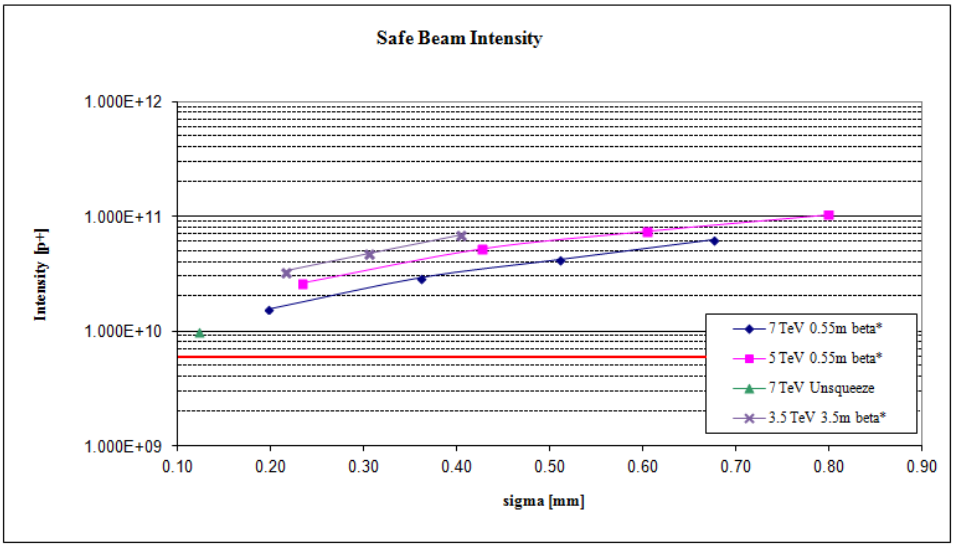

Figure 6.4: Safe beam intensity in protons for each scenario.

Collimator damage can be classified into three different levels depending on the severity of the damage [54]:

1. Level 1: Limited permanent jaw deformation; collimator does not need to be replaced.
2. Level 2: Collimator must be replaced. Other components may be damaged (Ex. screws).
3. Level 3: Long down time of LHC. Catastrophic damage of collimator (Ex. water leakage into vacuum pipe)

For a pilot beam impact the melting point of tungsten will not be reached. Damage on the jaw will be caused by plastic pressure waves. The damage will be severe but not catastrophic, thus it can be classified as Level 1. For higher beam intensities a hydrodynamic code is needed to properly assess the damage on the collimator (level 2 and 3 damage). Plastic pressure waves or even shock waves can reach the water cooling pipes provoking a level 3 damage. Molten material can be projected to the opposed jaw provoking damage.

Much more work has been carried out in the line of these simulations. On 2012, two dedicated experiments at HiRadMat were devoted to the study of beam impact on tertiary collimators [55] and impact of beam on different material samples [56].

6.6 Conclusion

- Although an asynchronous beam dump in which the collimator hierarchy is violated is a rare event (1 every 300 years), its consequences can be severe (level 2-3).
- For $2-2.5$ full intensity bunches melting point is reached and a more precise treatment with a hydrodynamic code is necessary.
- Water leakage into vacuum pipe is a catastrophic event that needs to be studied in detail.
- First results from HiRadMat experiments confirm that small beam intensities $1.04 \cdot 10^{12}$ p+ at low energy 450 GeV and with a relatively wide beam size $\sigma_x \times \sigma_y = 0.53 \times 0.36 mm^2$ can produce permanent plastic deformations on the tugnsten jaws. Although the parameters are quite different from this simulations, the results go in the same direction.

7 Low Intensity Beam Losses into Super-Conducting Structures

The LHC has around 10000 magnets distributed along the 27 km circumference. Around 1232 are superconducting dipoles and 392 are superconducting quadrupoles which are cooled down to 1.9 K. By doing this, the resistivity of the electrical cable falls to almost zero meaning almost no power losses. Also, the current density inside the magnet's coil can be very high as well as the magnetic field.

The interconnection in between the s.c. magnets and from them to the Electrical Distribution Feed Boxes (DFB) is made with a structure called bus-bar. It consists of a superconductor core made of Niobium-titanium alloy surrounded by a copper bar called 'copper stabilizer'.

Main superconducting bending magnets and main superconducting quadrupoles around the LHC are connected in series. There is one electrical circuit for the MB per sector in the LHC and two circuits for the MQ (one for the defocusing and the other for the focusing magnets). Superconducting magnets are connected to each other with bus-bars which are also superconducting.

During normal operation, all the current of the bus-bar flows through the superconducting core. However, a sudden and localized energy deposition in the bus-bar core can rise the temperature up to a point that it looses superconductivity; this is called 'quench'. A 'quench' is a local loss of superconductivity that rapidly grows with time extending the resistive region across the element (bus-bars, magnet coils).

When a bus-bar quenches, the current that was flowing through the core begins to flow through the copper stabilizer. This will temporarily prevent any damage to the core and the bus-bar. If the electro-magnetic energy stored in the magnets is not quickly extracted and the current flows for too much time throught the copper a quench can lead to permanent damage of the bus-bars and the superconducting coils of a magnet.

Two systems are installed to prevent any damage to the magnets and bus-bars in case of a quench. The first one (quench heaters) heats up the magnet if a quench is detected (increasing voltage across the magnet). By heating the magnet the resisitive region extends and thus the energy dissipated in the magnet is distributed along a bigger volume. The second system (energy extraction system) consists of a series of resistances that are switched into the circuit in series with the inductance in case a quench is detected. The system extracts the energy stored in the magnets as fast as possible (102 s for the MB circuit and 30 s for the MQ circuit). In addition to these systems, each main dipole magnet is equipped with a bypass diode that will begin conducting the current when the magnet quenches.

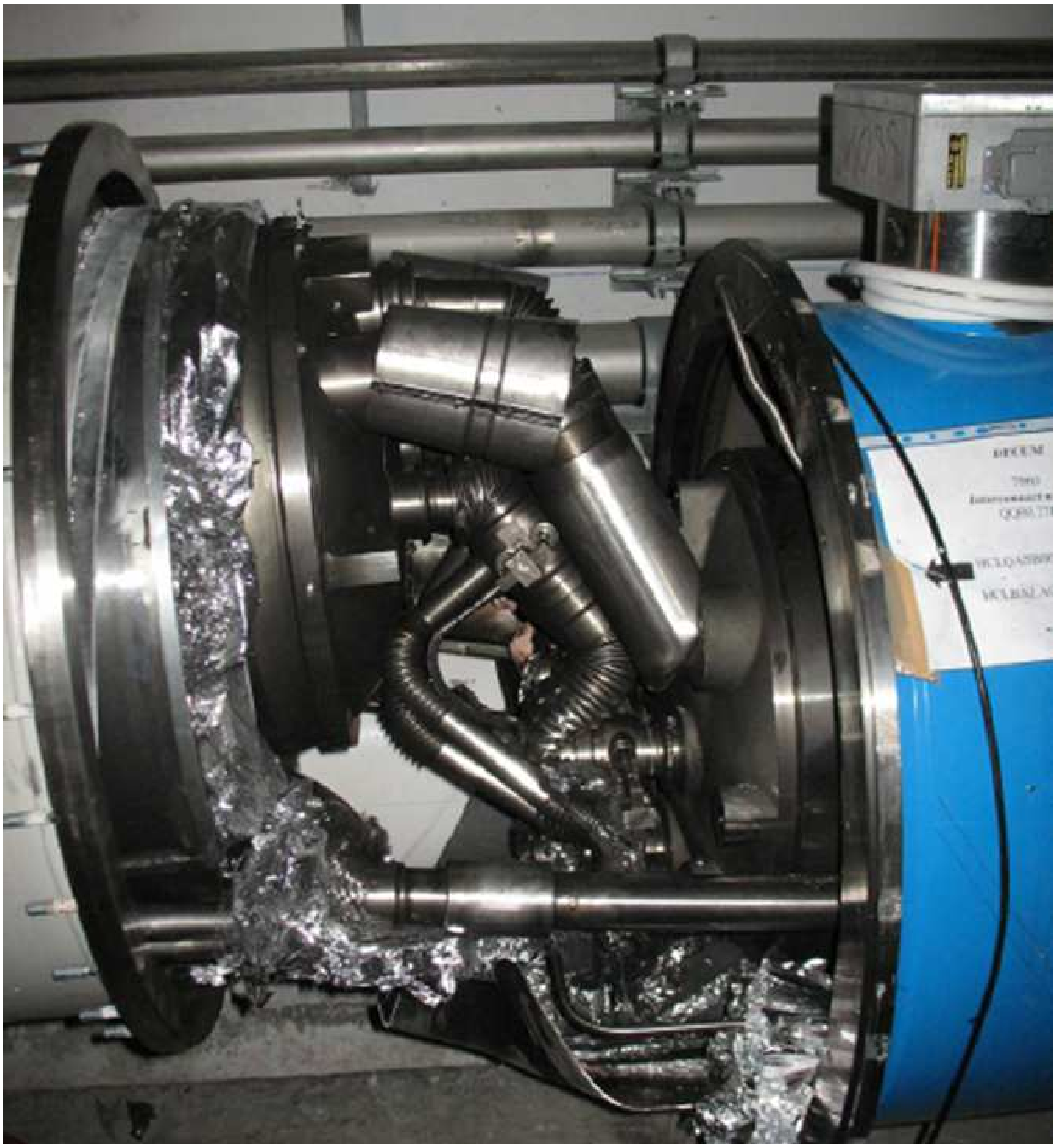

Figure 7.1: Accidental release of the energy stored in the main dipole circuit, 600 MJ in the dipole. (no beam).

The sudden release of the energy stored in the system (1.3 GJ energy in magnets for one sector) may damage the magnet and break the helium pipes. Figure 7.1 show the consequences after the 2008 accident in which 600 MJ of stored energy was suddenly released. If the electrical circuit (magnets, bus-bars and power converter) breaks, a situation similar to the accident of 2008 may occur.

Magnet quenches are detected by the quench protection system with enough time to extract the energy from the system before any damage can occur [57]. Until January-2010, quenches in the bus-bars were not being monitored. Hence, if a beam loss quenches a bus-bar without quenching a neighboring magnet a catastrophic accident may occur. This study addresses the likelihood of quenching a bus-bar before quenching a magnet for different loss patterns and scenarios.

7.1 Scenarios

Beam losses at three different locations from the LHC accelerator have been studied: the connection cryostat right of point 7, the MQ11 right of point 7 and the MQ12 right of point 7. These locations have been chosen because of its higher probability of quenching a bus-bar, before quenching a magnet coil.

Two different beam loss patterns have been studied for each location:

- Case a: A point-like loss with a 250 μm deflection angle in the horizontal plane.
- Case b: A distributed loss along the cryostat with a 250 μm deflection angle in the horizontal plane.

A point-like loss is an extreme case in which the whole loss is concentrated in a small region. On the contrary, a distributed loss is uniformly distributed along a large region. Any other loss pattern can be constructed as a combination of a point like and a distributed loss. Results will give an order of magnitude of the quench limits for bus-bars in terms energy deposition or number of protons. Both beam loss scenarios have the losses occur in the horizontal plane, at the beam-screen of the "beam 2" beam pipe.

The three scenarios considered are the following:

1. A 5 TeV proton beam loss in the connection cryostat in the dispersion suppressor region at the right of point 7.

   Figure 7.2 shows the beam loss location for the first scenario. The red cross, 'a' case, indicates the loss location, approximately at 50 cm before geometrical center of the connection cryostat. The maximum of the particle shower falls on the lyra of the connection cryostat. The lyra of the connection cryostat will be introduced later in the chapter. The blue arrow indicates the extension of the distributed loss, 'b' case, corresponding to the length of the connection cryostat.

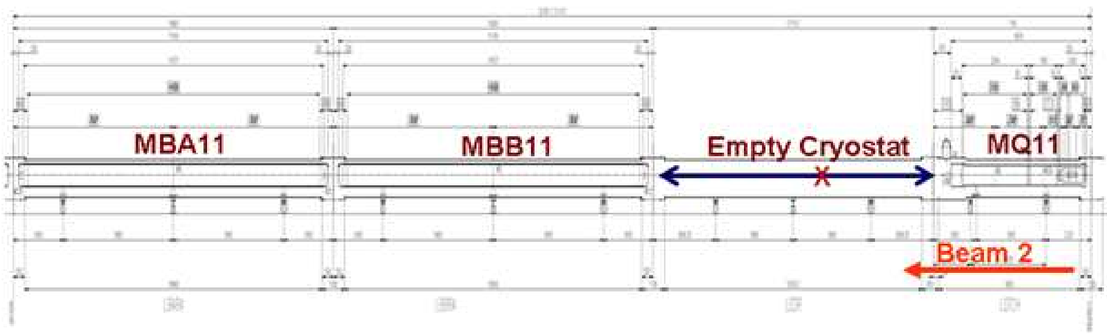

Figure 7.2: Scenario 1: 5 TeV proton beam loss in the connection cryostat on the dispersion suppressor region at the right of point 7.

2. A 5 TeV proton beam loss in the quadrupole magnet MQ11, right of point 7.

   Figure 7.3 shows the beam loss location for the second scenario. The red cross, 'a' case, indicates the loss location, approximately at 50 cm before the interconnection. The maximum of the particle shower falls on the interconnection between MQ11 and the connection cryostat. The connection cryostat is an empty MB magnet therefore the bus-bars are not surrounded by a magnet. The blue arrow indicates the extension of the distributed loss, 'b' case, corresponding to the length of the MQ11.

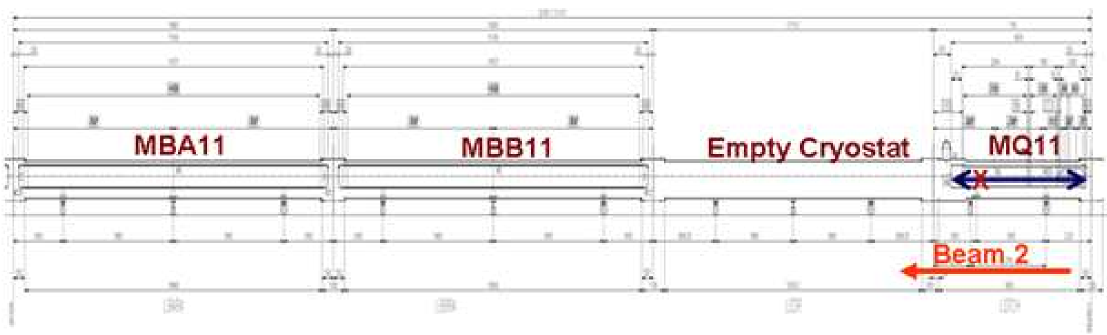

Figure 7.3: Scenario 2: 5 TeVproton beam loss in the quadrupole magnet MQ11, right of point 7

3. A 5 TeV and 3 TeV proton beam loss in the quadrupole magnet MQ12 at the right of point 7.

   Figure 7.4 shows the beam loss location for the third scenario. The red cross, 'a' case, indicates the loss location, approximately 50 cm before the interconnection. The maximum of the particle shower falls on the interconnection between MQ12 and the MBC12 dipole. The blue arrow indicates the extension of the distributed loss, 'b' case, corresponding to the length of the MQ12.

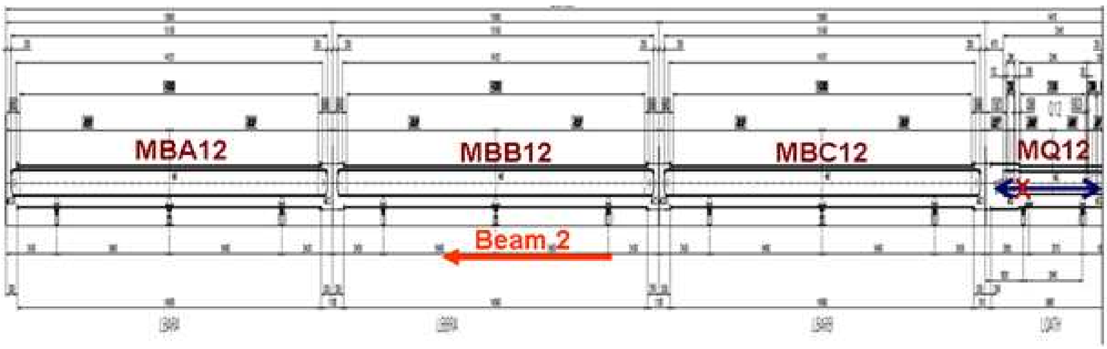

Figure 7.4: Scenario 3: 5 TeV and 3 TeV proton beam loss in the quadrupole magnet MQ12 at the right of point 7.

7.2 Geometry

All the simulations use the same FLUKA geometry. The geometry of the LHC interaction point 7 (IP7) and all the elements (dipoles, quadrupoles, sextupoles, etc.) have been developed by the FLUKA team. The layout for each scenario is dynamically generated by ad-hoc scripts [58]. The scripts read the latest LHC optic files that contain the lattice information of each element of the accelerator. Then the scripts place every element at its correct position and orientation. Magnetic fields are defined for the main magnets. This methodology has been already extensively used for collimators and other studies. The geometry covers a region of the LHC from the arc left of IP7 to the the arc right of IP7. In total, the geometry contains more than 200 objects.

Two new elements have been developed for this study and are now included into the IR7 geometry file: the connection cryostat at the dispersion suppressor region and the interconnection element used between cryostats.

7.2.1 Connection Cryostat FLUKA model

The connection cryostat [59] is located in the dispersion suppression regions of LHC. Its purpose is to reduce or remove the beam dispersion created in the arcs so the beam size at the interaction points minimizes.

It consists of an empty cryostat (cryogenic container), equal to the ones used for the main dipoles, but without magnets inside. A lead radiation shield is placed around the beam pipes to compensate the lack of yoke from the missing magnet.

As in any other cryostat the bus-bars have a lyra ('U-shape') to prevent any stress on the cables due to expansion or compression during cool-down and warm-up. The lyra is in the middle of the cryostat as opposed to the normal location at the end of the cryostat in the main dipoles. There are a total of three lyras, one for each bus-bar (M1, M2, M3). M1 corresponds to the bus-bar for the main bending magnets circuit. M2 and M3 corresponds to the bus-bar for the main focusing quadrupoles and main defocusing quadrupoles circuits. Unlike the beam pipes, the lyras are not enclosed by a radiation shield but instead they are inside a steel container filled with helium (see Figure 7.5).

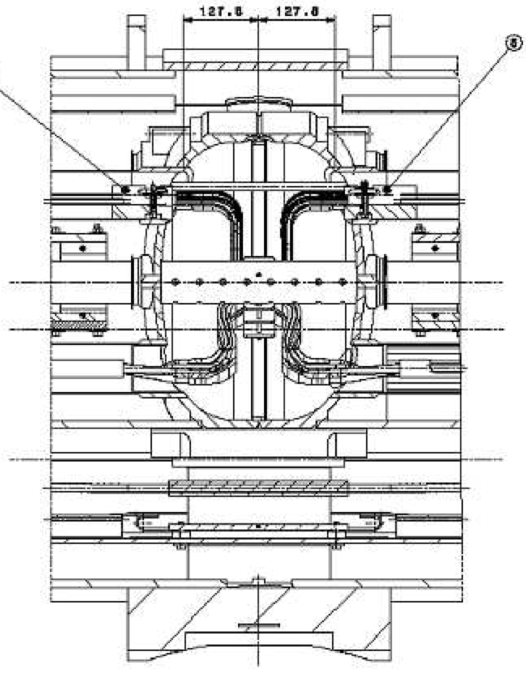

Figure 7.5: Detail of the central part of the connection cryostat. units (mm).

Figure 7.6 shows the central part and the front view of the connection cryostat FLUKA model. The three lyras, beam pipes, linear heat exchanger for the helium and the radiation shield at both sides can be seen.

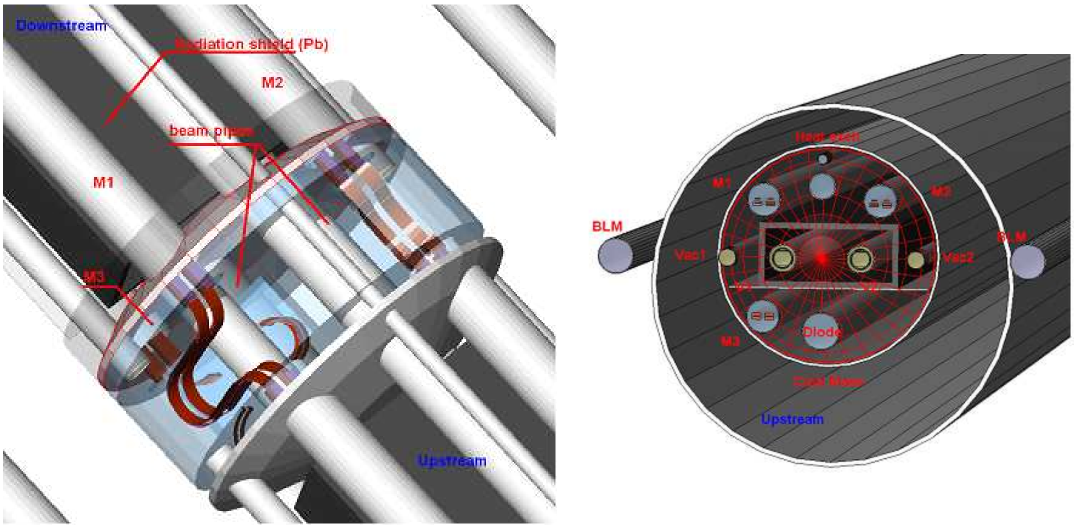

(a) Central part of the connection cryostat.

(b) Connection cryostat.

Figure 7.6: FLUKA model of the connection cryostat.

A BLM ionization chamber (IC) has been included into the model at both sides of the connection cryostat. The IC covers the full length of the connection cryoctat. It has been modeled as a steel cylindrical container filled with pressurized nitrogen. This non-realistic IC is used to plot the beam loss monitor signal as a function of the longitudinal position along the cryostat. This will show the best location (higher signal) for the BLM's.

7.2.2 Interconnection FLUKA model

It is the element that links two cryostats connecting the beam pipes, helium pipes, bus-bars, electrical cables, etc between them.

There are several configurations of the interconnection depending on what elements they connect and its position in the accelerator. All the configurations have been grouped into three different models. All of them share the same internal structure but differ in their longitudinal size.

Figure 7.7 shows the implementation of bus-bar lines for the dipoles, quadrupoles and the auxiliary circuits, the two beam lines (V1 and V2) and the heat exchanger lines X and Y in the interconnection model.

All three models perfectly reproduce the beam pipes transition elements: copper alloy RF contacts in the beam pipes, stainless tube, copper transition tube, etc.

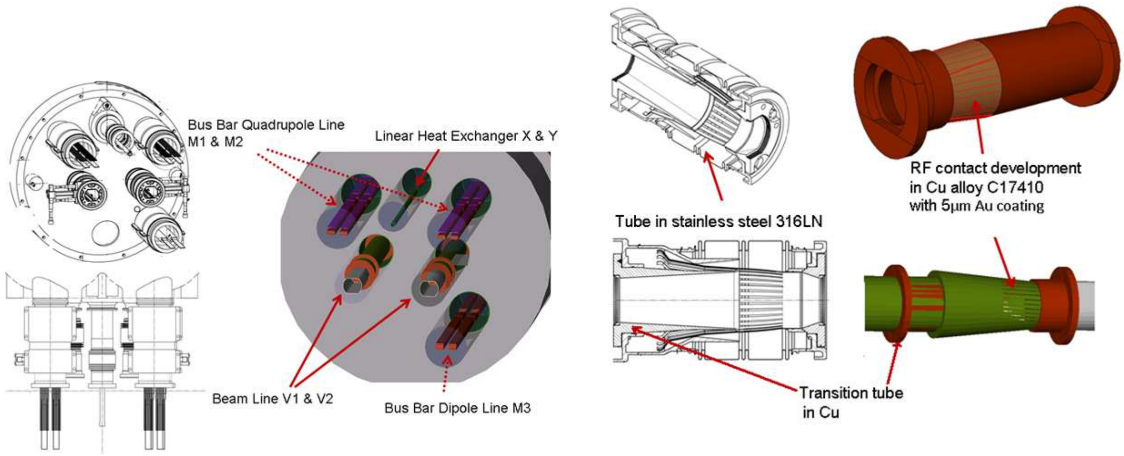

(a) Overview of the interconnection model. (b) Detail of the RF fingers.

Figure 7.7: FLUKA model of the interconnection.

7.3 Quench limits

The quench limits used in the analysis of the simulations are the ones considered in 2010. All the results presented in the following sections scale with these assumptions.

- Bus-bars:

  A quench limit of 10 mJ/cm is used as a preliminary value given by A.Verweij [60]. A quench in a bus-bar needs to be bigger than a critical volume in order to grow. For a bus-bar, the cross-section is a fixed value so the critical volumen translates into a critical length. Otherwise, the quench energy will be dissipated in the helium that surrounds the bus-bar. The quench limit is given as an energy deposition per unit length because the bus-bar cross-secion is fixed. The quench limit scales with the current through the bus-bar however, as a good approximation, it can be considered constant regardless the current carried.

  A critical length of 1 cm is used for both M1/2 and M3 bus-bar. The M1-2 bus-bar has a section of 160 mm^2 and corresponds to the quadrupole bus-bar. The M3, dipole bus-bar, has a section of 280 mm^2.

  In FLUKA, the energy deposited in the bus-bars is calculated as the average value in a volume of 1 cm x bus-bar cross section. In the lyra it is the peak value in both the transversal and the longitudinal plane.

- MB & MQ magnet coils:

  The quench limit for the superconducting magnets (main quadrupole and main bending magnets) is defined as an energy deposition of 1 mJ/cm^3. This quench limit is considered only for the case of an instantaneous beam loss. The limit is used independently of the beam energy (proportional to the magnetic field), in any case this should be considered as a preliminary assumption as it should scale with energy (not implemented).

The energy deposition in the coil is calculated by FLUKA as the peak energy deposition in the magnet coils on a 1 cm x 2 deg x 10 cm volume.

- Pre-Heating up to 80 K:

  The energy needed to heat a quadrupole bus-bar of 160 mm^2 up to 80 K [61] considering no heat exchange with the helium is 92 J/cm (c.f., A.Verweij). This value is also considered a preliminary assumption.

7.4 Results Scenario 1

This section presents the results of a 5 TeV proton beam loss located at the empty cryostat, right of point 7. Figure 7.8 shows an overview of the energy deposition in the tunnel between MQ11 to MB11 magnets for a distributed beam loss along the empty cryostat. The highest values appear in the empty cryostat, the interconnection and at the beginning of MBB11.

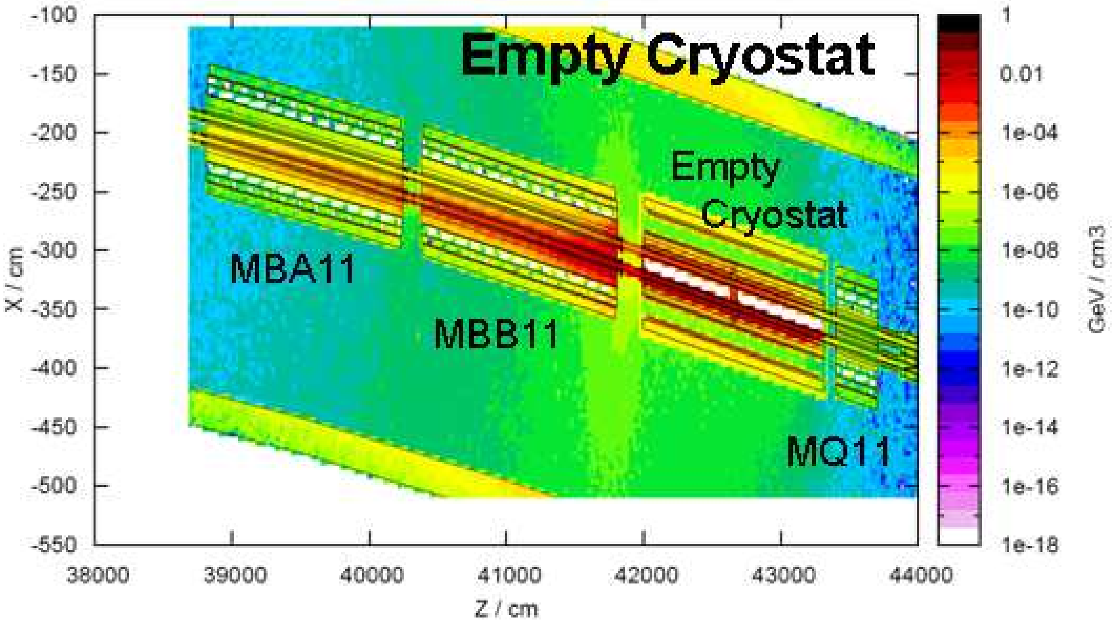

Figure 7.8: Energy deposition on the tunnel area from MQ11 to MB11 for a distributed beam loss. $[GeV/cm^3]$

Figures 7.9 and 7.10 show the energy deposition in the bus-bars and magnet coils and the BLM signal for the point and distributed loss. The maximum energy deposition on the bus-bars is located after the lyra of the empty crysostat for the point loss case. This is due to the particle showers initiated by the interaction of particles with the lyra's steel container. However, for the distributed loss case the maximum energy deposition on the bus-bars is located at the beginning of MB.B11 magnet due to the interaction of the particles with the yoke of the magnet. The maximum energy deposition on the magnet coils occurs at the beginning of MB.B11 magnet in both cases.

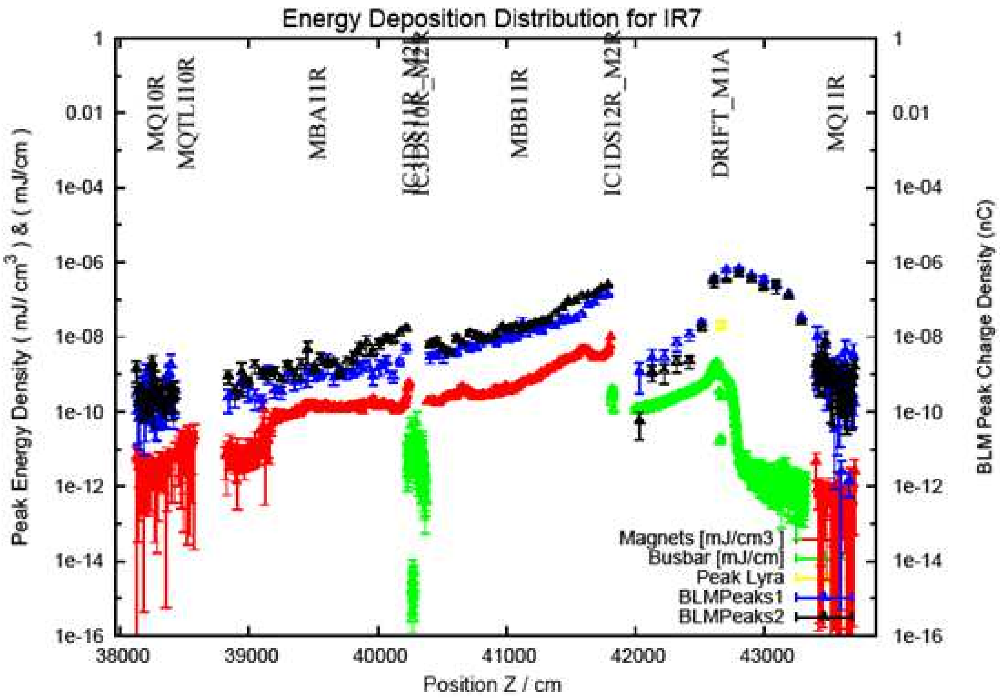

Figure 7.9: Peak energy deposition and BLM signal per proton for the point-like beam loss. (Scenario 1)

Figure 7.11 shows the energy desition on the M1 and M2 lyras for the point loss and the distributed loss. The maximum energy deposition on the lyra increases by a factor 10× when going from a distributed loss to a point loss.

7.4.1 Point-like result analysis

Table 7.1 summarizes the results for the point-like loss case. The first column shows the name of the element: magnet, interconnection or empty cryostat. The second and third column show the peak energy deposition on the bus-bars and magnet coils. The applied quench limit and the number of protons needed to quench it are shown on the fourth and fifth columns. The last column shows the calculated signal read on the ionization chambers in case of a quench.

The magnets (MB, MQTL and MQ10) quench at about the same time (similar number of protons) as the bus-bars in the connection cryostat. 1.03×10^{8} p+ are needed to quench the

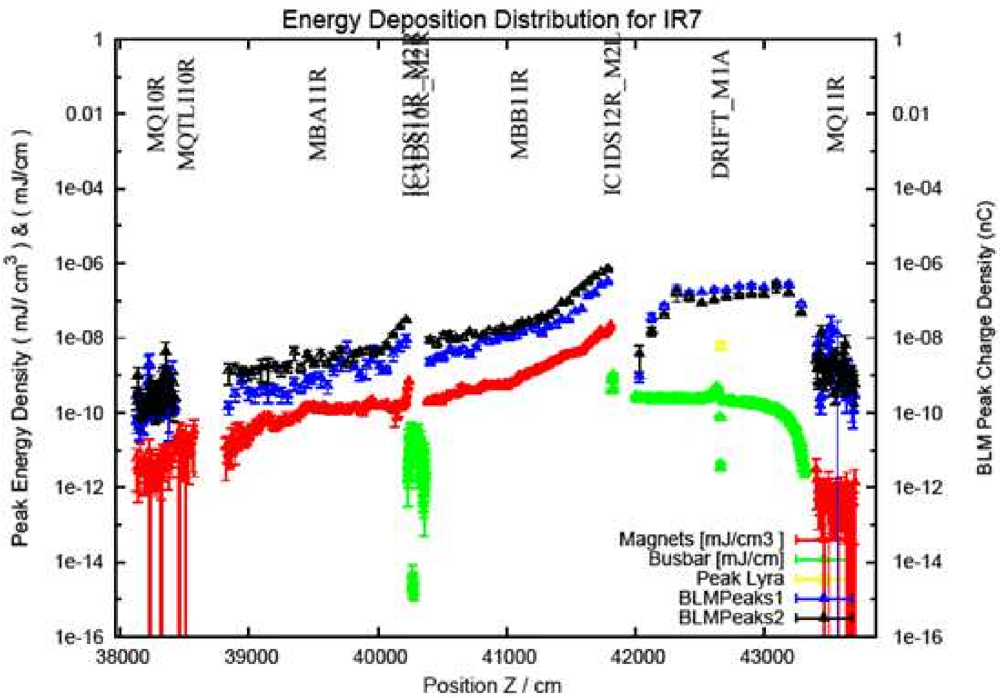

Figure 7.10: Peak energy deposition and BLM signal per proton for the distributed beam loss.

MB coil compared with 4.79×10^8 p+ to quench the bus-bar in the connection cryostat.

Element	Peak Energy Deposition $(GeV/cm^3/p+)$ $(GeV/cm/p+)$	Peak Energy Deposition $(mJ/cm^3/p+)$ $(mJ/cm/p+)$	Quench Limit (mJ/cm^3) (mJ/cm)	Protons to quench	Peak BLM $(nC/p+)$	Peak BLM for DRFT Quench (nC)
MQ.10R7.B1	$4.87 \cdot 10^{-5}$	$7.78 \cdot 10^{-12}$	1	$1.28 \cdot 10^{11}$	$1.95 \cdot 10^{-9}$	0.9
MQTLI.10R7.B1	$1.40 \cdot 10^{-4}$	$2.24 \cdot 10^{-11}$	1	$4.47 \cdot 10^{10}$		
MB.A11R7.B1	$3.68 \cdot 10^{-3}$	$5.88 \cdot 10^{-10}$	1	$1.70 \cdot 10^{9}$	$1.72 \cdot 10^{-8}$	8.2
IC1.DS11R7.B1	$2.67 \cdot 10^{-4}$	$4.28 \cdot 10^{-11}$	10	$2.34 \cdot 10^{11}$		
IC3.DS10.R7.B1	$3.20 \cdot 10^{-4}$	$5.13 \cdot 10^{-11}$	10	$1.95 \cdot 10^{11}$		
MB.B11R7.B1	$6.09 \cdot 10^{-2}$	$9.75 \cdot 10^{-9}$	1	$1.03 \cdot 10^{8}$	$2.43 \cdot 10^{-7}$	116.4
IC1.DS12R7.B1	$2.47 \cdot 10^{-2}$	$3.95 \cdot 10^{-10}$	10	$2.53 \cdot 10^{10}$		
DRFT.11R7.B1 (Busbar)	$1.30 \cdot 10^{-2}$	$2.08 \cdot 10^{-9}$	10	$4.81 \cdot 10^{9}$		
DRFT.11R7.B1 (Lyra)	$1.31 \cdot 10^{-1}$	$2.09 \cdot 10^{-8}$	10	$4.79 \cdot 10^{8}$	$6.50 \cdot 10^{-7}$	311.3

Table 7.1: Scenario 1: energy deposition per proton on the coils and bus-bars. (Point-like loss)

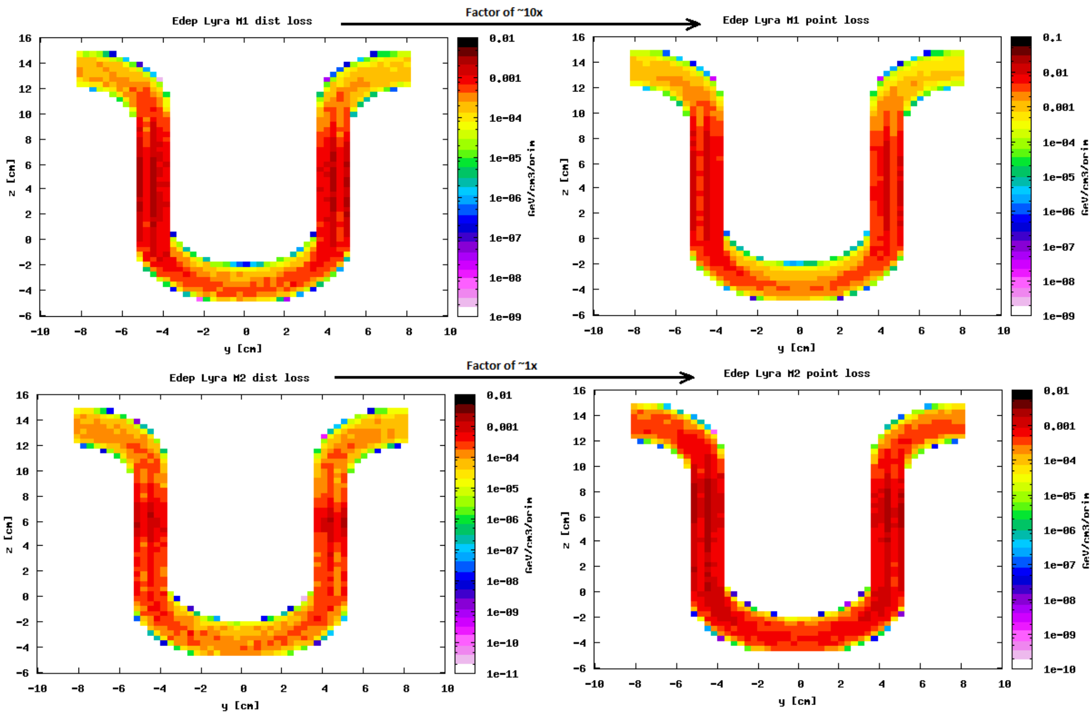

Figure 7.11: Energy deposited on the lyras for point-like and distributed beam loss.

Figure 7.12 shows the calculated BLM signal and the associated simulation error for each element of the geometry. The maximum signal, best BLM position, occurs towards the end of the empty cryostat. The BLM quench limit threshold is $\sim 0.3\,\text{nC}$.

7.4.2 Distributed result analysis

Table 7.2 contains the results for the distributed loss case. MB.B11 magnet quenches with only 0.01% of the protons compared to the bus-bars in the connection cryostat. $4.73 \cdot 10^{7}$ p+ are needed to quench MB.B11 compared to $1.61 \cdot 10^{9}$ p+ for the connection cryostat. In case of a quench in the bus-bars of the empty cryostat, the calculated BLM signal is in the order of $\sim 100\,\mu\text{C}$, that is bigger than the BLM dump threshold limit.

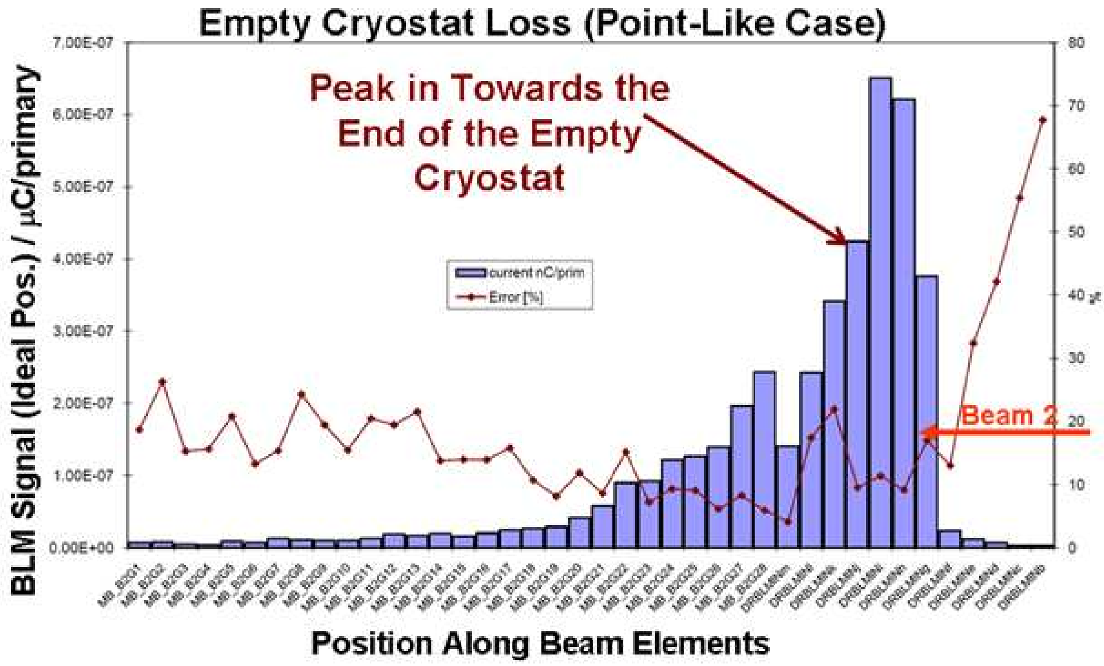

Figure 7.12: BLM signal along the connection cryostat for the point-like beam loss.

Element	Peak Energy Deposition $(GeV/cm^3/p+)$ $(GeV/cm/p+)$	Peak Energy Deposition $(mJ/cm^3/p+)$ $(mJ/cm/p+)$	Quench Limit (mJ/cm^3) (mJ/cm)	Protons to quench	Peak BLM $(nC/p+)$	Peak BLM for DRFT Quench (nC)
MQ.10R7.B1	$8.15 \cdot 10^{-5}$	$1.30 \cdot 10^{-11}$	1	$7.67 \cdot 10^{10}$	$4.21 \cdot 10^{-9}$	6.8
MQTLI.10R7.B1	$2.01 \cdot 10^{-4}$	$3.22 \cdot 10^{-11}$	1	$3.11 \cdot 10^{10}$		
MB.A11R7.B1	$4.39 \cdot 10^{-3}$	$7.02 \cdot 10^{-10}$	1	$1.42 \cdot 10^{9}$	$2.95 \cdot 10^{-8}$	47.5
IC1.DS11R7.B1	$2.45 \cdot 10^{-4}$	$3.91 \cdot 10^{-11}$	10	$2.56 \cdot 10^{11}$		
IC3.DS10.R7.B1	$2.25 \cdot 10^{-4}$	$3.61 \cdot 10^{-11}$	10	$2.77 \cdot 10^{11}$		
MB.B11R7.B1	$1.32 \cdot 10^{-1}$	$2.12 \cdot 10^{-8}$	1	$4.73 \cdot 10^{7}$	$7.06 \cdot 10^{-7}$	1139
IC1.DS12R7.B1	$6.44 \cdot 10^{-3}$	$1.03 \cdot 10^{-9}$	10	$9.71 \cdot 10^{9}$		
DRFT.11R7.B1 (Busbar)	$3.09 \cdot 10^{-3}$	$4.95 \cdot 10^{-10}$	10	$2.02 \cdot 10^{10}$		
DRFT.11R7.B1 (Lyra)	$3.87 \cdot 10^{-2}$	$6.20 \cdot 10^{-9}$	10	$1.61 \cdot 10^{9}$	$2.88 \cdot 10^{-7}$	464.2

Table 7.2: Scenario 1: energy deposition per proton on the coils and bus-bars. (Distributed loss)

Figure 7.13 shows the calculated BLM signal and the associated simulation error for each element of the geometry. The best BLM position, maximum signal, is at the beginning of the MB.B11 with a value of 1139 nC.

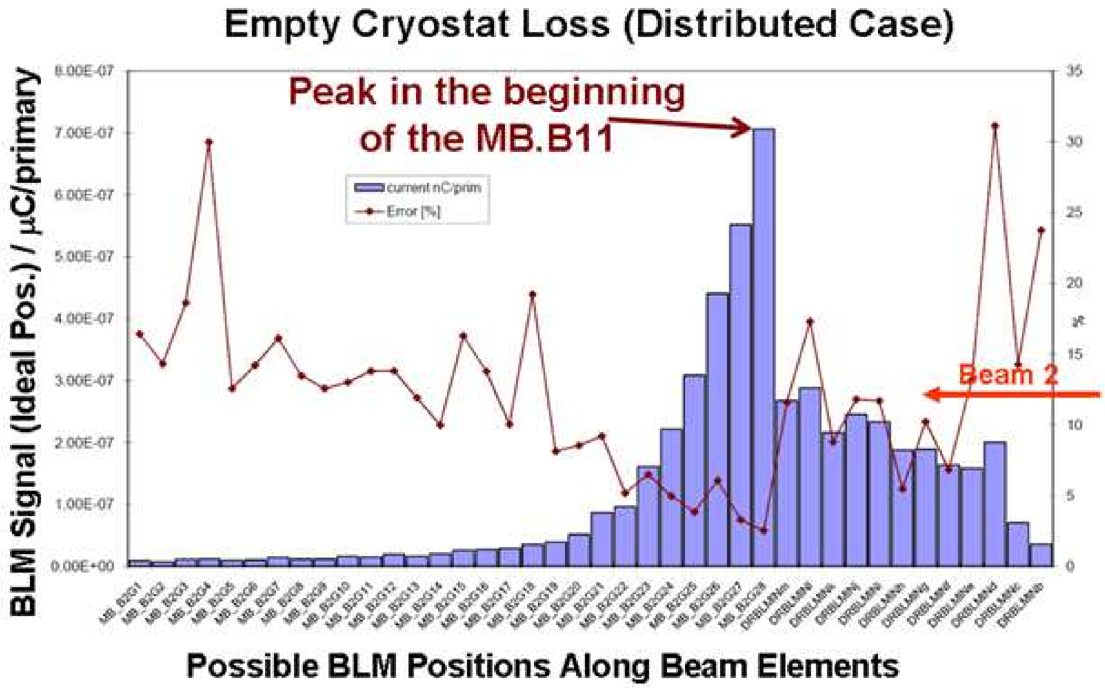

Figure 7.13: BLM signal along the connection cryostat for the distributed beam loss.

7.4.3 Comparative analysis

The number of protons needed to quench the bus-bars of the empty cryostat is $4.79 \cdot 10^8$ p+ for the point loss case and $1.61 \cdot 10^9$ p+ for the distributed loss case. For the distributed beam loss, MBB11 magnet will quench 'earlier' than the connection cryostat bus-bars. The magnet coils in MBB11 will quench with a lower number of protons than the bus-bars of connection cryostat. However, for the point-like beam, the MBB11 magnet coils and connection cryostat bus-bars require approximately the same number of protons to quench. In all cases, the BLM signals are well above the dump threshold.

7.5 Results Scenario 2

This section contains the results for a 5 TeV proton beam loss in the MQ11 quadrupole magnet, right of point 7. Figure 7.14 shows an overview of the energy deposition in the tunnel between MQ11 to MB11 magnets for a distributed beam loss along MQ11 magnet. The maximum energy deposition occurs in the interconnection between MQ11 and the empty cryostat.

Figure 7.15 shows the energy deposition in the bus-bars and magnet coils and the BLM signal for the point-like loss. The maximum energy deposition on the bus-bars is located at the interconnection between the MQ11 and the empty cryostat. The maximum energy deposition occurs in the magnet coils at the end of MQ11 magnet. In both cases, distributed loss and the

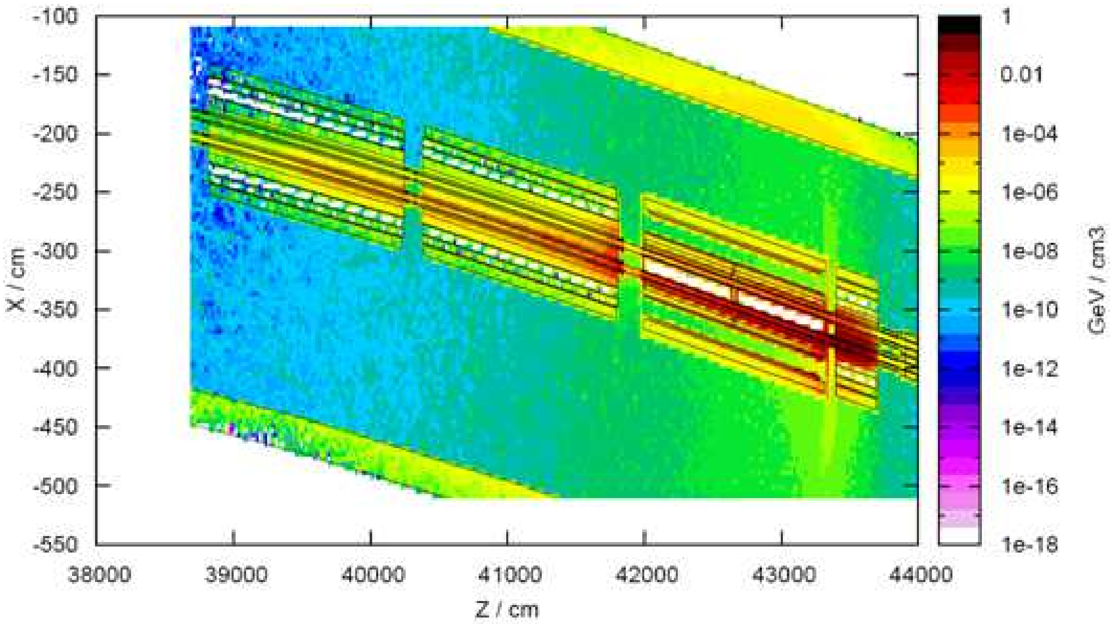

Figure 7.14: Global view of the energy deposited at IR7. (distributed beam loss)

point-like loss, the maximum energy deposition for the bus-bars and magnet coils occurs on the same elements. The maximum BLM signal for beam 1 is obtained towards the end of the empty cryostat while for beam 2, it's achieved at the end of MQ11.

Tables 7.3,7.4 show the energy deposition, the required number of protons and the calculated BLM signal for every element. The number of protons required for a bus-bar in the connection cryostat to quench is $1.75 \cdot 10^9$ for a point-like loss and $2 \cdot 10^9$ for a distributed loss. In both cases, the number of protons needed to quench is less than half of the intensity of a pilot beam ($5 \cdot 10^9$ p+). In both cases, point-like loss and distributed loss, MQ11 magnet will quench 'earlier' than the bus-bars.

In case of a quench in the MQ11 magnet, the calculated BLM signal will not exceed the ~ 0.3 nC threshold. The BLM system might not trigger but the quench protection system will detect the quench and dump the beams. On the contrary, the BLM signal for the distributed loss case is sufficiently high for the BLM system to trigger.

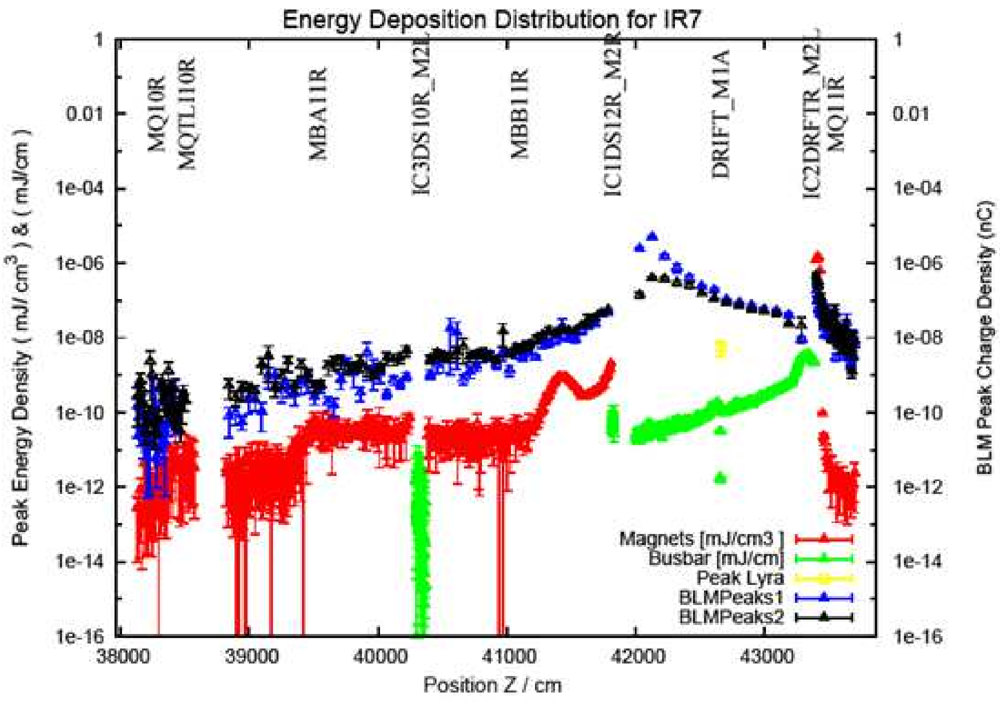

Figure 7.15: Peak energy deposition and BLM signal per proton for the point-like beam loss. (Scenario 2)

Element	Peak Energy Deposition $(GeV/cm^3/p+)$ $(GeV/cm/p+)$	Peak Energy Deposition $(mJ/cm^3/p+)$ $(mJ/cm/p+)$	Quench Limit (mJ/cm^3) (mJ/cm)	Protons to quench	Peak BLM $(nC/p+)$	Peak BLM for DRFT Quench (nC)
MQ.10R7	$8.04 \cdot 10^{-5}$	$1.29 \cdot 10^{-11}$	1	$7.77 \cdot 10^{10}$	$2.37 \cdot 10^{-9}$	0.002
MQTLI.10R7	$7.80 \cdot 10^{-5}$	$1.25 \cdot 10^{-11}$	1	$8.01 \cdot 10^{10}$		
MB.A11R7	$4.68 \cdot 10^{-4}$	$7.49 \cdot 10^{-11}$	1	$1.34 \cdot 10^{10}$	$4.52 \cdot 10^{-9}$	0.003
IC3.DS10R7	$4.37 \cdot 10^{-5}$	$6.99 \cdot 10^{-12}$	10	$1.43 \cdot 10^{12}$		
MB.B11R7	$1.26 \cdot 10^{-2}$	$2.02 \cdot 10^{-9}$	1	$4.96 \cdot 10^{8}$	$5.53 \cdot 10^{-8}$	0.04
IC1.DS12R7	$6.67 \cdot 10^{-4}$	$1.07 \cdot 10^{-10}$	10	$9.37 \cdot 10^{10}$		
DRFT.11R7 (Busbar)	$1.97 \cdot 10^{-2}$	$3.15 \cdot 10^{-9}$	10	$3.17 \cdot 10^{9}$	$5.01 \cdot 10^{-6}$	3.4
DRFT.11R7 (Lyra)	$3.59 \cdot 10^{-2}$	$5.75 \cdot 10^{-9}$	10	$1.74 \cdot 10^{9}$	$5.01 \cdot 10^{-6}$	3.4
IC2.DRFTR7	$2.41 \cdot 10^{-2}$	$3.86 \cdot 10^{-9}$	10	$2.59 \cdot 10^{9}$		
MQ.11R7	9.27	$1.48 \cdot 10^{-6}$	1	$6.74 \cdot 10^{5}$	$4.66 \cdot 10^{-7}$	0.3

Table 7.3: Scenario 2: energy deposition per proton on the coils and bus-bars. (Point-like loss)

Element	Peak Energy Deposition ($GeV/cm^3/p+$) ($GeV/cm/p+$)	Peak Energy Deposition ($mJ/cm^3/p+$) ($mJ/cm/p+$)	Quench Limit (mJ/cm^3) (mJ/cm)	Protons to quench	Peak BLM ($nC/p+$)	Peak BLM for DRFT Quench (nC)
MQ.10R7	$4.55 \cdot 10^{-5}$	$7.28 \cdot 10^{-12}$	1	$1.37 \cdot 10^{11}$	$4.43 \cdot 10^{-9}$	0.01
MQTLI.10R7	$1.61 \cdot 10^{-4}$	$2.58 \cdot 10^{-11}$	1	$3.88 \cdot 10^{10}$		
MB.A11R7	$7.54 \cdot 10^{-4}$	$1.21 \cdot 10^{-10}$	1	$8.29 \cdot 10^{9}$	$6.01 \cdot 10^{-9}$	0.02
IC3.DS10R7	$9.50 \cdot 10^{-5}$	$1.52 \cdot 10^{-11}$	10	$6.58 \cdot 10^{11}$		
MB.B11R7	$1.07 \cdot 10^{-2}$	$1.71 \cdot 10^{-9}$	1	$5.85 \cdot 10^{8}$	$3.79 \cdot 10^{-8}$	0.1
IC1.DS12R7	$5.98 \cdot 10^{-4}$	$9.57 \cdot 10^{-11}$	10	$1.04 \cdot 10^{11}$		
DRFT.11R7 (Busbar)	$1.00 \cdot 10^{-2}$	$1.60 \cdot 10^{-9}$	10	$6.25 \cdot 10^{9}$	$1.06 \cdot 10^{-6}$	3.4
DRFT.11R7 (Lyra)	$3.10 \cdot 10^{-2}$	$4.96 \cdot 10^{-9}$	10	$2.02 \cdot 10^{9}$	$1.06 \cdot 10^{-6}$	3.4
IC2.DRFTR7	$1.15 \cdot 10^{-2}$	$1.85 \cdot 10^{-9}$	10	$5.42 \cdot 10^{9}$		
MQ.11R7	1.92	$3.07 \cdot 10^{-7}$	1	$3.25 \cdot 10^{6}$	$6.73 \cdot 10^{-7}$	2.2

Table 7.4: Scenario 2: energy deposition per proton on the coils and bus-bars. (distributed loss)

7.6 Results Scenario 3

This section contains the results for the simulations of a 5 TeV and 3 TeV proton beam loss in the MQ12 quadrupole magnet. Figure 7.16 shows an overview of the energy deposition in the tunnel between MQ12 to MBA12 magnets for a 5 TeV distributed beam loss along MQ12 magnet.

Figure 7.15 shows the energy deposition in the bus-bars and magnet coils for the four different cases. In all cases, the highest energy deposition is in a bus-bar occurs at the inteconnection between MQ12 and MBC12 and in a magnet coil at the end of the MQ12 magnet.

The number of protons needed to quench both the bus-bar at the interconnection at 5 TeV for the point-like loss case is $2.86 \cdot 10^9$ (approx. half a pilot beam), while for the distributed case is $5.56 \cdot 10^9$ (slightly more than a pilot beam). At 3 TeV, the number of protons needed for the point-like loss case is $4.35 \cdot 10^9$ (almost a pilot beam), while for the distributed case is $1.00 \cdot 10^{10}$ (twice a pilot beam). The energy deposition scales in energy by a factor of $\times 1.8$ between 5 TeV and 3 TeV protons. In case of a quench in the bus-bars of the interconnection , all magnet coils and bus-bars, downstream of the loss location, up to MBB12 will quench (in all four cases).

The BLM signal scales by a factor $\times 1.7$ with energy from 3 TeV to 5 TeV. Going from a distributed loss to a point loss leads to an increase of the BLM signal by a factor of $\times 1.8 - 1.9$.

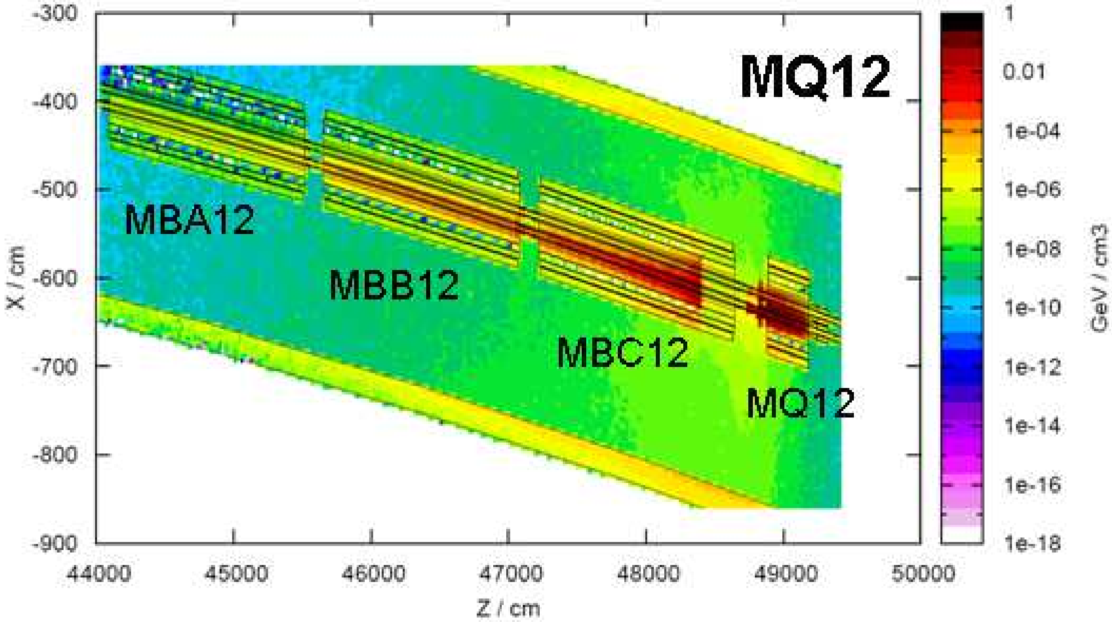

Figure 7.16: Global view of the energy deposited at IR7. (distributed beam loss at 5 TeV)

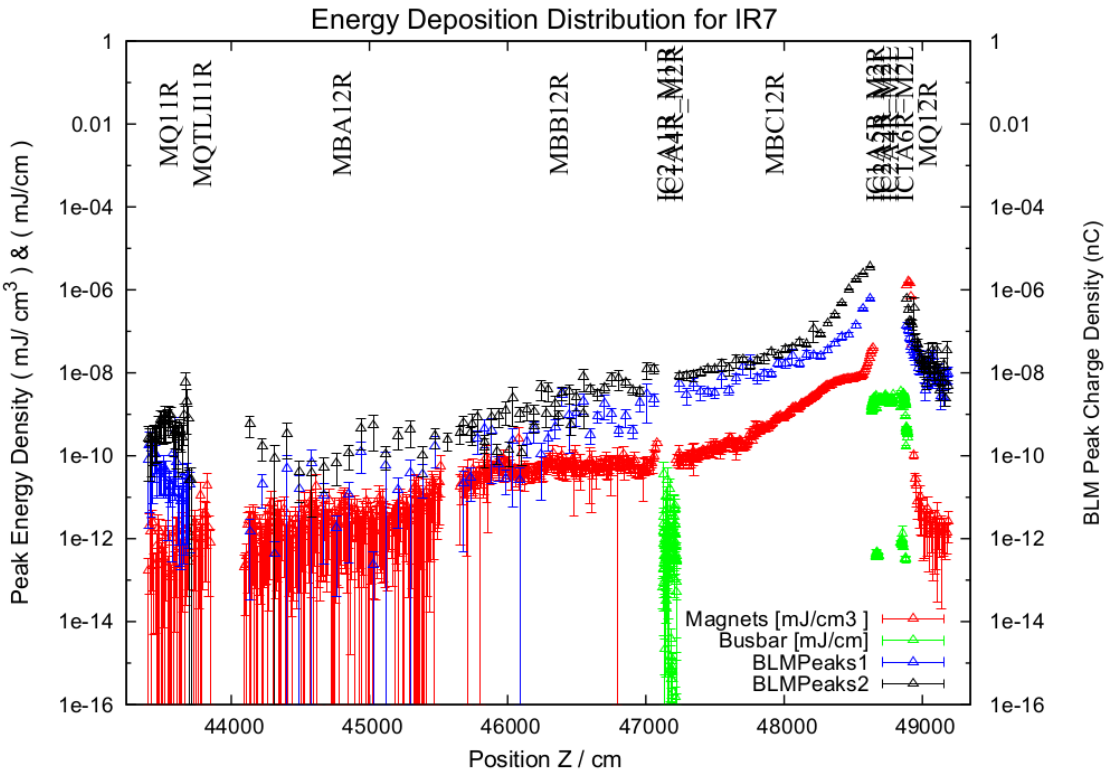

(a) Point loss 5 TeV

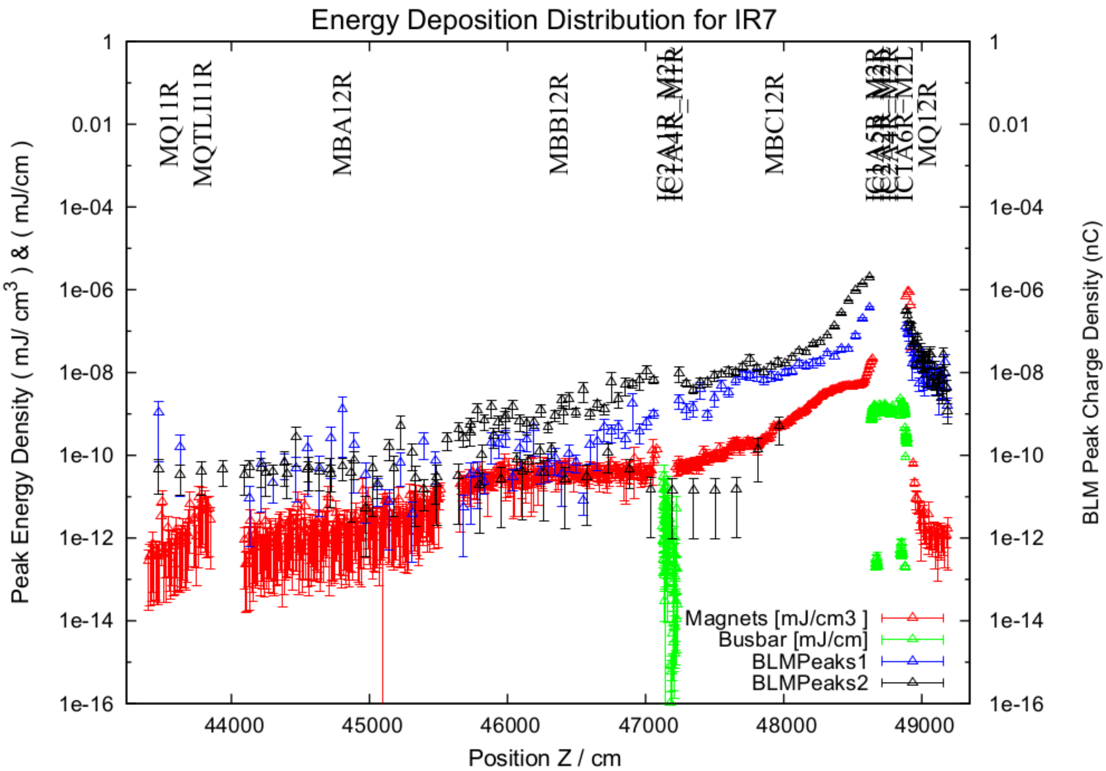

(b) Point loss 3 TeV

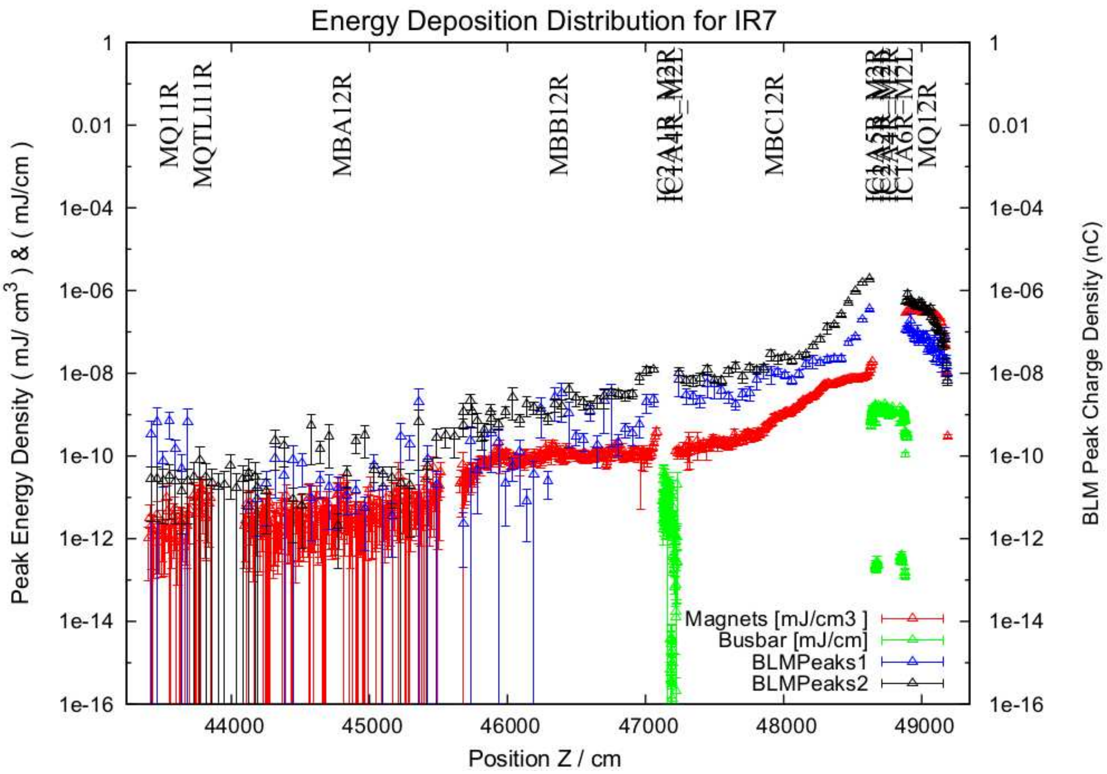

(c) Ditributed loss 5 TeV

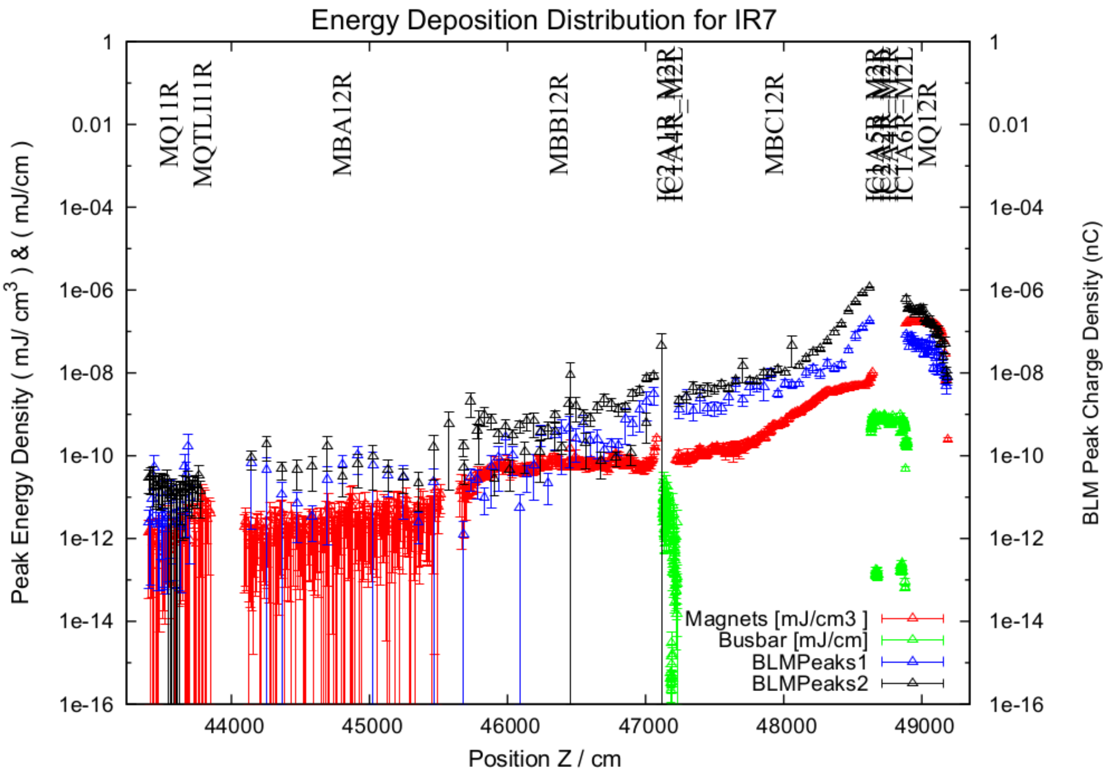

(d) Ditributed loss 3 TeV

Figure 7.15: Global view of the energy deposited and BLM signal at IR7.

7.7 Results Pre-Heating to 80 K

The Table 7.5 summarizes the required number of protons to warm up a bus-bar up to 80 K. If the bus-bars are instantly warmed up to 80 K, the energy extraction system can not extract fast enough all the energy from the circuit. If this occurs, the bus-bar could melt with the situation similar to the accident of 2008. The required energy to warm up a MB type bus-bar is ≈ 92 J.

In all cases the required number of protons to warm-up the bus-bar is in the order of 10^{13} that is two orders of magnitude bigger than the required number of protons to quench the bus-bar. The required energy to quench a bus-bar is five to six times bigger than the energy to quench a magnet. On average, in all scenarios, ~ 300 LHC nominal bunches of $1.15 \cdot 10^{11}$ protons are required for the bus-bar to reach a temperature of 80 K. A beam loss of ≥ 300 LHC nominal bunches will provoke a major damage to accelerator components, even bigger than the resulting damage of an incomplete energy extraction. For such a beam loss the Machine Protection Systems will react and dump the beam inmediately.

Loss Element	Loss Scenario	Energy [TeV]	Peak E-Dep [$mJ/cm/pp$]	Element Name	Number of Protons to pre-Heat to 80 K
MQ12	Point	5	$3.51 \cdot 10^{-9}$	IC1.A6R7.B1	$2.62 \cdot 10^{13}$
		3	$2.26 \cdot 10^{-9}$		$4.07 \cdot 10^{13}$
	Distributed	5	$1.76 \cdot 10^{-9}$	IC2.A4R7.B1	$5.21 \cdot 10^{13}$
		3	$9.59 \cdot 10^{-10}$	IC1.A6R7.B1	$9.60 \cdot 10^{13}$
MQ11	Point	5	$5.75 \cdot 10^{-9}$	IC2.DRFTR7.B1	$1.60 \cdot 10^{13}$
	Distributed	5	$4.96 \cdot 10^{-9}$		$1.86 \cdot 10^{13}$
Connection Cryostat	Point	5	$2.09 \cdot 10^{-8}$	DRFT.11R7.B1 (Lyra)	$4.40 \cdot 10^{12}$
	Distributed	5	$6.20 \cdot 10^{-9}$		$1.48 \cdot 10^{13}$

Table 7.5: Number of protons needed to pre-heat the bus-bar up to 80 K.

7.8 Conclusions

- Pre-Heating to 80 K requires a large beam loss which in itself is a major accident.
- 10^6 protons are sufficient to quench a magnet. (10^8 for the connection cryostat case).
- $10^9 - 10^{10}$ protons are required to quench a bus-bar. (10^8 for the connection cryostat case).
- A magnet will quench at a significantly lower level, 4 – 380 times, than adjacent bus bars.
- Peak values and locations are loss scenario dependent, however general conclusions can be drawn within about one order of magnitude (given the assumptions). Energy deposition dependence between a point loss and a distributed loss is about a factor of two.
- A combined bus-bar and magnet quench can not be excluded (worst case scenario with a 5 TeV beam point-like loss at the connection cryostat).
- Applied 'quench limits' require an iteration with the magnet experts as all the results scale accordingly.
- Energy deposition dependence between 5 TeV and 3 TeV is about a factor of two, this is in same order as the loss scenario dependence.
- According to the present studies it's very unlikely to quench the bus-bar only (not observed in these studies).

8 High Intensity Beam Losses

In this chapter we discuss high intensity beam losses into materials due to accidental beam losses or intentionally into beam absorbers. Machine protection systems prevent accidents. However, accidents may still occur either because of failures or bad MPS designs. From the MPS point of view it is important to test different beam loss scenarios and beam parameters to estimate: the consequences, likelihood, spare materials and elements, etc.

In the case of the LHC, the worst accident would be an instantaneous loss of the full beam at top energy. Although, a loss of a small fraction of the LHC beam at injection energy is capable of doing severe damage to the accelerator.

8.1 HiRadMat Facility

HiRadMat [62] (High Irradiation to Materials) is a new facility at CERN. It is designed to allow testing of accelerator components, in particular those of LHC, to the impact of high-intensity pulsed beams. The facility is designed to provide $\approx 10^{16}$ protons per year, distributed among ≈ 10 experiments, each having a total of 10^{15} p+ or about 100 high-intensity pulses. The facility has been built in the former WANF (West Area Neutrino Facility) tunnel during the years 2010 and 2011.

8.1.1 Parameters

The facility uses a 440 GeV proton beam coming from the CERN SPS. The beam has a pulse length of 7.2 μs giving a maximum pulse energy of 3.4 MJ. Apart from protons, ion beams with an energy of 173.5 GeV/nucleon and a total pulse energy of 21 kJ, can be used. Beam parameters can be tuned to match the needs of each experiment (see Table 8.1).

The 440 GeV proton beam can have a focal size down to 0.1 mm, thus providing a very dense beam (energy/size). The size can be tuned ranging from 0.1 mm to 2 mm.

Parameter	Symbol	Protons	Ions
Particle Energy	E	440 GeV	36.9 TeV
Bunch Intensity	N_b	$1.7 \cdot 10^{11}$	$7 \cdot 10^{7}$
Max. number of bunches per pulse	n_{max}	288	52
Max. pulse intensity	$N_p = n_{max} \cdot N_b$	$4.9 \cdot 10^{13}$ protons	$3.64 \cdot 10^{9}$ ions
Bunch spacing	Δt_b	25 ns	100 ns
Min. beam size (rms)	σ_{beam}	0.1 mm	0.1 mm
RMS bunch length	σ_z	11.24 cm	11.24 cm
Pulse length	t_p	7.2 μs	5.2 μs

Table 8.1: HiRadMat Beam Properties

8.1.2 Layout

The HiRadMat experimental area is located at the TNC tunnel (ex. WANF facility target & secondary beam tunnel) in the SPS-BA7 area. The beam is extracted from the SPS accelerator through the TT60 transfer line. A set of eight powerful switching magnets at the end of TT60 deflect the beam either to the LHC via Ti2 transfer line or to HiRadMat via TT66 transfer line. Finally, the beam is transported along ~ 200 m to the experimental area.

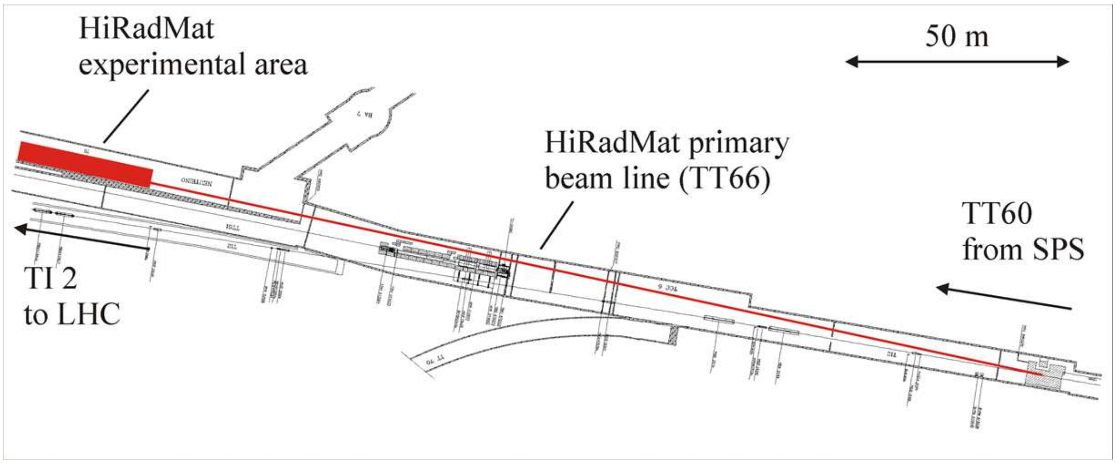

Figure 8.1: HiRadMat transfer line schema.

Four strong bending magnets deflect the beam up in the vertical plane; the experimental area is tilted up. The flexibility in beam size is achieved with a set of five quadrupole magnets at the end of the TT66. There are six different predefined optics, each one for a different beam size and focal spot.

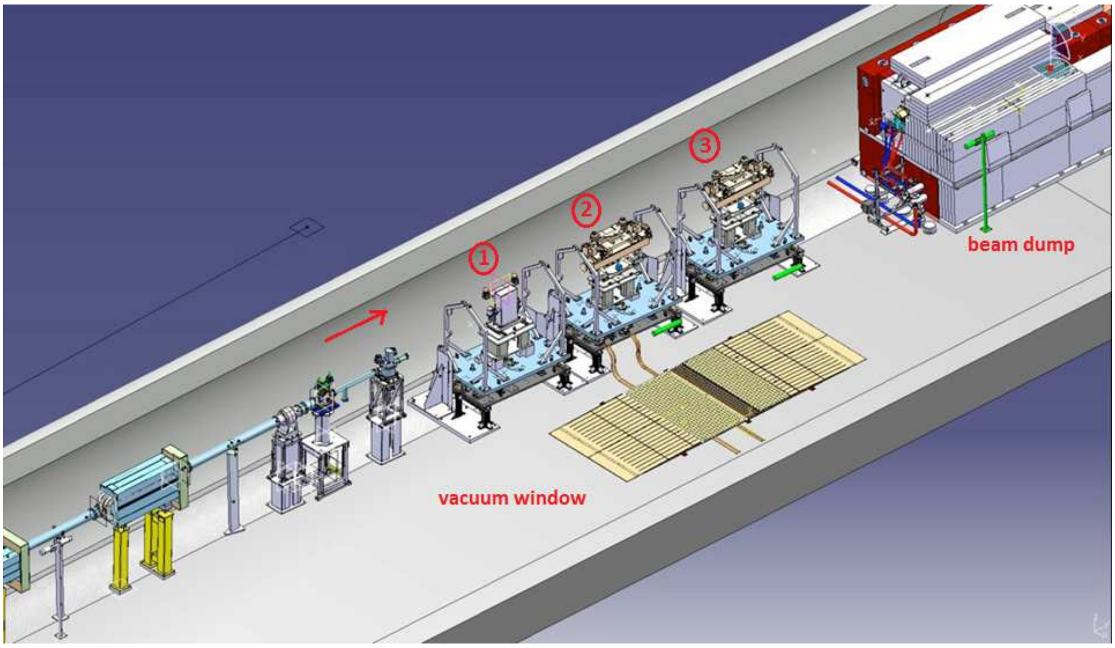

Figure 8.2: HiRadMat layout.

The facility has three test stands for experiments. Up to three experiments can be installed at the same time in the tunnel. However, only one experiment should be exposed to the beam at a given moment. The beam can be focused at the beginning of each test stand. Each stand is ~ 2 m long, giving a total length for the experimental area of ~ 9 m. Installation and removal of the experiments is done remotely using a crane.

Figure 8.3: HiRadMat facility.

8.2 High-Intensity High-Dense Beams On Low-Z Materials

A 60 mm aperture vacuum window will separate the vacuum of the beam line, which is kept under high vacuum 10^{-6} Pa (10^{-8} mbar), from the test area which is at atmospheric pressure. This window has to resist collapse due to the beam passage. The window will suffer from repeated dynamic thermal load due to the beam passage. HiRadMat beam has an energy of 440 GeV for protons and a maximum intensity of 288 bunches of $1.7 \cdot 10^{11}$ protons/bunch. The repetition rate of the beam is up to 1/18 Hz.

Protons passing through the window will lose energy in accordance to the Bethe-Bloch formula (stopping power). Part of the energy loss will be deposited on the window. The energy deposition will be extremely localized. The heat load on the window can produce elastic pressure waves, plastic pressure waves or even shock waves that can modify the material properties and permanently damage the window. If the window is damaged, the facility will have a long downtime for repairs.

Conventional windows made of stainless steel, aluminum, etc. will not withstand these extreme conditions. New materials and calculations are presented here.

8.2.1 Materials

Several materials were studied. These materials were chosen because of its superior properties: low atomic number (Z), good thermal and mechanical properties and a relatively high melting point.

The materials analyzed are the following:

- Beryllium: Metallic material with low atomic number ($Z = 4$) and low density. These makes Beryllium almost transparent for high intensity particles. It has good mechanical properties like flexural rigidity and a good thermal conductivity. On the other hand, beryllium is a highly toxic substance that should not be used unless no other possibilities are available (CERN Safety Instruction [63]). The limit temperature of operation is relatively low (773 K).
- Carbon Fiber reinforced Carbon [64] (CFC): Is an extremely strong porous material (coefficient of permeability of $5 \cdot 10^{-2}\,\mathrm{cm}^2/\mathrm{s}$) made of carbon fibers. It is mostly composed of carbon atoms (C) which has a low atomic number ($Z = 6$) and low density. It has a the highest sublimation point 3915 K of any element and very high thermal conductivity. On the other hand, it does not provide vacuum tightness and therefore it requires to be combined with a leak tight material. The maximum operating temperature is 3273 K. However, in presence of air carbon combustion can happen well bellow this temperature.
- Titanium alloy (Ti6Al4V): Titanium Grade 5, has good mechanical properties, resistance to corrosion and vacuum tightness. But it has a low temperature operating limit 723 K.
- Aluchrom: (Fe70//Cr25//Al5) Alloy designed for high temperature applications with excellent resistance to oxidation at elevated temperatures. The high contents of aluminium and chromium in combination with yttrium and hafnium of the alloy give a good high temperature stability. Melting point 1793 K. The maximum operating temperature is 1273 K.

8.2.2 Methodology

The beam energy deposition was calculated on each material using ultimate beam parameters (worst case): 288 bunches with $1.7 \cdot 10^{11}$ protons/bunch. Three different beam sizes (0.1 mm, 0.25 mm and 0.5 mm) were used in each case. The beam was assumed gaussian with a round shape $\sigma_x = \sigma_y$ (at the window location). For simulations the material thickness was set to 100 μm. Energy deposition profiles were calculated using two methods: FLUKA and an analytical formula. Although the facility can run on ions, only protons were considered; the energy deposition due to stopping power is twice as much for the proton beam than for the lead ion beam. This factor of two comes from the ratio between atomic number and beam intensity: $288 \cdot 1.7 \cdot 10^{11}$ p+ over $52 \cdot 7 \cdot 10^{7}$ fully stripped lead ions $\cdot Z^2$.

FLUKA calculations were done using a conservative approach in which the contribution of high energy delta electrons were not considered for the energy deposition (restricted stopping power). Delta electrons are secondary electrons with enough energy to escape a significant distance away from the primary radiation beam and produce further ionization [65]. In thin materials, high energy delta electrons can have sufficient energy to escape from the material. The electron transport threshold was lowered accordingly. The energy threshold was taken from tables from the Particle Data Group [1] that corresponds to an electron range of 100 μm in the material. The mesh size should be small enough to obtain the maximum value of energy deposition. In FLUKA it was set to 1/3 of the beam sigma.

The analytical calculation was done using the following formula [66]:

$$\Delta T_{inst} = \left(\frac{dE}{\rho dx}\right) \frac{nN_b}{2\pi C_p \sigma^2_{beam}} \tag{8.1}$$

Where:

- ΔT_{inst}: is the instantaneous increment of temperature.
- dE/dx: Stopping power for protons in Beryllium.
- rho: Beryllium density.
- nN_b: Total number of beam particles.
- C_p: Beryllium heat capacity.
- σ_{beam}: beam sigma.

For each material and for every beam size combination, the peak temperature was calculated using empirical heat capacity data (as a function of T). If the resulting temperature is higher than the maximum allowable operation temperature, no further calculations were done. On the contrary, if the temperature is within the temperature operation range then a numerical analysis with ANSYS of the thermal, pressure load and pressure wave generation was done. The ANSYS analysis was done by Michael Monteil (TE-VSC group at CERN).

8.2.3 Results

The following tables show the energy deposition values calculated with FLUKA [67]. The error shown in the following tables 8.2 to 8.4 corresponds to the statistical error given by FLUKA. The total simulation error is: statistical error + geometry error + physics models error.

Ti6Al4V and Aluchrom materials are not suited for this application because the peak temperature exceeds the maximum operating temperature in every case. Carbon fiber composite

Material	Energy $[GeV/cm^3/p]$	temp [C]	error [%]	Max operating temp [C]
C-C	0.184	623.2	0.5	3825
Be	0.201	492.5	5	500
Ti6Al4V	0.490	1411.4	0.8	450
Aluchrom	0.807	$> T_{melt}$	1.2	1250

Table 8.2: Energy deposition and peak temperature for an ultimate SPS-beam with $\sigma = 0.5$ mm and $288 \cdot 1.7 \cdot 10^{11}\,p+$.

Material	Energy $[GeV/cm^3/p]$	temp [C]	error [%]	Max operating temp [C]
C-C	0.692	1749.4	0.3	3825
Be	0.739	$> T_{melt}$	1.9	500
Ti6Al4V	1.856	$> T_{melt}$	0.5	450
Aluchrom	3.101	$> T_{melt}$	0.5	1250

Table 8.3: Energy deposition and peak temperature for an ultimate SPS-beam with $\sigma = 0.25$ mm and $288 \cdot 1.7 \cdot 10^{11}\,p+$.

Material	Energy $[GeV/cm^3/p]$	Temp [C]	error [%]	Max operating temp [C]
C-C	3.87	$> T_{triple}$	0.8	3825
Be	4.09	$> T_{melt}$	1.1	500
Ti6Al4V	10.53	$> T_{melt}$	1.4	450
Aluchrom	17.86	$> T_{melt}$	2.2	1250

Table 8.4: Energy deposition and peak temperature for an ultimate SPS-beam with $\sigma = 0.1$ mm and $288 \cdot 1.7 \cdot 10^{11}\,p+$.

temperature for 0.25 mm and 0.5 mm beam sigma is well below the 3273 K limit. Also, Beryllium does work for the case of 0.5 mm sigma beam. CFC and beryllium are the only materials, from the ones analyzed that can withstand the beam load for this requirements.

Carbon fiber composite is a porous material and therefore is not vacuum tight. If the window is only made of CFC, the system will require a stronger vacuum pumping system. Another solution is to add a thin layer of a non-porous material that preserves the vacuum. We chose a combination of carbon fiber composite and beryllium (metallic non-porous material). A first layer of 0.5 cm carbon fiber composite followed by a 0.254 mm beryllium layer (on exterior side).

Table 8.5 shows the energy deposition calculated by FLUKA and with the analytical formula for a beryllium window assuming a beam intensity of $288 \cdot 1.7 \cdot 10^{11} p+$ and beam size of $\sigma = 0.5$ mm.

method		temperature [C]
FLUKA	Hottest spot	493
Formula	dE/dx (conservative)	481

Table 8.5: Comparison of calculated temperature by FLUKA and with an analytical formula.

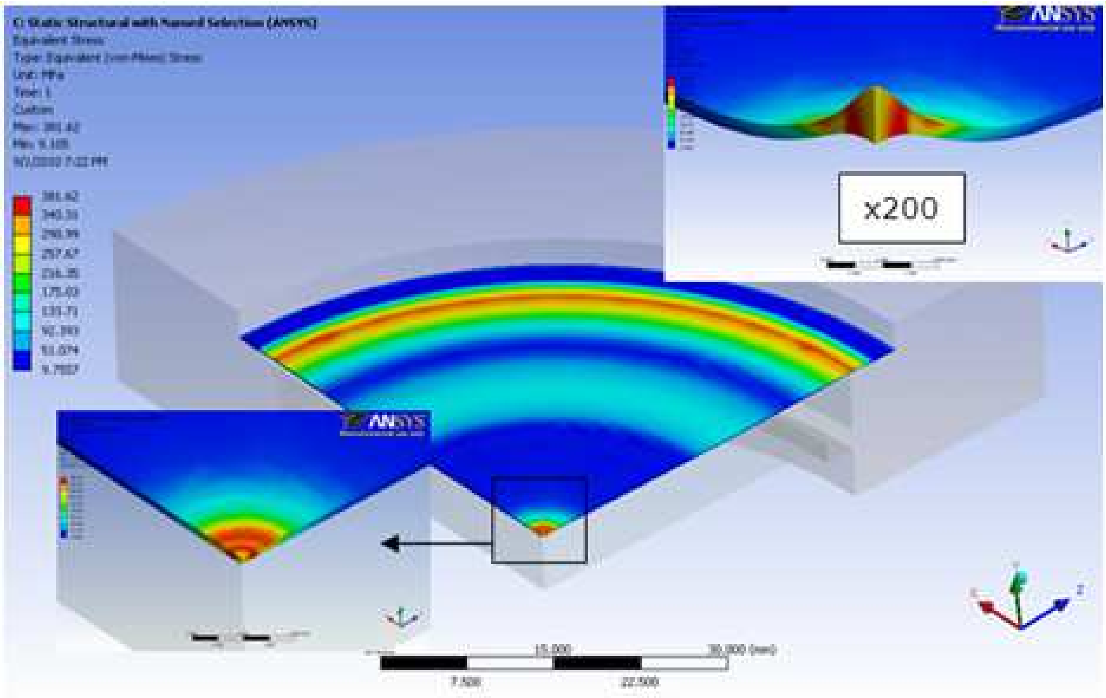

Figure 8.4: Stresses in the beryllium foil partially flattered on the CFC plate with a 1 atm load and right after a HiRadMat proton pulse. (M. Monteil)

8.2.4 Final window design

The final window design [67] consisted of a first layer of 0.5 cm thick CFC plate (grade SIGRABOND 1501G from SGL Carbon) and a second layer 0.254 mm thick beryllium foil (grade PF-60) as a leak-tight. This foil is diffusion bonded on a ISO-CF DN63 flange. Figure 8.5 shows the assembly of the window and the flange.

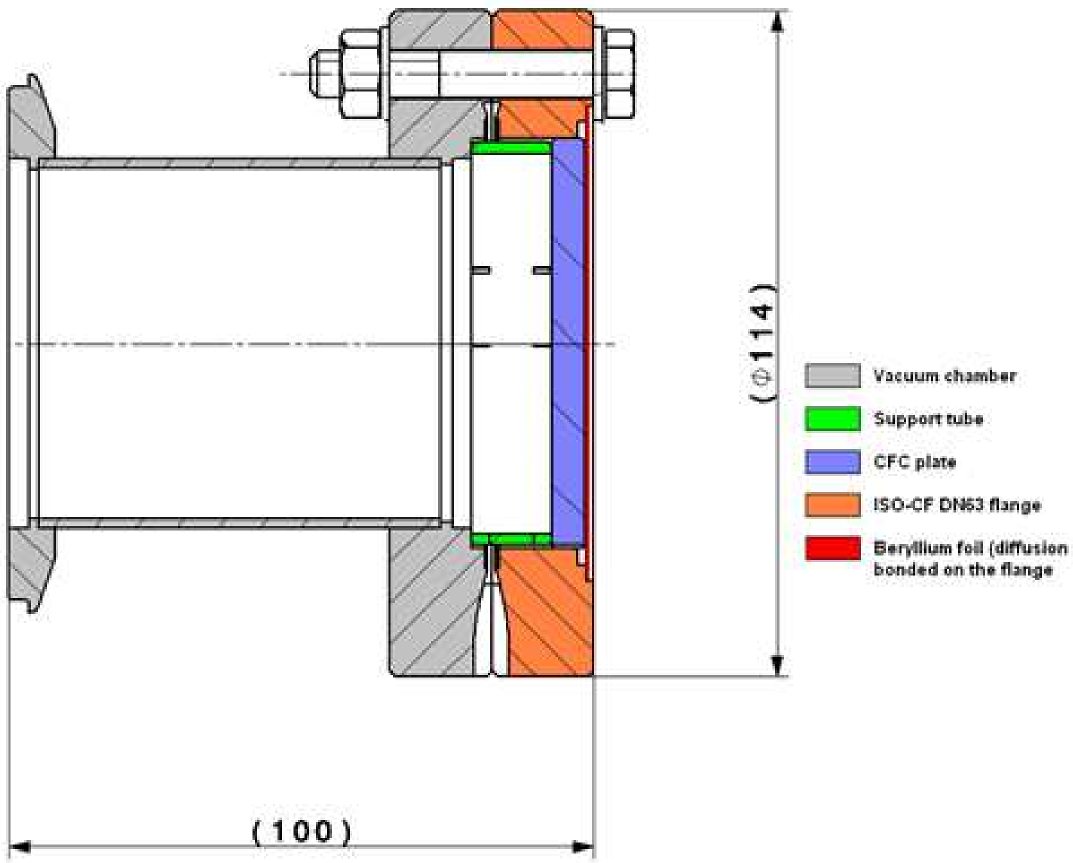

Figure 8.5: Window assembly diagram.

The beryllium foil was supplied by Brush-Wellman company. Due to the CERN regulations [63] concerning beryllium manipulation, the supplier did a leak detection test on the foils. The measured leak-rate was 10^{-9} mbar·l/s of helium. During the test, the window plasticized remaining a residual convex shape of about 0.4 mm. The beryllium foil was installed on the high pressure side of the window (exterior side), since the out-gassing rate of the CFC is low (10^{-8} Torr·l/s/cm^2 without bake-out and 10^{-8} Torr·l/s/cm^2 with a 24h-long bake-out at 300 C) [68]. The window design is such as that, under vacuum, the beryllium foil is partially flattened on the CFC plate.

The HiRadMat window withstands one of the smallest and most intense beams at CERN. The study of different materials showed that there are not many materials and configurations suitable for these conditions. The HiRadMat beam window was manufactured in 2010, installed in 2011 and was correctly working until today.

8.3 High-intensity high-dense beams on High-Z materials

The LHC and the future linear colliders (CLIC, ILC, etc.) operate with very high energy stored in the beams (in the order of several hundred MJoules for LHC) or very high power (for linear colliders). Beam sizes are small, for the LHC down to 10 μm and for linear colliders below one μm. The energy stored in each LHC beam is 362 MJ sufficient to melt 500 kg of copper and equivalent to the kinetic energy of a 200 m train running at 155 km/h. An accidental release of even a very small fraction of the beam energy can result in severe damage to the accelerator equipment. Correct operation of the machine protection systems is essential to avoid any accident. However, accidents may occur so it is important to understand what are the consequences. One of the worst possible accidents is the loss of the full LHC beam at a single point. This accident could happen if the Beam Energy Tracking System (BETS) provides the wrong energy to the extraction kickers at point 6 and hence the beam is deflected with a wrong angle.

What are the consequences of a full LHC beam impact in materials? This is being discussed in this chapter.

An example of a significant damage caused by a beam loss is shown in Figure 8.6. It shows the damage of the QTRF vacuum pipe at SPS TT40 area. The beam caused a 25 cm opening along the beam pipe and melted material inside the pipe. It was the result of an incorrect extraction of $3.5 \cdot 10^{13}$ p+ at 450 GeV. The beam intensity involved in the accident is only a small fraction of the nominal LHC intensity [69].

Credit: *V. Kain*

Figure 8.6: Damage of the QTRF vacuum pipe at SPS TT40 area with $3.5 \cdot 10^{13}$ p+ at 450 GeV.

In collaboration between GSI and CERN, extensive simulations [70] of the impact of high-intensity high-dense beams on different materials have been carried out over the past years. These simulations study the hydrodynamic evolution of a target while and after being irradiated by a proton beam. To understand the consequences of a catastrophic LHC accident, a full LHC beam at 7 TeV impacting into a carbon cylinder of 6 m length and 5 cm radius was simulated. The results of these studies show that the penetration of the beam is much larger than the one expected for the case in which no hydrodynamic motion is considered. The hydrodynamic effect that leads to a further beam penetration is called "hydrodynamic tunneling". Hydrodynamic tunneling is a hydrodynamic effect caused by the interaction of the beam in which matter is transported away from the the beam heated region (beam path). The displacement of matter is the result of a radial pressure wave created by the beam-target interaction. As the density along the beam path decreases, the beam particles impact further inside the target.

The experimental verification of the results is very important for both the machine protection point of view and the validation of computer codes and methodology. An experiment involving the full LHC beam is very dangerous and furthermore there is no facility at CERN prepared for it. Nevertheless, HiRadMat facility at CERN can provide high-intensity high-dense beams. New calculations using the SPS beam (440 GeV) were done following the same methodology used for the LHC ones. SPS simulations will be compared with the results from an experiment installed in HiRadMat. This experiment and its results will be presented in the next chapter.

Previous simulations with high-intensity high-dense beam have been carried out to study the impact of a 20 TeV beam into Superconducting Super Collider (SSC) beam dump by D. C. Wilson, C. A. Wingate, J. C. Goldstein, R. P. Godwin and N. V. Mokhov. [71].

8.3.1 BIG2-FLUKA simulation methodology

The interaction of the proton beam with the target generates a strong heated region. This region experiments an extreme temperature increase. Ultimately, this is translated into a rise of pressure that drives a hydrodynamic motion in the target. The beam energy deposition profile evolves with time due to the hydrodynamic motion. If the hydrodynamic motion is strong enough it cannot be ignored in the simulations.

For LHC and SPS simulations, the hydrodynamic motion must be treated. The problem has been addressed by coupling together two computer codes. The interaction and tracking of particles with matter is done using the computer package FLUKA and the 2-D hydrodynamic calculation is done using BIG2.

An initial energy deposition profile is calculated using FLUKA. The beam parameters (energy, beam size, divergence, particle distribution, etc) and the initial target geometry are used in FLUKA. Initially the whole target is a solid block of material with a specific measures. In all the simulations, the initial geometry of the target is a cylinder that extends along the z-axis. The beam enters through the center of the cylinder's flat face. The beam axis matches the z-axis.

The calculated initial energy deposition profile is used as an input to BIG2. BIG2 runs for a time interval and produces a new density map file. The density map file reflects the final state of the target after the first iteration. A new FLUKA geometry is then generated using the new density map file. This sequence of FLUKA $\Rightarrow$ BIG2 $\Rightarrow$ FLUKA $\cdots$ is run until the beam stops.

Then, only BIG2 code is needed.

The time interval for which BIG2 is run on every step is determined by a maximum allowable density change of 15-20%.

FLUKA and BIG2 are programs from two different domains of physics. The manner in which the problem geometry is described by FLUKA and BIG2 is very different. FLUKA uses combinational geometry to define regions. BIG2 uses a quadrilateral mesh to solve the thermodynamical and mechanical properties of the problem. The density map generated by BIG2 needs to be translated into a format that FLUKA can understand. The translation process is done using two *Python* scripts.

Density file translation

A first script reads the density file generated by BIG2. The density file is a sequence of coordinates (x, y, z) and its corresponding density (ρ) values. The target might be divided into regions. These regions might not share the same grid. The script reads a configuration file which includes:

- Names of the input and output files.
- Target material properties and dimensions: Z, A, ρ, length, etc.
- Algorithm values: maximum number of iterations, thresholds, etc.
- Format of the density map input file: number of regions, region position, region binning, etc. BIG2 might divide the target geometry in regions with a different mesh.
- Beam parameters: particle type, energy, beam size, etc.
- FLUKA input file syntax.

The first step is to arrange the density (r, z, ρ) data into a matrix format. The data is given in cylindrical coordinates for $\theta = 0$ due to the axial symmetry of the problem. The density data from each region is re-arranged into an individual matrix. One matrix is generated for each region. Then, all individual matrices are assembled together. In other to be able to do this, the structure of regions in BIG2 has to fulfill that the number of bins for the a given dimension (x or y) for adjacent regions are equal. As an example, Figure 8.7 shows a target divided into 4 regions with different bin size that fulfills the requirement.

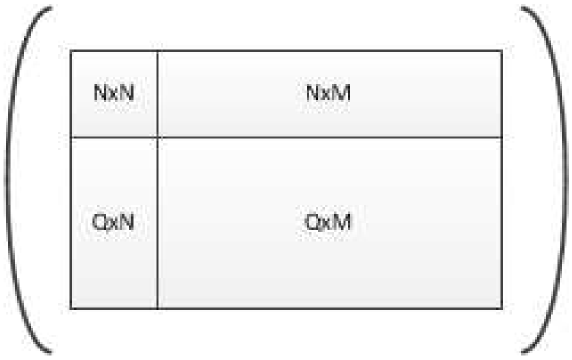

Figure 8.7: Matrix representation of the regions in which the target is divided for simulation.

The second step is to interpolate the data into a common mesh. The data points from BIG2 might not correspond to the geometry mesh. Also, different regions might have different meshes. The interpolation is done using *scipy.interpolate.Rbf* function in python from the scipy package.

The third step is to create a new set of regions (group of adjacent points) in which the density change is limited. For one region, the accumulated gradient in both directions x & y axis must not exceed a certain value. This value is calculated in a way that the total number of regions, at this step, does not exceed 10000. Different values for the total number of region have been tested and 10000 gives a good compromise between a precise density map and a the maximum number of regions that FLUKA can handle (by default). The greatest change in density (gradient) occurs around the beam axis in the strong heated region. For regions close to the beam axis, the density gradient increases with time as a result of the radial pressure waves.

Regions are defined, using combinational geometry, by intersecting cylinders with different radius with planes (Rθ planes) at different longitudinal positions. The boundaries of the regions in the radial direction (cylinders) are defined so that the gradient in the radial direction inside one region does not exceed a certain value. The region boundaries in the longitudinal direction (x-y planes) are determined using the same method.

At this point, a set of $(Number_{cylinders}+1)\cdot(Number_{planes}+1)$ regions are defined. The number of regions should not exceed 10000, previously mentioned. By default, FLUKA does not support more than ≈ 700 materials. The scripts use only one region per material so the total number of regions needs further reduction. The total number of regions is reduced by combining regions with similar densities. The density of the a new region created by combining one or more regions, is calculated as a weighted average of densities with the volume.

Finally, a FLUKA input file is generated using the new geometry, beam parameters, materials, etc .

As an example, Figures 8.8 and 8.9 show a 2D representation of the regions defined in a copper target after 300 ns and 6800 ns respectively. After 6800 ns, the density gradient in the heated regions is larger than at 300 ns. More regions are needed to reproduce the density map at 6800 ns.

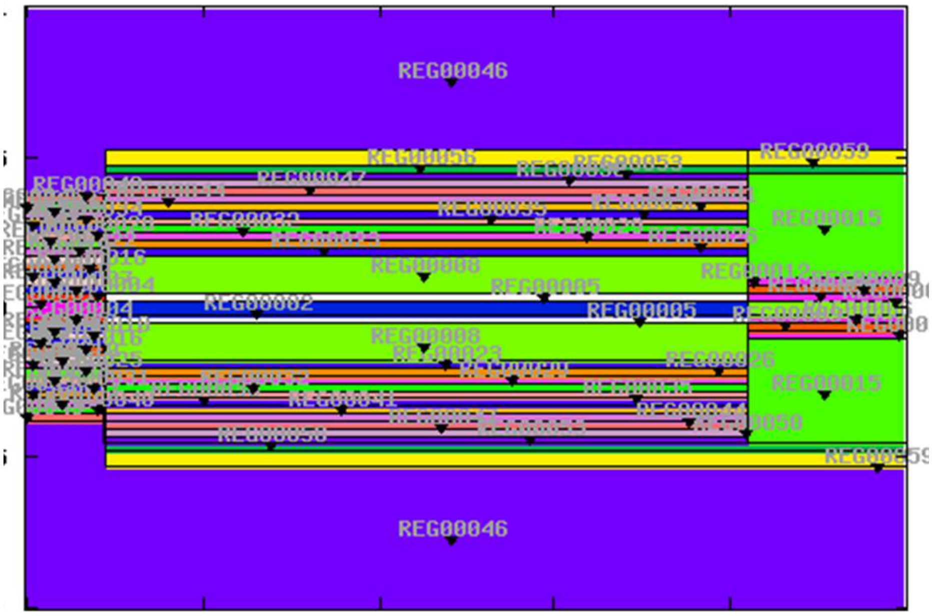

Figure 8.8: Overview of the regions defined in FLUKA after 300 ns irradiation of SPS beam in copper.

8.3.2 Impact of LHC beam in a carbon target

Calculations of an LHC-type beam of 2808 bunches with $1.15 \cdot 10^{11}$ p+ /bunch at 7 TeV irradiating a carbon target are presented here. The beam size at the impact point is $\sigma_{rms} = \sigma_x = \sigma_y = 0.5$ mm. The bunch separation is 25 ns and the total beam time is 89 μs. The target is a solid block of carbon with an uniform density of 2.28 g/cm^3. The target has a cylindrical shape with a total length of 6 m and a radius of 5 cm. The beam impacts on the center of the front side and has the same direction as the cylinder symmetry axis. The simulation has an axial symmetry that will be exploited in FLUKA and BIG2 reducing the complexity from a 3D to a 2D problem. The beam parameters and the target material have been chosen so the calculations will reproduce an hypothetical accident of the LHC beam into the 6 m TCDQ carbon collimator at point 6.

The multiphase, multicomponent EOS used by BIG2 for carbon comes from [72]. The time step of iterations between BIG2 and FLUKA is 2.5 μs that is approximate the time in which the density along the axis decreases by a 15%-20%. In SSC calculations [71], the time step varies from one iteration to another and it is determined by the following formula $\delta t = 0.2\sigma_{beam}/vr_{max}$. Where δt is the calculated time step and vr_{max} is the maximum fluid velocity in the radial direction.

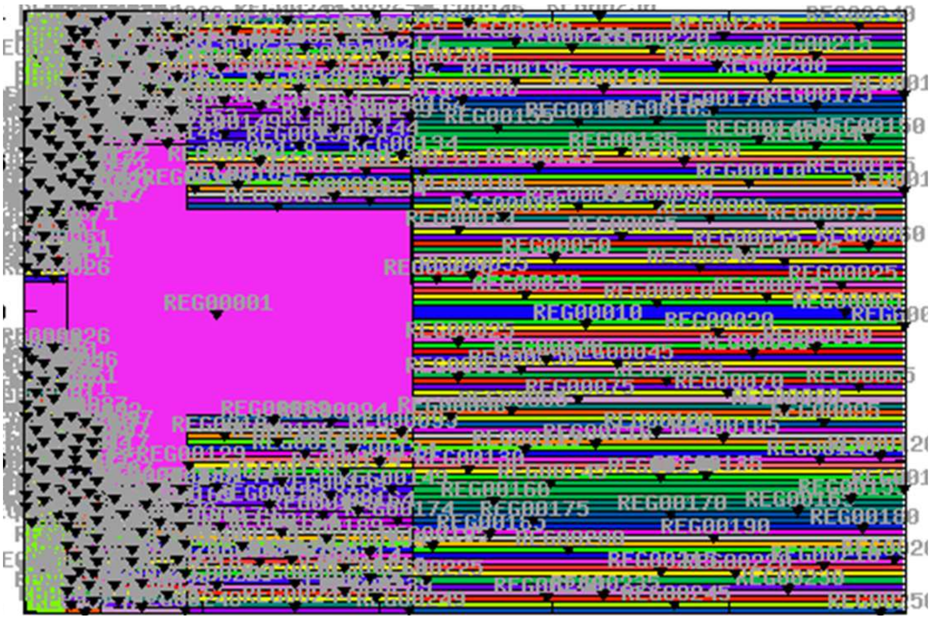

Figure 8.9: Overview of the regions defined in FLUKA after 6800 ns irradiation of SPS beam in copper.

Figure 8.10 shows the energy deposition profiles of the proton beam on the carbon target at different times. The peak energy deposition moves along the beam axis with time. Particle showers develops further inside the target because the density of the target in the beam heated region decreases (λ_{tot} and X_0 increases). Particle showers and the beam heated region elongate with time and so the energy density decreases.

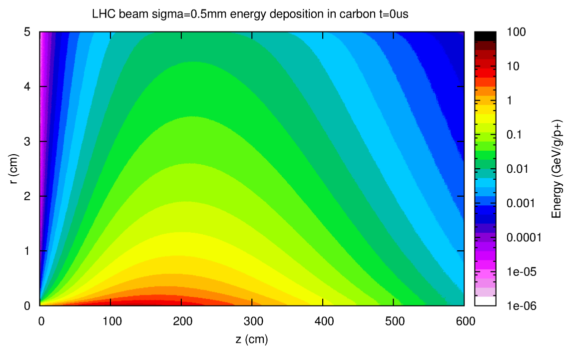

(a) Time = $0\mu s$

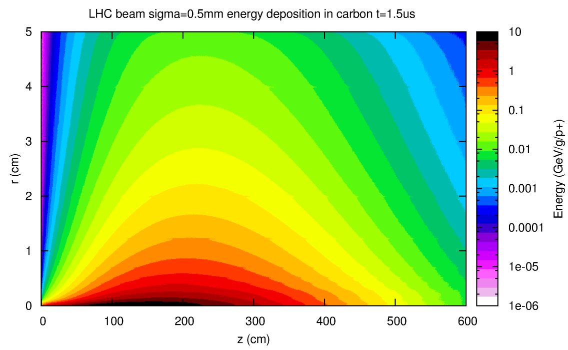

(b) Time = $1.5\mu s$

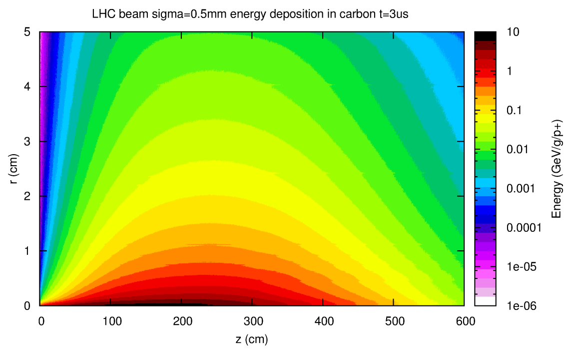

(c) Time = $3\mu s$

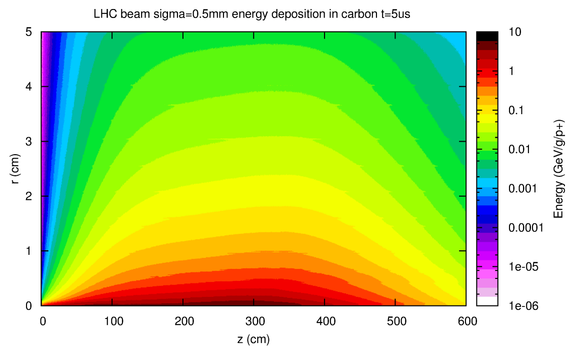

(d) Time = $5\mu s$

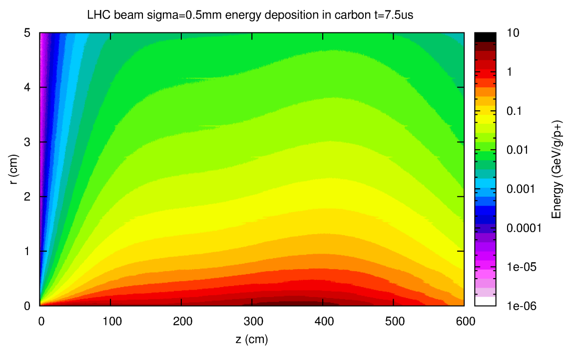

(e) Time = $7.5\mu s$

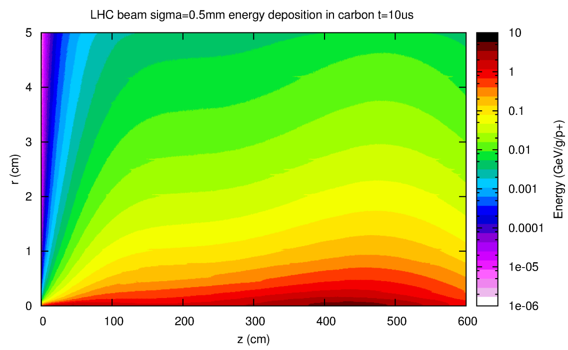

(f) Time = $10\mu s$

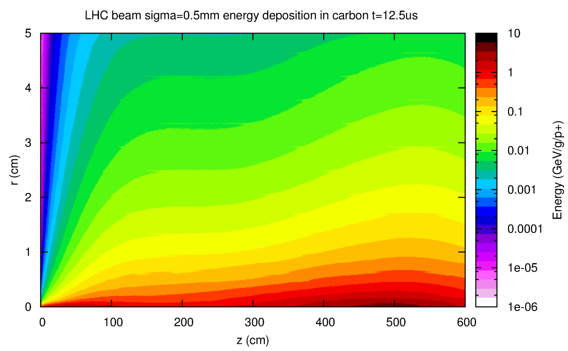

(g) Time = $12.5\mu s$

Figure 8.10: Energy deposition evolution in $(GeV/g/p+)$ calculated by FLUKA for LHC beam in a carbon target.

Initially, the beam heated region is ≈ 3 m long; after $5\,\mu$s it has extended to ≈ 4 m and the peak energy density has decreased from 11.1 GeV/g/p+ to 5.1 GeV/g/p+. For $t = 10\,\mu$s it extends to ≈ 5 m. After $15\,\mu$s the beam heated region covers the entire length of the target 6 m. The beam penetrates through the whole length. The penetration length is defined as the part of the target above the melting point.

Energy deposition can be considered a local phenomenon. The rate of heat transfer by conduction is much smaller than the rate at which the energy is deposited by the beam. Considering the beam time scale (tens of μs), heat conduction, even at high densities, is negligible.

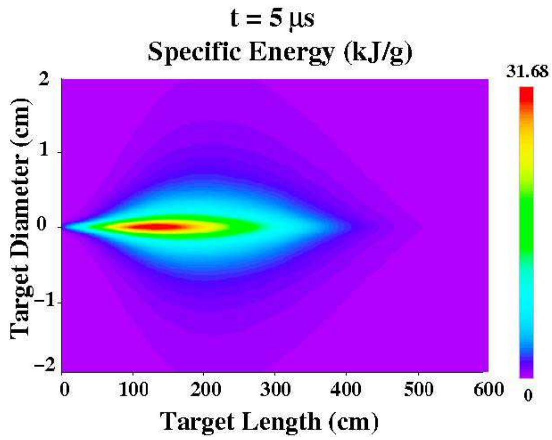

(a) Energy, $t = 5\mu s$

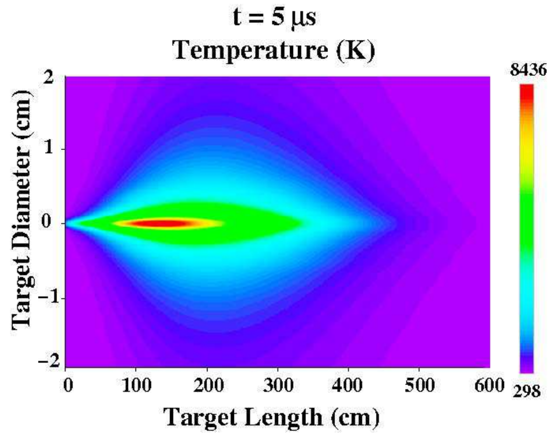

(b) Temperature, $t = 5\mu s$

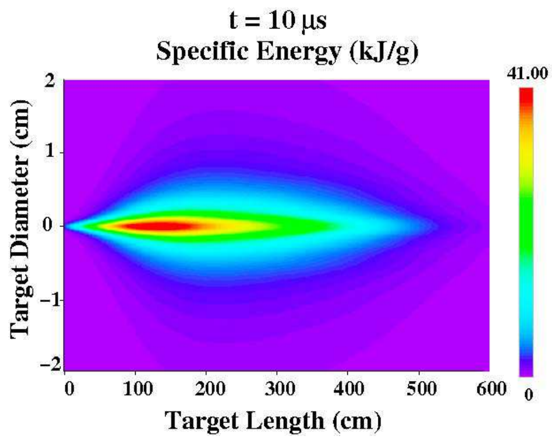

(c) Energy, $t = 10\mu s$

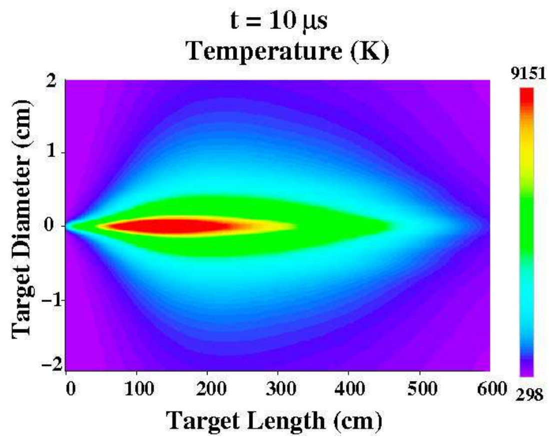

(d) Temperature, $t = 10\mu s$

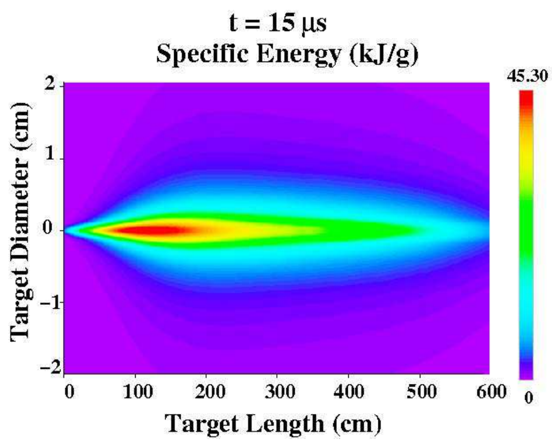

(e) Energy, $t = 15\mu s$

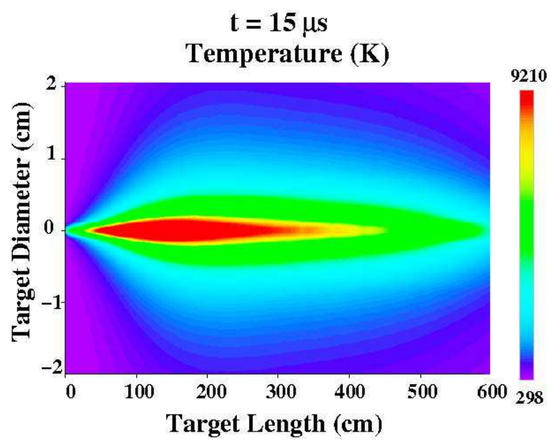

(f) Temperature, $t = 15\mu s$

Figure 8.11: Specific energy deposition (kJ/g) and temperature (K) evolution calculated by BIG2 for LHC beam in a carbon target.

The specific energy deposition (kJ/g) increases with time because the density decreases faster than the energy deposition; the ratio between them increases.

The maximum temperature of the target after 5 μs is ≈ 8400 K reaching a saturation point of ≈ 9100 K after the next 5 μs. At 15 μs the temperature remains ≈ 9100 K. The fast and concentrated energy deposition around the target axis provokes a sudden temperature rise and also a compression pressure wave that travels radially outwards. There is also a longitudinal compression wave but it is weaker than the radial one. The pressure evolution with time is shown in Figure 8.12. Between 5 μs and 10 μs the pressure wave moving radially bounces back on the lateral surface and and generates a negative pressure (restoring force).

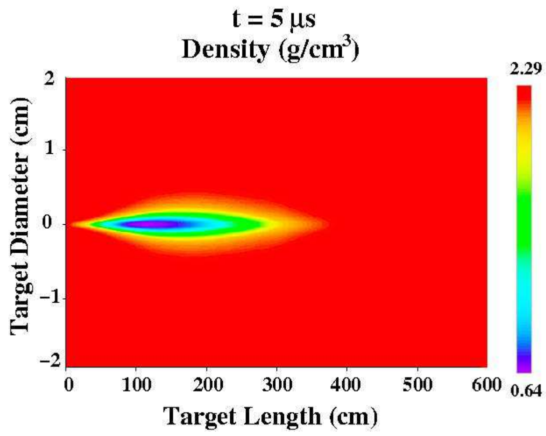

(a) Density, $t = 5\mu s$

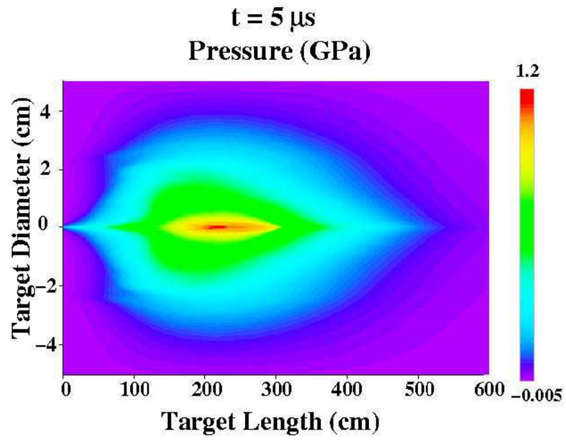

(b) Pressure, $t = 5\mu s$

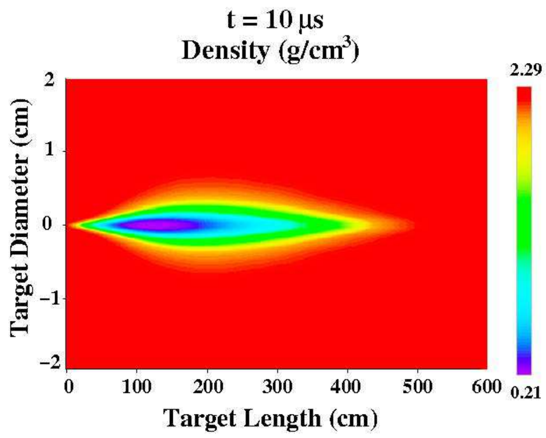

(c) Density, $t = 10\mu s$

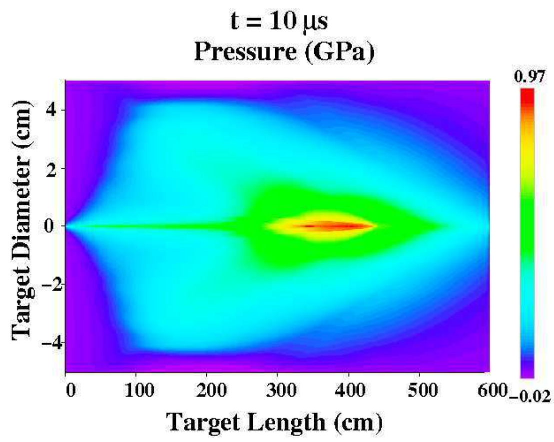

(d) Pressure, $t = 10\mu s$

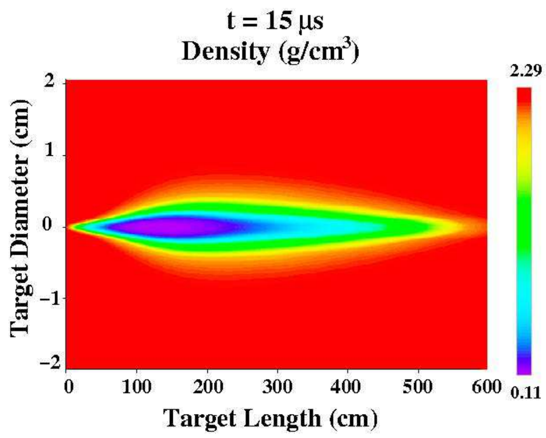

(e) Density, $t = 15\mu s$

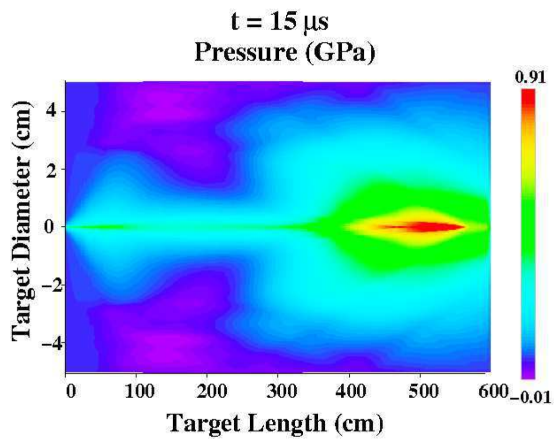

(f) Pressure, $t = 15\mu s$

Figure 8.12: Density (g/cm^3) and pressure (GPa) evolution calculated by BIG2 for LHC beam in a carbon target.

"Hydrodynamic tunneling" [73] can be seen in Figure 8.12 and 8.13. The density profiles show an initial low density region ($5\,\mu$s) that extends with time along the beam axis.

After $\approx 15\,\mu$s a large part of the target has entered into the Warm Dense Matter [74, 75, 76, 77, 78, 79, 80, 81, 82, 83, 70] (WDM) regime. The density towards the end of the target has not decreased a lot, while the temperature is around 0.5 eV and the pressure is in the order of 7 kbar. This is an important result, that suggest that the LHC machine would be able to produce large samples of WDM.

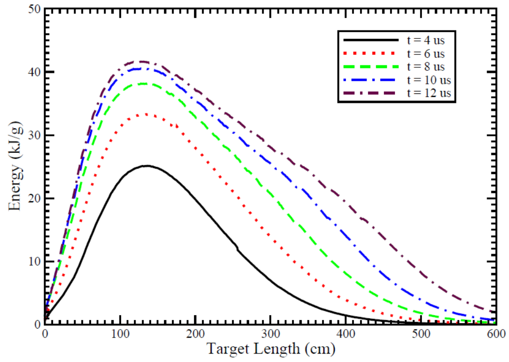

(a) Specific Energy (kJ/g)

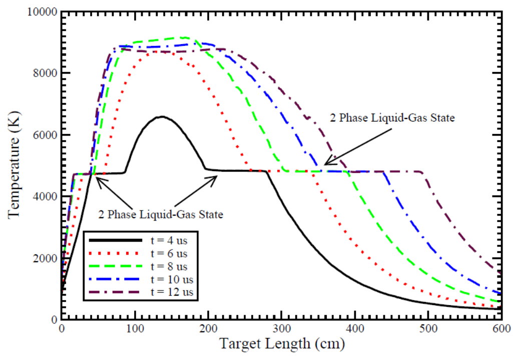

(b) Temperature (K)

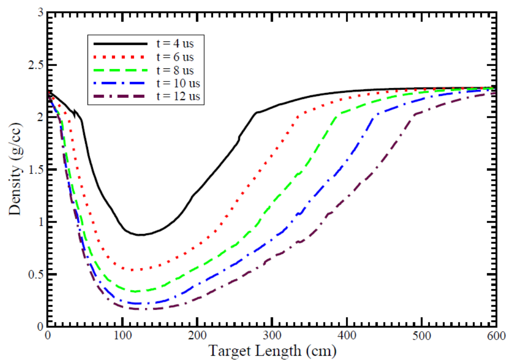

(c) Density (g/cm^3)

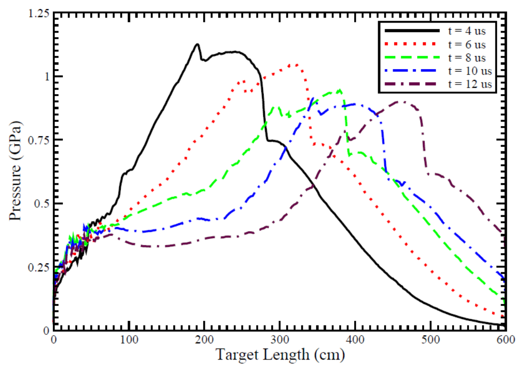

(d) Pressure (GPa)

Figure 8.13: Specific Energy, temperature, density and pressure along the beam axis calculated by BIG2 for LHC beam in a carbon target.

The constant temperature regions shown in Figure 8.13 are regions of the target in which a change of phase occurs (liquid-gas). The region above the constant temperature line is in gaseous or plasma state.

The density depletion region extends at a speed of $\approx 25\,\text{cm}/\mu\text{s}$, therefore during the remaining $86\,\mu$s of beam time the region will extend up to 25 m. SSC calculations show a penetration speed of $70\,\text{cm}/\mu\text{s}$ for a 20 TeV proton beam with a flux of 10^{19} p+/s and a beam size of $sigma = 2$ mm and $7\,\text{cm}/\mu\text{s}$ for a 20 TeV proton beam with a flux of $4.5 \cdot 10^{17}$ p+/s and a beam size of $sigma = 2$ mm. Result presented here are in the same order of magnitude as the ones from SSC. However, a scaling factor between simulations is difficult to obtain.

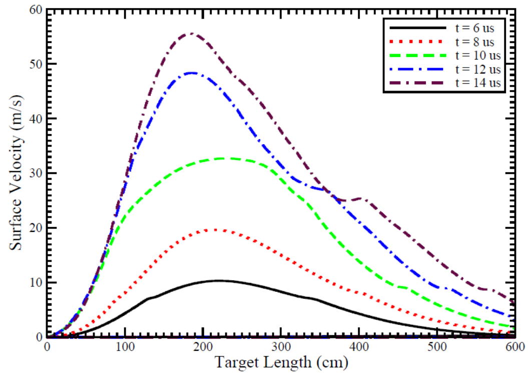

Figure 8.14: Surface velocity along the target length calculated by BIG2 for LHC beam in a carbon target.

Figure 8.14 shows the surface velocity at different times. When the pressure wave reaches a boundary (target walls) and bounces back, the wall vibrates. The surface velocity rapidly increases during the first 10 μs to 12 μs and then begins to decelerate because of the tensile force generated by the yield strength of the material. If the material remains in the elastic regime then the target boundary will oscillate around the equilibrium position. The von Mises parameter M indicates whether or not the region remains in elastic regime

$$M = \left[3 \frac{\sigma_{xx}^2 + 2\sigma_{xy}^2 + \sigma_{yy}^2}{2 Y_0^2} \right], \tag{8.2}$$

where σ is the corresponding component of the stress tensor and Y_0 is the graphite's yield strength (70 MPa).

The von Mises parameter is ≤ 1 for all regions that remains solid, meaning they remain in the elastic regime.

The simulations suggest that the 6 m carbon composite fiber collimator TCDQ at point 6 LHC will not be sufficient to fully stop the LHC beam at top energy in case of an accident. A part of the beam energy will be dissipated on the collimator itself while the rest will escape. Particles escaping the collimator will have large spread in angle and energy.

8.3.3 Impact simulations of SPS beam in a copper target

This section presents simulations of an SPS-type beam of 288 bunches with $1.15 \cdot 10^{11}$ p+/bunch at 440 GeV irradiating a copper target. Three different beam size at the impact point are considered $\sigma_{rms} = \sigma_x = \sigma_y = 0.5$ mm, 0.2 mm and 0.1 mm. The beam bunch separation is 25 ns;

the total beam time is 7.2 μs. The target is a solid block of copper with an uniform density of 8.93 g/cm^3. The target has a cylindrical shape with a total length of 1.5 m and a radius of 5 cm. The beam impacts on the center of the front side and follows the direction of the cylinder symmetry axis. The simulation has an axial symmetry that will be exploited in FLUKA and BIG2 geometries to reduce the problem complexity.

As a comparison, Figures 8.15 show simulations in which hydrodynamic motion was not simulated. These simulations have been done using only FLUKA. No 'hydrodynamic tunnel effect' is expected. The penetration length for each case is: 49 cm for the $\sigma = 0.5$ mm and 69 cm for $\sigma = 0.1$ mm. These simulations are the baseline with which the following simulations (with hydrodynamic motion) have to be compared.

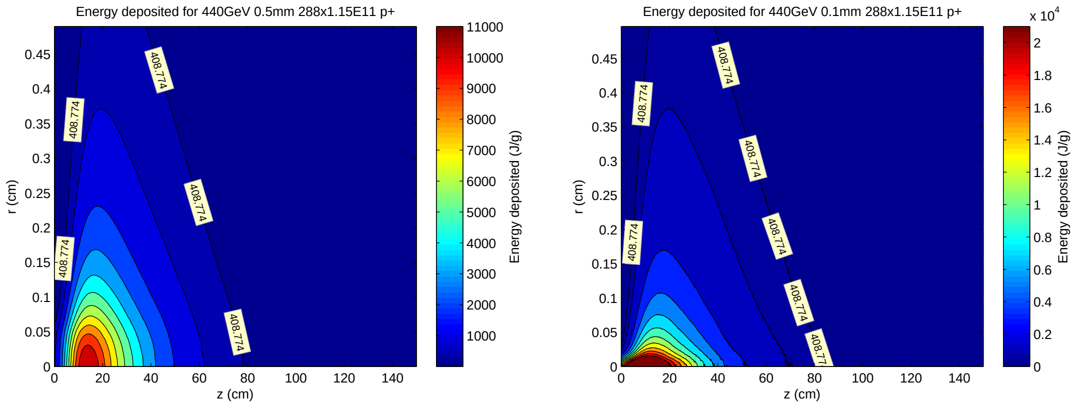

(a) $\sigma_{beam} = 0.5\ mm$

(b) $\sigma_{beam} = 0.1\ mm$

Figure 8.15: Energy deposition for a proton beam of $288 \cdot 1.5 \cdot 10^{11}$ protons at 440 GeV by FLUKA only (No BIG2).

The BIG2 hydrodynamic calculations have been done using a semi-empirical equation of state for copper [84, 85, 86]. The equation of state is a set of values of thermodynamic parameters (pressure, temperature, density) defined for different states of the matter of a material.

The time for which the hydrodynamic simulations are run using BIG2 was set to 1 μs. The time step was chosen so that the maximum density change in copper does not exceed 15%-20%.

Figure 8.16 shows the energy deposition profile on the copper target for different times. The peak energy deposition moves with time along the beam axis. Particle showers develop further inside the target due to the decrease in density along the beam path. The beam heated region expands with time, resulting in a decrease in energy density.

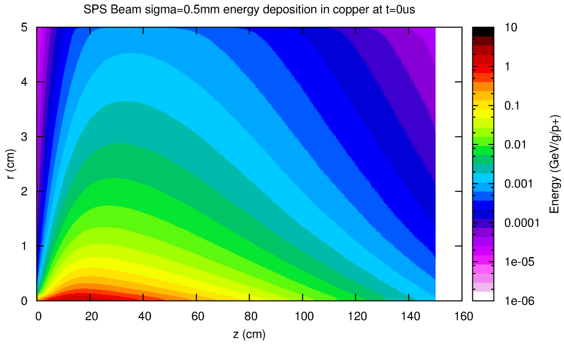

(a) Energy, $t = 0\mu s$

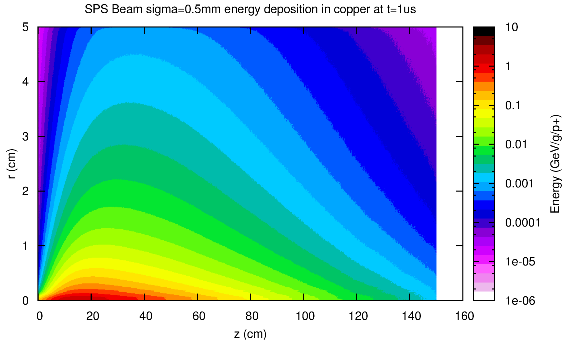

(b) Energy, $t = 1\mu s$

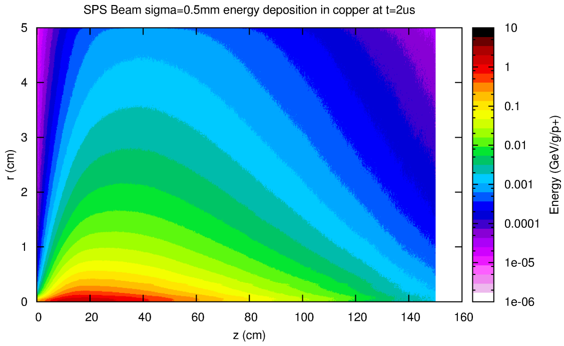

(c) Energy, $t = 2\mu s$

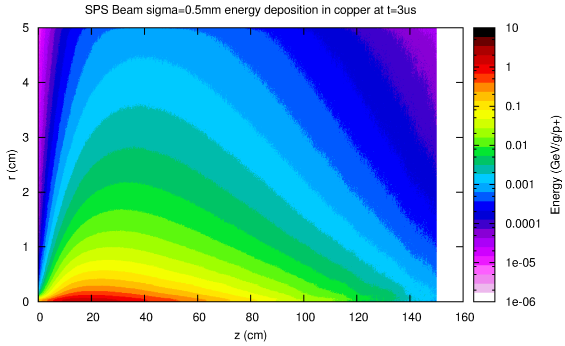

(d) Energy, $t = 3\mu s$

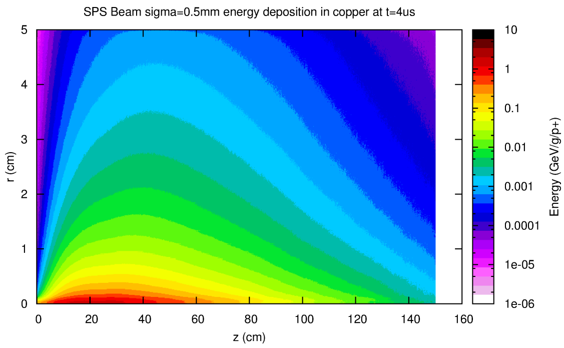

(e) Energy, $t = 4\mu s$

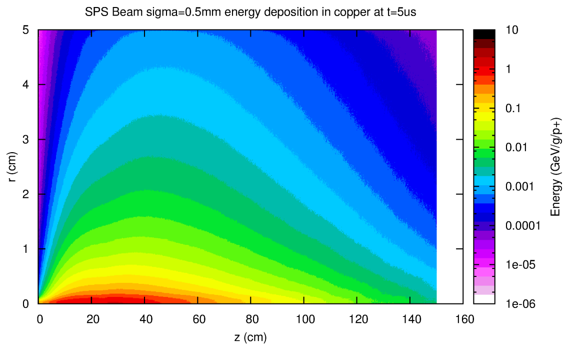

(f) Energy, $t = 5\mu s$

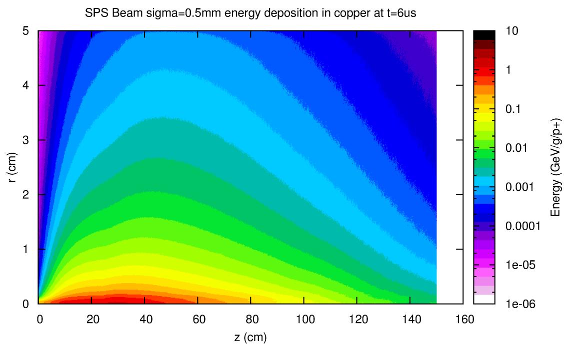

(g) Energy, $t = 6\mu s$

Figure 8.16: Energy deposition evolution in $(GeV/g/proton)$ calculated by FLUKA for SPS beam in a copper target.

Initially, the heated region covers ≈ 75 cm in the longitudinal direction with a peak energy density of ≈ 2.1 GeV/g/p+; after 6 μs the heated region has extended to ≈ 100 cm while the peak energy density has decreased to ≈ 1.4 GeV/g/p+.

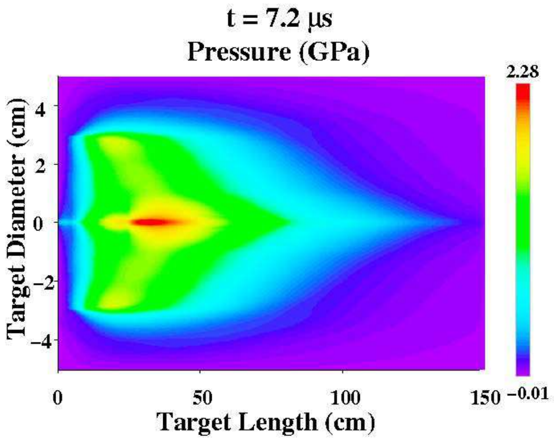

(a) Pressure, $t = 7.2\mu s$

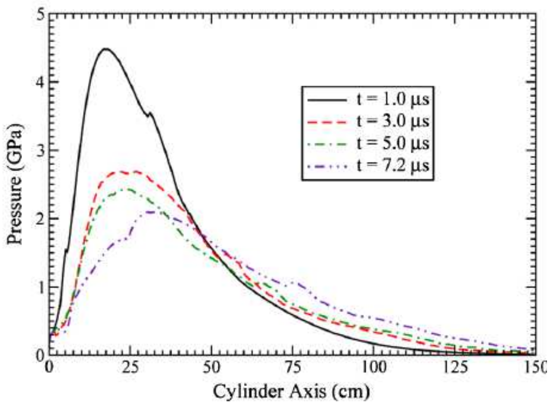

(b) Pressure evolution.

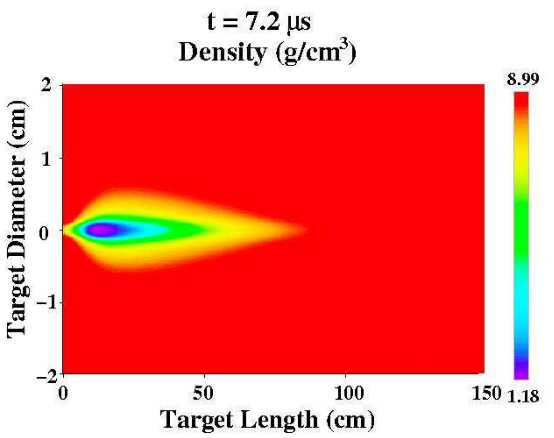

(c) Density, $t = 7.2\mu s$

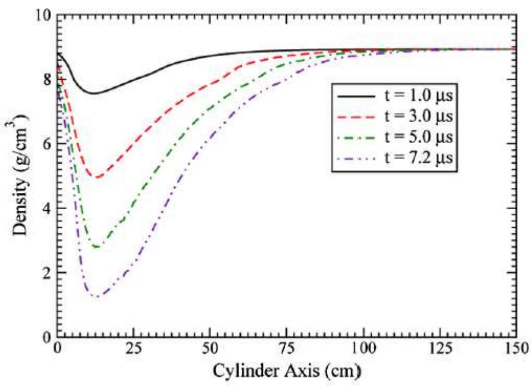

(d) Density evolution.

Figure 8.17: Pressure (GPa) and density (g/cm^3) evolution calculated by BIG2 for SPS beam in a copper target.

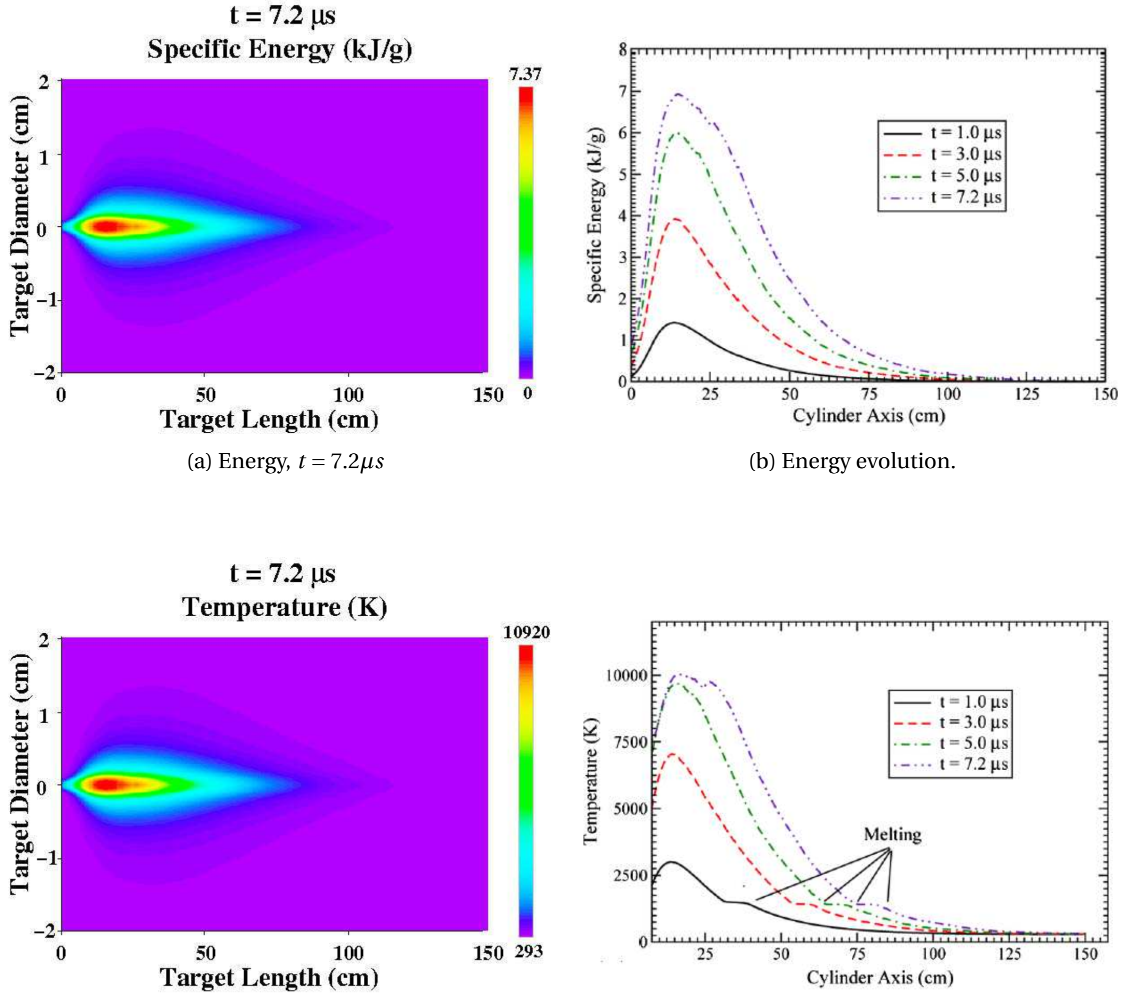

(a) Energy, $t = 7.2\mu s$

(b) Energy evolution.

(c) Temperature, $t = 7.2\mu s$

(d) Temperature evolution.

Figure 8.18: Specific energy deposition (KJ/g) and temperature (K) evolution calculated by BIG2 for SPS beam in a copper target.

The specific energy deposition (KJ/g) increases with time (as it happened with carbon) because the density decreases faster than energy is deposited ($GeV/cm^3/proton$) and so the ratio between them increases.

The maximum temperature of the target at 7.2 μs is ≈ 10000 K = 0.86 eV. The fast and concentrated deposition of energy around the target axis provokes a sudden temperature rise ($\delta T_{7.2\mu s-1\mu s} \approx 7000K$) and also creates a compression pressure wave ($\approx 2-4GPa$). The pressure evolution with time that can be seen in Figure 8.17. At 12 μs the pressure wave reaches the lateral surface of the cylinder and bounces back into the target. The surface wall starts to vibrate. At 14 μs the pressure wave has completely bounced back and a negative pressure (restoring force) appears near the surface. The tensile strength of the material tends to restore the target boundary back into its original position. The core of the target develops a negative pressure due to the stretching of the material in that region as a consequence of the pressure wave propagating radially.

The pressure wave is attenuated with time, at 7.2 μs the peak pressure is ≈ 2.28 GPa after 12 μs the peak pressure decreases to ≈ 0.8 GPa, reaching ≈ 0.11 GPa at 20 μs. At a certain point the target enters the plastic regime and the material will stop behaving linearly (strain ($\mu m/m$) no longer proportional to stress). In the plastic regime, pressure waves propagate at a speed lower than the sound speed in the material.

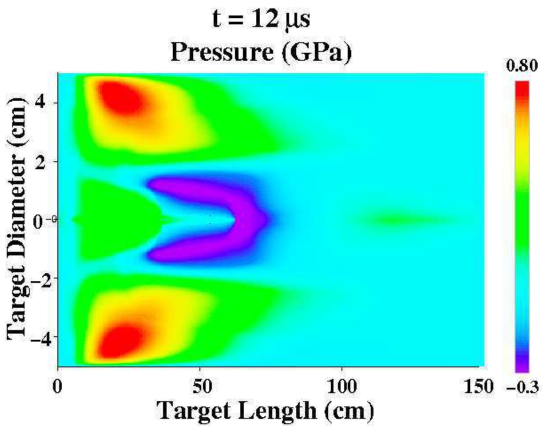

(a) Pressure, $t = 12\mu s$

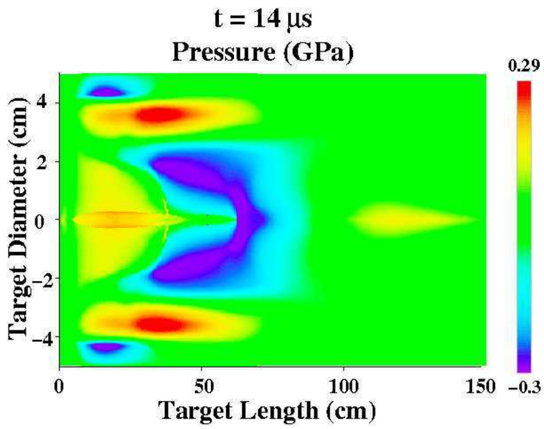

(b) Pressure, $t = 14\mu s$

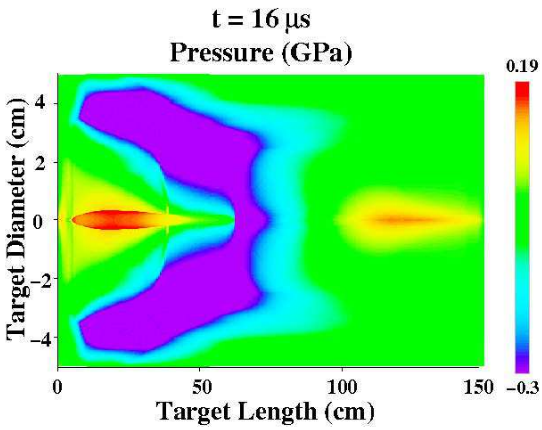

(c) Pressure, $t = 16\mu s$

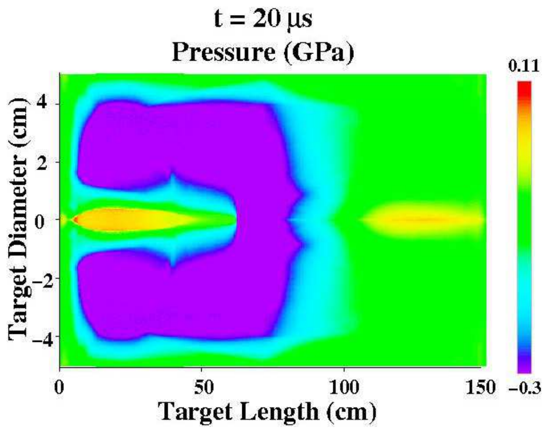

(d) Pressure, $t = 20\mu s$

Figure 8.19: Pressure evolution calculated by BIG2 for SPS beam in a copper target. (GPa)

The constant temperature regions shown in Figure 8.18 are regions of the target in which a change of phase liquid-gas occurs. The region above that line are in gaseous or plasma state.

At 1 μs the front of the melted region is at 40 cm. At 3 μs it reaches 60 cm, at 5 μs 70 cm and at 7.2 μs it reaches ≈ 81 cm. From the plot of the density evolution with time, it is possible to obtain the speed at which the molten region expands ('penetration speed'). After the initial 5 μs, the penetration speed becomes constant and has a value of ≈ 5 cm/μs.

At 7.2 μs the peak temperature along the beam axis is ≈ 10000 K = 0.86 eV. The density in that region has decreased to 1.18 g/cm^3 that is about 10% of the solid density. The pressure is approximately 15 kbar. Considering those values of temperature, density and pressure, the matter in that region is in the form of strong coupled plasma ($\Lambda << 1$).

Figure 8.19 shows the evolution of the pressure in the target after the beam is switched off. The pressure wave in the target are not amplified after the beam stops. The copper target will survive the impact of the SPS beam with the exception of the central part that will suffer severe damage.

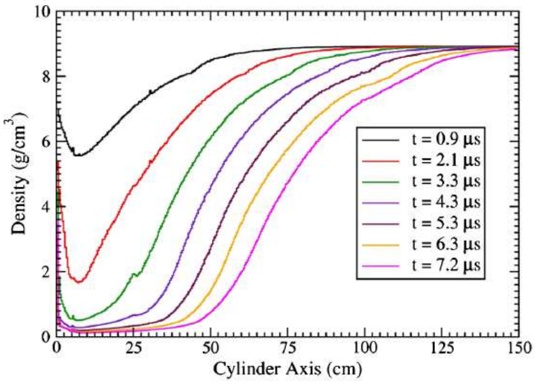

Figure 8.20: Density (g/cm^3) evolution calculated by BIG2 for SPS beam ($sigma = 0.1$ mm) in a copper target.

The "hydrodynamic tunneling effect" can be seen in Figure 8.17. The density profiles show an initial low density region (1 μs) that extends with time. This effect is more pronounced for smaller beam sizes. For the same SPS beam but with a beam size 5 times smaller ($sigma =$ 0.1 mm) the hydrodynamic tunneling develops faster (see Figure 8.20). The expansion velocity ('penetration speed') of the melted region is ≈ 8 cm/μs. A reduction of 5 times the beam size, reflects into a 60% increase of the penetration speed (all other simulation parameters are equal except for the iteration time step).

The von Mises parameter M indicates whether or not the region remains in elastic regime. Figure 8.21 shows the von Mises for a $\sigma = 0.5$ mm SPS beam in copper. During the first 14 μs the solid part of the cylinder may remain in the elastic regime ($M \leq 1$). However, at 19 μs a large area of the target has entered into the plastic regime ($M \geq 1$).

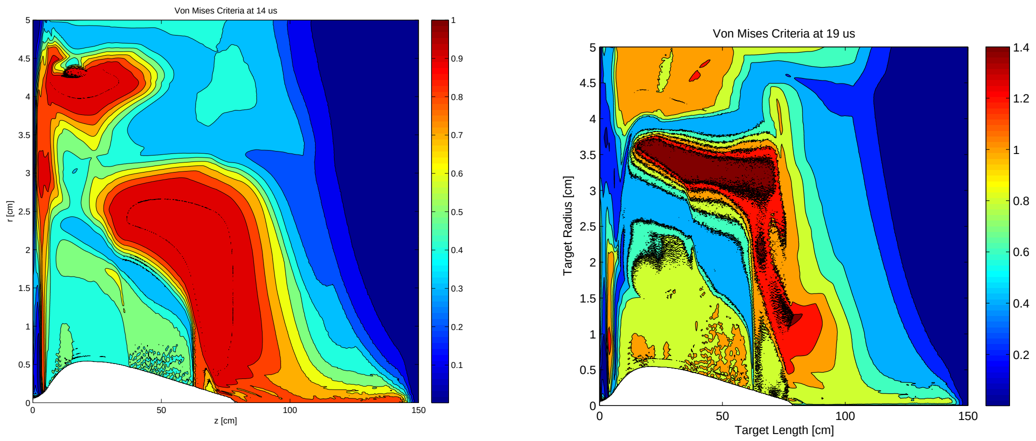

(a) $t = 14\ \mu s$ (b) $t = 19\ \mu s$

Figure 8.21: Von Mises parameter.

8.4 Conclusions

- The damage potential (range) of high intensity high dense beams (LHC type, SPS type, etc.) is much greater than traditional energy deposition simulations suggest due to "Hydrodynamic tunneling".
- Understanding the real damage potential of high intensity high dense beams (ex. LHC beams) is crucial for a correct Machine Protection assessment.
- The impact of the full LHC beam $3.2 \cdot 10^{14}$ p+ /bunch at 7 TeV in carbon may have a real penetration range of 25 m and hence TDDQ collimator may not stop the whole beam in case of accident.
- LHC and SPS simulations show the 'hydrodynamic tunneling effect'.
- An experiment at HiRadMat with the SPS parameters would validate the SPS simulation results and would give more confidence to the LHC results.

9 Tunneling Experiment

Extensive simulation studies of the full impact of the ultra-relativistic proton beam generated by the Large Hadron Collider (LHC) on solid targets of different materials of interest have been presented in the last chapter. Simulations predict that LHC protons can penetrate between 10–40 m [70]. This large penetration length is due to a density depletion channel created along the beam axis (hydrodynamic tunneling effect). If confirmed, this will have an important impact in machine protection: damage thresholds, protection thresholds, damage assessment, spare equipment...

Therefore, the experimental verification of the numerical simulations is very important from the machine protection point of view. However, this is not possible with the LHC beam. Already in 2005, a beam impact experiment [69] was performed in the CERN-SPS TT40 extraction line. Up to $8 \cdot 10^{12}$ p+ were shot onto a target and the onset of damage was measured. FLUKA simulations and experimental observations agreed, however these results cannot be extrapolated to LHC regime since the beam intensity was far below the onset of hydrodynamic tunnelling.

For this purpose, an experiment [87] was performed, during summer 2012, at an experimental facility named HiRadMat (High Radiation Materials). This facility allows to study High Energy Density physics as the provided energy density is high enough to create plasma in the core of materials such as copper or tungsten and to produce strong enough shock waves that creates a density depletion channel along the beam axis (hydrodynamic tunneling effect). To assist designing of suitable experiments, extensive numerical simulations of heating of solid copper cylinders using the SPS beam were performed. Hydrodynamic tunneling effect is also clearly observed in these simulations. Confirmation of the existence of this phenomenon in the HiRadMat experiments will partially validate the simulations for the LHC beam.

The main experimental objective is to reproduce the hydrodynamic tunneling effect observed in simulations. Further objectives are to measure density, temperature and shock waves during the beam-target interaction. However, the success of the experiment was not linked to the operation of the detectors since a thorough investigation of the target after the experiment

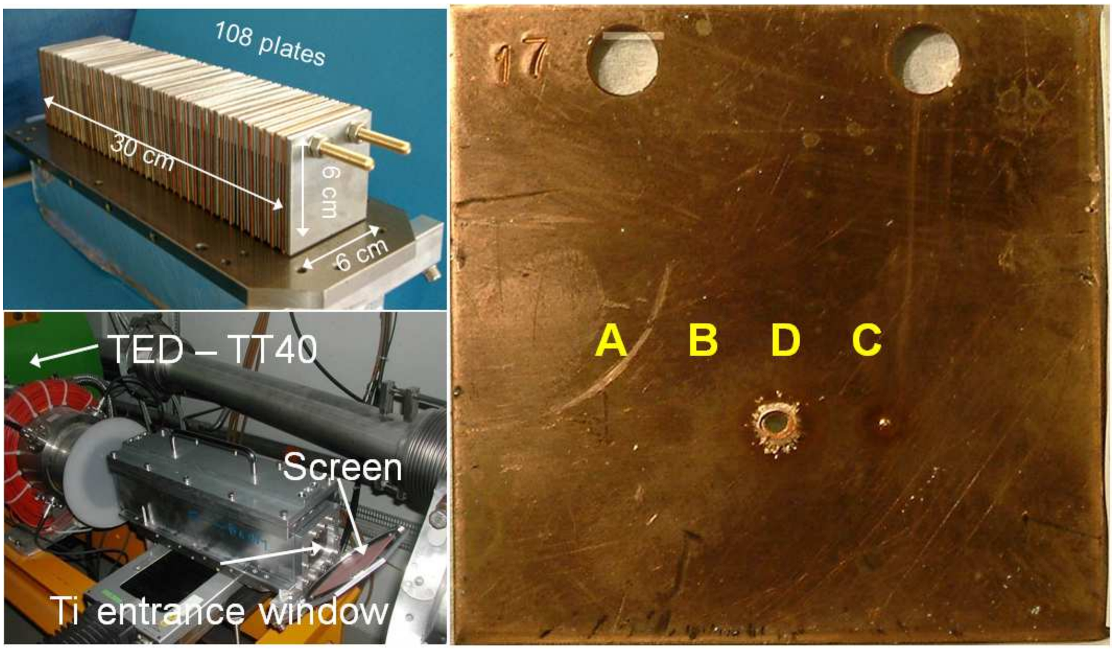

Credit: *V. Kain & R. Schmidt*

Figure 9.1: TT40 experiment.

will show if there was hydrodynamic tunneling. The additional information gathered with the instrumentation will improve the understanding of the experiment.

9.0.1 HiRadMat Beam-Commissioning

On Wednesday 14 September and Monday 19 September 2011, high intensity proton beam was sent for the first time down the HiRadMat primary beam line (thereafter TT66) onto the beam dump located in the HiRadMat experimental cavern. This high intensity beam commissioning followed a first period of low intensity beam commissioning which took place on Wednesday 22 June 2011.

During the low intensity beam commissioning [88], it was checked that all beam line equipment operated as specified. Energy matching and beam steering were performed; optics checks did not reveal any optical errors.

Aperture measurements confirmed that there were no bottlenecks. A typical beam with a 1σ radius of 0.5 mm at focal point 1 was used. Orbit oscillations were induced for both vertical and horizontal planes using two corrector magnets, at the beginning of TT60 line. Two beam current transformers, one at TT60 line and the other at the end of TT66 line were used to monitor any possible loss of particles. In addition, the signal from the BLM along the line was also monitored. The oscillations were induced for 0°, 30°, 60°, 90°, 120°, 150° and 180° and for different amplitudes raging from -10σ up to 10σ [89, 90, 91]. No significant intensity decrease has been observed between the two fast current transformers and no beam losses above background have been detected with the beam loss monitors.

Figures 9.2-9.3 show a comparison between the oscillations measured and the expected values from simulations for the horizontal and vertical plane at two different phase advance.

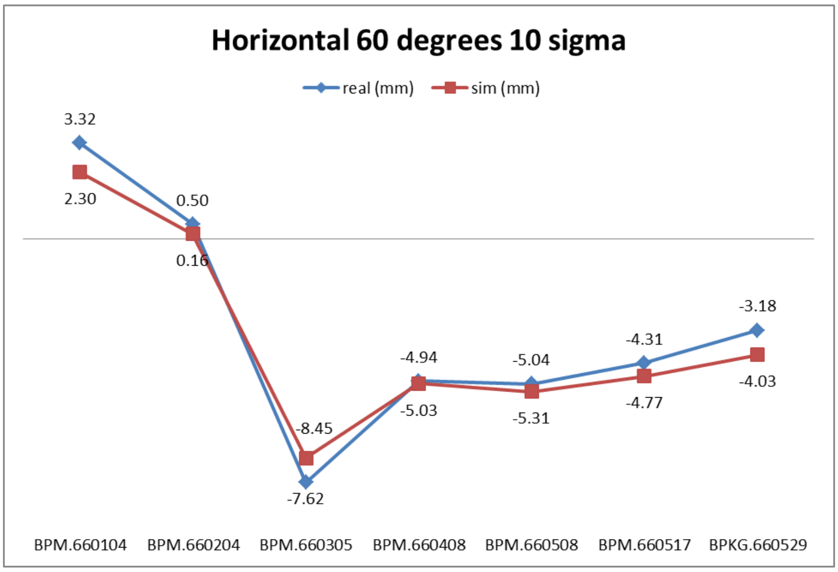

Figure 9.2: Betatron oscillation: simulation and measurement for the horizontal plane.

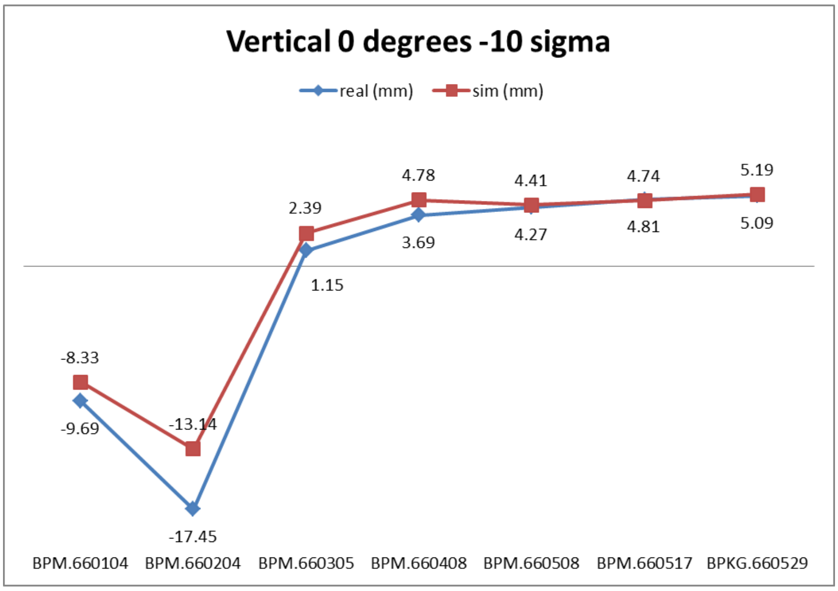

Figure 9.3: Betatron oscillation: simulation and measurement for the vertical plane.

Radiation protection monitoring worked as expected and the measurements were within expectation. Only LHC Pilot type beam of about $\sim 8 \cdot 10^9$ p+ was used during this low intensity beam commissioning. It is to be noted that pulses were only sent on request; a total of $\sim 3.4 \cdot 10^{12}$ p+ were sent to the HiRadMat beam dump during the commissioning period. The checks performed during the beam commissioning are summarized below.

During the high intensity beam commissioning [92, 93], pilot bunches were sent down the beam line to check the trajectory and re-establish the low-intensity commissioning reference. The MKE kick was re-synchronized (Figure 9.4), using 12 bunches, before extracting into the beam line. Up to 4 batches of 36 bunches were sent through TT66. The trajectory was checked and found to be very similar to the reference trajectory recorded during the low intensity beam commissioning.

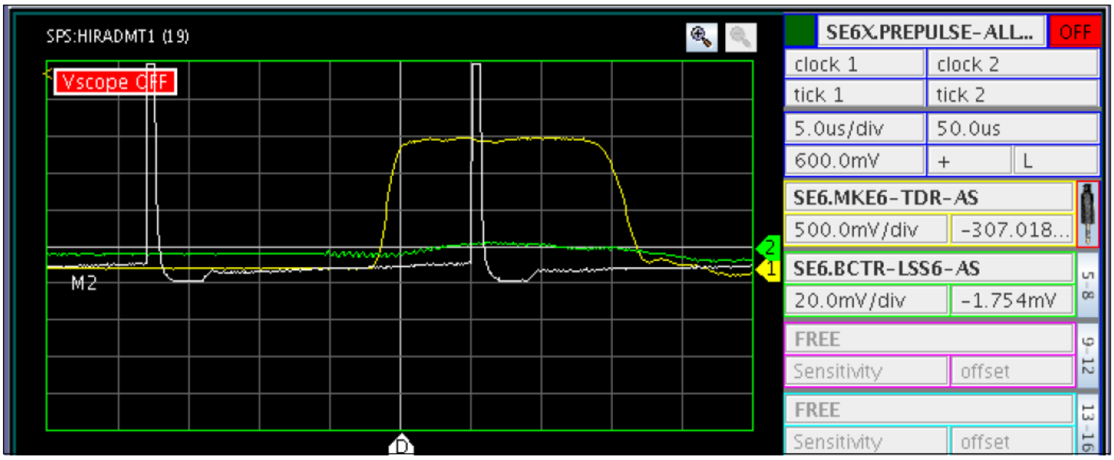

Figure 9.4: Kicker application. White signal shows 12 bunches.

9.1 Experimental Setup

9.1.1 Target

The experiment consist of three copper targets. Each target is composed of 15 cylinders of 4 cm radius and 10 cm length. The total target length of 150 cm is longer than the maximum penetration length of 450 GeV protons into copper plus a safety margin for a 0.1 mm σ beam. The radius of the target has been chosen as a compromise between material cost, target weight, maximum pressure at the border and radioactive waste. 4 cm radius ensures that even for the most extreme beam parameters (288 bunches of 1.15 protons per bunch with a 0.1 mm σ beam) the ultimate tensile strength is not exceeded. In between the cylinders there is a 1 cm gap. This gap has no impact on the transverse hydrodynamics and particle interaction thus giving a way to inspect the effects of the beam in the target along the longitudinal dimension. The three targets are placed, side by side, parallel to the beam direction. Figure 9.5 shows the target structure.

The first target is used to get a reference scenario in which no hydrodynamic tunneling is expected. The other two targets are irradiated with two different beam intensities in which tunneling is expected.

The three targets are enclosed into an aluminum sleeve which embraces them. The thickness of the sleeve is 2 cm with a 1 cm longitudinal indent on the top and bottom plate that accommodates the copper cylinders. The sleeve is made in two pieces: upper and lower; the two pieces are fixed one to the other with a set of closures on the perimeter. Each piece has two aluminum mushrooms that can be caught by the crane. The first set is used to move the whole setup while the second set is used to raise the upper part and expose the copper cylinders. The target can be remotely opened with the crane and then inspect the copper cylinders with the help of the cameras installed on the crane.

For the HiRadMat experiment, it is important not only to know that the lateral side of the target will survive the beam irradiation but also to understand what happens on the front and rear sides of the target. The front side of the cylinder is where the beam impacts. The experiment will not have a beam window on the front and rear sides; the front and rear faces of the cylinders will be directly exposed to the air. Any kind of contamination from the target to the facility has to be avoided.

It was studied the hydrodynamic evolution of the first copper block of the target being irradiated with an SPS-type beam of 288 bunches with $1.15 \cdot 10^{11}$ p + /bunch at 440 GeV. Figure 9.6 shows the profiles of temperature, pressure, density and surface velocity along the first 10 cm of the first copper block at 4.5 μs.

After 4500 ns, $\approx$ 180 bunches, the peak temperature on the front face of the first copper cylinder has reached $\approx$ 3280 K so the material is mostly in the expanded hot liquid state ($\rho = 6.6\,\mathrm{g/cm^3}$) with very little gas bubbles. The surface velocity reaches a maximum of 58 m/s at 13 μs and then decreases. At 17 μs it has decreased to 37 m/s. For longer times, the surface velocity may reach a point where it becomes negative (surface vibrates).

Figure 9.7 shows the surface velocity profile of the front and rear sides of the first copper block. The cohesion forces of the liquid might make it remain together however the physics of BIG2 for this regime is not very accurate [94]. Liquid copper splashes are not excluded and therefore an aluminum protection structure needs to be installed to capture them. Gas bubbles will solidify in contact with the aluminum structure. Quickly after the beam is switch off, the melted region at the beginning of the target will solidify preventing additional splashes.

The front and rear sides of the target are closed with a 5 mm aluminum structure that has three cylinders of 4 cm radius and 18.5 cm length. Figure 9.8 shows the aluminum protection structure at the front side. The cylinders are aligned with each of the three targets. Each cylinder has a 0.5 cm radius hole that allows the beam to pass through. In case liquid copper is ejected from the target the aluminum structure will prevent any contamination to the facility. An aluminum foil was wrapped around the aluminum structure, adding an additional protection against contamination from ejected material (see Figure 9.9).

Phase	Position	real position (mm)
Beam line setup	OFF-POSITION	1
Irradiation target 1	TARGET1	82.90
Irradiation target 2	TARGET2	167.66
Irradiation target 3	TARGET3	249.68
LIM+ 3	OUTER LIMIT	252

Table 9.1: Table positions.

The experiment is installed on the third position at HiRadMat. The third position gives the biggest ratio of $\sigma_{\text{TT66 window}}/\sigma_{\text{table 3 focal spot}}$, meaning that, while respecting the constrains of the transfer line beam window, a greater beam intensity than nominal is achievable if necessary.

9.1.2 Experimental table

The target [61, 94] is mounted on a movable table made of aluminum. Aluminum was chosen due to its relatively low activation and good mechanical properties. Figure 9.10 and Figure 9.11 show the table assembly. The table is equipped with three articulated arms attached to the side. These arms can be regulated to achieve different positions (x,y) in the perpendicular plane. Each arm will host one diamond detector that will be introduced later. The table is equipped with a DC motor that regulates the lateral displacement of the table. There are four predefined positions. Table 9.1 shows the relation between the experimental phases, the predefined positions and the real lateral position of the table.

The table position is controlled by reading the resistance of a linear potentiometer. The potentiometer is fixed to the moveable table so the a change in lateral position is translated into a change in resistance. For safety reasons, the maximum allowable, in and out, limits of the table are interlocked via bumper switches. All controlled signals are routed to the surface control room, in BA7, and connected to a PLC that implements the logic. The PLC is only accessible through the CERN technical network.

The table is mounted onto a stainless steel support provided by the HiRadMat team. The whole setup: support table, experimental table and experiment target are aligned on the surface with an instrumentation laser. The support table assures that the alignment done on the surface is preserved after lowering the whole setup to the experimental cavern.

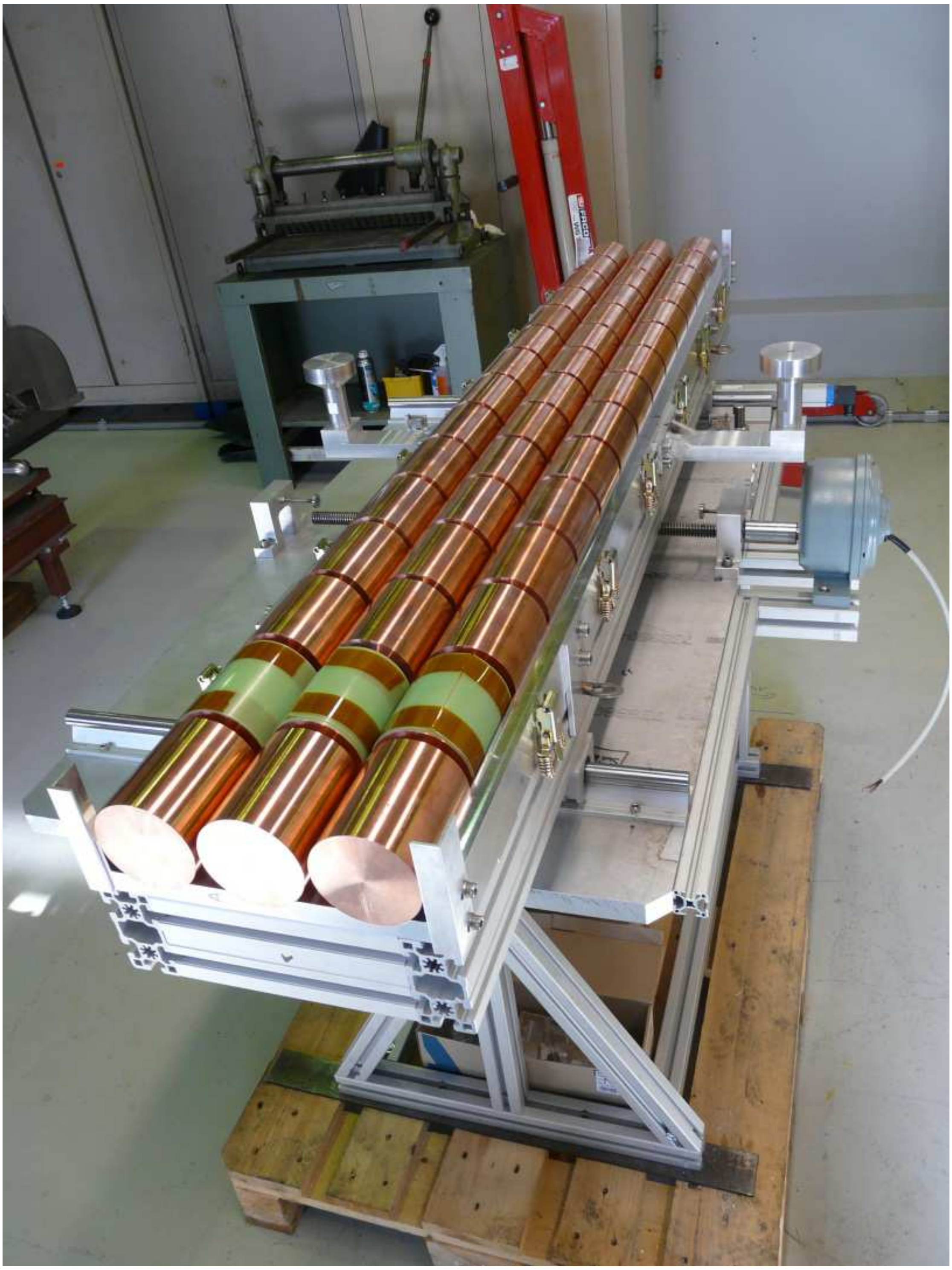

Figure 9.5: Interior view of the target.

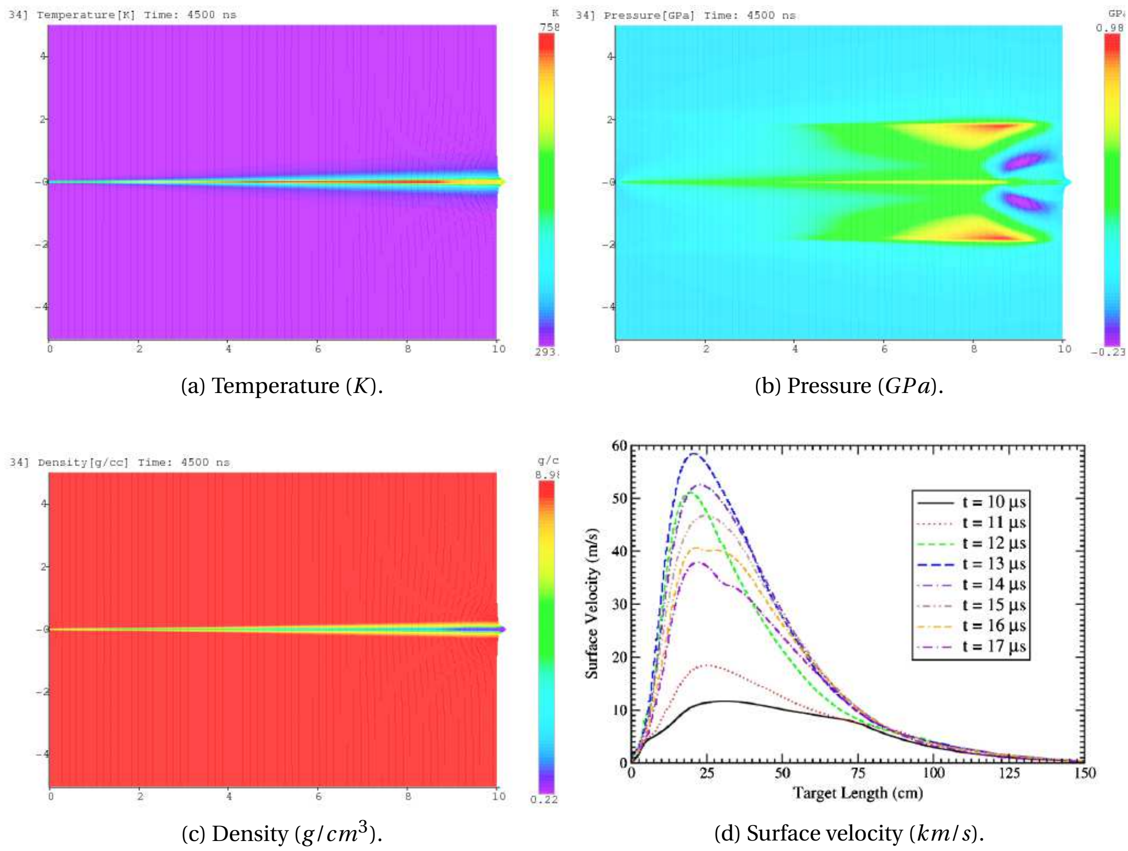

(a) Temperature (K).

(b) Pressure (GPa).

(c) Density (g/cm^3).

(d) Surface velocity (km/s).

Figure 9.6: Temperature, pressure, density and surface velocity profiles along the first copper block at 4.5 μs.

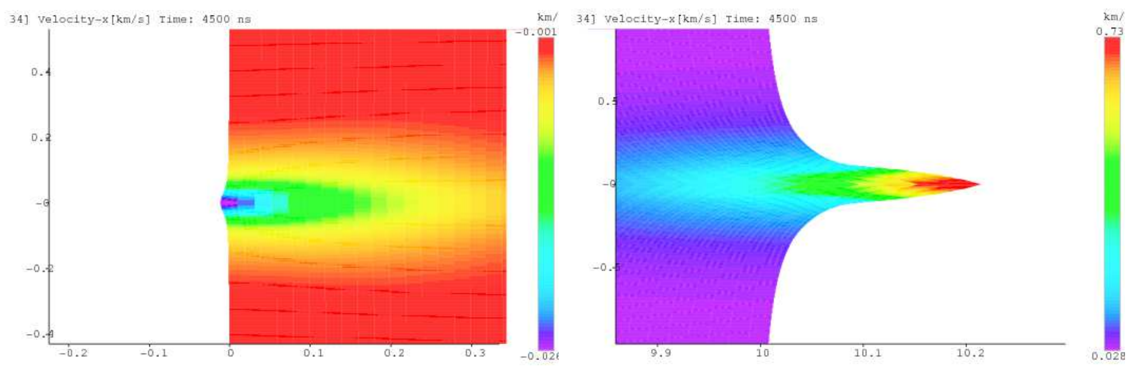

(a) Front side of the first copper block.

(b) Rear side of the first copper block.

Figure 9.7: Surface velocity km/s on the lateral sides of the first copper block after 4.5 μs.

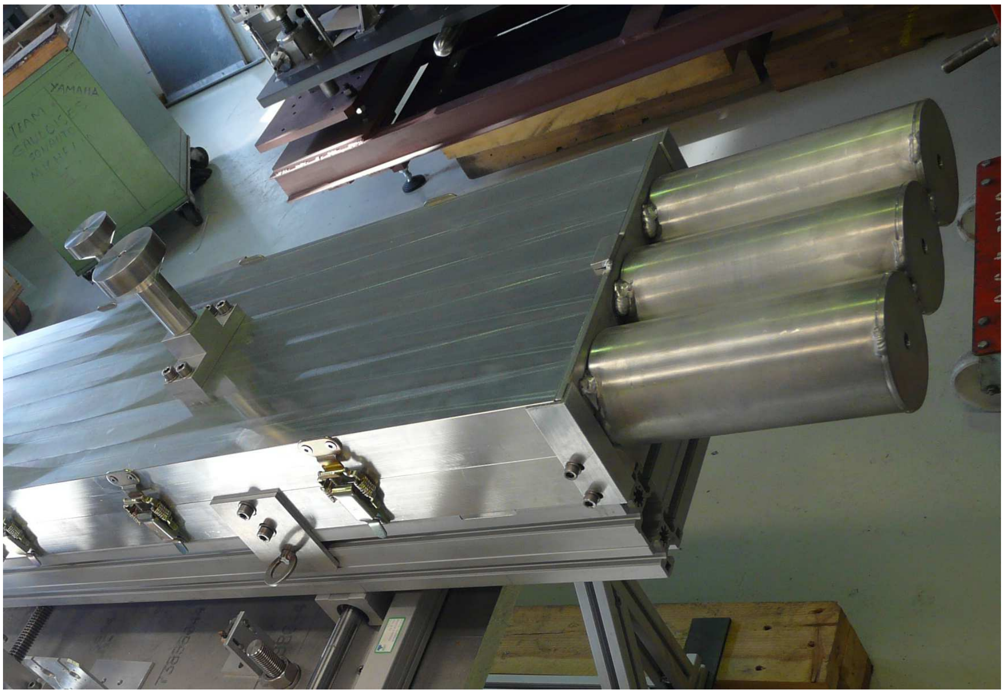

Figure 9.8: Aluminum protection cylinders

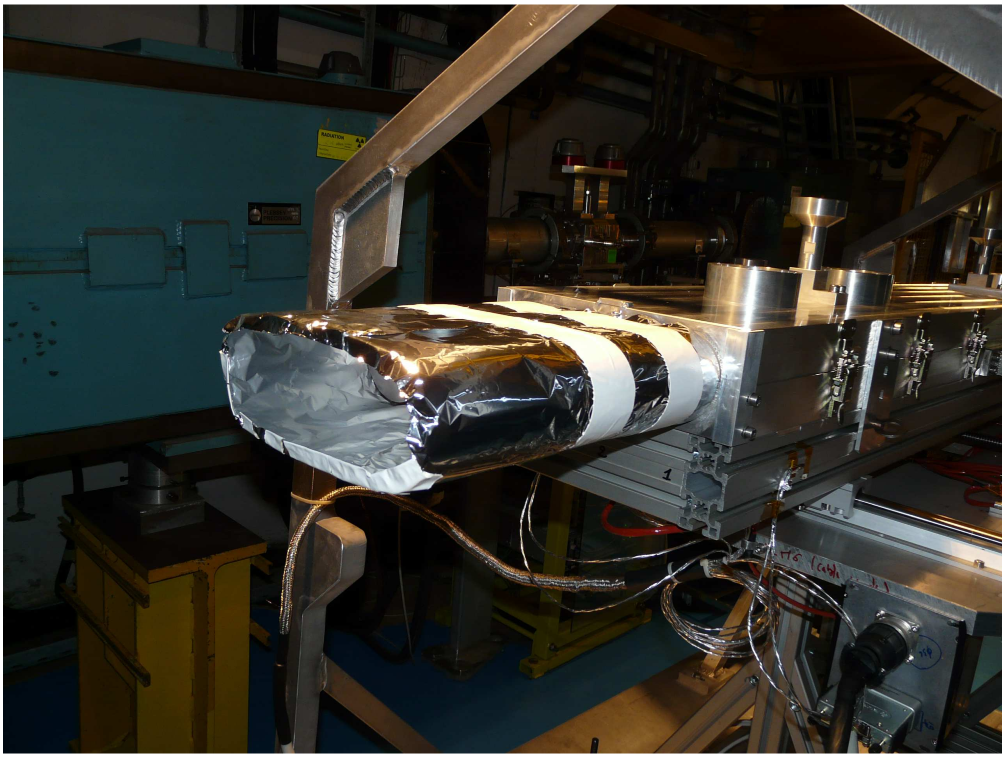

Figure 9.9: Aluminum foil added around the protection cylinders.

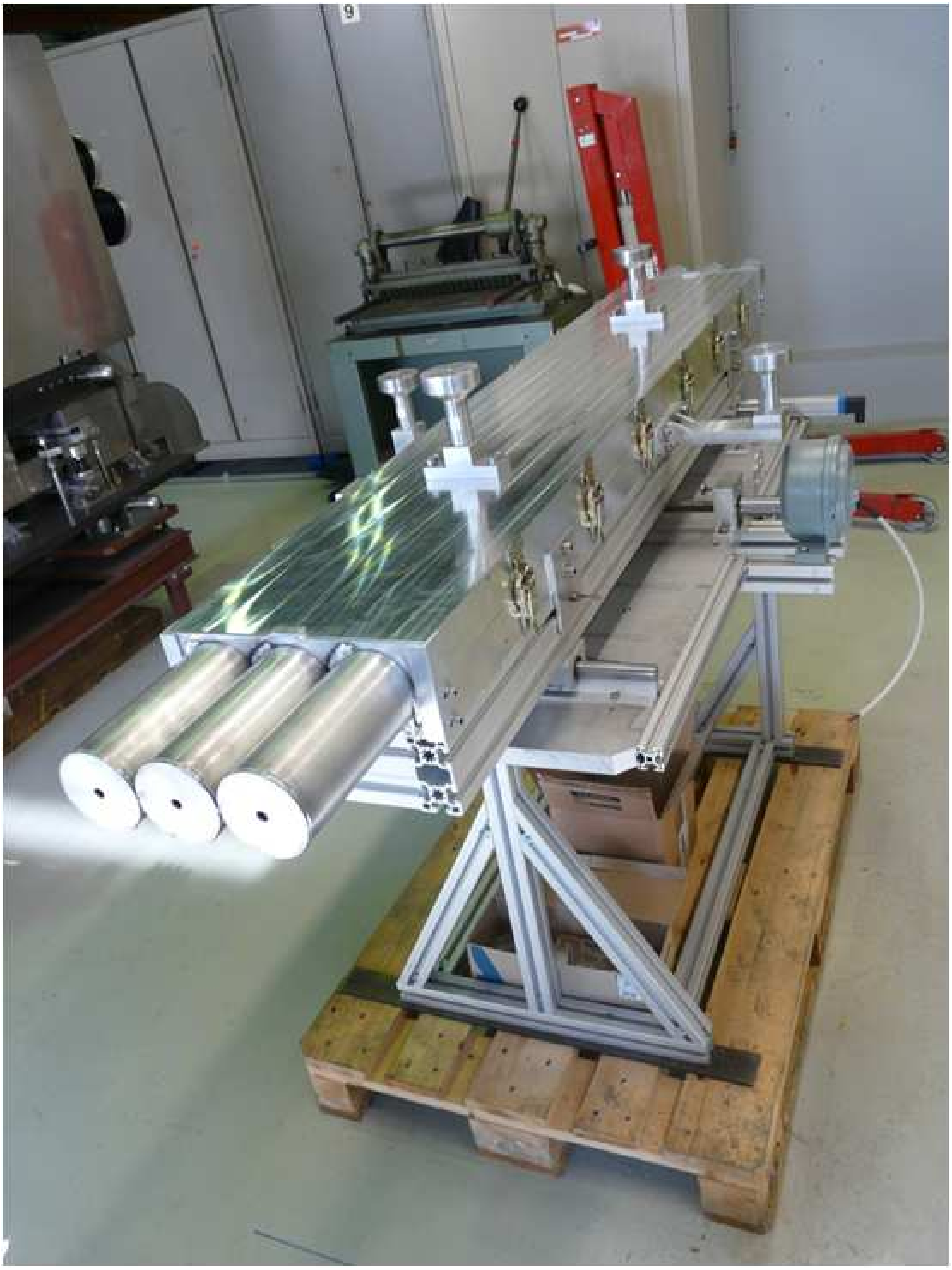

Figure 9.10: Target assembly.

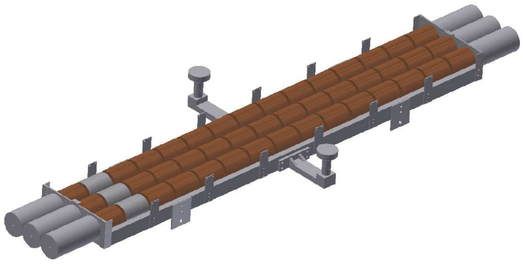

(a) 3D view of the copper blocks.

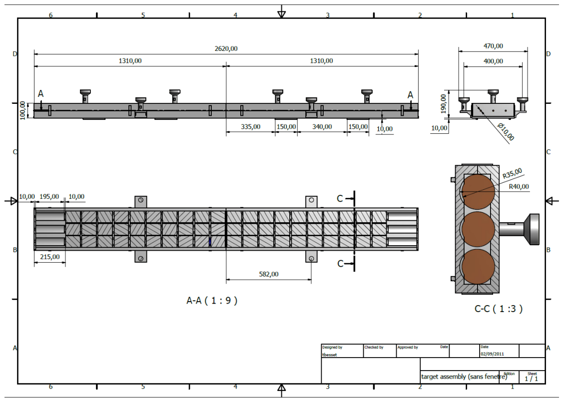

(b) Schema of the target.

Figure 9.11: Target design.

9.2 Experiment Detectors

The main objective of the experiment is to reproduce the conditions achieved in simulations that result in hydrodynamic tunneling and observe the result. After the irradiation, the target is altered due to the effects of the hydrodynamic tunneling. As already explained, the target and its support table is design in way that allows to be opened for inspection. The main results form the experiment come from the analysis of the target and its comparison with the simulations.

In parallel, several detectors are installed around the experiment. The idea is, if possible, to gather as much information as possible during the beam interaction time. The objective is to not only see the final results of the tunneling effect but to follow the evolution of the target in real time. This information is very valuable for the validation of the simulations as it provides some information of the status between the initial and the final state.

9.2.1 Diamond detectors

Diamond is known as the hardest substance on earth and women best friend, its hardness is a consequence of its uniquely stable structure in which each atom form four covalent bonds with the neighboring carbon atoms. Carbon atoms are arranged in a variation of the face-centered cubic crystal structure called a diamond lattice. Due to this, diamond has extraordinary properties: hardness, thermal conductivity, optical properties that make diamond the most popular gemstone. Among other properties, diamond has the highest melting point of any material.

Most natural diamonds are formed at high temperature and pressure at depths of 140 to 190 kilometers in the Earth's mantle. Carbon-containing minerals provide the carbon source, and the growth occurs over periods from 1 billion to 3.3 billion years (25% to 75% of the age of the Earth). Diamonds are brought close to the Earth's surface through deep volcanic eruptions by a magma, which cools into igneous rocks known as kimberlites and lamproites.

In the early 40's experiments with natural diamonds and alpha particles revealed a new field of application as particle detectors. However, natural diamonds and their quality and properties are not uniform. For this reason artificial diamond techniques were pursued. High Pressure High Temperature (HPHT) technique was developed in 40's-50's allowing to transform graphite into diamond. In the late 70's, a new technique, Chemical Vapor Deposition (CVD), was developed. A gas with high carbon content is decomposed; diamond crystals grow on a substrate. At first, only polycrystalline CVD (pCVD) diamonds were possible but after several technological improvements, high purity single crystalline CVD (scCVD) were created in the year 2000.

Due to the growth process, in which synthetic diamonds grow on a substrate, grains are very small close to the substrate and get bigger up to sizes of hundreds of microns the farther from the substrate. Figure 9.12 shows a 100 μm pCVD diamond in which the crystals that have formed near the substrate are smaller than those on the surface. The grain size directly affects the response behavior of the diamond.

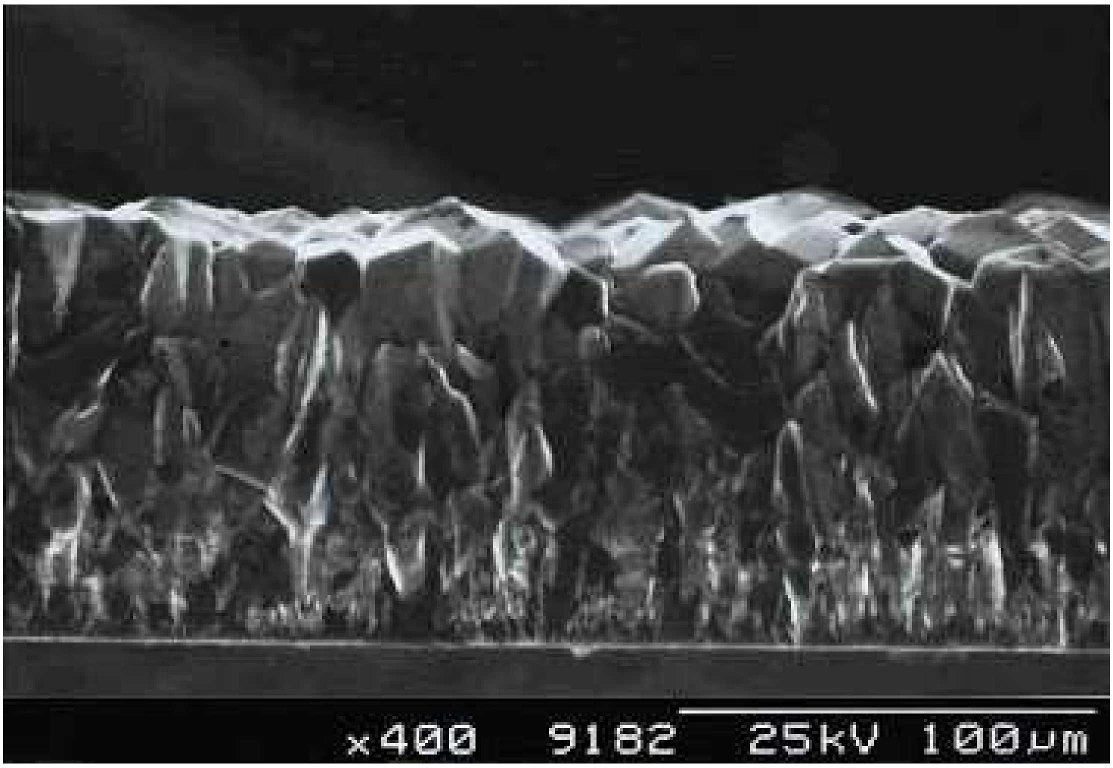

Credit: *University of Bristol*

Figure 9.12: pCVD diamond grain size growth.

Working principle

As a solid, diamond electron and hole states can be described by the energy band model. The energy band gap, that is the energy in between the conduction and the valence band, for diamond is 5.5 eV therefore, diamond is considered an insulator. As an insulator, there is a negligible concentration of carrier electrons in the conduction band at room temperature 300 K. Figure 9.13 show a simplified model of electronic band structure for an insulator. If enough energy is transferred, electrons in the valence band can be excited to the conduction band. These electrons, and holes created, can be collected if an electric field is applied across the diamond.

When a charged particle crosses the diamond detector it loses energy mainly due to Coulomb interactions (Bethe equation). If enough energy is transferred from the incident particle to the valence electrons, electron-hole pairs are created at the point where the energy is loss. Generated electrons and holes are accelerated towards the electrode by the electric field. Electrons drift towards the positive electrode or anode while holes drift towards the

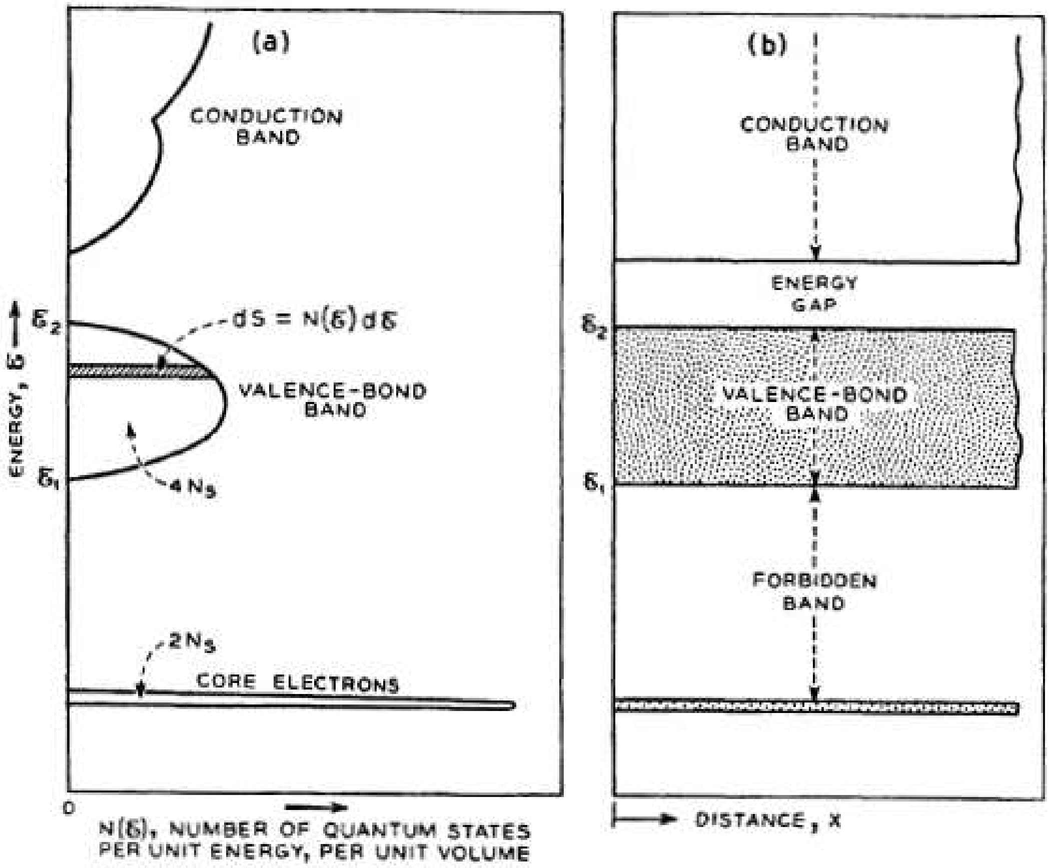

Credit: *H. Spieler*

Figure 9.13: Band gap, valence electrons and core electrons of an insulator [5].

negative electrode or cathode. Typical electric field values used for pCVD are around $1\,\text{V}/\mu\text{m}$. Figure 9.14 shows the e-h generation process.

A Minimum Ionizing Particle (MIP) crossing a diamond detector creates $36\,\text{e}-\text{h}/\mu\text{m}$. A MIP is a particle whose mean energy loss rate through matter (stopping power dE/dx) is close to the minimum. The charge collection time of electrons and holes is very fast in the order of nanoseconds. Diamond is a material with a high electron and hole mobility. The charge collection distance (c.c.d.), is the effective collection distance, is a key parameter to calculate the effective signal. The c.c.d. depends on the grain size and its change along the thickness therefore cannot be easily calculated. The smaller the grain size the more trapping effect happens. C.c.d. can be approximated as the sum for electrons and holes of the mean free path when they drift towards the electrodes. The ratio c.c.d over the thickness gives a parameter that can be used to describe the quality of the diamond. This parameter will be refereed as efficiency of diamond as it relates signal given by a pCVD compared to a scCVD detector.

A diamond detector can be modeled as an ideal current source in parallel with a small capacitance (see Figure 9.14). The ideal current source models the signal generated in the diamond

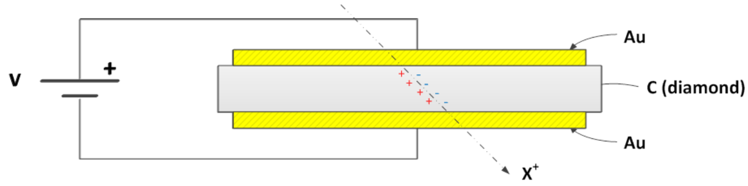

(a) Ionization of a diamond detector.

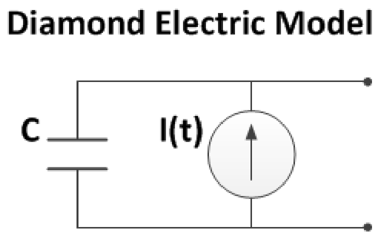

(b) Electrical equivalence of pCVD diamond.

Figure 9.14: Diamond detector.

by the crossing particles. Diamond, as an insulator, with the electrodes has an intrinsic small capacitance.

Characteristics

A brief summary of the relevant properties of diamond detectors [95]. Diamond has a relatively wide band gap that translates into a low leakage current (DC current). On the other hand, the high band gap makes the required ionization energy to create an electron-hole higher hence the produced signal is relatively low. The high electron and and hole mobility translates into a fast response of the detector.

The low dielectric constant gives a low capacitance. This contributes to the fast response of the whole detector. The high thermal conductivity helps spreading the energy deposited in the diamond along the whole volume. Due to the high displacement energy needed, diamond can be considered radiation hard. The sensitivity of the detector is proportional to the square root of the energy needed to create an e-h pair, giving a good sensitivity for diamond.

scCVD diamonds give higher and longer signal per charged particle, than pCVD. The signal's shape depends on the particle type.

Implementation

The experiment will be irradiated with several 10^{13} p+ during all the duration of the experiment. FLUKA simulations point to a high fluence of secondary particles around the target. Any detector or electronic system placed in the experimental area must be radiation tolerant. Also, the fluence of particles around the target varies with time as tunneling is intrinsically a dynamic process.

The whole interaction process last only $\sim 7.2\,\mu$s that corresponds to beam length. The detector must be fast enough to react faster than a microsecond. Moreover, the beam is structured in 144 bunches of particles spaced by 50 ns. This implies that, if we want to see the evolution of

Property	Value
Band Gap $[eV]$	5.5
Breakdown field $[V/cm]$	10^7
Resistivity $[Ohm-cm]$	$>10^{11}$
Electron Mobility $[cm^2V^{-1}s^{-1}]$	1800
Hole Mobility $[cm^2V^{-1}s^{-1}]$	1200
Saturation Velocity $[km/s]$	100
Thermal Conductivity $[W/mk]$	~ 2000
Mass Density $[g/cm^3]$	3.52
Atomic Charge	6
Dielectric Constant	5.7
Displacement Energy $[eV/atom]$	43
Energy to create e-h pair $[eV]$	13
Radiation Length $[cm]$	12.2
Spec. Ionization Loss $[MeV/cm]$	4.69
Ave. Signal Created100um $[e]$	3600
Ave. Signal Created0.1% X_0 $[e]$	4400

Table 9.2: Diamond Properties. [7, 8]

the target after every bunch of particles, the detector and electronics must react in ≤ 50 ns.

Three diamond detectors are installed in the experiment. The detectors are fixed to the part of the table that does not move, its position is fixed and independent of the position of the table movement. They are attached with an aluminum arm. The vertical position of the detectors is adjusted at 50 cm from the beam axis. On the horizontal plane, the detectors are aligned with the beam axis. Longitudinally, they are placed over the third, sixth and thirteenth blocks. This translates to 27 cm, 60 cm and 137 cm respectively.

The signal given by the diamond detectors is proportional to the energy deposited in the detector ($13eV/e-h$). This energy is proportional to the fluence of secondary particles from the target. The fluence varies with the degree of beam penetration. Therefore, the process of 'hydrodynamic tunneling' can be measured by recording the evolution of the particle fluence coming out of the target.

The conditions under which diamond detectors have to operate exceeds the regimes found in literature. The maximum expected fluence in the diamonds, from simulations, is in the order of $6\cdot10^{-3}$ chargedparticles/cm^2/p+. The total fluence for the SPS beam ($1.15\cdot10^{11}$ p+ per bunch with 288 bunches) is in the order of 10^8-10^9 particles/cm^2. Considering that all particles have high energy, the energy deposition can be approximated as the one of a minimum ionizing particle (MIP), the signal generated in a 500 μm pCVD diamond is in the order of 300 A. It is clear that a new design that uses a smaller and more inefficient diamond was needed. A new design was developed in collaboration with CIVIDEC instrumentation

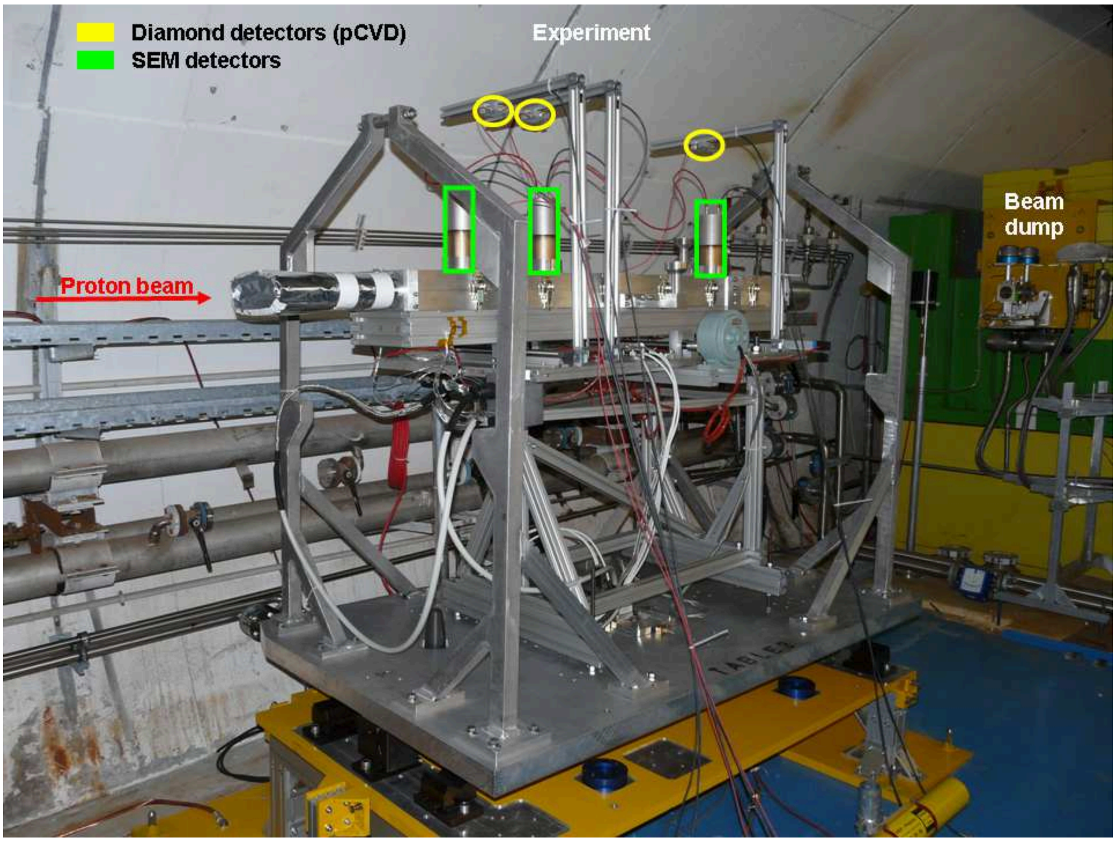

Figure 9.15: Setup of the diamond detectors in the experiment.

GmbH [96]. The pCVD diamond was purchased at Diamond Materials GmbH company in Germany. They are specialized in the production of CVD diamonds.

The detectors have a thickness of $100\,\mu$m and a radius of 2.5 mm with rounded gold electrodes of 1.5 mm radius. The overall grain size is small, giving an efficiency of $\sim 1/3 - 1/2$. The bias voltage is set to 100 V, which corresponds to $1\,\mathrm{V}/\mu$m that is a typical value for a pCVD.

The high voltage side of the diamond detector is connected to a high voltage power supply, while the other electrode of the diamond is directly connected (DC) to the transmission line up to the surface building and finally, using a current divider, to the oscilloscope. Three sets of current dividers were used during the experiment (20 dB, 40 dB and 60 dB).

The calculated signal for a bunch of $1.15 \cdot 10^{11}$ p+ with an expected fluence in the diamonds of $\sim 3.77 \cdot 10^{6}$ particles/cm^2 is shown in Figure 9.17.

The expected maximum current is in the order of 1.4 A for 1 SPS bunch, that gives a voltage drop of 66.5 V across the $50\,\Omega$ resistor of an oscilloscope. The expected voltage drop and current across the oscilloscope will severely damage it. The voltage drop across the diamond is so large that the assumed collected charged is not valid. The oscilloscope maximum input voltage drop is 5 V. A voltage higher than that can damage the oscilloscope electronics. A set

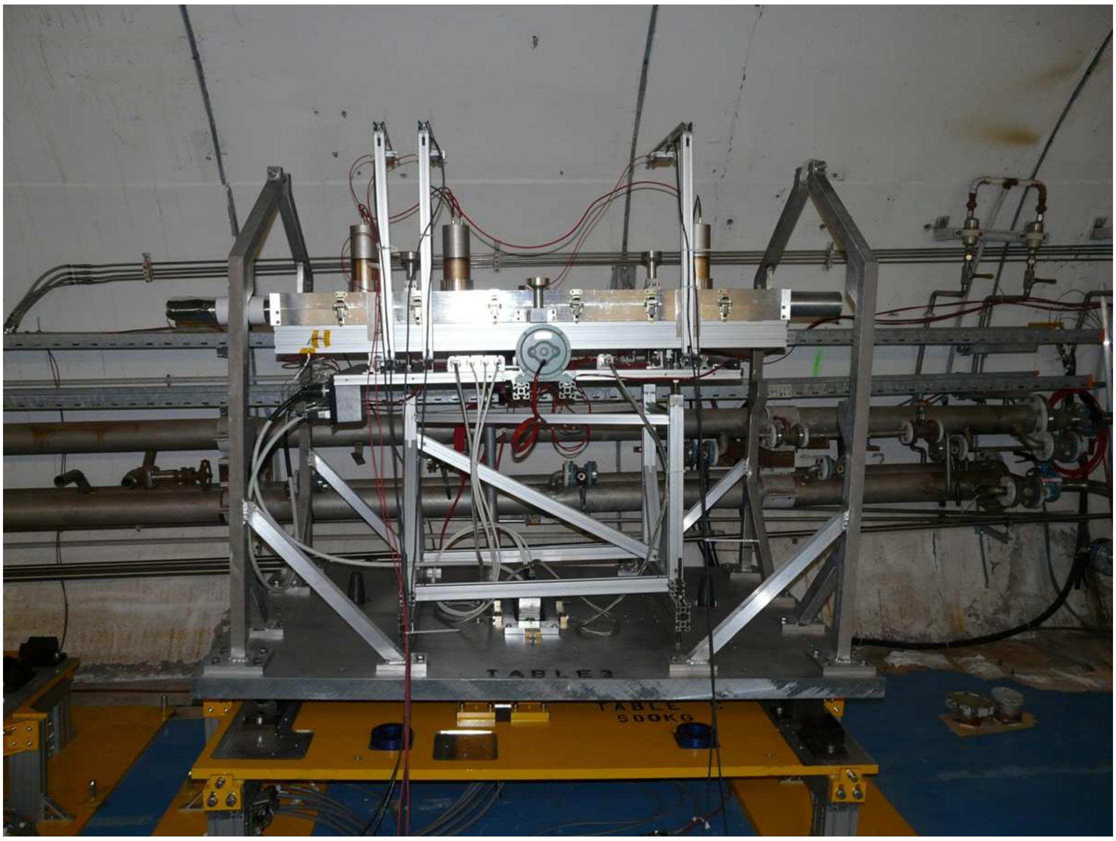

Figure 9.16: Setup of the diamond detectors in the experiment.

of current dividers are used to reduce the voltage at the oscilloscope input.

9.2.2 Secondary Electron Emission Monitors

Secondary Electron Emission Monitors [6] (SEM) have been developed at CERN to be used at locations in the LHC accelerator with high loss rates in which standard IC BLMs saturate. SEM detectors are radiation hard and its sensitivity is much smaller than LHC IC.

Unlike an ionization chamber in which a gas is ionized by incoming charged particles, a SEM detector uses the Secondary Emission Yield (SEY) of a material to generate a signal.

The process is the following: when primary electrons hit a solid surface, secondary electrons leave the surface into free space. The main parameter describing the SEE is the Secondary Emission Yield (SEY), which is the average number of electrons emitted when an incident projectile enters or exits a surface. Figure 9.18 shows the SEE process.

The basic geometry of the LHC SEM detector is derived from the LHC Ionization Chamber (IC) BLM. The vacuum part in the SEM is enclosed in a 100 mm long cylindrical tube with a 2 mm thick wall. The cylinder is closed on each side by a welded 5 mm thick covers. The top cover

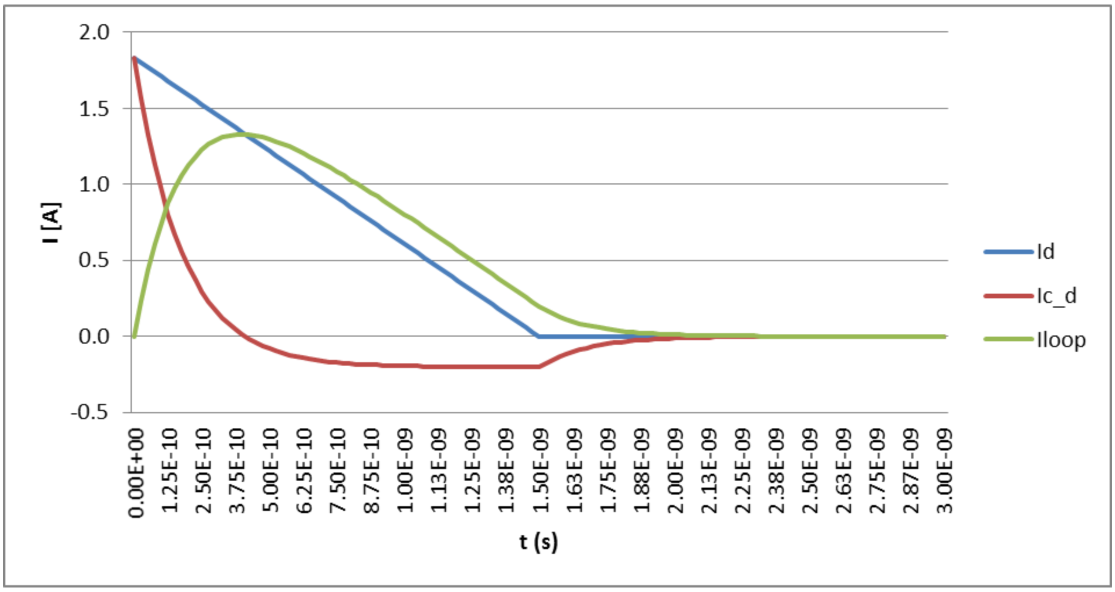

Figure 9.17: Simulated diamond signal for an SPS bunch. Ouput current (green). Ideal current (blue). Current charging the diamond capacitance (red).

houses a 120 mm long copper tube (used for pumping during the production) and two signal feedthroughs with copper wires and ceramic insulation. Additional active pumping getter was added inside the chamber to absorb gases released during the lifetime of the SEM from the internal components. The copper tube is hermetically sealed-off at the end of the production cycle, when the required vacuum is reached. The sensitive part of the detector is composed of three parallel plate electrodes with the bias voltage connected to the two outer ones and the inner electrodes is connected to the front end electronics. The insulation between the biased parts, the signal electrode and the grounded walls is ensured by the ceramic electrode holders and the feedthroughs. Additional contact insulation was applied on the external part of the signal feedthrough.

Three SEMs detectors are placed on top of the aluminum enclosure, over the 3rd, 6th and 13th cylinders. The bias voltage for the SEM detectors is set 1.5 kV. The high voltage power supply is placed in an underground area close by. To drive the voltage, high-voltage low-current cables are placed from the experimental area to TA7. Special Safe High Voltage (SHF) connectors are used.

LHC SEM characteristics

Figure 9.19 shows the SEM linearity measurements with a 450 GeV LHC type beam dumped after acceleration. Every point represents a dose integrated during 10 ms for the given number of protons dumped (x-axis) .

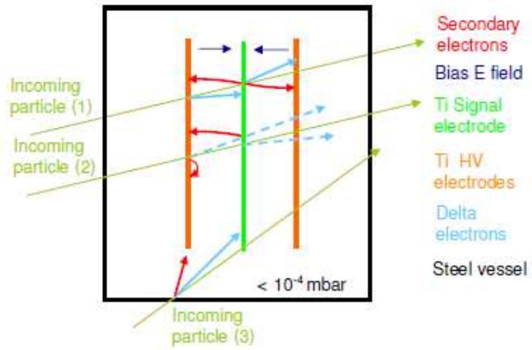

Credit: *D. Kramer*

(a) Secondary electron emission process.

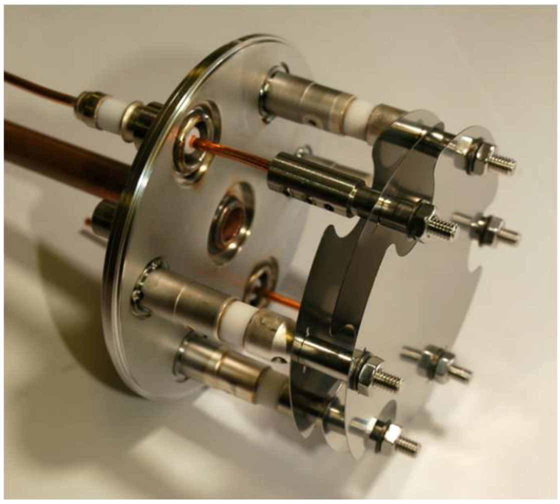

(b) Inside view of a SEM detector.

Figure 9.18: SEE detector.

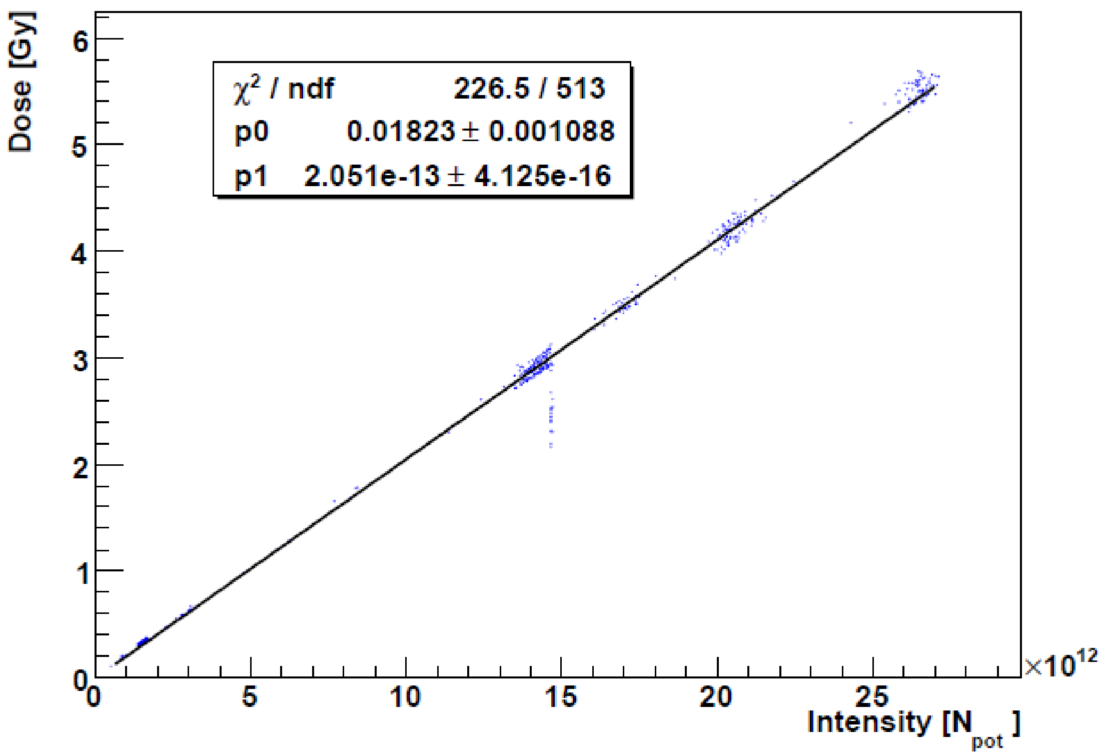

Credit: *D. Kramer*

Figure 9.19: SEM linearity measurement [6]

9.2.3 Strain Gauges

A strain gauge is a device used to measure the strain of a material. A strain is a normalized measure of deformation representing the displacement between particles in the body relative to a reference length. strains are dimensionless and are usually expressed as a percentage or a decimal fraction (Ex: 1%, $\mu m/mm$...).

There are eight strain gauge sensors placed in the experiment. Four of them are glued to the aluminum enclosure. The other four sensors are glued to the third cylinder of target II. The sensors are placed on the cylinder surface at diametrical opposite points. Two of them on the beam direction and the other two perpendicular to the beam direction (following the circumference of the cylinder).

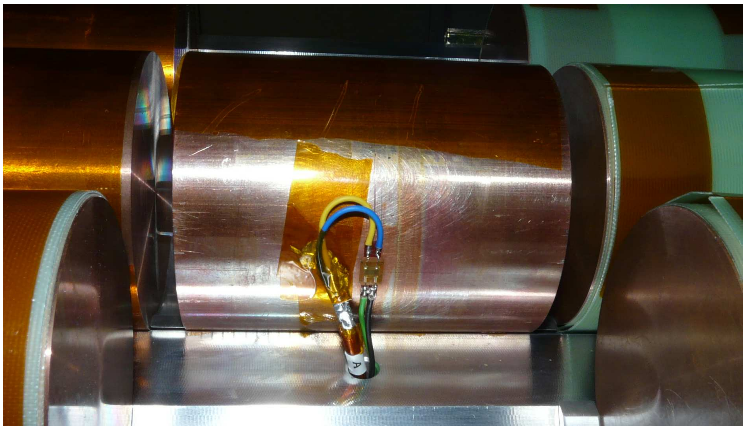

Figure 9.20: Strain gauge installation.

Working principle

A strain gauge takes advantage of the physical property of electrical conductance and its dependence on the conductor's geometry. When an electrical conductor is stretched within the limits of its elasticity such that it does not break or permanently deform, it will become narrower and longer, changes that increase its electrical resistance end-to-end. Conversely, when a conductor is compressed it will broaden and shorten, changes that decrease its electrical resistance end-to-end. From the measured electrical resistance of the strain gauge, the amount of applied stress may be inferred. A typical strain gauge arranges a long, thin conductive strip in a zig-zag pattern of parallel lines such that a small amount of stress in the direction of the orientation of the parallel lines results in a multiplicatively larger strain measurement over the effective length of the conductor surfaces in the array of conductive lines—and hence a multiplicatively larger change in resistance—than would be observed with a single straight-line conductive wire.

9.2.4 Temperature Sensors

Resistance Temperature Detectors (RTD) are sensors used to measure temperature by correlating the resistance of the RTD element with temperature. Most RTD elements consist of a length of fine coiled wire wrapped around a ceramic or glass core. The element is usually quite fragile, so it is often placed inside a sheathed probe to protect it. The RTD element is made from a pure material, platinum, nickel or copper. For the case of platinum they are called PT100 which has a nominal resistance of 100 Ω at 0 °C. Platinum is a noble metal and has the most stable resistance-temperature relationship over the largest temperature range. The unique properties of platinum make it the material of choice for temperature standards over the range of −272.5 °C to 961.78 °C, and is used in the sensors that define the International Temperature Standard, ITS-90 [97]. Platinum is chosen also because of its chemical inertness. RTD sensors have the following advantages:

- Cheap
- High accuracy
- Low drift
- Wide operating range
- Simple implementation

Among its disadvantages are:

- Slow time response
- Repeatability: hysteresis
- Calibration/Interpolation

The linear approximation of the resistance versus the temperature between 0 °C and 100 °C for a resistive element is called alpha (α). Equation 9.1 describes the definition of alpha, its units are $\omega/\omega/\circ C$.

$$\alpha = \frac{R_{100} - R_0}{100 \cdot R_0} \tag{9.1}$$

The sensors used on the experiment are PT100 film base sensors with a tolerance of $\pm 0.3\,\omega$ at 100 °C (class B). The dimensions are 10 mm x 2 mm. The suitable measuring range of the sensor goes from −50 °C to 600 °C.

Eight of those sensors are installed on the experiment. Six of them along target 3, glued inside a hole in the copper block, at cylinder 4^{th}, 6^{th}, 8^{th}, 10^{th} and 12^{th}. The other two sensors are also glued inside a hole in the copper block of the second cylinder or target 1 and 2.

The steady state temperature of each block is determined by the penetration of the beam. The temperature profile of a whole target would be measured and compared to simulations, to get an independent estimation of the penetration range.

The sensors are mounted in a 4-wires configuration. Two of the four wires are connected to a stable current source while the other two are connected to a data acquisition (DAQ) system that measures the voltage. With the 4-wire configuration, the resistance of the cables does not influence the measurement.

The current source was design in-house; its consist of a simple Wilson current source using MOSFET transistors. The DAQ is a commercial one from National Instruments (NI USB-6259 BNC). The DAQ is connected via USB to a computer running a logging application developed in LabView by EN-ICE at CERN. All current sources and the data acquisition system are placed in the surface building at SPS-BA7.

9.2.5 Microphones

Several microphones were installed in the HiRadMat tunnel (see Figure 9.21). The microphone signal shows a linear behavior with respect to the beam intensity [98]. The microphone linear behabiour is shown in Figure 9.22.

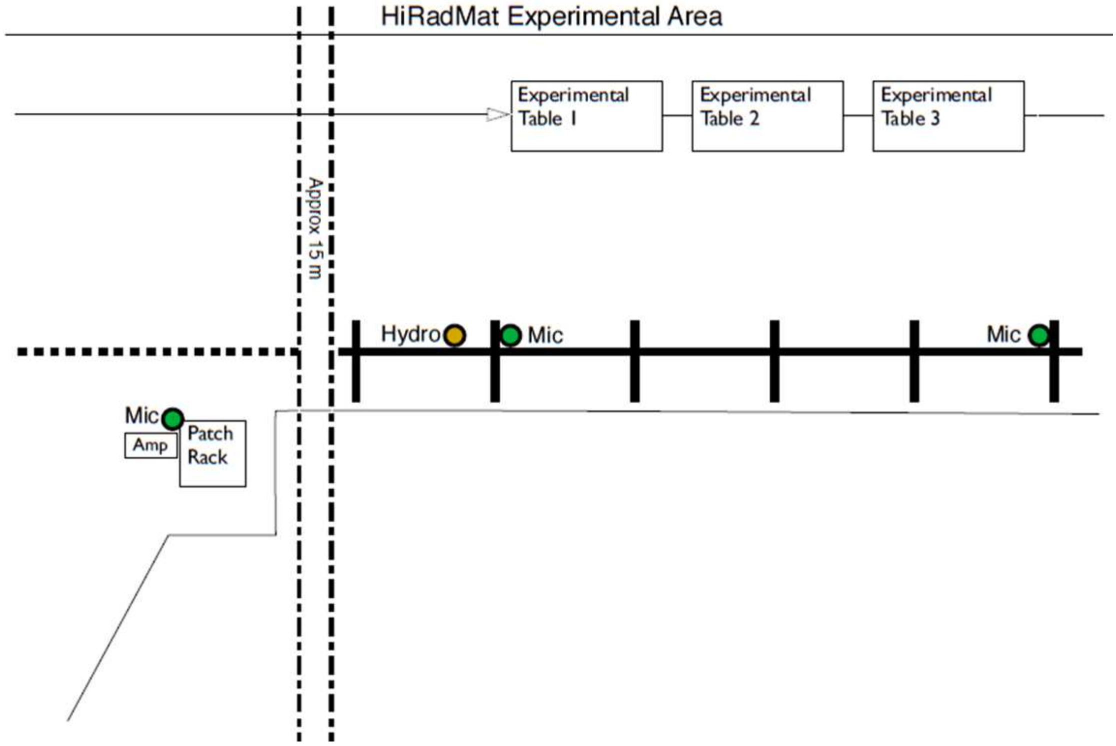

Credit: *D. Deboy*

Figure 9.21: HiRadMat microphones location.

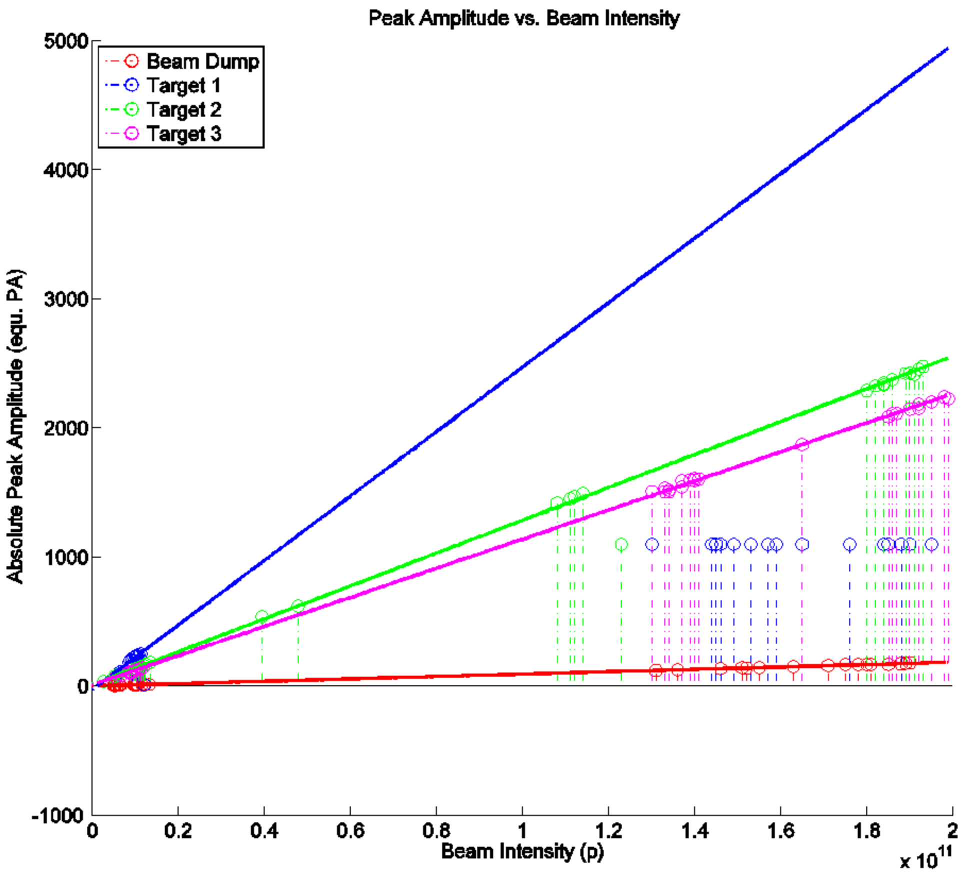

Credit: *D. Deboy*

Figure 9.22: Peak amplitude vs beam intensity.

9.3 Conclusions

The conclusions of this chapter are included in the conclusions of Chapter 10.

10 Experiment Results

This chapters presents the results of the experiment done at HiRadMat during June/July 2012. Firstly, the different phases and tests of the experiment are introduced. Then, results of the diamond detectors and post-irradiation exam are discussed. The chapter concludes with an assessment of the experiment and the performance of the detectors.

10.1 Experimental Phases

The experiment was done in two phases [99]. During Phase I, the performance of the diamond detectors was done using low intensity and high intensity beams. The objective of the first phase was to check the operation of the diamond detectors using low intensity beams. In Phase II, the experiment was irradiated with high-intensity beams to reproduce the 'hydrodynamic tunneling'. The post-irradiation exam consisted on a close visual exam of the interior of the target.

10.1.1 Installation

The target was transported from the manufacturing area to the surface building at SPS-BA7 (CERN) for the final assembly of the detectors. Using a metrology laser, the target was aligned to the beam on the surface. Once in the tunnel and before moving it to the experimental area, a test involving opening the target with a remote crane was done. Figure 10.1 shows a picture during the opening operation and a test photo of the space between the copper cylinders.

10.1.2 Phase I

On the 22nd of June, 2nd and 3rd of July 2012 the target was irradiated with a series of low intensity bunches at 440 GeV with an intensity ranging from $5 \cdot 10^9 - 2 \cdot 10^{11}$. The beam size was $\sigma_{focal} \approx 0.2$ mm. To check the alignment of the target with respect to the beam for all table positions, three photographic paper sheets were fixed at the front of each target. After a

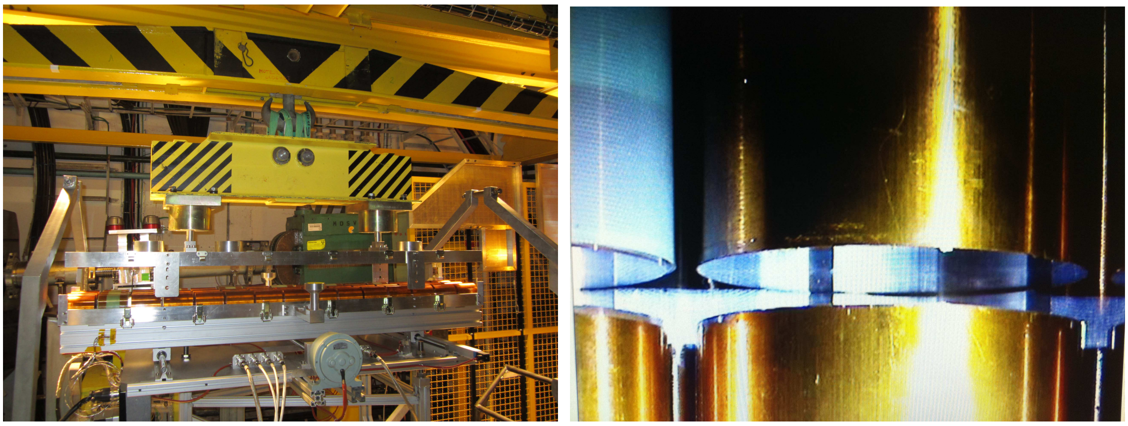

(a) Remote opening of the target with the crane at HiRadMat.

(b) Image taken with crane of the space between copper blocks.

Figure 10.1: Remote opening of the target.

couple of low intensity bunches, the photographic paper was recuperated. The alignment was good enough for the beam to pass through the hole of the aluminum cylinders. Nevertheless, the beam was slightly displaced to the left (see Figure 10.2).

These first low intensity beam shots were also used to verify that the diamond detectors and SEM detectors were working correctly and that the installation and cabling was correct. The bias voltage used during this phase for the diamond detectors was 2 V/μm.

On the 6th of July 2012, Target 1 was irradiated with a series of multi-bunch beam shots. The beam consisted on six/twelve bunches with $1.4 \cdot 10^{11}$ / $0.7 \cdot 10^{11}$ protons per bunch respectively. The beam size was $\sigma \approx 0.2$ mm.

The bias voltage for the diamond detectors was readjusted to 1 V/μm. The FWHM and efficiency of the diamond decreases with a smaller bias voltage.

The objective was to verify that the diamond detectors response was sufficiently fast to avoid any overlap of the signal between consecutive bunches. The diamond reaction time needs to be ≤ 50 ns that is the time between bunches. It was also verified that the bias voltage for the diamond detectors remained constant during the irradiation time. The bias voltage can decrease due to an insufficient capacitance on the high voltage side.

10.1.3 Phase II

On 12th of July 2012 phase II the destructive test to demonstrate hydrodynamic tunneling was performed with high intensity beams. Table 10.1 shows the main beam parameters used during this phase. Target 1 was irradiated with a high intensity but large beam. Due to the large beam size, no significant hydrodynamic motion is expected on target 1. On the contrary, target

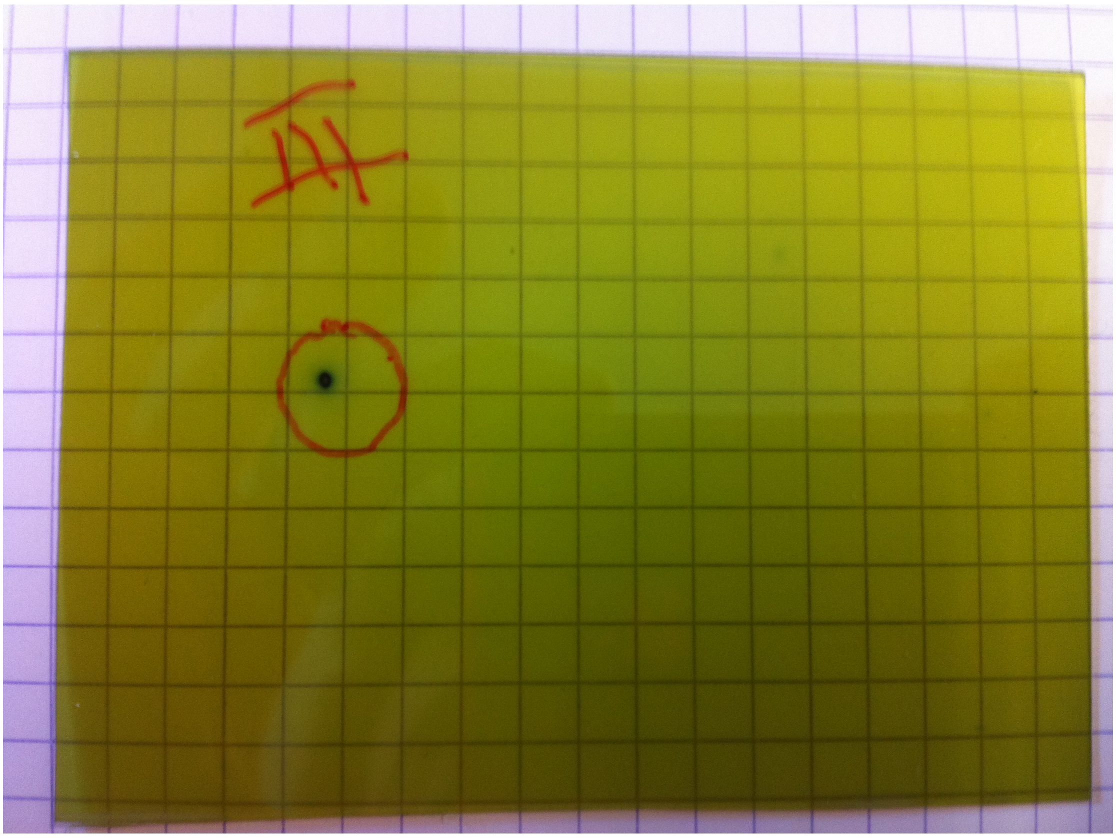

Figure 10.2: Photographic paper of target 3.

2 and 3 were irradiated with high intensity small beam. The beam size used was $\sigma = 0.2$ mm in both planes (vertical and horizontal). Hydrodynamic tunneling is expected on both target 2 and 3.

Target	# bunches	Beam size σ [mm]	Stored beam energy [MJ]	Peak energy density $[kJ/cm^3]$	Expectation
1	144	2.0	1.52	63.3	no tunneling
2	108	0.2	1.14	181.6	some tunneling
3	144	0.2	1.52	242.2	tunneling

Table 10.1: Beam parameters of the destructive tests for the three targets.

10.2 Diamond Detectors

Diamond detectors are very sensitive devices whose typical application is for low radiation environments. The expected particle fluence in the experiment is $\sim 6 \cdot 10^{-3}$ particles/cm^2/proton (at 50 cm distance) that can be considered extremely high. Diamond detectors have never been used before in high radiation environments due to their high sensitivity. However, if the sensitivity could be reduced, its radiation tolerance and simplicity would make them very attractive for this application. In the last chapter it a new design for a diamond detector was introduced in which the sensitivity has been reduced by decreasing the diamond volume. As presented in the last chapter, the detector design was done according to the requirements of the HiRadMat experiment: low efficiency, fast response, high current output, etc.

The detector was tested in the HiRadMat facility during the first phase of the experiment. Single bunch shots with a wide range in intensity were shot on each targets. Figure 10.3 shows the signals from the three diamonds mounted on the experiment. The signal have a very fast rise time ~ 2 ns and an exponential decay with a FWHM ≈ 5 ns. Time constants are bigger than the ideal ones shown in Figure 10.4 because of space-charge effects. The ideal signal response was calculated using electron and hole saturation speed and without considering space-charge effects.

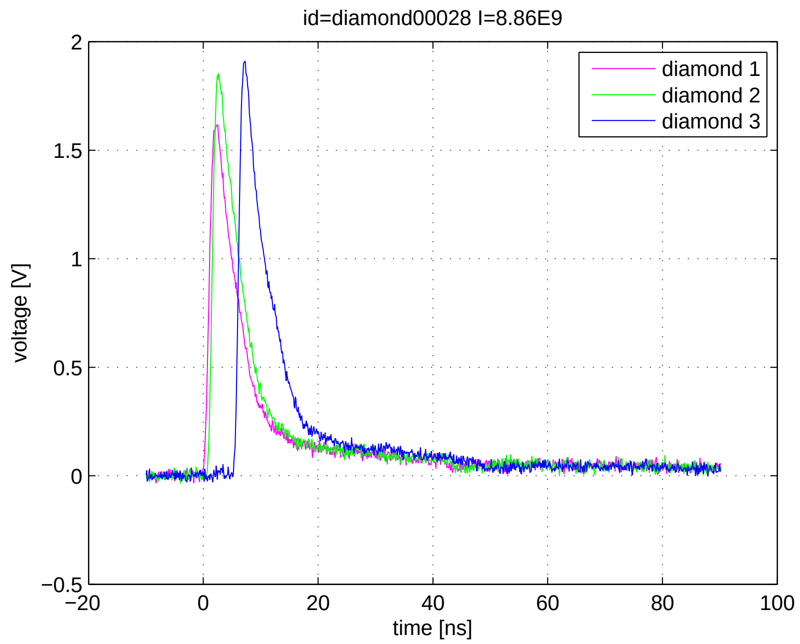

Figure 10.3: Diamond response to a single bunch. Red: diamond 1. Green: diamond 2. Blue diamond 3.

In high radiation environments there are several effects that affect the signal response: space-charge, trapping, decrease in bias voltage, etc. Figure 10.5 shows the relation between the beam intensity and the FWHM of the diamond signal. For higher intensities, space-charge

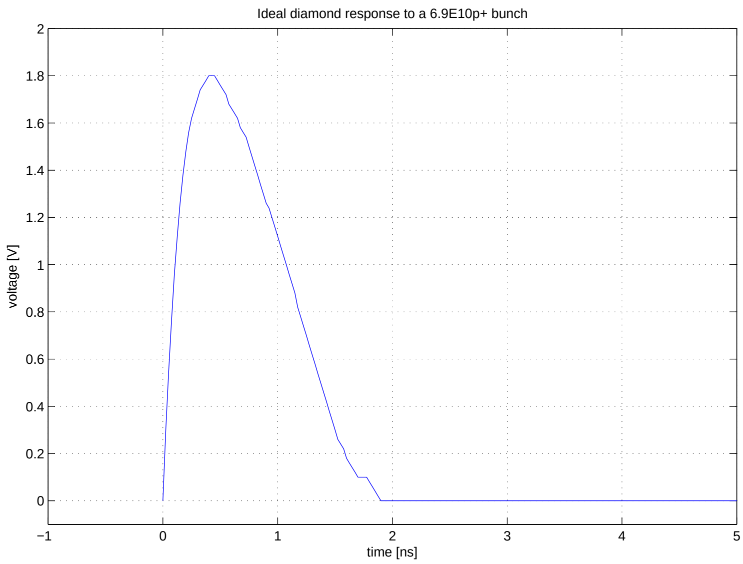

Figure 10.4: Ideal diamond response to a single bunch.

effects and the bias voltage drop becomes important. Space-charge effects increase the charge collection time. A decrease in the bias voltage reduces the charge collection distance and decreases the diamond efficiency.

Figure 10.6 shows the linearity plot for a diamond detector. The detector has a linear behavior over a wide intensity range from $\sim 10^9 - 10^{11}$ protons. The error in the beam intensity measure that can partially explain the linearity error comes from the FBCT.

Figure 10.7 shows the diamond response for 12 high intensity bunches. The beam was scraped with collimators in the PS to reduce the beam intensity by half. A large bunch to bunch intensity difference can be seen in the signal. The signal amplitude is proportional to the bunch intensity. On the contrary, the signal response for 6 high intensity bunches without scraping shows a small difference in the bunch bunch amplitude.

The signal for 12 high intensity bunches shows an offset in the signal that grows during the first 3-4 bunches and then stabilizes at ~ 50 mV. Part of the signal offset can be explained by the large signal tail that lasts 50 ns (see Figure 10.3)

There is a signal offset that grows to ≈ 50 mV during the first three bunches and the stabilizes. This offset can be partially explained by the pile-up of the signal tail from every bunch. If the signal from one single bunch is copied 12 times with a time separation of 25 ns and then the resulting signals are convoluted the offset appears [100]. This can explain 60% of the signal offset. Figure 10.8 shows the resulting convoluted signal. After the third bunch the offset reaches the asymptotic value of ~ 29.2 mV.

The remaining part of the offset (~ 20 mV) could be explained by a small DC current across

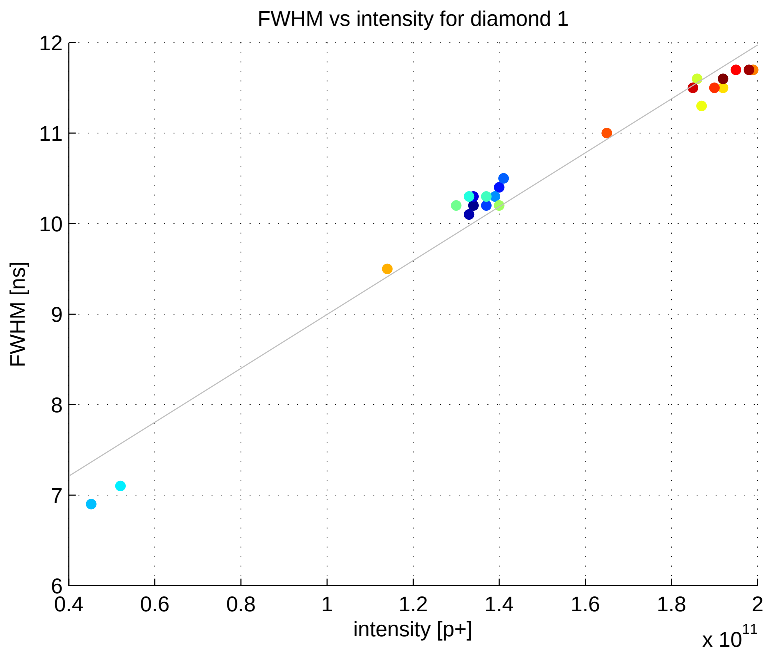

Figure 10.5: FWHM vs beam intensity. Each point represents a measurement taken with the diamond detector.

the diamond. In moderated radiation environments, the typical diamond DC current is in the order of hundred pA [101] and the typical resistance for a thickness of 100 μm is in the order of 10^9 Ohms. Then, the typical voltage offset is ~ 100 μV. However, in more extreme environments with a higher electron-hole generation rate the diamond resistance might decrease and the DC current increase leading to an increase in the DC voltage. A DC voltage of ~ 1 V, that is a factor of 100x more, might explain the 20 mV offset seen on the oscilloscope (NOTE: 40 dB attenuation factor between diamond and oscilloscope).

During all tests, the new diamond design operated as expected and fulfilling all requirements: low signal to noise ratio, fast response, low pile-up between bunches, good linearity, etc.

The second part of the experiment was the destructive test of each of the copper targets. Target 1 was irradiated with a high intensity wide beam for which no hydrodynamic tunneling effect was expected. For target 1, the signal from the diamond detectors should not change with time. On the contrary, for target 2 and 3 substantial hydrodynamic tunneling is expected and so diamond signals should evolve with time reflecting the density changes in the target.

Figures 10.9-10.11 show the signals for the irradiation of target 1. Unlike it was expected, the signal changes with time. The amplitude of the signal falls by 35% from the first to the last bunch. The change in amplitude can be explained as a result of the discharge of the High-voltage capacitor. The charge generated in the diamond by one high intensity bunch is $\sim 3 \cdot 10^{-9}$ C. The high-voltage capacitor is discharged by the same amount. The discharge of

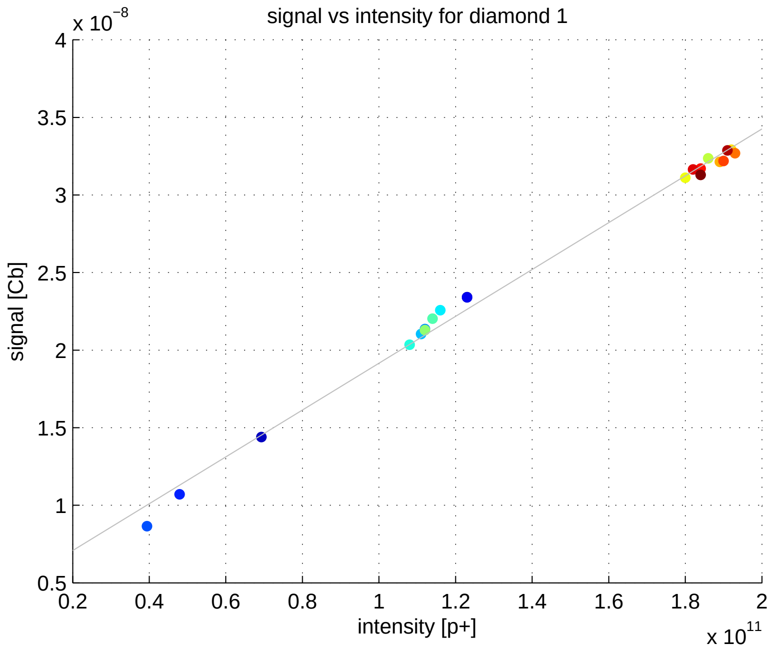

Figure 10.6: Diamond signal vs beam intensity. Each point represents a measurement taken with the diamond detector.

the HV capacitor results in a decrease of the diamond bias voltage that ultimately affects the charge collection distance and efficiency of the diamond. The HV capacitor has a large time constant of $111\,\text{nF} * 1\,\text{M}\Omega = 111\,\text{ms}$ compared to the beam duration $7.2\,\mu$s so the HV capacitor does not recharge during beam time.

The signals from the diamonds need to be corrected for this effect. The correction function is deduced from the signals of target 1, where no tunneling is expected, and obtained in the following way:

1. Initial bias voltage 100V.
2. First bunch $N = 1$
3. Calculate the voltage drop due to the charge generated by the bunch N.
4. Obtain the correction factor: $ratio = signal_{bunch_N} / signal_{bunch_3}$.
5. Next bunch: $N = N + 1$
6. Goto 3.

Using the calculated correction curves for each diamond, the signals for target 3 and 2 are corrected (see Figures 10.13 and 10.14). The correction applies to the signal integral per bunch

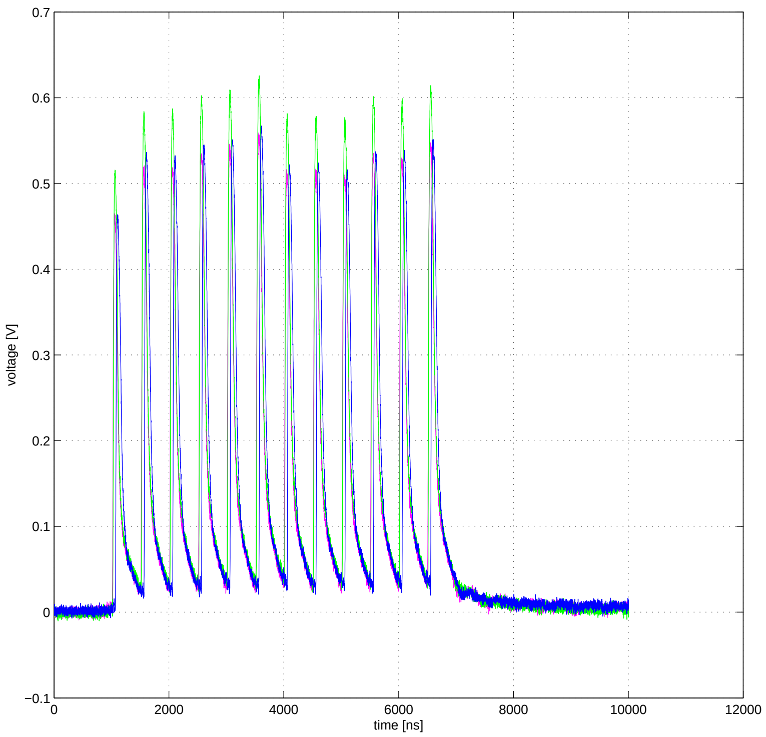

Figure 10.7: Diamond response for a 12 bunch beam.

and not the amplitude or FWHM. Only the signal integral should be considered for calculation purposes.

On both targets 2 and 3 the signal integral develops in the expected direction. Figure 10.15 shows the simulated diamond signal response with time for narrow beam (0.1 mm) of 288 bunches with $1.15 \cdot 10^{11}$ protons per bunch and 50 ns bunch to bunch separation. This simulated signal is the expected fluence of particles (proportional to the signal) across the diamond detectors if no saturation and space-charge effects are present. Although the beam parameters are different, diamonds 1 and 2 experiment a decrease in signal with time for both the experiment and the simulation. On the contrary, diamond 3 experiences an increase of signal with time. However, the increase/decrease of signal in percentage in the experiment is approximately two orders of magnitude smaller than in simulations. Table 10.2 shows the signal change in percentage for each diamond. The diamond signal from target 3 and 2 cannot be compared because the geometry is different. The mushrooms for the crane are placed over target 2.

Table 10.2 summarizes the diamond signal evolution for targets 2 and 3. In both cases, the time evolution of the signal for all three diamonds, changes in the same direction as in the simulations (σ_{beam} = 0.1 mm). However, simulation results cannot be extrapolated to the

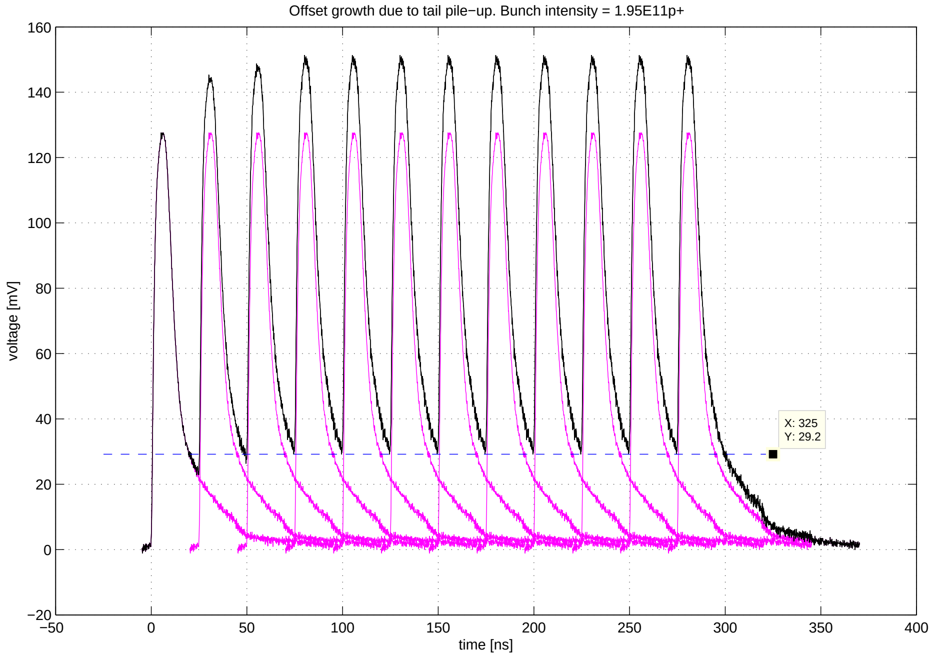

Figure 10.8: Offset growth due to tail pile-up.

	Diamond 1	Diamond 2	Diamond 3
Target 2	−13%	−8%	+7%
Target 3	−15%	−7.5%	+10%

Table 10.2: Total diamond signal change from experimental data. (%).

experiment parameters.

No simulations of the diamond detectors response with the same parameters of the experiment were done during the thesis. For this reason it is not possible to further quantify the diamond results presented in Table 10.2. Hydrodynamic and particle interaction simulations with the beam parameters used in the experiment will continue within the CERN-GSI collaboration [102]. At the end of this chapter the results obtained will be summarized.

The signal from the diamond detectors does not provide a clear evidence of hydrodynamic tunneling during the experiment. Space-charge effects need to be considered into the corrections for the diamonds. A more profound characterization of diamond detectors in high-radiation environments is needed.

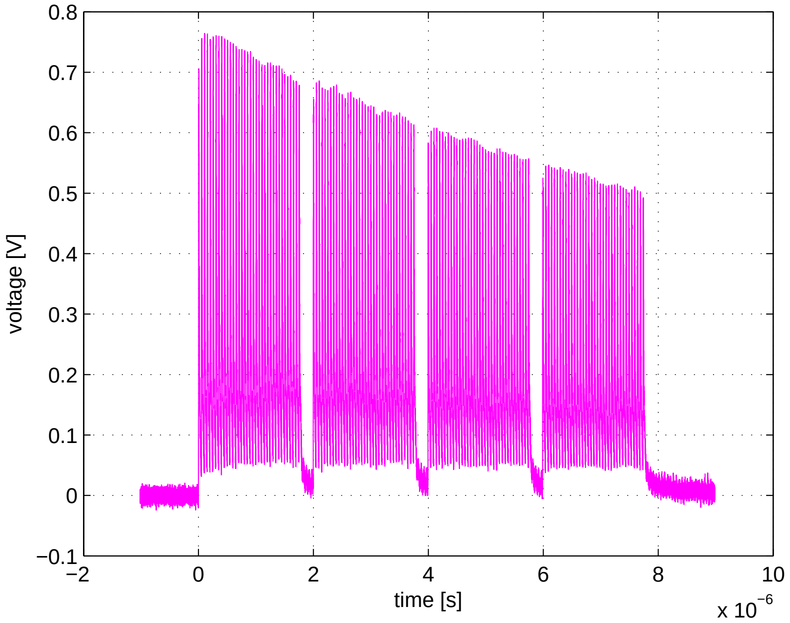

Figure 10.9: Target 1 diamond 1 signal (destructive test). The expected signal for no tunneling should be flat. However, the change in bias voltage across the diamond distorts the signal. The signal from the diamonds has to be corrected for this effect.

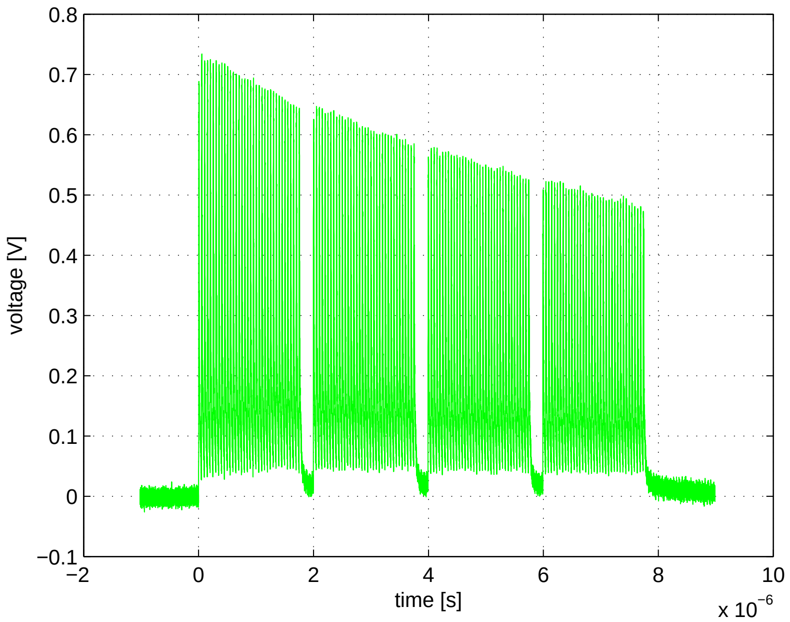

Figure 10.10: Target 1 diamond 2 signal (destructive test). The expected signal for no tunneling should be flat. However, the change in bias voltage across the diamond distorts the signal. The signal from the diamonds has to be corrected for this effect.

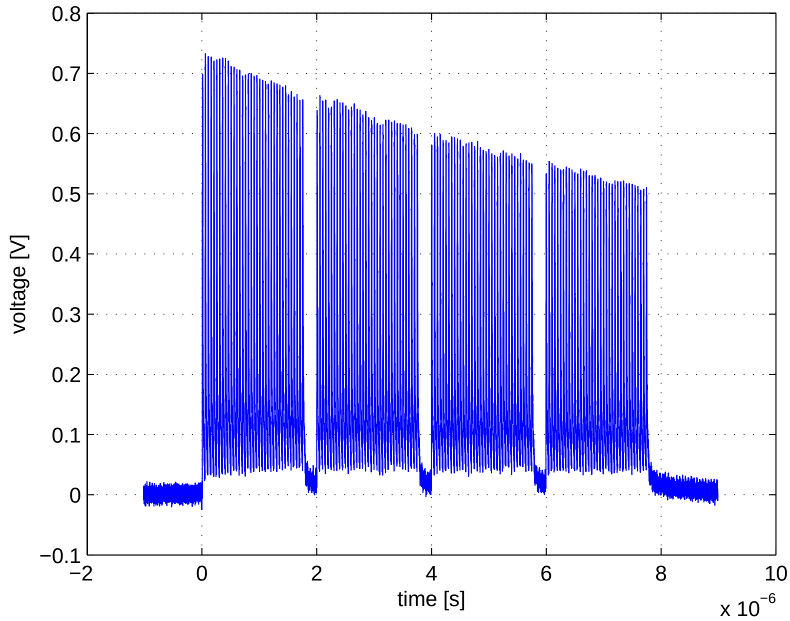

Figure 10.11: Target 1 diamond 3 signal (destructive test). The expected signal for no tunneling should be flat. However, the change in bias voltage across the diamond distorts the signal. The signal from the diamonds has to be corrected for this effect.

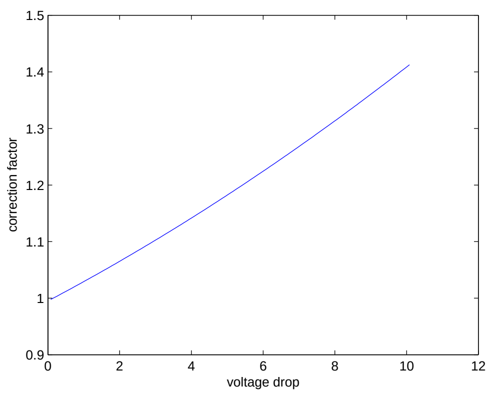

(a) The correction curve: signal correction factor (K) vs decrease in bias voltage (ΔV).

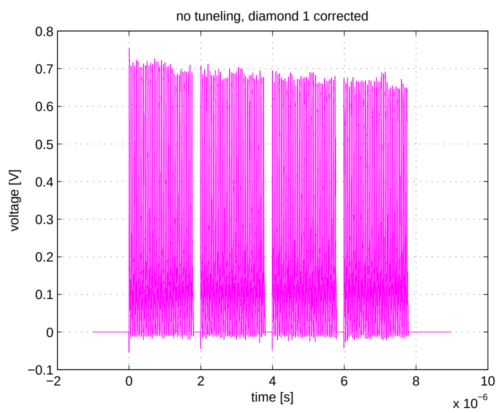

(b) Corrected signal from target 1 diamond 1.

Figure 10.12: Target 1 signal correction.

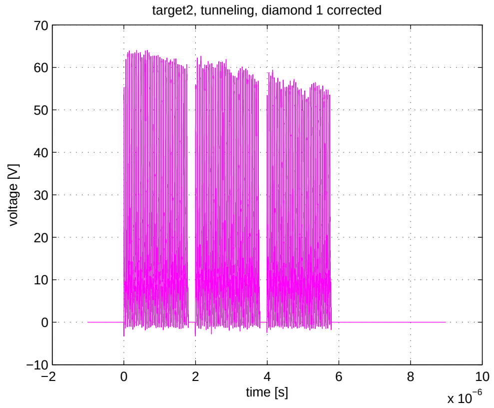

(a) Corrected signal for target 2 diamond 1.

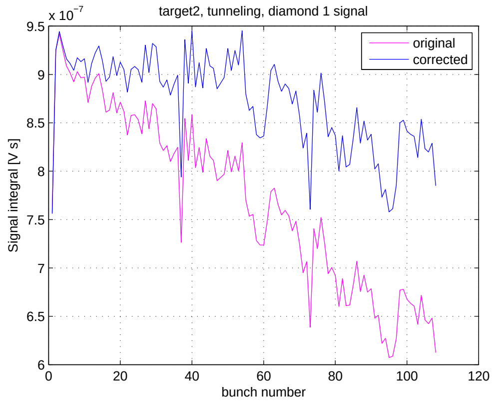

(b) Corrected signal integral for target 2 diamond 1.

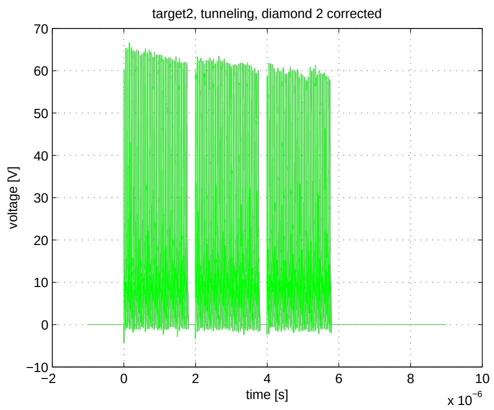

(c) Corrected signal for target 2 diamond 2.

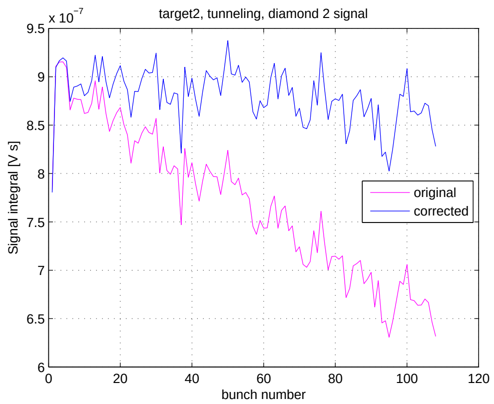

(d) Corrected signal integral for target 2 diamond 2.

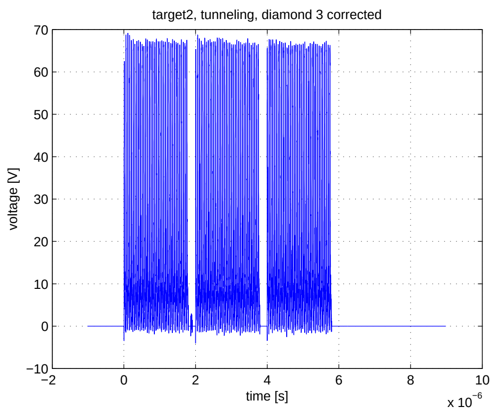

(e) Corrected signal for target 2 diamond 3.

(f) Corrected signal integral for target 2 diamond 3.

Figure 10.13: Target 2 signal correction.

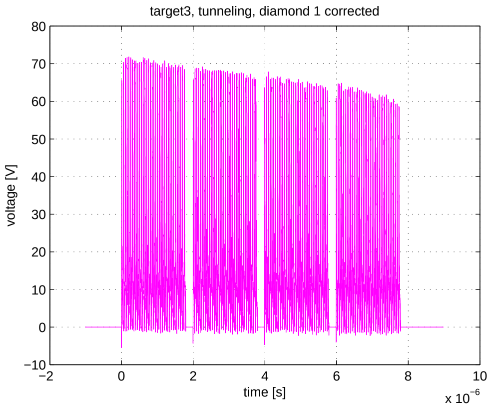

(a) Corrected signal for target 3 diamond 1.

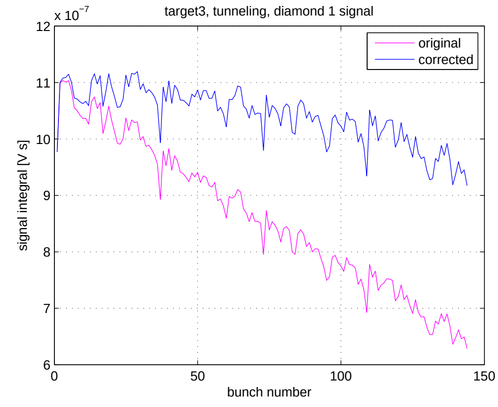

(b) Corrected signal integral for target 3 diamond 1.

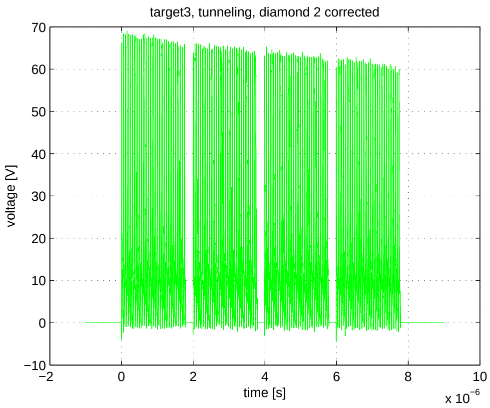

(c) Corrected signal for target 3 diamond 2.

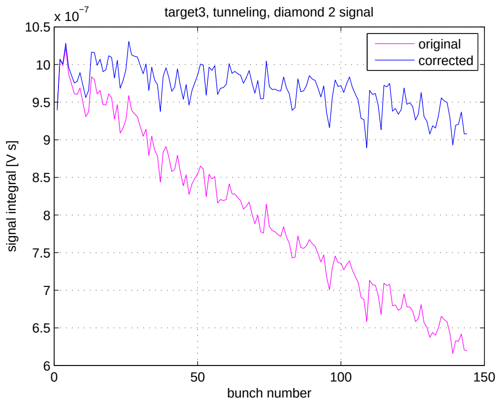

(d) Corrected signal integral for target 3 diamond 2.

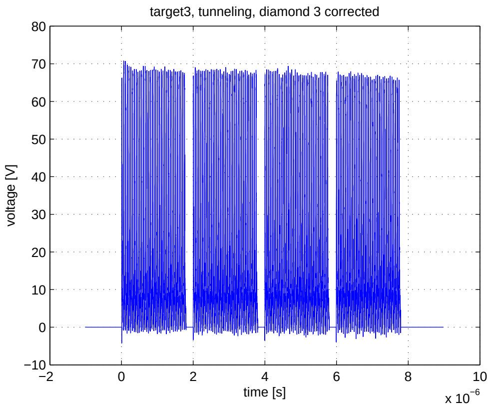

(e) Corrected signal for target 3 diamond 3.

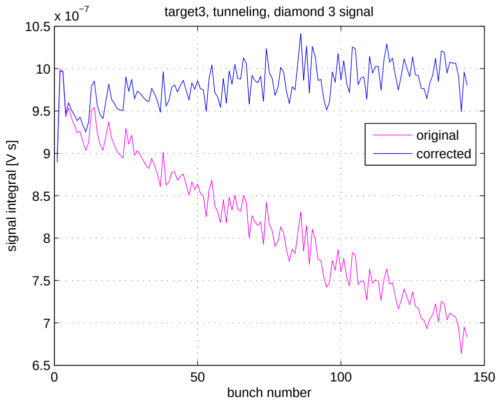

(f) Corrected signal integral for target 3 diamond 3.

Figure 10.14: Target 3 signal correction.

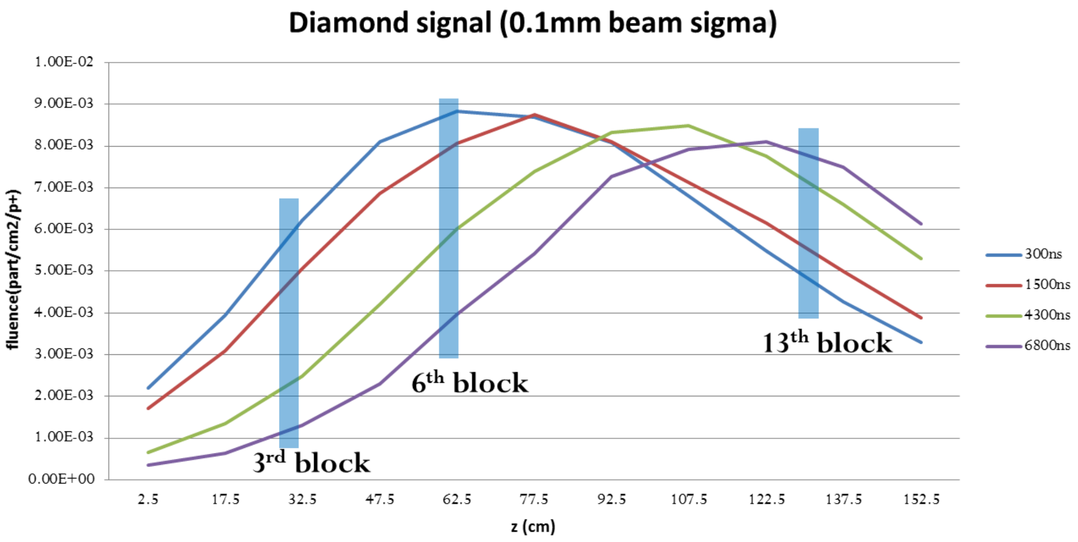

Figure 10.15: Simulated diamond signal response of 288 bunches of $1.15 \cdot 10^{11}$ p + /bunch at 440 GeV with a 25 ns bunch separation and $\sigma_{beam} = 0.1$ mm.

10.3 Post-Irradiation

The target was left for cool down for 8 months after it was irradiated. A preliminary study [103] of the target activation show that after a 4 month period the activation will decrease to ~ 90 μSv/h on copper cylinder's surface and to ~ 375 μSv/h in the cylinder's core.

When the copper melts or vaporizes, material escapes through the spaces between the copper cylinders and the entry hole created by the beam in the first cylinder. This material is visible, both in the caps and outside the target. Figure 10.16 shows the front aluminum cap after the irradiation of the target. Splashes of target material projected back into the front cap are clearly visible. The cap in front of target 1 shows no splashes. For target 3 there was significantly more material projected into the cap than for target 2. This result is confirmed by a visual inspection of the front surfaces of the three targets, which showed that the front face of target 1 was not damaged. For target 2 a slight damage was observed, and for target 3 a hole at the position of the beam impact was clearly visible.

The targets are enclosed in an aluminum housing. After beam impact molten material is projected to the outside, in particular against the top cover (see Fig. 10.17). These projections allow to estimate the depth of the damaged zone without a destructive analysis of the cylinders or a tomographic scan and provide an idea if hydrodynamic tunneling took place or not. The traces of projected copper between the 10 cm long cylinders of the targets are clearly visible. For target 1 (bottom) the molten zone ends in the 6th cylinder, i.e. the copper was molten over a length of 55 ± 5 cm. For target 2 (mid) the molten zone goes up to cylinder 8, i.e. 75 ± 5 cm. For target 3 (top) the molten zone goes up to cylinder 9, i.e. 85 ± 5 cm.

As the updated simulations with the combination of FLUKA and the hydrodynamic code, BIG2, are still ongoing, experiment results are compared with the SPS simulations presented in 8.3.3. Results from the simulations are scaled down to match the intensity used in target 2 and 3. This scaling is an approximation so that updated simulations are needed. Figure 10.18 shows the results of the simulations. For target 2 the molten region along the beam axis extends up to 77 cm and for target 3 up to 85 cm.

FLUKA simulations (without BIG2) have been performed with the beam parameters of the experiment to calculate the expected energy deposition in the three targets. The expected length of the molten zone without hydrodynamic tunneling when reducing the beam size from 2 mm to 0.2 mm was calculated.

Figure 10.19 shows the energy deposition in the copper target along the beam axis for the beam parameters of target 3. The dashed blue line indicates the melting threshold of copper. The expected length of the molten zone without hydrodynamic tunneling is derived from these simulations. Table 10.3 compares the expected lengths of the molten zone to the measured lengths. For target 1 the measured molten zone is similar to what is expected. The length increases to 65 cm for beam impacting on target 2 and to 69 cm beam impacting on target 3.

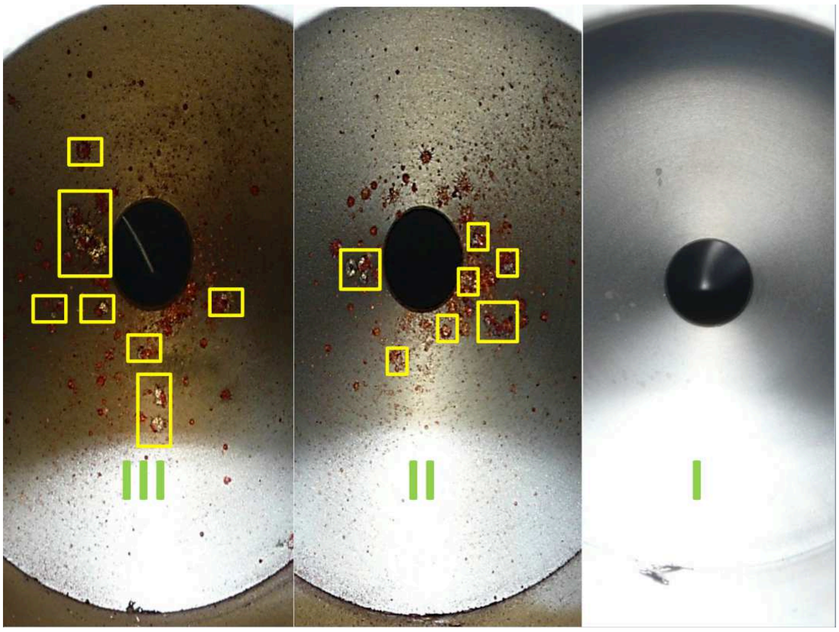

Figure 10.16: Splashes on the front aluminum cap (III=target 3, II=target 2, I=target 1), indicating that the front face of target 1 was not damaged. For target 3 there is significantly more material projected from the first cylinder into the aluminum cap than for target 2.

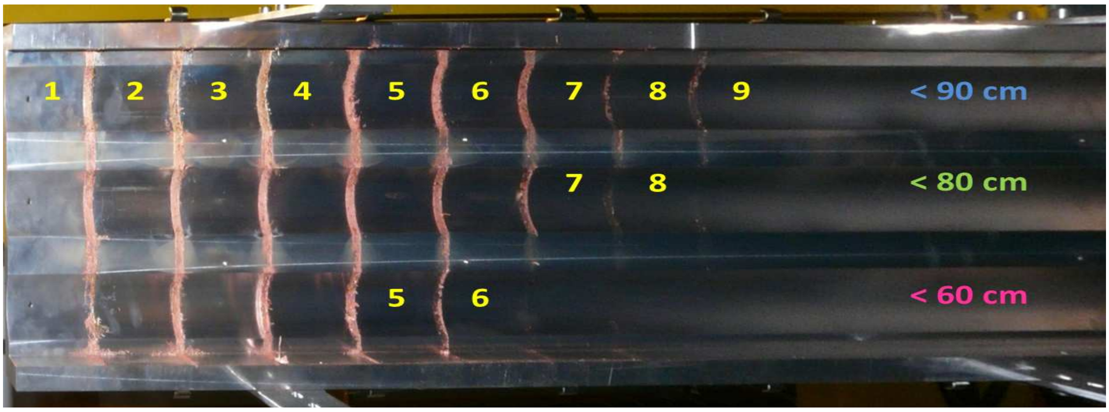

Figure 10.17: Top cover of the experimental set-up after the irradiation. Traces of projected copper between the 10 cm long cylinders of the targets indicate the length of the melting zone. For target 1 (bottom) the molten zone ends in the 6th cylinder, i.e. the copper was molten over a length of 55 ± 5 cm. For target 2 (mid) the molten zone goes up to cylinder 8, i.e. 75 ± 5 cm. For target 1 (top) the molten zone goes up to cylinder 9, i.e. 85 ± 5 cm.

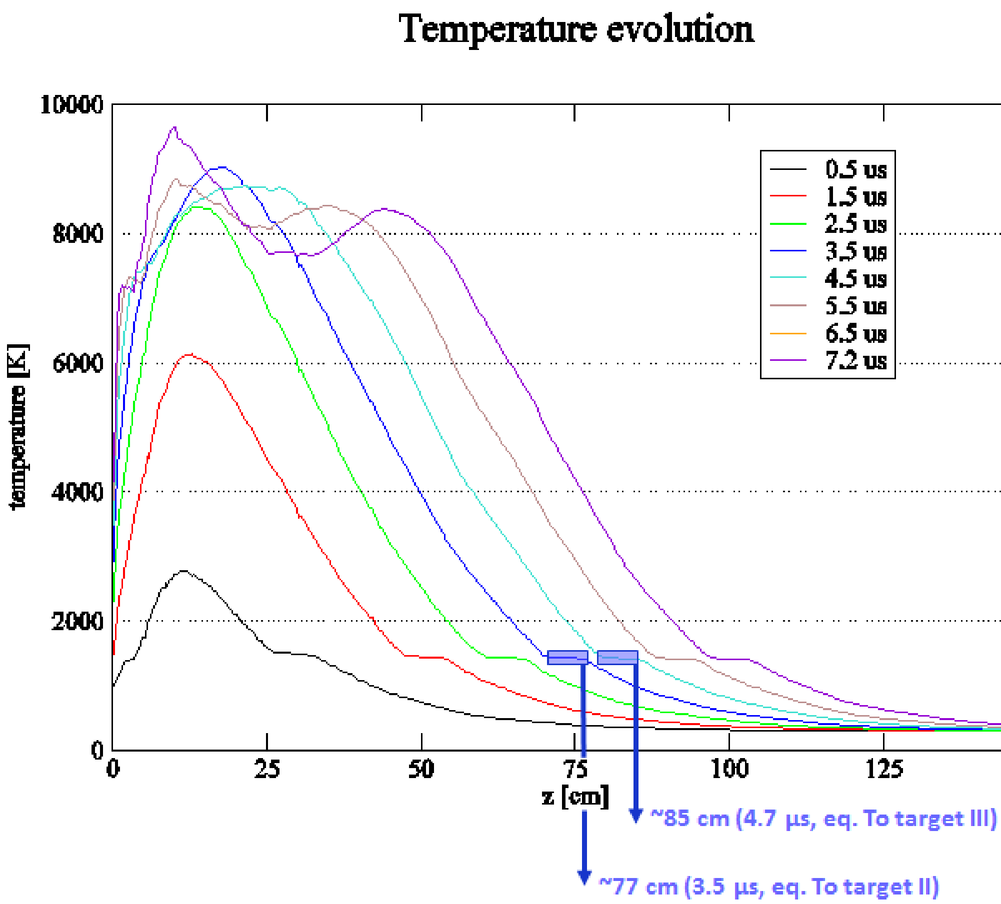

Figure 10.18: Simulated temperature in a copper target along the beam axis. The beam parameters are: $\sigma = 0.2\,\text{mm}$, 288 bunches of $\sim 1.15 \times 10^{11}$ p/bunch. The blue arrows indicates the melting point of copper for a beam intensity (beam time) that corresponds to the one of target 2 and 3. This simulation shows that the length of the molten zone would be expected to be 77 cm for target 2 and 85 cm for target 3 (with hydrodynamic tunneling).

This is significantly different from the experiment, where the measurements show an increase of the length of the molten zone with respect to the simulations by 16 cm for target 3 and 10 cm for target 2.

The expected lengths of the molten zone calculated from tunneling simulations, with the results scaled down to match the experiment intensity, fit the measured lengths from target 2 and 3.

Both, the large difference from static simulations with the experiment and the good agreement of FLUKA-BIG2 simulations are a strong indication of hydrodynamic tunneling [104].

Target	Simulated no tunneling [cm]	Δ to target 1 [cm]	Measured [cm]	Simulated tunneling* [cm]	Δ measured-simulated no tunneling [cm]	Δ measured-simulated tunneling [cm]
1	49 ± 5	-	55 ± 5	-	6	-
2	65 ± 5	16	75 ± 5	77 ± 5	10	-2
3	69 ± 5	20	85 ± 5	85 ± 5	16	0

Table 10.3: Comparison of the expected and measured length of molten zone. Simulations considering tunneling does not used the same beam parameters as in the experiment thus results are scaled down. The simulations performed with solely with FLUKA show the expectations if no hydrodynamic tunneling takes place.

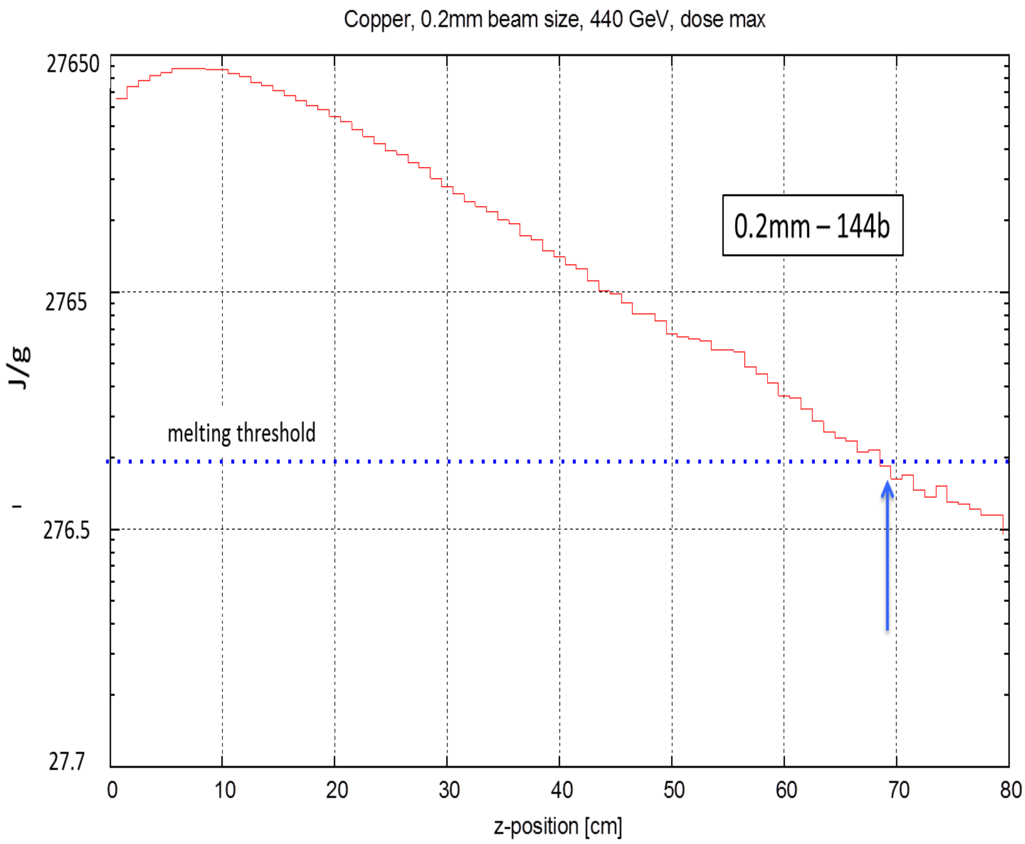

Figure 10.19: Simulated energy deposition in a copper target along the beam axis. The beam parameters are the same as for target 3 ($\sigma = 0.2$ mm, 144 bunches of $\sim 1.5 \times 10^{11}$ p/bunch). The dashed blue line indicates the melting point of copper (620 J/g). This simulation shows that the length of the molten zone would be expected to be 69 ± 5 cm without hydrodynamic tunneling.

10.4 Instrumentation for high-radiation environments

Apart from the diamond detectors, the experiment was equipped with other type of instrumentation: SEM detectors, strain gauges and temperature probes. The experiment was a good opportunity to test new types of instrumentation for high radiation environments.

10.4.1 SEM Detectors

SEM detectors are installed in the LHC, in areas with high beam losses. They have a high linearity, low sensitivity and fast response. They are a good complement to the diamond detectors as both operate with particle losses and the signal response is linear. Because of their low sensitivity, they can be installed closer to the target, so they should be able to see higher signal changes than diamond detectors (tunneling would be more clear to identify).

The data obtained during the experiment from the SEM detectors does not match the expected detector response. Although the signal is strong (6 A), it has an unexpected shape: phase and amplitude. The signal exhibits and oscillating behavior. Figure 10.20 shows, the expected signal for a direct irradiation of the detector with a proton beam and the signal obtained during the experiment for a single bunch proton beam onto target 2.

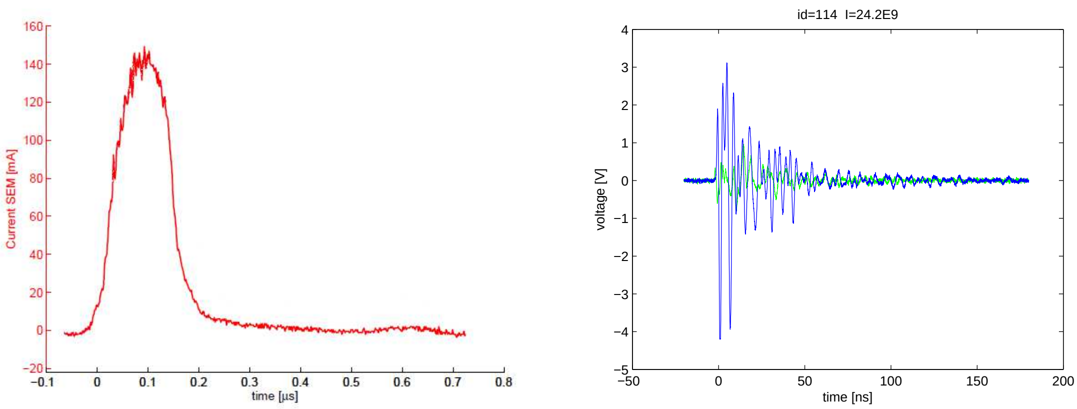

(a) SEM signal response to a single bunch of 160 ns, $1.1 \cdot 10^{11}$ $p+$ at 1.4 GeV

(b) SEM signal response to a single bunch of 0.5 ns, $4.52 \cdot 10^{10}$ $p+$ at 440 GeV.

Figure 10.20: SEM signal comparison.

Although the signal in general has a unexpected shape, the peak amplitude of the first oscillation might be modulated by the bunch intensity. Figure 10.21 shows the signal response of the diamond and SEM detectors to a 12 bunch beam. The beam was scraped in the SPS to reduce the intensity by half. Because of the scraping process the bunch to bunch intensity has large differences in amplitude. Ignoring the first two bunches, the peaks from both diamond and SEM signals share the same amplitude modulation.

The Fast Fourier Transform of the SEM signal shown on Figure 10.22 right has three peaks at

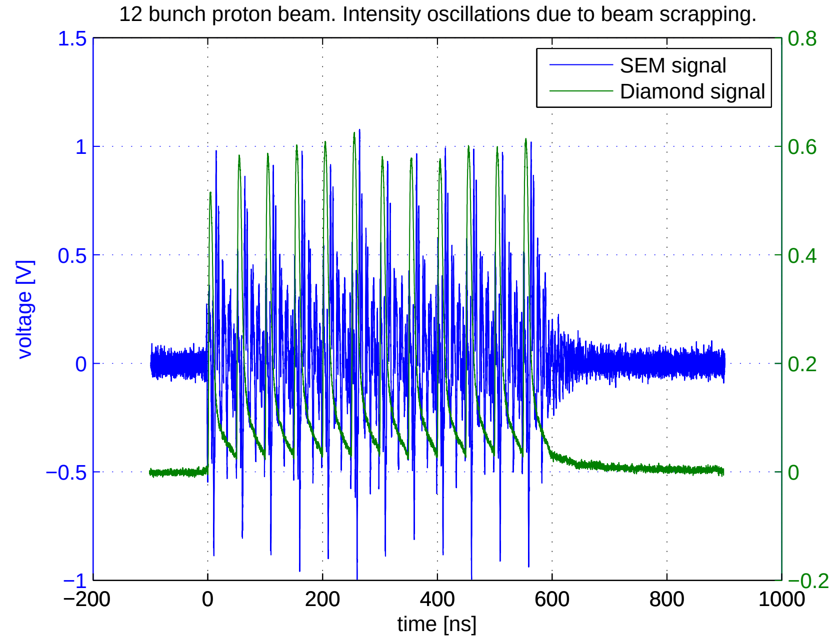

Figure 10.21: SEM and diamond signal response for a 12 bunch proton beam.

~ 0.14 GHz, ~ 0.19 GHz and ~ 0.33 GHz. The captured SEM data needs be further analyzed and understood which is beyond the scope of this thesis.

10.4.2 Strain Gauges

Strain gauges were a fundamental instrument of another experiments in HiRadMat [105, 56]. This experiment provided the opportunity to test the strain gauges detectors and electronics in advance.

Although a deep analysis of the data is beyond the scope of this thesis, it can be confirmed that the strain gauges were able to capture data during the experiment. Figure 10.23 shows the signal response of the horizontal strain gauges installed on target 2. The beam induced noise lasted ~ 15 μs that is more than twice the beam time (7.2 μs). Pressure waves take ~ 14 μs to reach the wall of the copper cylinder, so the beam induce noise will not have an impact into the recorded data. Beam induced noise becomes more important for smaller targets where the traveling time of the pressure wave is smaller because it can obscure the initial oscillations of the surface.

Using the difference in phase between the signals from the horizontal sensor it is possible to calculate the displacement of the right sensor with respect to the left one. Considering that the target remains in the elastic regime during the initial times. Pressure waves moves at a speed slightly lower than the sound velocity ($v_{Cu} \approx 3810\,\mathrm{m/s}$ at 298.15 K). The horizontal displacement can be calculated as:

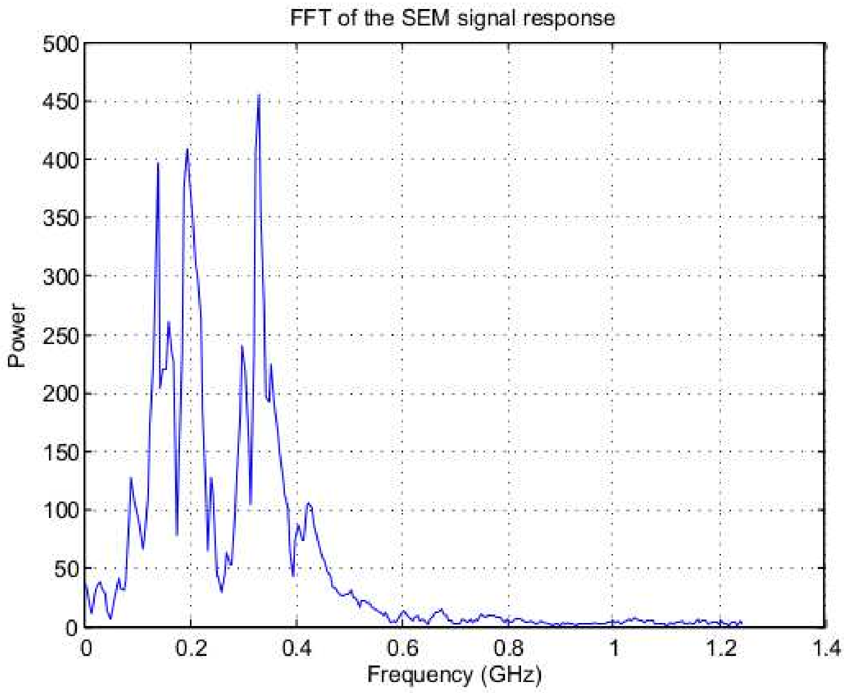

Figure 10.22: Fast Fourier Transform of the SEM signal.

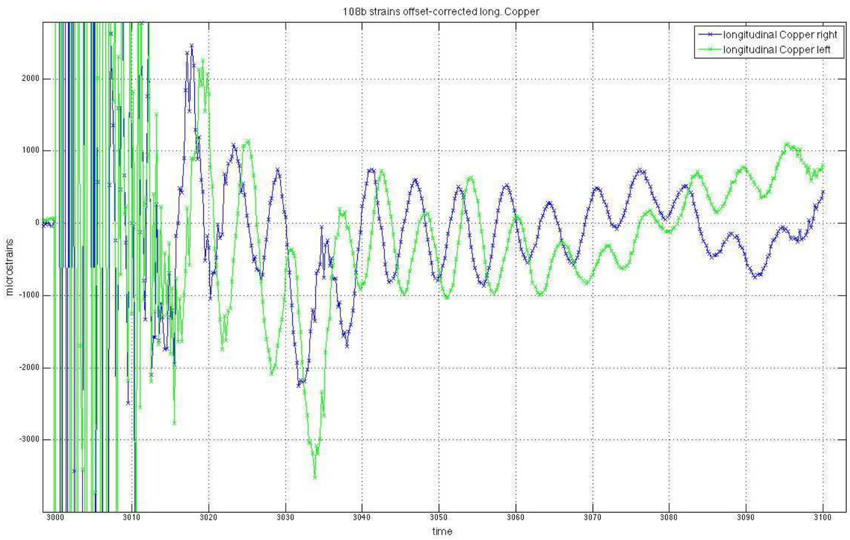

Figure 10.23: Signal response of the horizontal strain gauges. (Target 2. Time in μs)

$$\frac{\Delta t}{v_{sound} \cdot 2} \approx \frac{1.5\,\mathrm{ns}}{3810\,\mathrm{m/s} \cdot 2} = 2.38\,\mathrm{mm}$$

The data from the strain gauges could be used in the future as another parameter to compare between the experiment and simulations.

10.4.3 PT100

PT100 sensors are simple resistance detectors to measure the temperature made of a platinum wire. Eight PT100 sensors were installed in the experiment: six in target 3, one in target 2 and another one in target 1. The detectors were powered by independent Wilson current mirrors installed on the surface buildings. The readout system was based on a national instrument DAQ with a resolution of 12bits that translates into $6.10 \cdot 10^{-4}\,\mathrm{V} \approx 0.23\,\mathrm{K}$.

The calculated steady-state temperature for the case of tunneling and for no tunneling effect is shown in Figure 10.24. If no tunneling effect happens during the experiment, the beam penetration will be smaller and particles showers will be more concentrated: higher peak temperature. If tunneling effect happens during the experiment, particle showers will spread across the target length resulting in a lower and less pronounced peak temperature.

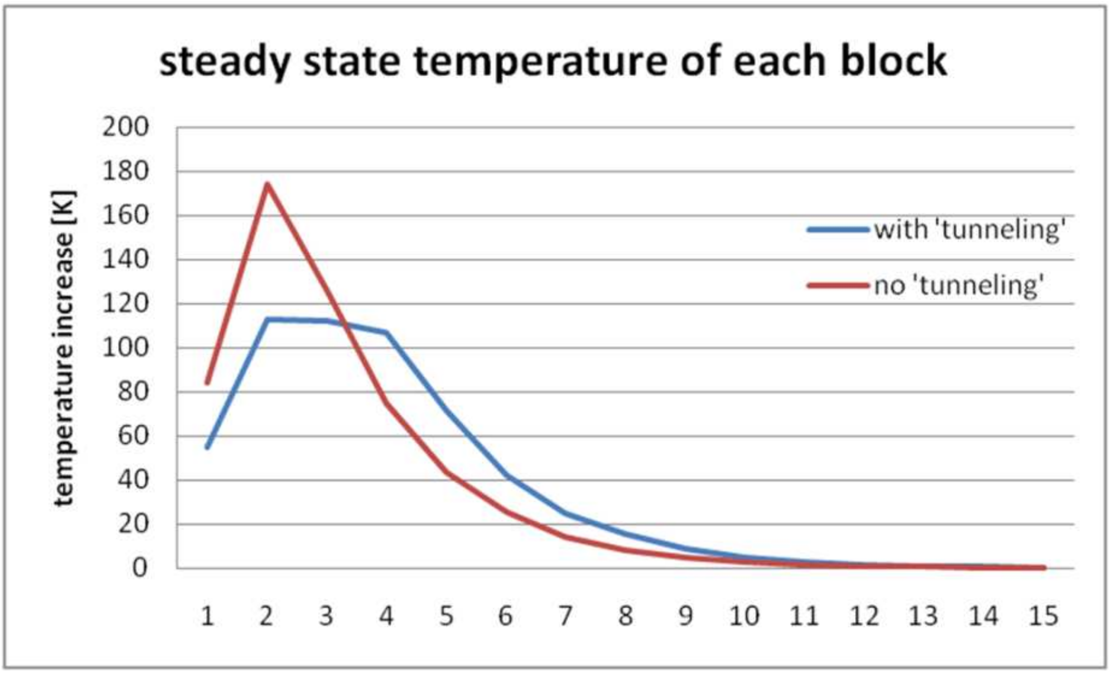

Figure 10.24: Simulated steady-state temperature for a beam of 288 bunches of $1.15 \cdot 10^{11}\,\mathrm{p+/bunch}$ at 440 GeV with a 25 ns bunch separation and $\sigma_{beam} = 0.1\,\mathrm{mm}$ with and without considering tunneling effect.

After phase I, several detectors began to give wrong readout values. The detectors were responding to vibrations from the movement of the experiment table. Figure 10.25 shows the signal obtained while moving the experimental table from the *OUT* position to *Target 3* position. Sensor 1,3,7,8 gave wrong readout values for most of the time during phase I and II. No significant temperature increase was observed on the targets during phase I.

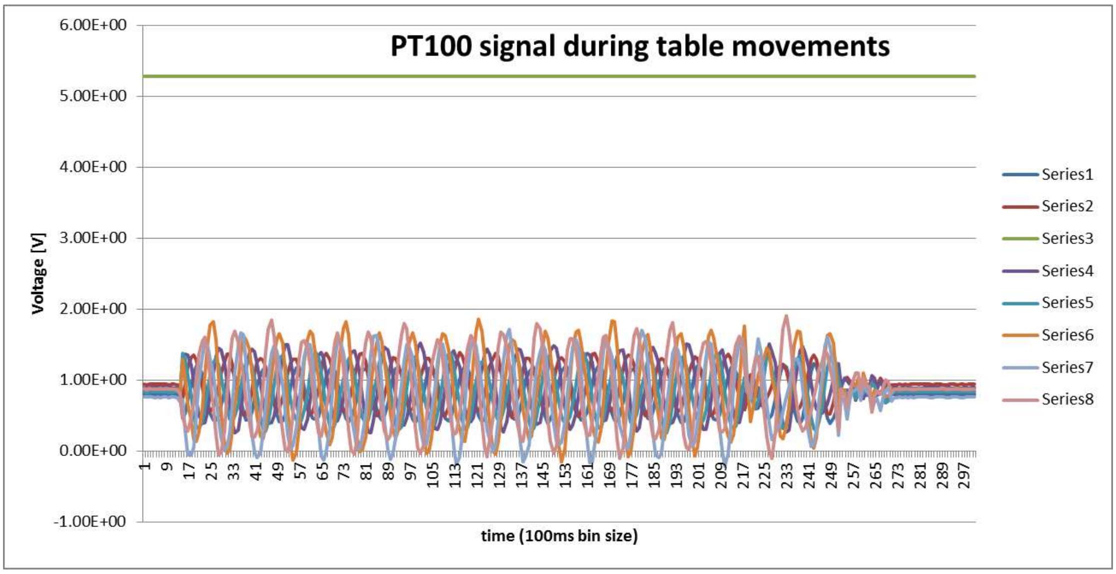

Figure 10.25: PT100 signal during movements of the experimental table.

10.5 Conclusions

- Hydrodynamic tunneling was measured with a visual examination. The experiment successfully reproduced the foreseen effect.
- Experiment and hydrodynamic simulations are in good agreement.
- New methods are needed to reduce the uncertainty of the penetration length which currently is 1 copper block = 10 cm.(Ex: ultrasound, hard X-rays).
- CVD diamond detectors performed extremely well during the experiment. Although there is still place for improvements.
- CVD diamond signal is well understood in low-fluence environments however for high-fluence environments space-charge effects need to be further investigated.
- New instrumentation was tested under high-fluence environments: strain gauges worked.
- Secondary Electron Emission Monitors signal is not understood, further analysis is required.

- New simulations, with the same parameters as the ones in the experiment, are needed for a proper comparison.
- This experiment has proven very valuable to understand the consequences of catastrophic beam accidents in high-energy high-brightness accelerators.
- It was evident that new simulations with proper parameters were needed. These simulations were performed by the CERN-GSI collaboration. A brief summary of the results will be presented in the following section.

10.6 Beyond this thesis: Simulations of the experiment

Simulations with the method as presented in this thesis using FLUKA and BIG2 and the beam parameters for the HiRadMat experiment were performed after this thesis was completed by N. A. Tahir and F. Burkart, within the collaboration framework between CERN and GSI. Preliminary results show a penetration length of 79 cm for the case of target 2 and 89 cm for target 3. This corresponds to a depth of tunnelling into cylinder 8 for target 2 and cylinder 9 for target 3. The simulation results are therefore fully consistent with the analysis of the target after the experiment. A publication on the details of the simulations and final results is in preparation [102].

11 Conclusions

The energy stored in each beam of the LHC is 362 MJ, sufficient to melt 500 kg of copper. An accidental release of even a small fraction of the beam energy can result in severe damage to the accelerator and equipment. Machine protection systems are essential to safely operate the accelerator and handle all possible accidents.

This thesis deals with the study of different failure scenarios and its possible consequences. It addresses failure scenarios for low and high intensity beam losses. For low intensity beam losses the impact on equipment made out of high-Z materials (e.g. tungsten collimators) and superconductors is addressed. For high intensity beam losses hydrodynamics effects and beam interaction on graphite and copper collimators are studied.

The study of low intensity losses on high Z materials was focused on the unlikely event (assumed to happen once in 300 years) of an asynchronous beam dump in the LHC combined with a wrong setting of the collimation system. In this event, up to 2.5 full intensity bunches could hit the tertiary collimators protecting the focusing triplet superconducting magnets near the interaction points. If this occurs, tertiary collimators can be severely damaged leading to permanent plastic deformations of the jaws or a rupture of the water cooling system.

The study was done using FLUKA to calculate the energy deposition on the collimator but without including a thermo-mechanical analysis. The damage thresholds obtained might be optimistic since transient heat deposition induced pressure waves (elastic, plastic) can damage materials well below the melting point. Pressure waves can travel deep inside the collimator support and damage the water cooling pipes. Water into the ultrahigh vacuum of the beam pipes is considered to be a very serious event. Recently, damage tests [105, 56] on tungsten collimators were performed at the HiRadMat facility from HiRadMat experiments confirm that small beam intensities $1.04 \cdot 10^{12}$ p+ at low energy 440 GeV and with a relatively wide beam size $\sigma_x \times \sigma_y = 0.53 \times 0.36 mm^2$ can produce permanent plastic deformations on the tungsten jaws. Although the parameters are quite different from simulations, the results are compatible.

After the accident of 19/09/2008, that happened at LHC during powering tests, it was necessary to understand the problems related to bad joints between the stabilized superconducting cables (bus-bar) for the LHC main dipole and quadrupole magnets. When a bus-bar quenches, and the quench is not detected in time, the bus-bar might be damaged. This might lead to an open circuit with consequences similar to the accident in 2008. After a quench is detected, the magnet energy is extracted with a time constant of 100 s (dipoles) and 30 s (quadrupoles), and during this time the bus-bar must be able to carry the current without damage. In the case that a beam loss would heat the bus-bar up to a temperature slightly above the transition temperature (80 K) the energy could not be discharged in time and the bus-bar would melt during discharge.

Beam losses at three different locations from the LHC accelerator have been studied: the connection cryostat right of point 7, the MQ11 right of point 7 and the MQ12 right of point 7. These locations have been chosen because of its higher probability of quenching a bus-bar, before quenching a magnet coil. Simulations were done using the FLUKA package. Results show that magnets will quench at a significantly lower level, 4-380 times, of beam loss than adjacent bus-bars (in inter-connects or the connection cryostat). 10^6 protons are sufficient to quench the magnets while for quenching a bus-bars $10^9 - 10^{10}$ are protons required. The quench of a bus-bar without quenching the adjacent magnet was not observed in these studies.

Energy deposition results are scenario dependent, however general conclusions can be drawn. The main result is that for heating of a bus-bar to 80 K massive beam loss would be required. Such beam loss would have other consequences, for example damaging the vacuum pipe which is in itself is a major accident. The machine protection system should always prevent that this ever happens.

Several failures at the LHC could lead to the full beam deflected with non-nominal angle, into a 10 m long graphite absorber, into a septum magnet, or into superconducting magnets. Understanding the damage potential of high intensity high dense beams (ex. LHC beams) is crucial for a correct Machine Protection assessment. Extensive simulations of the impact of high-intensity high-dense beams on different materials have been carried out. These simulations study the hydrodynamic evolution of a target while and after being irradiated by a proton beam. To understand the consequences of a catastrophic LHC accident, a full LHC beam impacting into a carbon cylinder was simulated using a new methodology that combines a particle transport and interaction code with a hydrodynamic code. Conventional beam loss simulations solely use a particle transport and interaction code. However, when dealing with high-intensity high-dense beams hydrodynamic processes occurring during and after the interaction cannot be neglected. The proposed methodology combines in a step by step schema two codes: FLUKA and BIG2. Simulations suggest the presence of a hydrodynamic motion that boosts the beam penetration range. The full LHC proton beam penetrates up to 25 m in carbon whereas the range of the shower from a single proton in carbon is just about 3 m. The absorbers that are installed downstream of the beam dump kicker (TCDQ) are not sufficient to stop the whole beam in case of accident. Due to the extreme temperatures $\sim 1\,\text{eV}$ and high pressure $7\,\text{kbar}$ in the target, a large part of the absorber enters into the Warm Dense Matter state.

The hydrodynamic tunneling effect also appears in the calculations for the SPS beam hitting a copper target. The effect is more pronounced for smaller beam sizes and materials with higher atomic number (Z). The damage potential of high intensity high dense beams (LHC type, SPS type, etc.) is much greater than traditional energy deposition simulations suggest due to "Hydrodynamic tunneling".

An experiment to reproduce the hydrodynamic tunneling seen in simulations was performed at the High Radiation to Materials (HiRadMat) facility at the CERN-SPS on July 2012. The experimental setup consists of 3 targets. Each target consists of three assemblies of fifteen copper cylinders each. During the destructive test to demonstrate hydrodynamic tunneling each target was irradiated with high intensity beam. The beam on the first target was very wide and no hydrodynamic motion was expected to happen. On the contrary the beam on target 2 and 3 was very narrow so significant hydrodynamic motion was expected.

The experiment uses a new type of diamond detection system (diamond crystal + electronics) designed for applications where a high radiation pulse is created. The new design was developed at CERN in collaboration with a private company. The system performed very well during the experiment. However, there is still room for improvements in the design: a re-design of the high voltage side is suggested to avoid bias voltage changes during high irradiation.

The experiment was also a good opportunity to test new types of instrumentation for high radiation environments: SEM detectors, strain gauges and temperature probes. Strain gauges successfully captured data during the experiment but its analysis is not cover in this thesis. The signal from the SEM detectors does not resemble the expected. Further analysis of the signal is required. Temperature probes were very sensitive to radiation and vibration from the table.

Results of the experiment are consistent with hydrodynamic tunneling of protons: FLUKA simulations ignoring tunneling deviate from the results of the experiment for targets 2 and 3; results from FLUKA-BIG2 taking into account tunneling are in good agreement with the observations.

The uncertainties in the experiment results can be improved; in particular the extension of the molten zone could only be predicted with limited accuracy. New methods are needed to reduce the measurements uncertainty: ultrasound, hard X-rays. A new simulation campaign started, with the same beam parameters as in the experiment, as the initial simulations were performed for slightly different beam parameters. First results confirm experimental data. Nevertheless, we believe that hydrodynamic tunneling has been observed and this result gives confidence to the methodology used for the LHC and SPS calculations with FLUKA and BIG2 codes. Work is ongoing to along these ideas to improve the comparison between simulations and experiment, and the results will be published in a future paper.

A lot has been learned during the preparation and realization of the experiment. This experiment has laid the foundation for more complex future experiments.

Bibliography

[1] Particle Data Group, Institute of Physics Publishing, http://pdg.lbl.gov/, "Review of particle physics."

[2] B. Rossi, *High Energy Particles.* Englewood Cliffs, NJ: Prentice-Hall, 1952.

[3] J.H. Hubbell, H. Gimm, and I. Øverbø, "Pair, Triplet, and Total Atomic Cross Sections (and Mass Attenuation Coefficients) for 1 MeV 100 GeV Photons in Elements Z=1 to 100," *J. Phys. Chem.*, vol. Ref. Data 9, p. 1023, 1980.

[4] A. Veyssiere et al. *Nucl. Phys.*, vol. A159, p. 561, 1970.

[5] H. Spieler, "Silicon Detectors," in *Detector Techniques*, 1998.

[6] D. Kramer et al., *Design and Implementation of a Detector for High Flux Mixed Radiation Fields.* PhD thesis, Liberec Tech. U., Liberec, 2008.

[7] H. Spieler, *Semiconductor detector systems.* Semiconductor Science and Technology, Oxford: Oxford Univ. Press, 2005.

[8] R. S. Sussmann, *CVD diamond for electronic devices and sensors.* John Wiley & Sons, 2009.

[9] O. S. Brüning, P. Collier, P. Lebrun, S. Myers, R. Ostojic, J. Poole and P. Proudlock, "LHC Design Report Volume 1," tech. rep., CERN-2004-003-V-1, CERN, Geneva, 2004.

[10] F. G. J. Incandela and R. Heuer, "CERN Conference: New boson observed announcement, ATLAS announcement: http://www.atlas.ch/news/2012/latest-results-from-higgs-search.html, CMS announcement: http://cms.web.cern.ch/news/observation-new-particle-mass-125-Gev," 2012.

[11] V. Shiltsev et al., "Achievements And Lessons From Tevatron," in *Proc. International Particle Accelerator Conference, San Sebastian, Spain*, 2011.

[12] S. G. for Future High Energy Projects, *The CERN design study for a 300-GeV proton synchrotron.* Rerpot No. CERN-AR-Int-SG-63-22, CERN, Geneva., 1963.

[13] D. A. Edwards and M. J. Syphers, *An introduction to the Physics of High Energy Accelerators.* Wiley Beam Phys. Accel. Technol., New York, NY: Wiley, 1993.

[14] H. Wiedemann, *Particle accelerator physics.* Springer, 2007.

[15] G.W. Hill, "On the Part of the Motion of Lunar Perigee Which is a Function of the Mean Motions of the Sun and Moon," *Acta Math*, vol. 8, p. 1–36, 1886.

[16] A. Ferrari, and P.R. Sala , "Physics of showers induced by accelerator beams," in *Proc. 1995 "Frédéric Joliot" Summer School in Reactor Physics, Cadarache, France*, (Cadarache, France), "Frédéric Joliot" Summer School in Reactor Physics, August Aug. 1995.

[17] A. Ferrari and P.R. Sala, "The Physics of High Energy Reactions," in *Proc. Workshop on Nuclear Reaction Data and Nuclear Reactors Physics, Design and Safety, Miramare-Trieste, Italy*, 1996.

[18] H.A. Bethe, "Zur Theorie des Durchgangs schneller Korpuskularstrahlen durch Materie," *Ann. Physik*, vol. 5, pp. 325–400, 1930.

[19] H.A. Bethe, "Bremsformel fuer Elektronen relativistischer Geschwindigkeit," *Z. Phys.*, vol. 76, pp. 293–299, 1932.

[20] H.A. Bethe and W. Heitler, "On the stopping of fast particles and on the creation of positive electrons," *Proc. Roy. Soc.*, vol. A146, pp. 83–112, 1934.

[21] F. Bloch, "Zur Bremsung rasch bewegter Teilchen beim Durchgang durch die Materie," *Ann. Phys.*, vol. 16, p. 287, 1933.

[22] F. Bloch, "Bremsvermoegen von Atomen mit mehreren Elektronen," *Z. Phys.*, vol. 81, pp. 363–376, 1933.

[23] F. Bloch, "Zur Bremsung rasch bewegter Teilchen beim Durchgang durch die Materie," *Ann. Phys.*, vol. 16, p. 287, 1933.

[24] G. Z. Molière, "Theorie der Streuung schneller geladener Teilchen II. Mehrfach- und Vielfachstreuung," *Z. Naturforsch*, vol. 3a, pp. 78–97, 1948.

[25] H. A. Bethe, "Molière's Theory of Multiple Scattering," *Physical Review*, vol. 89, pp. 1256–1266, March 1953.

[26] Y.S. Tsai, "Pair production and bremsstrahlung of charged leptons.," *Rev. Mod. Phys.*, vol. 46, p. 815, 1974.

[27] T. Ferbel, *Experimental Techniques in High Energy Physics.* Addision-Wesley, 1987.

[28] G. Battistoni et al., "The FLUKA code: Description and benchmarking," in *Proc. Hadronic Shower Simulation Workshop 2006*, Fermilab, September 2006.

[29] A. Fasso et al., "The FLUKA code: present applications and future developments," in *Conf. on Computing in High Energy and Nuclear Physics, La Jolla, USA*, 2003.

[30] Energy & Technology Review, https://www.llnl.gov/etr/pdfs/12_94.5.pdf, "Science on the NIF," tech. rep., 1994.

[31] N. R. C. Committee on High Energy Density Plasma Physics, Plasma Science Committee, *Frontiers in High Energy Density Physics: The X-Games of Contemporary Science*. National Academies Press, ISBN-10: 030908637X, Apr. 2003.

[32] J. E. Bailey et al., "Experimental investigation of opacity models for stellar interior, inertial fusion, and high energy density plasmas," *Physics of Plasmas*, vol. Vol. 16 Issue 5, p. 058101, May 2009.

[33] N. A. Tahir et al., "Prospects of warm dense matter research at HiRadMat facility at CERN using 440 MeV SPS proton beam," *High Energy Density Physics*, vol. 9, p. 269, 2013.

[34] N. A. Tahir et al., "The Large Hadron Collider and the Super Proton Synchrotron at CERN as Tools to Generate Warm Dense Matter and Non–Ideal Plasmas," *Plasma Phys.*, vol. 51, p. 299, 2011.

[35] N. A. Tahir et al., "Generation of warm dense matter and strongly coupled plasmas using the High Radiation on Materials facility at the CERN Super Proton Synchrotron," *Physics of Plasmas*, vol. 16, p. 082703, 2009.

[36] V. E. Fortov, et al., "Numerical simulations of nonstationary fronts and interfaces by the Gudonov method in moving.," *Nucl. Sci. Eng.*, vol. 123, p. 169, 1996.

[37] S. K. Godunov, "A Difference Scheme for Numerical Solution of Discontinuous Solution of Hydrodynamic Equations," *Math. Sbornik*, vol. 47, pp. 271–306, 1959.

[38] C. Hirsch, *Numerical Computation of Internal and External Flows*. ISBN-10: 0471924520, Apr. 1990.

[39] J. Wenninger and R. Schmidt, "Protection against accidental beam losses at the LHC," in *Proc. 21st IEEE Particle Accelerator Conference, Knoxville, TN, USA*, May 2005.

[40] J. B. Jeanneret et al., "Quench levels and transient beam losses in LHC magnets," Tech. Rep. LHC-Project-Report-44, CERN Technical Rerport: LHC-PROJECT-REPORT-044, May 1996.

[41] S. Wagner et al., "A Failure Catalogue for the LHC," in *Proc. 2nd International Particle Accelerator Conference, San Sebastian, Spain*, Sep 2011.

[42] R. Schmidt and J. Wenninger, "LHC Injection Scenarios," tech. rep., LHC-PROJECT-NOTE-287, CERN, 2002.

[43] V. Kain, *Machine Protection and Beam Quality during the LHC Injection Process*. PhD thesis, Vienna University of Technology, Viena, 2005.

[44] T. Kramer and B. Goddard, *LHC Beam Dump System: Analysis of beam commissioning, performance and the consequences of abnormal operation.* PhD thesis, Graz, Tech. U., Graz, 2011.

[45] N.V. Mokhov, et al., “Machine-induced Backgrounds: their origin and loads on ATLAS/CMS,” in *Proc. LHC Workshop on Experimental Conditions and Beam-Induced Detectors Backgrounds, CERN, Geneva, Switzerland*, May 2008.

[46] R. Bruce, “Collimation margins and beta*,” in *Proc. LHC Collimation Review 2011, CERN, Geneva*, 2011.

[47] R. W. Assmann et al., “The final collimation system for the LHC,” in *Proc. EPAC, Edinburgh, Scotland*, 2006.

[48] E. B. Holzer et al., “Beam Loss Monitoring System for the LHC,” in *Proc. IEEE Nuclear Science Symposium Conference Record*, 2005.

[49] K. Dahlerup-Petersen et al., “The Protection System for the Superconducting Elements of the Large Hadron Collider at CERN,” in *Proc. 18th Biennial Particle Accelerator Conference, New York, NY, USA*, 1999.

[50] R. Schmidt et al., “Protection of the CERN Large Hadron Collider.,” *New J. Phys.*, vol. 8, p. 290. 31 p, 2006.

[51] M. Zerlauth, “Magnet powering with zero downtime - a dream?,” in *Proc. Chamonix Workshop on LHC Performance, Chamonix, France*, 2012.

[52] B. Todd, *A Beam Interlock System for CERN High Energy Accelerators.* PhD thesis, Brunel U., West London, 2006.

[53] V. Kain et al., “Beam induced damage - What is a safe beam?,” in *Proc. Chamonix 2009 Workshop on LHC Performance, Chamonix, France*, 2009.

[54] A. Bertarelli et al., “Limits for Beam Induced Damage: Reckless or too Cautious?,” in *Proc. Chamonix Workshop on LHC Performance, Chamonix, France*, 2011.

[55] M. Cauchi et al., “High Energy Beam Impact Tests on a LHC Tertiary Collimator at CERN HiRadMat Facility,” in *Proc. 4th International Particle Accelerator Conference, Shanghai, China*, May 2013.

[56] A. Bertarelli et al., “First Results of an Experiment on Advanced Collimator Materials at CERN HiRadMat Facility,” in *Proc. 4th International Particle Accelerator Conference, Shanghai, China*, May 2013.

[57] F. Sonnemann, *Resistive transition and protection of LHC superconducting cables and magnets.* PhD thesis, RWTH Aachen U., Geneva, 2001.

[58] M. Santana, et. al., “Energy Deposition Studies for the Betatron Cleaning Insertion (IR7) of LHC,” in *Proc. 21st IEEE Particle Accelerator Conference, Knoxville, TN, USA*, May 2005.

[59] S. Marque, et al., “Connection Cryostats For LHC Dispersion Suppressors,” in *Proc. 9th European Particle Accelerator Conference, Lucerne, Switzerland* (S. Proceedings of EPAC 2004, Lucerne, ed.), Jul 2004.

[60] “A. Verweij. Private Communication..”

[61] “R. Schmidt. Private Communication..”

[62] I. Efthymiopoulos et al., “HiRadMat: A New Irradiation Facility for Material Testing at CERN,” in *Proc. 2nd International Particle Accelerator Conference, San Sebastian, Spain*, Sep. 2011.

[63] CERN, “CERN Safety rules: Safety Regulation SR-C Chemical Agents, https://edms.cern.ch/file/940853/LAST_RELEASED/SR-C_E.pdf,” 2011.

[64] SGL Group, “SIGRABOND 1501g Specification, https://www.sglgroup.com/cms/_common/downloads/products/product-groups/gs/sintering-plate-charging-systems/SIGRABOND_Carbonfaserverstaerkter_Kohlenstoff_und_Graphit_e.pdf.”

[65] E.B. Podgorsak, *Radiation Oncology Physics: A Handbook for Teachers and Students*. International Atomic Energy Agency, ISBN-10: 9201073046, Sep. 2005.

[66] A. Ferrari, et al., “Conceptual Design of a Vacuum Window at the Exit of the CLIC Post-Collision Line,” *Phys. Rev. A*, vol. 12, p. 0210001, Feb 2009.

[67] M. Monteil, J. Blanco and R. Veness, “A transparent vacuum window for high-intensity pulsed beams,” *Vacuum*, vol. 85, pp. 1165–1169, 2011.

[68] T. Deville and B. Versolatto, “Mesure de degasage de composites Carbone-Carbone,” tech. rep., CERN/LHC Vacuum. Technical Note 98-22, 1998.

[69] V. Kain, “Damage Levels: Comparison of Experiment and Simulation,” in *Proc. 2nd LHC Project Workshop, CERN, Geneva, Switzerland*, 2005.

[70] N. A. Tahir et al., “Impact of high energy high intensity proton beams on targets: Case studies for Super Proton Synchrotron and Large Hadron Collider,” *Phys. Rev. ST Accel. Beams*, vol. 15, p. 051003, May 2012.

[71] D.C. Wilson et al., “Hydrodynamic Calculations of 20-TeV Beam Ineractions with the SSC Beam Dump,” in *Proc. 15th IEEE Particle Accelerator Conference, Washington, DC, USA*, May 1993.

[72] G.I. Kerley, “Multi–Component, Multi–Phase Equation of State for Carbon, Sandia Nat. Lab. Rep.,” 2001. SAND2001-2619.

[73] N.A. Tahir et al., “Large Hadron Collider at CERN: Beams Generating High-Energy-Density Matter,,” *Phys. Rev. E*, vol. 79, p. 046410, 2009.

[74] N.A. Tahir et al., “Numerical simulations and theoretical analysis of proposed heavy-ion-matter experiments at the GSI Darmstadt accelerator facility,” *Phys. Plasmas*, vol. 5, p. 4426, 1998.

[75] N.A. Tahir et al., “Heavy-ion-beam-induced hydrodynamic effects in solid targets,” *Phys. Rev. E*, vol. 60, p. 4715, 1999.

[76] N.A. Tahir et al., “Shock compression of condensed matter using intense beams of energetic heavy ions,” *Phys. Rev. E*, vol. 61, p. 1975, 2000.

[77] N.A. Tahir et al., “Metallization of hydrogen using heavy-ion-beam implosion of multi-layered cylindrical targets,” *Phys. Rev. E*, vol. 63, p. 016402, 2001.

[78] N.A. Tahir et al., “Necessity of bunch compression for heavy-ion-induced hydrodynamics and studies of beam fragmentation in solid targets at a proposed synchrotron facility,” *Phys. Rev. E*, vol. 63, p. 036407, 2001.

[79] N.A. Tahir et al., “Influence of the equation of state of matter and ion beam characteristics on target heating and compression,” *Phys. Rev. ST Accel. Beams*, vol. 6, p. 020101, 2003.

[80] N.A. Tahir et al., “Proposal for the study of thermophysical properties of high-energy-density states in matter using current and future heavy ion facilites at the GSI Darmstadt,” *Phys. Rev. Lett*, vol. 95, p. 035001, 2005.

[81] S. Udrea et al., “Measurements of electrical resistivity of heavy ion beam produced high energy density matter: Latest results for lead and tungsten,” *Nucl. Instr. Meth. A*, vol. 577, p. 257, 2007.

[82] N.A. Tahir et al., “Interaction of Super Proton Synchrotron Beam with Solid Copper Target: Simulations of Future Experiments at HiRadMat Facility at CERN,” *Nucl. Inst. Meth. A*, vol. 606, p. 186, 2009.

[83] N.A. Tahir et al., “Generation of plane shocks using intense heavy ion beams: Application to Richtmyer–Meshkov instability growth studies,” *Phys. Plasmas*, vol. 18, p. 032704, 2011.

[84] A. V. Bushman and V. E. Fortov *Sov. Tech. Rev. B Therm. Phys.*, vol. 1, p. 219, 1987.

[85] I. V. Lomonosov et al., “Multi-phase equation of state for aluminum,” *Laser Part. Beams*, vol. 25, p. 567, 2007.

[86] I. V. Lomonosov and N.A. Tahir, "Theoretical Investigation of Shock Wave Stability in Metals," *Appl. Phys. Lett*, vol. 92, p. 101905, 2008.

[87] J. Blanco Sancho et al., "An Experiment At HiRadMat: Irradiation Of High-Z Materials," in *Proc. 2nd International Particle Accelerator Conference, San Sebastian, Spain*, 2011.

[88] J. Blanco Sancho et al., "HiRadMat Low Intensity Beam Commissioning," tech. rep., CERN Internal Note: CERN-ATS-Note-2011-055 PERF, CERN. Geneva, ATS Department, Jul 2011.

[89] "V. Kain. Private Communication.."

[90] "B. Goddard. Private Communication.."

[91] "M. Meddahi. Private Communication.."

[92] J. Blanco Sancho et al., "HiRadMat High Intensity Beam Commissioning," tech. rep., CERN Internal Note: CERN-ATS-Note-2011-126 PERF, CERN, Geneva. ATS Department, Nov 2011.

[93] C. Hessler et al., "Results from the HiRadMat Primary Beam Line Commissioning," in *Proc. 2nd International Particle Accelerator Conference, San Sebastian, Spain*, Sep 2011.

[94] "N. A. Tahir. Private Communication.."

[95] E. Griesmayer et al., "A Fast CVD Diamond Beam Loss Monitor for LHC," in *Proc. 10th European Workshop on Beam Diagnostics and Instrumentation for Particle Accelerators, Hamburg, Germany*, May 2011.

[96] CIVIDEC instrumentation GmbH, http://www.cividec.at/home.html.

[97] "International Temperature Standard ITS90, http://www.bipm.org/utils/en/pdf/ITS-90.pdf."

[98] "D. Deboy. Private Communication.."

[99] S. Evrard, "Technical & Safety review HiRadMat Experiment: HRMT-12 LPROT.".

[100] F. Burkart et al., "Diamond Particle Detector Properties during High Fluence Material Damage Tests and their Future Applications for Machine Protection in the LHC," in *Proc. 4th International Particle Accelerator Conference, Shanghai, China*, May 2013.

[101] E. Griesmayer et al., "Test of the LHC DIAMOND Beam Loss Monitors," in *CERN Internal Note: CERN-ATS-Note-2011-048 TECH*, Jun. 2011.

[102] "F. Burkart and N.A. Tahir Private Communication.."

[103] "C. Theis Private Communication.."

[104] J. Blanco Sancho et.al., "Results of an Experiment on Hydrodynamic tunneling at the SPS HiRadMat," in *Proc. 4th International Particle Accelerator Conference, Shanghai, China*, May 2013.

[105] A. Bertarelli et al., "An Experiment to Test Advanced Materials Impacted by Intense Proton Pulses at CERN HiRadMat Facility," tech. rep., CERN Technical Note: CERN-ATS-Note-2013-005 TECH, ATS Department, CERN, Geneva, 2013.

Personal Information:

Date of birth: 24 July 1981
Marital Status: single
Telephone: +34 620248429
Email: pafate@gmail.com
Address: Principe Asturias 22, bajo C, 28221, Majadahonda, Madrid (Spain)

Education:

1984 - 1999 Los Robles School (Madrid, Spain).
C/ Osa Mayor nº 239 Aravaca 28023 Madrid, Spain.

- **College title and Secondary School title. (Titulo Bachillerato Superior y COU).**

1999-2004 Master Bachelor, Industrial Engineering (ICAI Universidad Pontificia de Comillas)

- Industrial Engineering Bachelor of Engineering, Master of Engineering (5 years).
- Master Project:
  Real time tracking system and captured of moving objects by a PUMA robot arm. (9.5/10)

2009 - 2013 Doctoral Student in Physics at CERN and Ecole Polytechnique Federale de Lausanne (EPFL).

The PhD thesis *"Machine Protection and High Energy Density States in Matter for High Energy Hadron Accelerators"*.

Other knowledge:

Conferences:

- 4th International Particle Accelerator Conference, Shanghai, China, 2013, "Results of an Experiment on Hydrodynamic tunneling at the SPS HiRadMat"

Papers:

- N. A. Tahir, J. Blanco Sancho et al., "Impact of high energy high intensity proton beams on targets: Case studies for Super Proton Synchrotron and Large Hadron Collider," Phys. Rev. ST Accel. Beams, vol. 15, p. 51003,May 2012.
- M. Monteil, J. Blanco Sancho, R. Veness, "A transparent vacuum window for high-intensity pulsed beams", Vacuum 85 (2011) 1165-1169
- J. Blanco Sancho, C. Maglioni, R. Schmidt, N. A. Tahir, "An experiment at HiRadMat: Irradiation of high-Z materials", IPAC 2011, San Sebastian, Spain.
- J. Blanco Sancho et al., "HiRadMat High Intensity Beam Commissioning," tech. rep., CERN Internal Note: CERN-ATS-Note-2011-126 PERF, CERN, Geneva. ATS Department, Nov 2011.
- J. Blanco Sancho et al., "HiRadMat Low Intensity Beam Commissioning," tech. rep., CERN Internal Note: CERN-ATS-Note-2011-055 PERF, CERN. Geneva, ATS Department, Jul 2011.
- N. A. Tahir, J. Blanco Sancho, R. Schmidt, A. R. Piriz and A. Shutov, "LHC Beam Impact on Materials Considering the Time Structure of the Beam", IPAC 2011, San Sebastian, Spain.
- C. Hessler, M. Arruat, J. Bauche, K. Bestmann, J. Blanco Sancho, et al., "Results from the HiRadMat Beam Line Commissioning", IPAC 2011, San Sebastian, Spain.
- N. A. Tahir, A. Shutov, V. Kim, J. Blanco Sancho, R. Schmidt, and A.R. Piriz, "LHC and SPS at CERN as Tools to Study Warm Dense Matter in the Laboratory", IFSA2011, Bordeaux-Lac, France.
- N. Tahir, J. Blanco, R. Schmidt. 46th ICFA Advanced Beam Dynamics Workshop. "An Experiment at SPS-HiRadMat as a Tool to Study Beam-Matter Interaction".
- B. Todd, R. Schmidt, M. Zerlauth, B. Puccio, A. Dinius, J. Blanco. "The CERN Beam Interlock System" for the ISCS.

Courses:

- JUAS 2010 (Joint Universities Accelerator School), 4th January to 5th February, 2010 at Archamps France rated with an ETCS grade A.
- High-Energy-Density-Physics (HEDP) Summer School, 26th July to August 1st, 2009 at University of California, Los Angeles (UCLA).
- FLUKA Course (A fully integrated particle physics MonteCarlo simulation package), June 23-27, 2008 at CERN Geneva. FLUKA has many applications in high energy experimental physics and engineering, shielding, detector and telescope design, cosmic ray studies, dosimetry, medical physics and radio-biology.
- USPAS (U.S. Particle Accelerator School), "Laser Plasma Accelerators" June 16-20, 2008 at Annapolis, Maryland rated with "*Outstading*".
- CAS (CERN Accelerator School), "Beam Diagnostics", 28 May - 6 June 2008 at Gif-sur-Yvette, France. In collaboration with SOLEIL.
- USPAS (U.S. Particle Accelerator School), "Fundamentals of Charged Particle Optics in High Energy Accelerator" rated with "*Outstading*". January 14-25, 2008 at Santa Rosa, California.
- Course "Safety Systems", January 2007, CERN.
- Comprehensive VHDL for FPGA Design by CADENCE, December 3-7, 2007 at CERN.

Languages:

English, French.

Professional engineering programs:

- Fluka, MAD X, Matlab, LabView, Altium, P-cad, Autocad, Autocad Inventor, Gams, Opera Vector Field, Derive, pSpice, StatGraphics, ISE Xilinx, Synplify, Modelsim.

Programming languages:

- Matlab, C, python, Sql, VHDL.

Professional experience:

2001 to 2004, Aragon architecture and projects, Undergraduate Engineer.

Worked for Aragon architecture studio aiding in the realization of plots, normative specifications and specifications for office and home buildings.

2004 to spring 2006, Invesyde, Electric Consulting Engineer.

Worked for Invesyde, an engineering consulting company, managing and developing projects for the leading companies of the Spanish electrical sector. (Iberdrola Enterprise, Alabe, Foret,…)

June 2006 to December-2008, CERN (European Organization for Nuclear Research), Protection System Engineer.

Worked for CERN in collaboration with a Spanish Research Institute CIEMAT. Joined the AB Division team responsible for LHC Machine Interlocks. Started working for the Powering Interlock System, which protects the superconducting LHC Magnets from quenches and then for the Beam Interlock System, which protects the LHC from damage due to beam losses.

Spring 2008 started doing energy deposition studies for different beam loss scenarios concerning the Machine Protection of LHC.

March 2009 to June 2012, CERN Physics PhD Student.

Started as doctoral student on applied physics attached to the Ecole Polytechnique Federale de Lausanne (EPFL). Since Apr-09 I have been working on my PhD thesis at TE/MPE/PE. During this period, I have participated in the Beam Commissioning of the TT66 line, made studies of bus-bar quenches, TCT collimators, diamond detectors and high-density high-intensity beam-matter interaction.

2013 to date, R&D and Energy Trading.

Currently works on its own companies (Ledesma Energia S.L. , Happy Monkey S.L.) dedicated to energy trading and R&D. Also, works as director of R&D in Invesyde S.L.